

Processing and Field Cycling Impacts on the Properties and Performance of Ferroelectric Hafnium Oxide Thin Films

A
Dissertation
Presented to
the faculty of the School of Engineering and Applied Science
University of Virginia

in partial fulfillment
of the requirements for the degree
Doctor of Philosophy

by

Samantha Tomiko Jaszewski

August 2023

Approval Sheet

This
Dissertation
is submitted in partial fulfillment of the requirements
for the degree of

Doctor of Philosophy

Author: Samantha Tomiko Jaszewski

Advisor: Dr. Jon F. Ihlefeld

Committee Member: Dr. Stephen J. McDonnell

Committee Member: Dr. Petra Reinke

Committee Member: Dr. Arthur W. Lichtenberger

Committee Member: Dr. Steven Consiglio

Accepted for the School of Engineering and Applied Science:

A handwritten signature in black ink that reads "Jennifer L. West". The signature is written in a cursive style with a large initial 'J' and 'W'.

Jennifer L. West, School of Engineering and Applied Science

August 2023

Dedication

To my family

Abstract

Since the first report of ferroelectricity in hafnium oxide (HfO_2) doped with SiO_2 in 2011, significant research efforts have been directed toward understanding the switchable spontaneous polarization in this material. HfO_2 is chemically compatible with silicon, is currently used as a high- κ dielectric in complementary metal-oxide semiconductor (CMOS) devices, and in the ferroelectric phase, is not susceptible to the thickness scaling effects that impose application limitations on traditional ferroelectrics. Thus, this material presents opportunities for technological developments in devices, such as renewed scaling of ferroelectric random access memory (FeRAM), ferroelectric field effect transistors (FeFETS), and new devices such as ferroelectric tunnel junctions (FTJs) that previously required epitaxial growth.

The wide-scale adoption of ferroelectric HfO_2 into devices is constrained, in part, by an inability to prepare phase-pure films. In equilibrium at room temperature and atmospheric pressure, HfO_2 exists in the nonpolar monoclinic phase. Multiple metastable phases exist, including a polar orthorhombic phase, an antipolar orthorhombic phase, and a nonpolar tetragonal phase, each of which can be stabilized by various factors. Ferroelectricity in HfO_2 has been attributed to the polar $Pca2_1$ orthorhombic phase. Several factors have been shown to impact phase constitution, including dopant type and concentration, biaxial stress, oxygen vacancies, and film thickness or grain size. The work in this dissertation will show the results of an evaluation of the use of deposition and processing parameters to tailor film properties to better understand and control the factors that stabilize the ferroelectric phase in this material.

First, a process for the deposition of ferroelectric HfO_2 films using high-power impulse magnetron sputtering (HiPIMS) is developed. Since oxygen vacancies significantly affect the performance of ferroelectric HfO_2 -based thin films, the impact of plasma oxygen content during HiPIMS deposition of HfO_2 films is investigated. It is shown that the oxygen content in the plasma directly relates to the oxygen content in the films, and this oxygen content has a strong influence on phase formation and ferroelectric performance. The oxygen vacancy concentration plays a larger role in phase stability than grain size at this approximately 20 nm size scale. Neutral oxygen vacancies, which are often overlooked in the literature, are also identified in crystalline HfO_2 films. These results demonstrate that oxygen content can be used to dictate phase nucleation in HfO_2 films.

Next, infrared (IR) spectroscopy is demonstrated as a means by which phases can be unambiguously assessed in this material system. While grazing-incidence X-ray diffraction (GIXRD) is commonly used to distinguish between phases, it has difficulty unambiguously differentiating between the ferroelectric orthorhombic phase and other metastable phases that may exist. Using three HfO₂ films consisting primarily of the monoclinic, polar orthorhombic, and antipolar orthorhombic phases, respectively, the unique signatures of each phase are identified using synchrotron nano-Fourier transform infrared spectroscopy (nano-FTIR) measurements. Vibrational spectroscopy is demonstrated as a means to characterize phases present in this material.

Ion bombardment is assessed using two methods – during film growth via the HiPIMS pulse width and irradiation of HfO₂ and hafnium zirconium oxide (HZO) films with 2.8 MeV Au²⁺. The HiPIMS pulse width, which affects the ionization fraction of the depositing species, is shown to alter nucleation behavior and the phases that form during crystallization. Similarly, heavy ion irradiation is demonstrated to affect nucleation and the phases that form in films grown by atomic layer deposition (ALD), although this method also results in the crystallization of the films.

One challenge facing this material is the so-called “wake-up” effect in which the remanent polarization increases with field cycling. Many mechanisms have been hypothesized to be responsible for this effect; using nano-FTIR measurements, it is proven here that phase transformations contribute to this effect. Further, the evolution of film stress during wake-up is quantified for the first time.

Ultimately, stabilization of the ferroelectric phase in HfO₂-based thin films is necessary for the implementation of this material into devices; the findings presented here offer insight into the mechanisms of phase stability in this material and provide engineering strategies to produce ferroelectric HfO₂-based devices with robust properties.

Acknowledgements

I would like to start by thanking my advisor, Dr. Jon Ihlefeld, for his mentorship, and encouragement throughout my time as a PhD student in the Materials Science and Engineering Department at the University of Virginia. Without him, none of this work would have been possible. I will always admire his work ethic, problem-solving skills, and leadership abilities. Under his guidance, and with the opportunities he has provided me, I have not only grown as a researcher but also developed many technical and non-technical skills that will undoubtedly help me throughout my career. I also need to thank my undergraduate research advisor, Dr. Fazel Tafti, from the Physics Department at Boston College. The undergraduate research experience I gained from working with Dr. Tafti inspired me to pursue a PhD and gave me the research foundation I needed to be successful.

It is difficult to express how grateful I am to have been a part of such a supportive, hard-working, kind, funny, and talented research group. It was a pleasure to have had the experience of walking into empty labs and assembling deposition systems, setting up equipment, and, most importantly, bending a lot of tubes with my lab mates Dr. Shelby Fields and Ian Brummel who were there from the start. Since then, the Ihlefeld Multifunctional Thin Film Group has grown significantly. More recent additions to the group include Alejandro Salanova, Dr. Takanori Mimura, Liron Shvilberg, Lauren Askew, Gabby Niculescu, Megan Lenox, and Benjamin Aronson. I have always been able to depend on my research group for help in the lab, stimulating research conversations, and the occasional commiseration. On top of being excellent colleagues, they have become some of my closest friends.

I would also like to acknowledge all of the professors, staff, and students in the Materials Science and Engineering department. It has been invaluable to work with them, learn from them, and collaborate. A special thanks to the Nanoscale Materials Characterization Facility staff including Dr. Diane Dickey, Dr. Helge Heinrich, Cathy Dukes, and Richard White for all of their help throughout my time at UVA. I have been fortunate to work with a number of collaborators outside of UVA through a project funded by the Semiconductor Research Corporation and as a part of an Energy Frontier Research Center (3DFeM: Center for 3D Ferroelectric

Microelectronics) funded by the Department of Energy. These collaborations have allowed me to develop a scientific network that I hope to continue expanding upon.

Last but not least, thank you to my friends (in Charlottesville and beyond) and my family. My parents, Naomi and Paul, and my brother, Ethan, have been a constant source of support, encouragement, and love, and I could not have achieved this without them.

Table of Contents

Abstract	4
Acknowledgements	6
Table of Contents	8
List of Figures	14
List of Tables	22
Chapter 1: Motivation and Outcomes	23
1.1. Motivation	23
1.2. Outcomes	23
Chapter 2: Introduction to Ferroelectricity and Ferroelectric Hafnium Oxide	25
2.1. Introduction to Ferroelectricity	25
2.1.1. Classification of Dielectric Materials	25
2.1.2. Important Features of Ferroelectricity	26
2.1.3. Ferroelectric Domains	27
2.1.4. A Brief History of Ferroelectrics	29
2.2. Ferroelectric HfO₂	30
2.2.1. Polymorphs of HfO ₂	30
2.2.2. Challenges Facing Ferroelectric HfO ₂	34
2.2.3. Factors Affecting Phase Stabilization	34
2.3. Summary	41

Chapter 3: Deposition Methods and Process Development **42**

3.4. Motivation	42
3.5. Background on Deposition Methods	42
3.5.1. Principles of Atomic Layer Deposition	42
3.5.2. Atomic Layer Deposition of Ferroelectric HfO ₂ -based Thin Films	44
3.5.3. Plasmas for Thin Film Growth	45
3.5.4. Principles of Sputtering	46
3.5.5. Pulsed DC Magnetron Sputtering and High-Power Impulse Magnetron Sputtering	47
3.5.6. Control of Microstructure by HiPIMS	50
3.6. HiPIMS Deposition of Ferroelectric HfO₂-Based Thin Films	52
3.6.1. Sputter System and Deposition Details	53
3.6.2. HiPIMS Process Development	54
3.6.3. HiPIMS Pulse Width and Plasma Oxygen Content	58
3.6.4. Challenges Associated with Reactive HiPIMS Deposition of HfO ₂ -Based Thin Films	61
3.7. Metal-Ferroelectric-Metal Capacitor Structures	62
3.7.1. Substrate, Electrode, and Contact Materials	63
3.7.2. Rapid Thermal Anneal	65
3.7.3. SC-1 Etch	65
3.8. Summary	66

Chapter 4: Characterization of HfO₂ Thin Films **67**

4.1. Motivation	67
4.2. Grazing-Incidence X-ray Diffraction	67
4.3. X-ray Reflectivity	71
4.4. Quantification of Biaxial Stress Using the Sin²Psi Technique	72
4.5. X-ray Photoelectron Spectroscopy	74
4.6. Scanning Electron Microscopy	77
4.7. Atomic Force Microscopy	78
4.8. Transmission Electron Microscopy	81
4.9. Fourier Transform Infrared Spectroscopy	82

4.10. Electrical Characterization	84
4.10.1. Polarization-Electric Field Measurement	84
4.10.2. Positive-Up, Negative-Down Measurement	84
4.10.3. Capacitance-Voltage Measurement	85
4.11. Summary	86

Chapter 5: Impact of Oxygen Content on Phase Constitution and Ferroelectric Behavior of Hafnium Oxide Thin Films Deposited by Reactive High-Power Impulse Magnetron

Sputtering **88**

5.1. Motivation	88
5.2. Abstract	89
5.3. Introduction	89
5.4. Experimental Procedures	92
5.4.1. Deposition Parameters	92
5.4.2. Characterization	93
5.5. Results and Discussion	96
5.5.1. Phase Characterization	96
5.5.2. Electrical Characterization	101
5.5.3. Microstructural Characterization	104
5.5.4. Leakage Current Measurements	108
5.5.5. Electron Energy Loss Spectroscopy	109
5.5.6. X-Ray Photoelectron Spectroscopy	112
5.5.7. Positron Annihilation Spectroscopy	114
5.6. Conclusions	119
5.7. Addendum	120
5.8. Acknowledgements	121

Chapter 6: Optical Properties as Identifiers of the Phases of Hafnium Oxide Thin Films 122

6.1. Motivation	122
6.2. Abstract	123
6.3. Introduction	124
6.4. Results and Discussion	126
6.4.1. Grazing-Incidence X-Ray Diffraction	126
6.4.2. Electrical Characterization	128
6.4.3. Transmission Electron Microscopy	130
6.4.4. Optical Band Gap Measurements	131
6.4.5. Fourier-Transform Infrared Spectroscopy	133
6.5. Conclusions	135
6.6. Experimental Methods	136
6.6.1. Sample Preparation	136
6.6.2. Characterization	137
6.6.3. Density Functional Theory Calculations	138
6.7. Acknowledgements	139

Chapter 7: Impact of High-Power Impulse Magnetron Sputtering Pulse Width on the Nucleation, Crystallization, Microstructure, and Ferroelectric Properties of Hafnium Oxide Thin Films 140

7.1. Motivation	140
7.2. Abstract	141
7.3. Introduction	141
7.4. Experimental Procedures	143
7.4.1. Deposition Parameters	143
7.4.2. Characterization	143
7.5. Results and Discussion	145
7.5.1. HiPIMS Conditions	145
7.5.2. X-ray Diffraction Characterization	148
7.5.3. Electrical Characterization	151

7.5.4. Crystallite Size and Microstructure	151
7.5.5. Discussion	155
7.6. Conclusions	156

Chapter 8: Phase Transformations Driving Biaxial Stress Reduction During Wake-Up of Hafnium Zirconium Oxide Thin Films **157**

8.1. Motivation	157
8.2. Abstract	158
8.3. Introduction	158
8.4. Results and Discussion	160
8.4.1. Electrical Characterization	160
8.4.2. Nano-Fourier Transform Infrared Spectroscopy	163
8.4.3. Measurement of Stress	165
8.4.4. Mechanisms Responsible for Stress Reduction After Wake-Up	167
8.5. Conclusions	169
8.6. Experimental Methods	170
8.6.1. Sample Preparation	170
8.6.2. AFM Tomography	170
8.6.3. Electrical Characterization	171
8.6.4. FTIR	171
8.6.5. Stress Measurement	171
8.7. Acknowledgements	171

Chapter 9: Effects of Heavy Ion Irradiation on HfO₂-Based Films **173**

9.1. Motivation	173
9.2. Introduction	173
9.3. Experimental Methods	175
9.3.1. Sample Preparation	175
9.3.2. Irradiation Conditions	175
9.3.3. Electrical Characterization	176

9.3.4. FTIR	176
9.3.5. X-ray Diffraction Measurements	177
9.4. Results and Discussion	177
9.4.1. X-ray Diffraction	177
9.4.2. Electrical Measurements	179
9.4.3. FTIR	182
9.5. Discussion	183
9.6. Conclusions	184
<u>Chapter 10: Future Work</u>	<u>185</u>
10.1. Nano-FTIR measurements of Hf_{1-x}Zr_xO₂ Thin Films	185
10.2. Ion Irradiation Effects in HfO₂-Based Thin Films	187
<u>Conclusions</u>	<u>189</u>
<u>References</u>	<u>191</u>

List of Figures

Figure 2.1: Classification of 32 point groups according to crystallographic symmetry.	25
Figure 2.2: Theoretical diagram of energy, U , as a function of polarization, P , for ferroelectric materials, with and without an applied electric field.	26
Figure 2.3: Polarization-electric field hysteresis loop for a ferroelectric material with the remanent polarization and coercive field labeled. The cartoon crystal structures in the top right and bottom left illustrate the shift in the position of the cation which results in a net dipole.	27
Figure 2.4: Illustration of a) a ferroelectric material with a uniform polarization, P_s , producing a depolarization field, E_d , and b) a ferroelectric material with 180° domains of opposite P_s in a more energetically favorable configuration.	29
Figure 2.5: Hf-O phase diagram adapted from Shin et al. ³⁰	31
Figure 2.6: HfO ₂ pressure-temperature phase diagram determined from Rietveld refinement of <i>in situ</i> synchrotron X-ray diffraction measurements taken under high pressure and high temperature adapted from Ohtaka <i>et al.</i> ³¹ Dotted lines represent assumed phase boundaries.....	32
Figure 2.7: Crystal structures of the polymorphs observed to be present in HfO ₂ -based thin films.	33
Figure 2.8: Computationally predicted phase dependence on grain size and zirconium content of 9 nm thick HZO films ³³ shown on the x and y axes, with experimentally measured grain size distribution from a 10 nm thick Hf _{0.5} Zr _{0.5} O ₂ film ³⁶ on the z axis.	35
Figure 2.9: Periodic table of the elements with dopants shown to promote ferroelectricity in HfO ₂ -based materials shown highlighted in orange.	38
Figure 3.1: General ALD process that consists of a precursor dose, a purge to remove unreacted precursor and reaction byproducts, an oxidation step, and a purge to remove unreacted oxidant and reaction byproducts. This process is repeated until the desired thickness is obtained.....	43
Figure 3.2: Oxford FlexAL II ALD system used for deposition of HZO thin films.	45

Figure 3.3: Schematic diagram of magnetron sputtering	47
Figure 3.4: Duty cycle vs. peak power density for different sputtering regimes including pulsed DC, modulated pulsed power (MPP), and high-power impulse magnetron sputtering (HiPIMS). The dashed line indicates the DC sputter limit, or target damage threshold. Adapted from Gudmundsson <i>et al.</i> ¹¹⁵	49
Figure 3.5: Adaptation of the extended structure diagram proposed by Anders. ¹³³ Axis values are provided for orientation reference and do not represent quantitative values. The black rectangle represents the region targeted for the HiPIMS depositions of HfO ₂	51
Figure 3.6: Sputter system used for HiPIMS depositions of HfO ₂ -based thin films.	54
Figure 3.7: Instantaneous plasma current and voltage waveforms during HiPIMS depositions of HfO ₂ with varied (a) pulse width, (b) pulse frequency, and (c) oxygen content in the plasma. ..	55
Figure 3.8: θ - 2θ X-ray diffraction patterns for thick HfO ₂ films deposited by HiPIMS with a 40 μ s pulse width, 200 Hz pulse frequency, and varying oxygen content. The indices for the tetragonal, polar orthorhombic, and monoclinic phases are shown below the data.	56
Figure 3.9: Grazing-incidence X-ray diffraction patterns for HfO ₂ films (approximately 20-40 nm thick) deposited by HiPIMS with a 40 μ s pulse width, 200 Hz pulse frequency, and varying oxygen content. The indices for the tetragonal, polar orthorhombic, and monoclinic phases are shown below the data.	57
Figure 3.10: Grazing-incidence X-ray diffraction patterns for a 9 nm thick HfO ₂ film before and after rapid thermal annealing at 600 °C in N ₂ for 30 s. The indices for the tetragonal, polar orthorhombic, and monoclinic phases are shown below the data.....	58
Figure 3.11: Grazing-incidence XRD patterns for 20 nm thick HfO ₂ films deposited by HiPIMS with varying pulse widths and plasma oxygen content. Monoclinic phase fractions increase as pulse width decreases and plasma oxygen content increases.	60
Figure 3.12: Polarization-electric field measurements after field cycling for 20 nm thick HfO ₂ films deposited by HiPIMS with varying pulse widths and plasma oxygen content.....	60

Figure 3.13: GIXRD patterns for 20 nm thick HfO ₂ films deposited with identical deposition conditions, deposited between August 2020 and May 2021.....	62
Figure 3.14: Process flow for fabrication of a metal-ALD ferroelectric-metal capacitor structure used for electrical characterization of ferroelectric HfO ₂ -based thin films.	63
Figure 3.15: Shadow mask designs used to pattern contacts onto HfO ₂ -based thin films.....	65
Figure 4.1: GIXRD patterns as a function of incident angle (ω) collected from a 20 nm thick HZO thin film. As the incident angle is increased, a shift in peak position is observed.	69
Figure 4.2: GIXRD pattern collected from a 20 nm thick HZO film, with the fit from LIPRAS superimposed. Indices for the possible phases present are shown above the plot.....	70
Figure 4.3: Geometries of out-of-plane and in-plane XRD measurements.	71
Figure 4.4: X-ray reflectivity profile of a 20 nm thick HfO ₂ thin film on 85 nm of TaN on Si with important features labeled.....	72
Figure 4.5: Measurement set up and geometry of area detector X-ray diffraction measurements for $\sin^2\psi$ analysis.	74
Figure 4.6: Hf 4 <i>f</i> and O 1 <i>s</i> XPS spectra acquired from a 20 nm thick HfO ₂ film. The spectra are fit using KolXPD software.....	75
Figure 4.7: Hf 4 <i>f</i> core levels for HfO ₂ films with varying oxygen content, with the intensity normalized to the Hf 4 <i>f</i> _{7/2} peak maximum. The inset shows the tail of the Hf 4 <i>f</i> _{7/2} peak where evidence of a Hf ³⁺ peak reside.	76
Figure 4.8: Plan-view secondary electron SEM image of a 20 nm thick HZO film deposited by HiPIMS.	78
Figure 4.9: AFM topography image of a 20 nm thick HfO ₂ thin film deposited by HiPIMS.	80

Figure 4.10: AC mode scan of an HZO film with electrodes consisting of 5 nm of Pt on top of 5 nm of TaN that has undergone 20 passes of with a diamond-coated tip in contact mode to selectively thin a 5 x 5 μm area on the electrode.	81
Figure 4.11: Pulse sequence for a positive-up, negative-down measurement.	85
Figure 4.12: Relative permittivity (left axis) and loss tangent (right axis) versus electric field for a 20 nm thick HZO film.	86
Figure 5.1: GIXRD patterns for as-deposited films.	97
Figure 5.2: GIXRD patterns of crystallized HfO ₂ samples with varying oxygen content in the plasma. Indexing for each peak is provided above the panel.	98
Figure 5.3: Relative o+t phase fractions (closed circles) and crystallite sizes (open squares) calculated from GIXRD patterns.	99
Figure 5.4: Area detector XRD measurements for crystallized (a) 7.1, (b) 7.4, (c) 7.6, and (d) 8.0 % films.	100
Figure 5.5: High temperature XRD measurements of films deposited with equivalence of (a) 7.4, (b) 7.6, and (c) 8.0 % oxygen.	101
Figure 5.6: Nested polarization hysteresis measurements after field cycling for the samples deposited with oxygen plasma concentrations of (a) 7.4 %, (b) 7.6 %, and (c) 8.0 %. (d) Remanent polarization from PUND (closed circles) and relative permittivity (open squares) versus % O ₂ in the plasma.	103
Figure 5.7: Nested polarization hysteresis measurements for the samples deposited with (a) 7.4 % O ₂ , (b) 7.6 % O ₂ , and (c) 8.0 % O ₂ before field cycling. (d) Relative permittivity versus % O ₂ in the plasma.	104
Figure 5.8: Plan-view SEM images of films with varying oxygen content during deposition..	105
Figure 5.9: Average lateral grain size calculated using the line-intercept method on the plan-view SEM micrographs with error bars representing 95 % confidence intervals.	105

Figure 5.10: Dark-field TEM images of annealed samples deposited with (a) 7.4, (b) 7.6, and (c) 8.0 % oxygen in the plasma. The red, blue, and green colors correspond to data collected for different electron beam rotations about the optic axis.	106
Figure 5.11: Leakage current density measurements for annealed films deposited with 7.4, 7.6, and 8.0 % oxygen in the sputtering atmosphere.	108
Figure 5.12: (a) Single-scattered core-loss EELS spectra showing the O-K ionization edge of films deposited with 7.4, 7.6, and 8.0 % oxygen. (b) Doublet peaks (A and B) at the edge onset with normalized maximum intensity of peak B.	110
Figure 5.13: Low-loss EELS spectra for hafnium oxide with varying oxygen. The grey line marks the center of the plasmon peak for the 8.0 % sample.	110
Figure 5.14: EELS spectra showing the Hf-M edge used for stoichiometry calculations of annealed films deposited with 7.4, 7.6, and 8.0 % oxygen in the sputtering atmosphere.	112
Figure 5.15: Hf 4 <i>f</i> core levels for (a) amorphous and (b) crystalline films with the intensity normalized to the Hf 4 <i>f</i> _{5/7/2} peak maximum. The insets show the tail of the Hf 4 <i>f</i> _{7/2} peak where evidence of a Hf ³⁺ peak resides.	114
Figure 5.16: (a) Positron annihilation spectroscopy S versus W parameters for amorphous and crystalline samples. Error bars are smaller than marker size. S parameter versus % O ₂ in the plasma for (b) amorphous and (c) crystalline samples.	117
Figure 6.1. GIXRD patterns of the films annealed under different conditions to achieve majority polar orthorhombic (o-p), antipolar orthorhombic (o-ap), and monoclinic phases (m). Indices for peak positions of these phases, in addition to the tetragonal phase (t), are shown at the top of the figure.	128
Figure 6.2. Nested polarization hysteresis measurements for pristine films consisting primarily of the (a) polar orthorhombic phase, (b) antipolar orthorhombic phase, and (c) monoclinic phase. Relative permittivity (left axis) and loss tangent (right axis) versus electric field for (d) polar orthorhombic, (e) antipolar orthorhombic, and (f) monoclinic films.	130

Figure 6.3. Antipolar (<i>Pbca</i>) and polar (<i>Pca21</i>) orthorhombic atomic models view along [001] and [100] zone axis, respectively (a). ADF (b and c) and dDPC images at low (d and e) and high (f and g) magnifications for both antipolar and polar films, respectively.	131
Figure 6.4. Tauc plots of $\alpha^{1/2}$ as a function of photon energy to obtain the indirect optical bandgap energies (E_g) of HfO ₂ films consisting primarily of the (a) polar orthorhombic phase, (b) antipolar orthorhombic phase, and (c) monoclinic phase.	132
Figure 6.5: (top) Normalized phase spectra of HfO ₂ films for the polar, antipolar, and monoclinic films as obtained by nanoFTIR. (middle) Positions of phase maxima in the experimental spectra compared to (bottom) positions predicted from theory. ⁴³	134
Figure 7.1: HiPIMS voltage and current waveforms collected during the deposition of the films with 50, 80, 110, and 140 μ s pulse widths.....	146
Figure 7.2: Hf 4 <i>f</i> and O 1 <i>s</i> XPS spectra for the HfO ₂ films deposited with 50, 80, 110, and 140 μ s pulse widths. The spectra are fit using KolXPD software.	147
Figure 7.3: Positive ion-to-neutral ratio calculated from the deposition rates of positive ions + neutrals to neutrals alone.	148
Figure 7.4: <i>In-situ</i> high-temperature XRD measurements of films deposited with (a) 50, (b) 80, (c) 110, and (d) 140 μ s pulse widths.	149
Figure 7.5: (a) GIXRD patterns for films deposited with 50, 80, 110, and 140 μ s pulse widths, rapid thermal annealed at 800 °C, and the (b) relative o+t phase fractions calculated from the GIXRD measurements.	150
Figure 7.6: Nested polarization hysteresis measurements after field cycling for the samples deposited with (a) 50 μ s, (b) 80 μ s, (c) 110 μ s, and (d) 140 μ s pulse widths.	151
Figure 7.7: In-plane XRD patterns for films deposited with 50, 80, 110, and 140 μ s pulse widths.....	152
Figure 7.8: Crystallite size calculated from in-plane and out-of-plane XRD measurements.	153

Figure 7.9: Plan-view SEM images of films deposited with (a) 50, (b) 80, (c) 110, and (d) 140 μs pulse widths.	154
Figure 7.10: AFM topography images of films deposited with (a) 50, (b) 80, (c) 110, and (d) 140 μs pulse widths.	154
Figure 7.11: Average lateral grain size calculated using the line-intercept method on the AFM images with error bars representing 95% confidence intervals.	155
Figure 8.1: (a) $P(E)$ response and (b) remanent polarization from PUND as a function of field cycling.	161
Figure 8.2. (a) Relative permittivity and loss tangent measured at 2.5 MV/cm as a function of field cycling. (b) Intrinsic relative permittivity, ϵ_{init} , and irreversible Rayleigh coefficient, α' , as a function of field cycling.	162
Figure 8.3. Normalized nano-FTIR phase of individual capacitors cycled from the pristine state to 10^6 square waves.	163
Figure 8.4: (a) PFM image taken after poling the sample with +10 V (top left) and -10 (bottom right), and leaving two intrinsic regions unbiased (bottom left and top right). (b) nano-FITR reflectance that shows reflection differences in the regions that were biased.	164
Figure 8.5: Nano-FTIR phase spectra of HZO films that underwent bias via PFM in an inert atmosphere. An increase in the feature at 750 cm^{-1} indicates that more polar orthorhombic phase is forming.	165
Figure 8.6: t+o d -spacing (filled in points, left axis) and normalized t+o intensity (open points, right axis) dependence on ψ angle and associated linear fit (red lines) used to calculate the post-processing biaxial stress states for the capacitors cycled with (a) 0, (b) 1, (c) 10, (d) 10^2 , (e) 10^3 , (f) 10^4 , (g) 10^5 , and (h) 10^6 square waves.	166
Figure 8.7. Biaxial stress of individual HZO capacitors cycled between pristine to 10^6 cycles.	167

Figure 9.1: Simulation of ion ranges and collision events for 2.8 MeV Au ²⁺ in HZO and HfO ₂	176
Figure 9.2: XRD patterns of 20 nm thick (a) HZO and (b) HfO ₂ films that underwent varying doses of 2.8 MeV Au ²⁺ irradiation, followed by a rapid thermal anneal at 600 °C.....	178
Figure 9.3: Nested polarization hysteresis measurements for HZO films that were not irradiated (a) before field cycling and (b) after field cycling with 5000 2.5 MV/cm square waves, and those irradiated with 10 ¹⁵ ions/cm ² (a) before field cycling and (b) after field cycling. Both films were rapid thermal annealed.	180
Figure 9.4: Relative permittivity (left axis) and loss tangent (right axis) versus electric field after field cycling with 5000 2.5 MV/cm square waves for HZO films that received (a) no ion dose, and (b) 10 ¹⁵ ions/cm ² (both RTA at 600 °C).	181
Figure 9.5: IR phase-signal spectra for (a) various irradiation conditions stacked, and (b) the annealed films, layered, to show the differences in their IR features.	183
Figure 10.1: Nano-FTIR phase measurements of films with compositions spanning from pure HfO ₂ to ZrO ₂ . The spectra have been offset for clarity. The ratios in the legend represent ALD Hf:Zr cycle ratios.	186
Figure 10.2: Grazing-incidence X-ray diffraction measurements of films with compositions spanning from pure HfO ₂ to ZrO ₂ . The ratios in the legend represent ALD Hf:Zr cycle ratios.	187

List of Tables

Table 2.1: Unit cell volume, lattice parameters, and Hf coordination number (CN) for the relevant phases present in HfO ₂ -based thin films; unit cell dimensions are taken from first-principles calculations performed by Batra <i>et al.</i> ³²	34
Table 2.2: Review of dopants show to promote ferroelectricity in polycrystalline HfO ₂ films deposited by chemical solution deposition (CSD) and atomic layer deposition (ALD).....	39
Table 3.1: HfO ₂ films deposited with 50, 80, 110, and 140 μs pulse widths and the corresponding ‘low,’ ‘medium,’ and ‘high’ plasma oxygen content for each one. The top row shows the instantaneous power calculated from voltage and current waveforms.	59
Table 3.2: Deposition details and conditions for electrode and contact materials used for MFM capacitors.	64
Table 5.1: Average grain size and 95% confidence interval from SEM images and average in-plane grain diameter and standard deviation from dark-field TEM images.	107
Table 5.2: Compositions of the amorphous films (from XPS) and crystallized films (from XPS and EELS).....	111
Table 6.1. Annealing conditions and resulting primary phase formed in the HfO ₂ films.....	126
Table 6.2. Predicted bandgaps of the monoclinic, polar orthorhombic, antipolar orthorhombic, and tetragonal phases calculated using DFT, and measured bandgaps for the three HfO ₂ films primarily consisting of the monoclinic, polar orthorhombic, and antipolar orthorhombic phases.	133
Table 7.1: Pulse width, pulse frequency, and plasma oxygen content used for the deposition of the HfO ₂ films, and the resulting instantaneous power and film oxygen content measured by XPS.	146

Chapter 1: Motivation and Outcomes

1.1. Motivation

Ferroelectric hafnium oxide (HfO_2) is promising for a wide range of microelectronic applications due to its silicon compatibility and improved scaling in comparison to conventional ferroelectric materials. However, before it can be integrated into devices, there are a number of challenges associated with this material that must be overcome. Many of these challenges are related to the inability to stabilize the phase responsible for ferroelectricity in this material, both during synthesis and under field cycling conditions that the material will encounter in devices. The motivation of this work is to better understand the factors that stabilize the ferroelectric phase in HfO_2 -based ferroelectric thin films and develop processing strategies to overcome these phase instabilities. These processing strategies can be used to engineer robust HfO_2 -based ferroelectric thin films for use in devices such as ferroelectric random access memory, ferroelectric field-effect transistors, and ferroelectric tunnel junctions.

1.2. Outcomes

The work shown in this dissertation resulted in the following outcomes:

- 1) The first known high-power impulse magnetron sputtering (HiPIMS) process for deposition of ferroelectric HfO_2 thin films was developed.
- 2) It was discovered that oxygen content can be used to dictate phase constitution in undoped HfO_2 thin films deposited by HiPIMS. Within a typical HfO_2 film thickness and grain size regime, the properties of ferroelectric HfO_2 thin films are highly sensitive to oxygen content. The ability to precisely control the concentration and charge of oxygen vacancies provides a path toward phase-pure ferroelectric HfO_2 .

- 3) Fourier-transform infrared spectroscopy was introduced as a method to differentiate the metastable phases in this material that were previously only distinguishable by transmission electron microscopy.
- 4) The band gaps of different phases were measured in undoped HfO₂ thin films for the first time.
- 5) It was shown that ion bombardment during HiPIMS film growth can be used to alter nucleation behavior and the phases that form during crystallization.
- 6) The evolution of stress during wake-up was quantified for the first time. It was revealed that phase transformations are, at least in part, responsible for wake-up, suggesting that phase purity in the pristine state can help eliminate instabilities during film cycling.
- 7) Heavy ion irradiation was demonstrated to affect nucleation and the phases that form in this material. It can also be used to crystallize amorphous HfO₂-based thin films at low temperatures.

Chapter 2: Introduction to Ferroelectricity and Ferroelectric Hafnium Oxide

2.1. Introduction to Ferroelectricity

2.1.1. Classification of Dielectric Materials

Dielectric materials are electric insulators that can be polarized by an electric field. Within the broad classification of dielectric materials are subclasses of materials that possess special properties, including piezoelectricity, pyroelectricity, and finally, ferroelectricity, which is the focus of this dissertation. These classifications are inherently connected to crystallographic symmetry; based upon symmetry, crystalline structures can be divided into 32 point groups,¹ as shown in **Figure 2.1**. Of the 21 non-centrosymmetric point groups, 20 of them comprise materials that are piezoelectric, meaning that the application of mechanical stress can induce a dipole moment in the material. 10 of the 20 piezoelectric point groups are additionally classified as pyroelectric and possess a spontaneous polarization whose magnitude can be controlled by temperature. The spontaneous polarization is a consequence of the unique polar axis within the crystal structure that results in a spontaneous electric dipole. Finally, a fraction of these 10 pyroelectric point groups exhibits ferroelectricity. Ferroelectricity describes a property of materials that have a spontaneous electric dipole that can be reversed by the application of an electric field. In order for a material to be defined as ferroelectric and not just pyroelectric, it must be possible to switch between the two polarization states at a sufficiently strong electric field known as the coercive field; this field must be smaller than the field at which the material undergoes dielectric breakdown. If the breakdown field is smaller than the field required to switch the polarization, then the material is only pyroelectric and not ferroelectric.

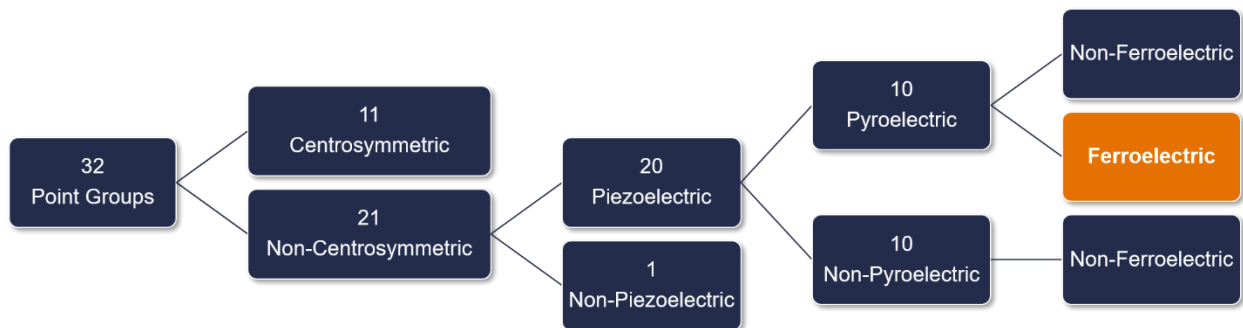


Figure 2.1: Classification of 32 point groups according to crystallographic symmetry.

The polarization in conventional ferroelectric materials has two equilibrium states which can be represented in a theoretical diagram of energy versus polarization, as shown in **Figure 2.2**. The two energy minima that represent the ‘up’ and ‘down’ states, or negative and positive spontaneous polarizations, are separated by a potential barrier. Through the application of an electric field, the potential barrier is lowered, and the polarization can be reversed.

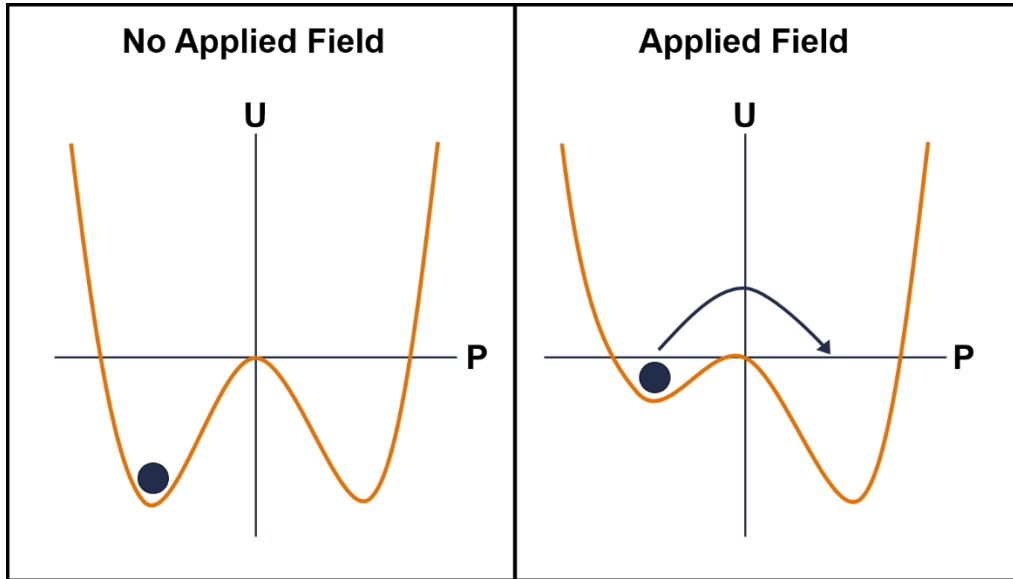


Figure 2.2: Theoretical diagram of energy, U , as a function of polarization, P , for ferroelectric materials, with and without an applied electric field.

2.1.2. Important Features of Ferroelectricity

Polarization-electric field ($P(E)$) measurements are often performed to assess ferroelectric switching in materials. These measurements result in a hysteresis loop that resembles that obtained in magnetization-magnetic field measurements of ferromagnetic materials. In fact, the term ‘ferroelectricity’ originates from the similarities in hysteretic behavior, although ferroelectric materials possess a remanent electric polarization rather than a permanent magnetic moment, and the underlying mechanisms of these behaviors differ. A typical $P(E)$ loop of a ferroelectric material is shown in **Figure 2.3**. Two important features are labeled – the coercive field (E_c) and remanent polarization (P_r). The coercive field represents the electric field at which the polarization is switched, where the net polarization is zero. The remanent polarization is defined as the polarization that remains when the applied electric field is removed. These remanent polarizations can be exploited for use as ‘0’ and ‘1’ states in memory applications. Shown in the top right- and

bottom left-hand corners of the figure are cartoon crystal structures that are used to illustrate the shift in the position of a cation up and down in the unit cell, respectively, which results in a net dipole.

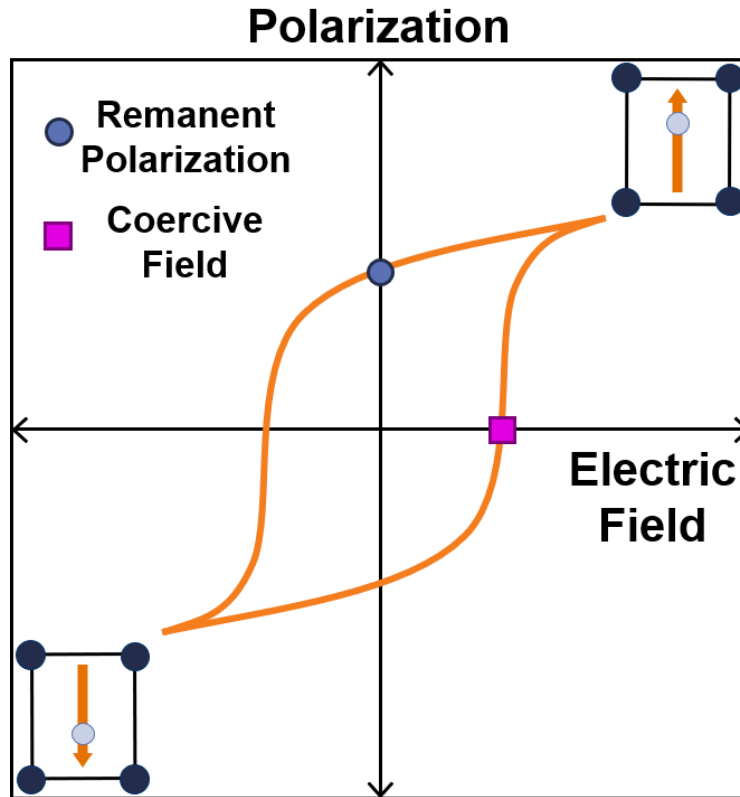


Figure 2.3: Polarization-electric field hysteresis loop for a ferroelectric material with the remanent polarization and coercive field labeled. The cartoon crystal structures in the top right and bottom left illustrate the shift in the position of the cation, which results in a net dipole.

2.1.3. Ferroelectric Domains

The switching characteristics of ferroelectric materials are highly dependent on the ferroelectric domain structure. Ferroelectric domains are regions in the material in which the ferroelectric dipoles are aligned in the same direction. These domains, separated by domain walls, may have different polarization orientations, which result in different switching characteristics. For a material with a single domain, switching often occurs at a single coercive field, resulting in a square hysteresis loop. Most often, thin film ferroelectrics have many domains. Because these domains have different switching characteristics, they possess a distribution of coercive fields that results in a tilted hysteresis loop, as is pictured in **Figure 2.3**.

Domains are formed in a process known as nucleation and growth. During nucleation, a small region with uniform polarization forms. This region grows through the movement of domain walls and continues to grow until it reaches a size determined by thermodynamics. The formation of ferroelectric domains is driven by the minimization of the total free energy of the system. The macroscopic polarization of a ferroelectric is due to a displacement of positive charge relative to negative charge. Consequently, surface charges form and produce electric fields known as depolarization fields (E_d) in the direction opposite to the polarization, as shown in **Figure 2.4**. These depolarization fields are energetically costly. In thin film ferroelectrics, the orientation of the polarization in-plane reduces these surface charges. The system can also reduce surface charges by forming domains. 180° domain walls form when the polarization direction between neighboring domains is antiparallel; these domain walls only move in response to an applied electric field and are thus classified as ferroelectric. 90° domain walls – or other angles, depending on the crystal structure – can also form; these domain walls have a strain associated with them and are considered to be both ferroelectric and ferroelastic in nature because both applied electric fields and strain can cause them to move.

The formation of domains comes at the cost of interfacial energy, and domains will form if the energy cost to form a domain is less than that associated with the electrostatic energy cost of surface charges. In thin films with mechanical boundaries due to their adhesion to substrates, domains may form to minimize mechanical strain energy. The formation of domains can also be triggered by external stimuli like the application of an electric field or intrinsic factors like defects in the material.

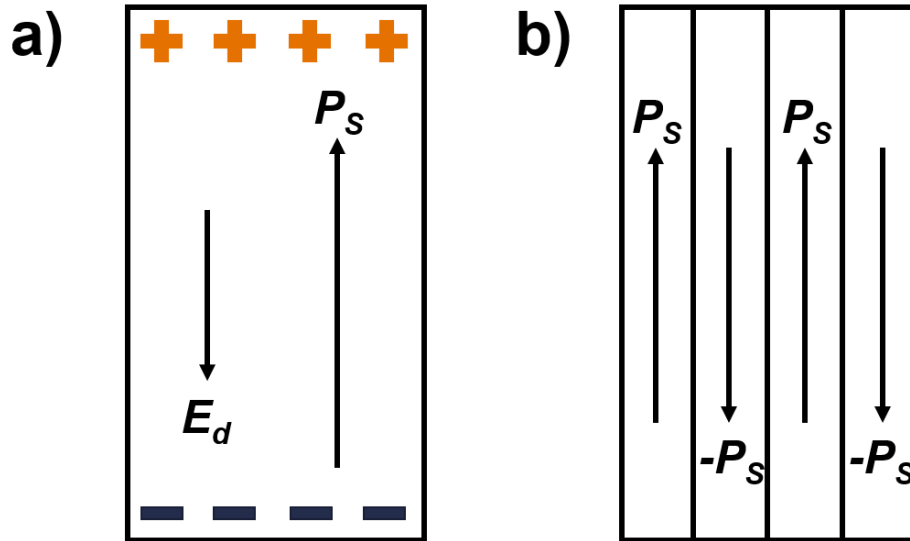


Figure 2.4: Illustration of a) a ferroelectric material with a uniform polarization, P_s , producing a depolarization field, E_d , and b) a ferroelectric material with 180° domains of opposite P_s in a more energetically favorable configuration.

2.1.4. A Brief History of Ferroelectrics

Ferroelectricity was first reported in single crystal Rochelle salt ($\text{KNaC}_4\text{H}_4\text{O}_6 \cdot 4\text{H}_2\text{O}$) by Joseph Valasek in 1921,² followed by a report of ferroelectricity in potassium dihydrogen phosphate salts (KH_2PO_4) by Busch and Scherrer in 1935.³ Due to the poor stability of Rochelle salt and potassium dihydrogen phosphate salts in atmospheric conditions, applications of these materials were limited. In the 1940s, ferroelectricity was discovered in barium titanate (BaTiO_3 , BTO) by groups in the United States, Russia, and Japan.⁴⁻⁶ Discovery of ferroelectricity in this more chemically stable inorganic perovskite material sparked interest in ferroelectric materials for applications such as capacitors in radio circuits.⁷ Since then, other perovskite-structured ferroelectric materials, including lead zirconate titanate ($\text{Pb}(\text{Zr}_{1-x}\text{Ti}_x)\text{O}_3$, PZT) and strontium bismuth tantalate ($\text{Sr}_{1-x}\text{Bi}_{2+x}\text{Ta}_2\text{O}_9$, SBT) and have been discovered and widely investigated.

Today, ferroelectrics have been commercialized for use in capacitors, sensors, actuators, transducers, energy harvesting, and non-volatile memory.^{8,9} Ferroelectrics have the potential to significantly impact the field of microelectronics with applications including ferroelectric random-access memory (FeRAM), ferroelectric field effect transistors (FeFETs), and ferroelectric tunnel

junctions (FTJs). Ferroelectric memory is advantageous in comparison to traditional random-access memory because it is non-volatile, meaning that information can be stored after power is removed. While FeRAM using perovskite ferroelectrics has been mass produced by companies including Fujitsu,^{10,11} Panasonic, Texas Instruments,¹² Rohm Semiconductor,¹³ and Ramtron International for over 20 years,¹⁴ extensive integration of ferroelectrics in microelectronics has been hindered by several factors. To start, conventional perovskite ferroelectrics are thermodynamically incompatible with silicon.¹⁵ Additionally, they have diminished ferroelectric properties below 50 nm in thickness,^{16,17} making it difficult to improve storage density and capacity and preventing their use in scaled semiconductor applications. Thus, there is a clear need for new ferroelectric materials that can overcome the limitations of traditional ferroelectrics.

2.2. Ferroelectric HfO₂

Hafnium oxide (HfO₂) has been investigated for its use in semiconductor technology for decades. Some of the properties that make it technologically interesting include its high melting temperature,¹⁸ high dielectric constant,^{19,20} large bandgap,^{21–24} and compatibility with silicon.¹⁵ One of the most significant advances using this material was in its amorphous form as a high-*k* gate dielectric to replace SiO₂ in Si-based field-effect transistors in 2007.^{25–27} In 2011, ferroelectricity was first reported in 20 nm thick HfO₂ films doped with silicon dioxide (SiO₂).²⁸ Not only does this material already exist in semiconductor fabrication facilities, but it has been shown to exhibit a ferroelectric response in films as thin as 1 nm.²⁹ In conventional perovskite ferroelectrics, ferroelectricity is suppressed in nanometer-scale thicknesses due to a number of factors that include intrinsic size effects and depolarizing fields arising from surface charges.¹⁶ However, in HfO₂ the polarization is stabilized against depolarization by polar-antipolar coupling,³⁰ and thus HfO₂ does not suffer from suppressed ferroelectricity at smaller thicknesses. Therefore, this material is promising for advancements in technology where conventional perovskite ferroelectrics have fallen short.

2.2.1. Polymorphs of HfO₂

HfO₂ can exist in various polymorphs depending on temperature, as shown in the binary phase diagram of hafnium and oxygen in **Figure 2.5**.³¹ At ambient conditions, HfO₂ exists in the monoclinic *P2₁/c* structure with seven-fold coordination. As the temperature is increased to 1743

°C, HfO₂ is transformed into the tetragonal $P4_2/nmc$ phase. Increasing the temperature to 2500 °C results in the formation of the cubic $Fm\bar{3}m$ structure. Therefore, a phase transformation from the monoclinic to tetragonal to cubic phase occurs as the temperature is increased from ambient to 2500 °C. High pressure can also induce phase transformations in this material, resulting in phases that are not present on the conventional temperature versus composition phase diagram. Using Rietveld refinement of *in situ* synchrotron X-ray diffraction measurements taken under high pressure and high temperature, Ohtaka *et al.* reported the stability of the orthorhombic $Pbca$ phase from 4 to 14.5 GPa below 1250 to 1400 °C, above which temperatures the tetragonal phase is stabilized. From 14.5 to 21 GPa, and up to 1800 °C, another orthorhombic phase, $Pmnb$, is stable.³² A pressure-temperature phase diagram based on these data is shown in **Figure 2.6**.

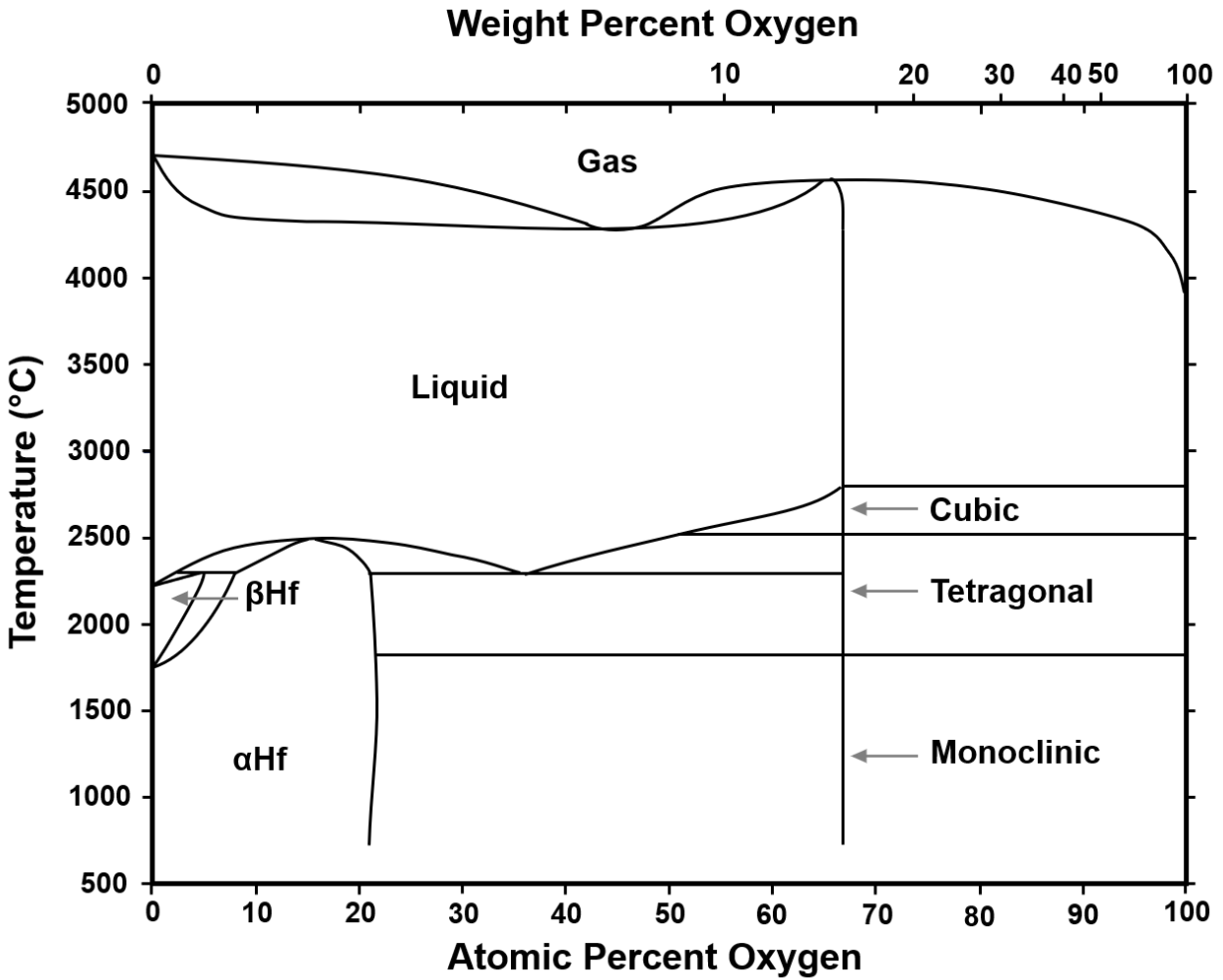


Figure 2.5: Hf-O phase diagram adapted from Shin *et al.*³¹

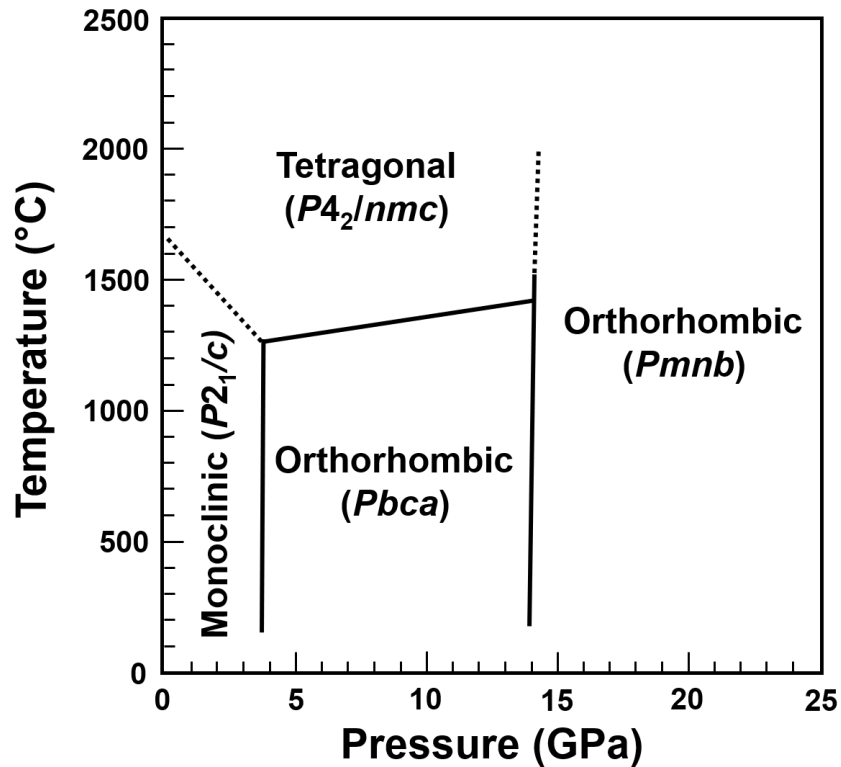


Figure 2.6: HfO₂ pressure-temperature phase diagram determined from Rietveld refinement of *in situ* synchrotron X-ray diffraction measurements taken under high pressure and high temperature adapted from Ohtaka *et al.*³² Dotted lines represent assumed phase boundaries.

All of the phases described above are centrosymmetric and, therefore, not ferroelectric. Ferroelectricity in this material has been attributed to the metastable, noncentrosymmetric orthorhombic $Pca2_1$ phase. In this structure, the oxygen atoms have two possible equilibrium positions, which correspond to a polarization direction. The application of an electric field displaces the oxygen atoms from one position to the other, resulting in polarization switching. Of the phases discussed above, not all are relevant to HfO₂ thin films. Five phases have been associated with HfO₂-based thin films – the cubic, monoclinic, tetragonal, polar orthorhombic, and antipolar orthorhombic phases. The crystal structures for the most relevant phases – the monoclinic, tetragonal, and orthorhombic phases – are shown in **Figure 2.7**, and the unit cell volume, lattice constants, and Hf coordination for these phases are provided in **Table 2.1**.

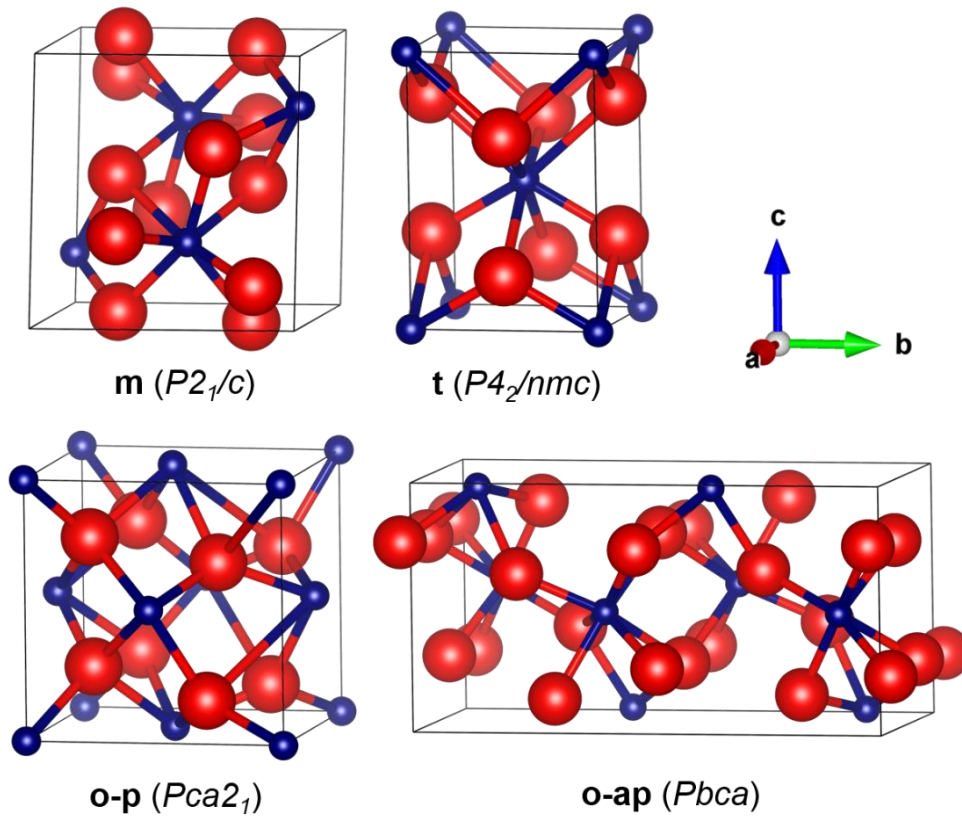


Figure 2.7: Crystal structures of the polymorphs observed to be present in HfO₂-based thin films.

Table 2.1: Unit cell volume, lattice parameters, and Hf coordination number (CN) for the relevant phases present in HfO₂-based thin films; unit cell dimensions are taken from first-principles calculations performed by Batra *et al.*³³

Phase	Space Group	Unit Cell Volume (Å ³)	Lattice Parameters (Å)	Hf ⁴⁺ CN
Monoclinic (m)	<i>P2₁/c</i>	35.15	<i>a</i> = 5.11 <i>b</i> = 5.17 <i>c</i> = 5.29	7
Tetragonal (t)	<i>P4₂/nmc</i>	33.78	<i>a</i> = 3.57 <i>b</i> = 3.57 <i>c</i> = 5.19	8
Polar Orthorhombic (o-p)	<i>Pca2₁</i>	33.90	<i>a</i> = 5.06 <i>b</i> = 5.09 <i>c</i> = 5.27	7
Antipolar Orthorhombic (o-ap)	<i>Pbca</i>	33.64	<i>a</i> = 5.03 <i>b</i> = 5.09 <i>c</i> = 5.25	7

2.2.2. Challenges Facing Ferroelectric HfO₂

Despite the benefits that HfO₂ offers over traditional ferroelectrics, the metastability of the ferroelectric phase^{33,34} remains one of the most significant challenges associated with this material.³⁵ For optimal device performance, high concentrations of the ferroelectric phase are necessary; however, often phase mixtures are often observed in HfO₂-based thin films. Four main factors have been shown to stabilize the ferroelectric phase: 1) film thickness/microstructure, 2) oxygen content, 3) dopants, and 4) biaxial stress – these factors are elaborated on below. Additionally, wake-up and fatigue, which describe the respective increase and decrease in remanent polarization with electric field cycling, are ongoing issues that are hypothesized to be related in part to phase instabilities in this material.

2.2.3. Factors Affecting Phase Stabilization

Microstructure and Film Thickness

Grain size has been shown to play a role in phase stabilization in HfO₂-based thin films because surfaces and interfaces have large contributions to the overall free energy in thin films.

Materlik *et al.* predicted that the polar orthorhombic phase is stabilized by grain radii ranging from 3-5 nm, with the tetragonal and monoclinic phases stabilized by smaller and larger grain sizes, respectively.³⁶ The relationship between phase and grain size was further evaluated by Künneth *et al.*, who determined the phase content for a given grain size and zirconium concentration in 9 nm thick hafnium zirconium oxide (HZO) thin films with columnar grain morphologies.³⁶ A phase diagram adapted from this work is shown in **Figure 2.8** with experimentally measured grain size distributions from 10 nm thick $\text{Hf}_{0.5}\text{Zr}_{0.5}\text{O}_2$ films superimposed in the third dimension with black markers.³⁷ The experimentally measured film, which exhibits ferroelectric behavior, contains large fractions of grains that fall within the experimentally predicted polar orthorhombic phase field.

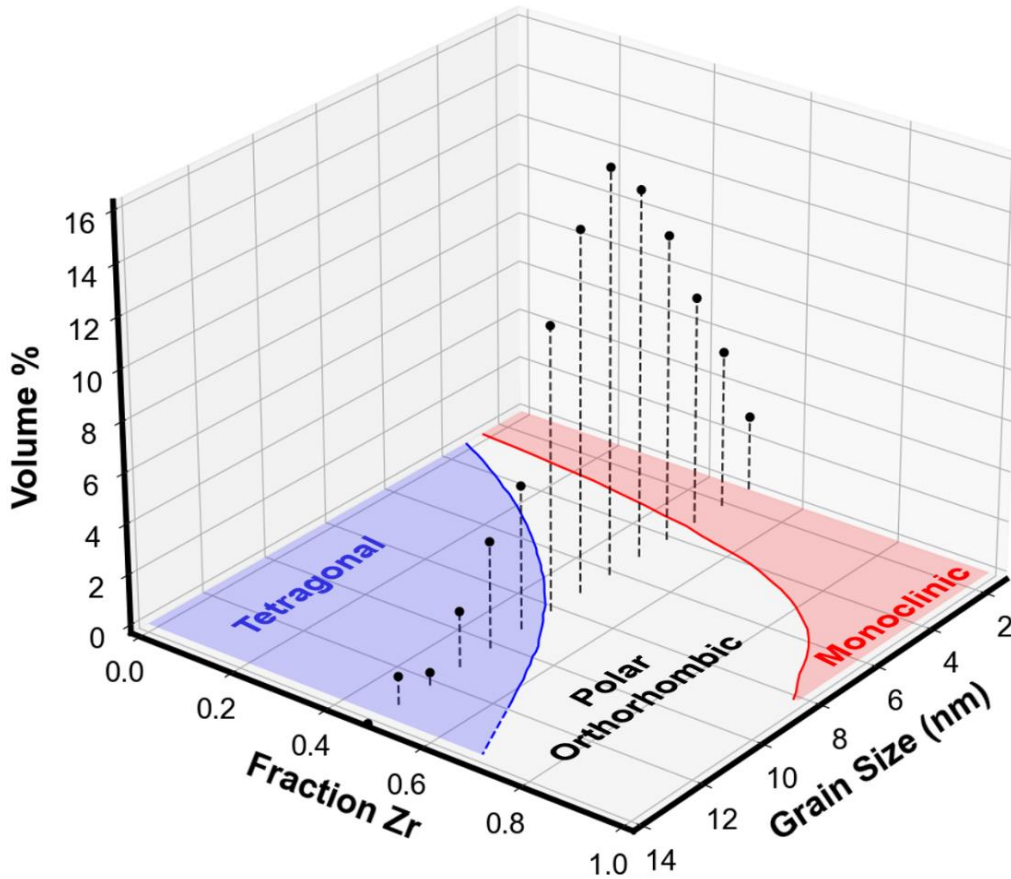


Figure 2.8: Computationally predicted phase dependence on grain size and zirconium content of 9 nm thick HZO films³⁴ shown on the x and y axes, with experimentally measured grain size distribution from a 10 nm thick $\text{Hf}_{0.5}\text{Zr}_{0.5}\text{O}_2$ film³⁷ on the z-axis.

Further supporting these computational results, degradation of the ferroelectric properties has been observed in doped HfO₂ films thicker than 20 nm due to increasing grain size with increasing film thickness which results in the stabilization of the monoclinic phase.^{38,39} However, Kim *et al.* showed that this effect could be mitigated in HZO films deposited by atomic layer deposition with thicknesses up to 40 nm by periodically inserting a 1 nm-thick Al₂O₃ interlayer that disrupts the continuous growth of the HZO. Similarly, the ferroelectric phase has been stabilized in HfO₂-based thin films deposited by chemical solution deposited (CSD) with thicknesses up to 70⁴⁰ and 136 nm⁴¹ where layer-by-layer thermal treatment during the deposition process allowed for grain size control. No film thickness dependence of ferroelectric properties was observed in Y-doped HfO₂ films deposited by pulsed laser deposition with thicknesses ranging from 10 to 930 nm;⁴² however, the films contained nanoscale crystallites. Additionally, the ferroelectric phase has been stabilized in bulk single crystals of HfO₂ stabilized with yttrium, demonstrating that ferroelectricity in this material is not limited to thin films.^{43,44} However, the crystallite size was not reported in this work; it is possible that dislocations result in traction of the lattice translational symmetry, which results in grain-like features in single crystals.

Oxygen Content

Another factor shown to impact the stability of the ferroelectric phase and the wake-up and fatigue behavior in this material is the concentration and distribution of oxygen vacancies. First-principles calculations of HfO₂ have shown that the incorporation of oxygen vacancies into the lattice reduces the total energy of the polar orthorhombic and tetragonal phases in comparison to the monoclinic phase.^{45,46} Oxygen vacancies are also involved in the field cycling behavior of these HfO₂-based thin films. Charged oxygen vacancies accumulate at electrode interfaces during processing¹⁰⁵ and redistribute into the bulk of the film during field cycling,⁴⁹ resulting in a phase transformation to the ferroelectric phase⁴⁸ and domain depinning.¹⁰⁶ This process contributes to the increase in polarization associated with wake-up.

Numerous studies have examined the impact of varying oxygen levels during the deposition process on the phase composition and ferroelectric properties of HfO₂-based ferroelectrics. Mittmann *et al.* discovered that by adjusting the oxygen flow during sputtering from a ceramic HfO₂ target, the concentration of oxygen vacancies could be controlled. They also observed that the polar orthorhombic phase was stabilized in oxygen-deficient films.⁴⁷ In the case

of HfO₂ films deposited by ALD, the duration of the oxidant dose during growth was reduced to increase the concentration of oxygen vacancies in the films, leading to a suppression of the monoclinic phase, and an increase in the polar orthorhombic phase.⁴⁸ Materano *et al.* modified the oxygen content in PVD and ALD-deposited HfO₂ films and found that higher oxygen content resulted in the stabilization of the monoclinic phase in both cases.⁴⁹ Similarly, an increasing fraction of the monoclinic phase has been shown to correlate with increasing oxygen content in zirconium-⁵⁰⁻⁵² and aluminum-doped⁵³ HfO₂ films.

Dopants

One of the most widely used methods to stabilize the ferroelectric phase in HfO₂ is the addition of dopants. The first report of ferroelectricity was made on SiO₂-doped HfO₂ thin films.²⁸ Since then, a number of cation dopants have been shown to promote ferroelectricity in this material, as summarized in **Figure 2.9** and **Table 2.2**. It must be noted that the work highlighted in Table 2.2 is not an exhaustive list of the studies that have been done on doped HfO₂ thin films; rather, they are selected to represent a fraction of the studies that have been done in this field. Additionally, they involve a number of different deposition techniques, chemical precursors, film thicknesses, electrode materials, annealing conditions, electric field cycling conditions, and measurement conditions, complicating direct comparisons between them. However, some general observations have been made.

Stabilization of the ferroelectric phase through the addition of dopants is attributed to a size mismatch between the dopant and hafnium cations, resulting in an expansion or contraction of the lattice that destabilizes the monoclinic phase.^{50,54-57} In general, it has been observed that dopants with larger ionic sizes result in films with higher remanent polarizations.^{50,57,58} Additionally, dopants have been shown to increase remanent polarizations in comparison to their undoped counterparts. Theoretical calculations found the maximum spontaneous polarization for undoped HfO₂ to range from 52 – 53 $\mu\text{C}/\text{cm}^2$,^{59,60} resulting in a maximum remanent polarization of approximately 26 $\mu\text{C}/\text{cm}^2$ for a randomly oriented polycrystalline film.⁶¹ Experimentally, the remanent polarization values of undoped polycrystalline HfO₂ films have been reported to range from 8 – 10 $\mu\text{C}/\text{cm}^2$.^{47,48,62} For polycrystalline HfO₂ films doped with Si, Y, Zr, and La, polarizations as high as 25,⁶³ 24,⁶⁴ 27,⁶⁵ and 28 $\mu\text{C}/\text{cm}^2$ ²⁵⁶ have been measured.

The ideal dopant concentration to achieve a maximum remanent polarization is below 15 mol% for most of the dopants studied. However, one main exception exists – Zr. The $\text{Hf}_{1-x}\text{Zr}_x\text{O}_2$ system displays a maximum remanent polarization at approximately 50 mol% Zr,⁶⁶ and has been shown to exhibit ferroelectricity in a compositional window of $0 < x < 0.8$.^{66–68} In addition to its wide compositional window that promotes ferroelectricity, Zr lowers the crystallization temperature of the ferroelectric phase.⁶⁶ This reduction in thermal budget is beneficial for back-end-of-line (BEOL) compatibility.

PERIODIC TABLE OF THE ELEMENTS

1 H Hydrogen 1.008																	2 He Helium 4.003
3 Li Lithium 6.941	4 Be Beryllium 9.012											5 B Boron 10.811	6 C Carbon 12.011	7 N Nitrogen 14.007	8 O Oxygen 15.999	9 F Fluorine 18.998	10 Ne Neon 20.180
11 Na Sodium 22.990	12 Mg Magnesium 24.305											13 Al Aluminum 26.982	14 Si Silicon 28.086	15 P Phosphorus 30.974	16 S Sulfur 32.065	17 Cl Chlorine 35.453	18 Ar Argon 39.948
19 K Potassium 39.098	20 Ca Calcium 40.078	21 Sc Scandium 44.956	22 Ti Titanium 47.867	23 V Vanadium 50.942	24 Cr Chromium 51.996	25 Mn Manganese 54.938	26 Fe Iron 55.845	27 Co Cobalt 58.933	28 Ni Nickel 58.693	29 Cu Copper 63.546	30 Zn Zinc 65.390	31 Ga Gallium 69.723	32 Ge Germanium 72.640	33 As Arsenic 74.922	34 Se Selenium 78.960	35 Br Bromine 79.904	36 Kr Krypton 83.800
37 Rb Rubidium 85.468	38 Sr Strontium 87.620	39 Y Yttrium 88.906	40 Zr Zirconium 91.224	41 Nb Niobium 92.906	42 Mo Molybdenum 95.938	43 Tc Technetium 98.000	44 Ru Ruthenium 101.070	45 Rh Rhodium 102.906	46 Pd Palladium 106.420	47 Ag Silver 107.868	48 Cd Cadmium 112.411	49 In Indium 114.818	50 Sn Tin 118.710	51 Sb Antimony 121.760	52 Te Tellurium 127.600	53 I Iodine 126.905	54 Xe Xenon 131.293
55 Cs Cesium 132.906	56 Ba Barium 137.327	57-71 La-Lu Lanthanides	72 Hf Hafnium 178.490	73 Ta Tantalum 180.948	74 W Tungsten 186.948	75 Re Rhenium 186.207	76 Os Osmium 190.230	77 Ir Iridium 192.227	78 Pt Platinum 195.078	79 Au Gold 196.967	80 Hg Mercury 200.590	81 Tl Thallium 204.383	82 Pb Lead 207.200	83 Bi Bismuth 208.980	84 Po Polonium 209.000	85 At Astatine 210.000	86 Rn Radon 222.000
87 Fr Francium 223.000	88 Ra Radium 226.000	89-103 Ac-Lr Actinides	104 Rf Rutherfordium 261.000	105 Db Dubnium 262.000	106 Sg Seaborgium 266.000	107 Bh Bohrium 264.000	108 Hs Hassium 277.000	109 Mt Meitnerium 278.000	110 Ds Darmstadtium 281.000	111 Rg Roentgenium 282.000	112 Cn Copernicium 285.000	113 Nh Nihonium 286.000	114 Fl Flerovium 289.000	115 Mc Moscovium 290.000	116 Lv Livermorium 293.000	117 Ts Tennessine 294.000	118 Og Oganesson 294.000
57 La Lanthanum 138.905	58 Ce Cerium 140.116	59 Pr Praseodymium 140.908	60 Nd Neodymium 144.240	61 Pm Promethium 145.000	62 Sm Samarium 150.360	63 Eu Europium 151.964	64 Gd Gadolinium 157.250	65 Tb Terbium 158.925	66 Dy Dysprosium 162.500	67 Ho Holmium 164.930	68 Er Erbium 167.259	69 Tm Thulium 168.934	70 Yb Ytterbium 173.040	71 Lu Lutetium 174.967			
89 Ac Actinium 227.000	90 Th Thorium 232.038	91 Pa Protactinium 231.036	92 U Uranium 238.029	93 Np Neptunium 237.000	94 Pu Plutonium 244.000	95 Am Americium 243.000	96 Cm Curium 247.000	97 Bk Berkelium 247.000	98 Cf Californium 251.000	99 Es Einsteinium 252.000	100 Fm Fermium 257.000	101 Md Mendelevium 258.000	102 No Nobelium 259.000	103 Lr Lawrencium 262.000			

Figure 2.9: Periodic table of the elements with dopants shown to promote ferroelectricity in HfO_2 -based materials shown highlighted in orange.

Table 2.2: Review of dopants shown to promote ferroelectricity in polycrystalline HfO₂ films deposited by chemical solution deposition (CSD) and atomic layer deposition (ALD).

Dopant	Author(s)	Deposition Method	t (nm)	Maximum Remanent Polarization Observed
Magnesium	Starschich and Boettger ⁵⁸	CSD	42	3 $\mu\text{C}/\text{cm}^2$ at 7.5 mol%
Aluminum	Starschich and Boettger ⁵⁸	CSD	42	3 $\mu\text{C}/\text{cm}^2$ at 5.2 mol%
	Müller <i>et al.</i> ⁶⁹	ALD	16	6 $\mu\text{C}/\text{cm}^2$ at 7.1 mol%
	Polakowski <i>et al.</i>	ALD	12	20 $\mu\text{C}/\text{cm}^2$ at N/A
Silicon	Böscke <i>et al.</i> ²⁸	ALD	8.5	10 $\mu\text{C}/\text{cm}^2$ at 3.1 mol%
	Yurchuck <i>et al.</i> ³⁸	ALD	9	24 $\mu\text{C}/\text{cm}^2$ at 4.4 mol%
	Richter <i>et al.</i> ⁶³	ALD	12 & 36	24 $\mu\text{C}/\text{cm}^2$ at 1.5 mol%
Cobalt	Starschich and Boettger ⁵⁸	CSD	42	3.8 $\mu\text{C}/\text{cm}^2$ at 5.2 mol%
Nickel	Starschich and Boettger ⁵⁸	CSD	42	3.8 $\mu\text{C}/\text{cm}^2$ at 5.2 mol%
Gallium	Starschich and Boettger ⁵⁸	CSD	42	~4 $\mu\text{C}/\text{cm}^2$ at 5.2 mol%
Strontium	Starschich and Boettger ⁵⁸	CSD	42	12.8 $\mu\text{C}/\text{cm}^2$ at 7.5 mol%
	Schroeder <i>et al.</i> ⁵⁰	ALD	10	~25 $\mu\text{C}/\text{cm}^2$ at ~5 mol%
Yttrium	Starschich <i>et al.</i> ⁴⁰	CSD	45	13 $\mu\text{C}/\text{cm}^2$ at 5.2 mol%
	Müller <i>et al.</i> ⁶⁴	ALD	10	24 $\mu\text{C}/\text{cm}^2$ at 5.2 mol%
Zirconium	Müller <i>et al.</i> ⁶⁶	ALD	9	17 $\mu\text{C}/\text{cm}^2$ at 60 mol%
	Lee <i>et al.</i> ⁶⁵	ALD	10	24 $\mu\text{C}/\text{cm}^2$ at 50 mol%
Indium	Starschich and Boettger ⁵⁸	CSD	42	5.2 $\mu\text{C}/\text{cm}^2$ at 5.2 mol%
Barium	Starschich and Boettger ⁵⁸	CSD	42	12.0 $\mu\text{C}/\text{cm}^2$ at 7.5 mol%
Lanthanum	Starschich and Boettger ⁵⁸	CSD	42	~14 $\mu\text{C}/\text{cm}^2$ at 5.2 mol%
	Schroeder <i>et al.</i> ⁵⁶	ALD	12	27.7 $\mu\text{C}/\text{cm}^2$ at 10 mol%
Cerium	Zheng <i>et al.</i> ⁷⁰	CSD	78	20 $\mu\text{C}/\text{cm}^2$ at 15 mol%
Neodymium	Starschich and Boettger ⁵⁸	CSD	42	~13 $\mu\text{C}/\text{cm}^2$ at 5.2 mol%
Samarium	Starschich and Boettger ⁵⁸	CSD	42	~14 $\mu\text{C}/\text{cm}^2$ at 5.2 mol%
Gadolinium	Mueller <i>et al.</i> ⁷¹	ALD	10	12 $\mu\text{C}/\text{cm}^2$ at 2 mol%
	Schroeder <i>et al.</i> ⁵⁰	ALD	10	~25 $\mu\text{C}/\text{cm}^2$ at ~5 mol%
Erbium	Starschich and Boettger ⁵⁸	CSD	42	~13 $\mu\text{C}/\text{cm}^2$ at 5.2 mol%

Biaxial Stress

Experimentally, mechanical stress has been correlated with higher polarization responses in HfO₂-based thin films.⁷² Computational studies have shown that compressive biaxial and hydrostatic stresses increase the stability of the polar orthorhombic and tetragonal phases over the monoclinic structure.⁷³⁻⁷⁵ Additionally, experimental investigations of stress effects on the material have demonstrated that these films possess tensile biaxial stress following thermal processing.^{35,57,72,76-80} These tensile stresses have been correlated with enhanced polarization resulting from larger fractions of the ferroelectric phase and alteration of the ferroelectric domain structure to yield a preferred orientation with the short, polar *b*-axis aligned out-of-plane.^{72,81}

Wake-Up and Fatigue

In addition to issues with the stability of the ferroelectric phase, HfO₂-based ferroelectrics have issues with polarization instability during electric field cycling.⁸² These increases and decreases in polarization, known as wake-up and fatigue, respectively,^{83,84} are hypothesized to result from the redistribution and generation of charged oxygen vacancies that occur during cycling.⁸⁴⁻⁸⁶ Wake-up has been shown to result from a combination of phase transformations from the tetragonal to polar orthorhombic phase,^{82,87} reductions in the concentration of pinned ferroelectric domains,^{88,89} and ferroelastic domain switching, where domains oriented with their polarization in-plane switch out-of-plane.^{90,91} More recently, Cheng *et al.* reported that wake-up coincided with a phase transformation from the antipolar orthorhombic *Pbca* phase to the polar orthorhombic *Pca2₁* phase rather than from the tetragonal to polar orthorhombic phase. Phase transformations and domain depinning during wake-up occur due to an accumulation of oxygen vacancies at the electrode interfaces during processing,⁹² which then redistribute into the bulk of the film when an electric field is applied. These oxygen vacancies stabilize the ferroelectric phase and cause domain depinning, both of which result in a higher remanent polarization. Fatigue has contributions from both phase transformations to the monoclinic phase and a rise in domain pinning that reduces the amount of switchable polarization.^{83,89,93,94}

2.3. Summary

Ferroelectric HfO₂-based thin films are poised to impact the microelectronics industry due to their scalability and silicon compatibility, which will enable technologies that were limited by conventional ferroelectric thin films. The phase responsible for ferroelectricity in this material, the polar orthorhombic $Pca2_1$ phase, is metastable, and one of the greatest challenges facing this material is understanding how to promote the stability of the ferroelectric phase to obtain optimal performance for devices. Factors such as microstructure, oxygen content, dopants, and biaxial stress have been shown to affect the stability of the ferroelectric phase; however, the interplay of these effects is still under consideration. In the following chapters, these stabilizing mechanisms will be evaluated in the context of processing and field cycling of HfO₂-based thin films to better understand how these factors can be harnessed to overcome the challenges facing this material.

Chapter 3: Deposition Methods and Process Development

3.4. Motivation

Two deposition methods were utilized to fabricate ferroelectric HfO₂-based thin films in this work – atomic layer deposition (ALD) and high-power impulse magnetron sputtering (HiPIMS). In this chapter, background information on these deposition methods is discussed. The benefits and shortcomings of each technique are identified. Since HiPIMS is a new technique for deposition of ferroelectric HfO₂, the relevant processing space was explored. Finally, a process for fabrication of metal-ferroelectric-metal devices used for electrical characterization is outlined.

3.5. Background on Deposition Methods

3.5.1. Principles of Atomic Layer Deposition

Atomic layer deposition (ALD) is a chemical vapor deposition technique that utilizes sequential, self-limiting reactions to grow thin films of various materials layer-by-layer. It is known to have a high degree of conformality and offers atomic-scale precision growth; for these reasons, ALD is commonly used in microelectronic processing.⁹⁵ A general ALD process is illustrated in **Figure 3.1**. This process consists of sequential alternating pulses of gaseous chemical precursors (often metal-organic compounds) that react with the substrate; these reactions between the precursors and substrate are known as ‘half-reactions.’ During each half-reaction, a precursor is introduced into the process chamber (with pressures in the milliTorr range), where the inorganic atom bonds with the inorganically terminated substrate surface, with the organic ligand outwardly exposed.⁹⁶ These half-reactions are self-limiting because they can only react with a finite number of reactive sites on the surface; thus, they produce no more than one monolayer. Next, the chamber is purged with an inert gas to remove unreacted precursor and the reaction byproducts. The ligand-terminated surface is then exposed to an additional precursor or oxidant, and the ligand is replaced with the new reactant species and a new ligand-terminated surface. This process is repeated for a number of cycles to achieve the desired film thickness.

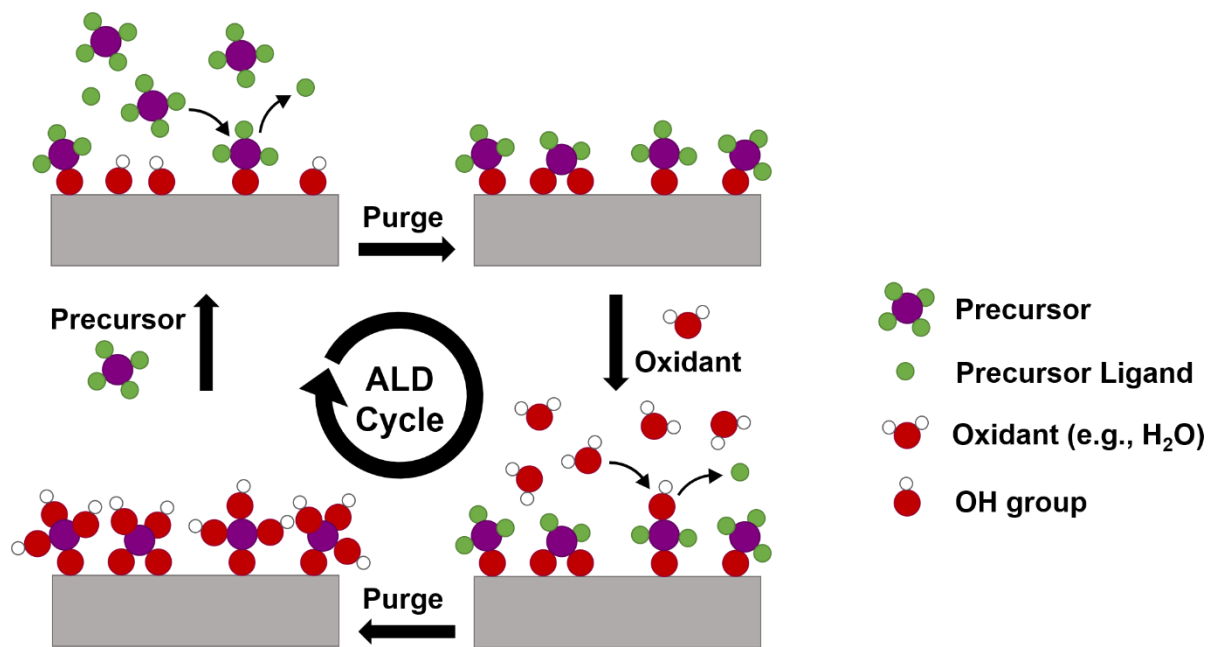


Figure 3.1: General ALD process that consists of a precursor dose, a purge to remove unreacted precursor and reaction byproducts, an oxidation step, and a purge to remove unreacted oxidant and reaction byproducts. This process is repeated until the desired thickness is obtained.

The amount of time the surface is exposed to the precursor is called the ‘dose time,’ and the time between doses during which an inert gas flows is called the ‘purge time.’ For successful ALD growth, the surface temperature must be high enough for the reactions to take place but lower than the degradation temperature of the precursor. Lower temperatures lead to slower growth due to reaction rate limitations, while high temperatures result in faster growth but can cause decomposition of the precursor. Thus, there is a careful balance between achieving fast growth while keeping the limitations of the selected precursor in mind. ALD growths typically occur below 350 °C, but the growth temperature is highly precursor-dependent.

ALD is the most commonly used deposition technique used for the fabrication of ferroelectric HfO₂-based thin films. In addition to its precise thickness control, HfO₂ is grown by ALD in semiconductor fabrication foundries for use as a high- κ dielectric.²⁵ For deposition of ferroelectric hafnium zirconium oxide (HZO) thin films, Tetrakis(ethylmethyamido)hafnium {Hf[N(CH₃)(C₂H₅)₄]₄, abbreviated as TEMA-Hf} or tetrakis(dimethylamino)hafnium {Hf[N(CH₃)₂]₄, abbreviated as TDMA-Hf}, and Tetrakis(ethylmethyamido)zirconium {Zr[N(CH₃)(C₂H₅)₄]₄, abbreviated as TEMA-Zr} or tetrakis(dimethylamino)zirconium

{Zr[N(CH₃)₂]₄, abbreviated as TDMA-Zr}, are typically used as the HfO₂ and ZrO₂ precursors, respectively. However, a wide range of precursors have been investigated for the deposition of this material.⁹⁷ Compositions are controlled by varying the ratio of Hf to Zr precursor cycles within a super cycle. For example, a super cycle can consist of 8 cycles of HfO₂ and 2 cycles of ZrO₂; this super cycle is repeated until the desired thickness is attained. It should be noted that different materials have different growth rates, so this should be considered when determining precursor ratios in substituent films. Oxidants used for these depositions include deionized water,^{45,98,99} gaseous¹⁰⁰ and plasma oxygen,^{100–102} ozone,^{103,69,104,48,53} and hydrogen peroxide.¹⁰⁵ Of these oxidants, plasma oxygen and ozone have enhanced reactivity which can enable lower deposition temperatures.^{106,107}

3.5.2. Atomic Layer Deposition of Ferroelectric HfO₂-based Thin Films

The details for ALD depositions of HZO films shown in this work are as follows. ALD depositions were performed on an Oxford FlexAL II ALD system, shown in **Figure 3.2**. Depositions were performed with a table temperature of 260 °C. TEMA-Hf and TEMA-Zr were used as the HfO₂ and ZrO₂ precursors, respectively. TEMA-Hf was stored at 70 °C, and TEMA-Zr was stored at 85 °C. During the HfO₂ and ZrO₂ cycles, the pulse times were 1.0 and 1.5 seconds. An oxygen plasma was used as the oxidant, with 15 mTorr of oxygen pressure, and 250 and 300 W of power were used for HfO₂ and ZrO₂ cycles, respectively. Long purge times of 90 seconds were used between precursor cycles since long purge times have been shown to improve ferroelectric phase fractions.⁹⁸ X-ray reflectivity was used to determine the growth rates for HfO₂ and ZrO₂, which were 1.1 Å/cycle and 1.2 Å/cycle, respectively.



Figure 3.2: Oxford FlexAL II ALD system used for deposition of HZO thin films.

3.5.3. Plasmas for Thin Film Growth

The term ‘plasma’ was first introduced by Irving Langmuir in 1928 to describe the behavior of ionized gases in a high-current vacuum tube.¹⁰⁸ Plasma is a distinct state of matter consisting of a significant number of electrically charged particles. In a normal gas, atoms are electrically neutral. A gas can become a plasma when the addition of energy causes a significant number of atoms to lose some or all of their electrons, resulting in positively charged ions and the freed electrons. When there are a sufficient number of ionized atoms to significantly affect the electrical characteristics of the gas, it is considered a plasma. Overall, plasmas are neutral, or quasi-neutral, because they contain roughly equal numbers of positive and negative charges.¹⁰⁹

Plasma science underlies a vast number of technological applications in many industries, including the microelectronics, automotive, and medical device industries. Today, plasmas are

widely used for material processing in semiconductor and thin film applications. These applications include physical vapor deposition (PVD) and plasma-enhanced chemical vapor deposition (CVD), both of which are utilized for the fabrication of HfO₂ thin films in this work. PVD describes a number of vacuum deposition methods in which physical means, like sputtering or evaporation, are used to remove atoms from a solid and deposit those atoms on a substrate to form a thin film. In comparison, CVD techniques involve chemical reactions of gases to form a thin film; however, plasma-enhanced CVD utilizes a plasma of the reacting gases.

3.5.4. Principles of Sputtering

Sputtering is one example of PVD that involves ejecting atoms from a solid material by bombarding the target surface with energetic particles. A brief description of the sputtering process is as follows:

1. A substrate is placed in a vacuum chamber that contains a target made of the material being sputtered.
2. The chamber is evacuated and then filled with a process gas.
3. The gas is ionized with a positive charge, creating a plasma.
4. The resulting ions are strongly attracted to the target, which carries a negative charge.
5. As the ionized gas ions impact the target, target atoms are physically removed from the target and some of these removed atoms land on the substrate.

In conventional diode sputtering, electrons are created that escape the effective plasma area near the target. In order to overcome this issue, Chapin introduced the first planar magnetron sputtering device in 1974.¹¹⁰ In magnetron sputtering, magnets are placed behind the target to capture escaping electrons and confine them close to the target. This increases the density of the ionized atoms that hit the target, resulting in faster deposition rates. A schematic diagram of a typical setup for magnetron sputtering is shown in **Figure 3.3**.

First, the chamber is evacuated to high vacuum to create a low-pressure environment for sputtering and minimize contaminants. The sputtering gas is flowed into the chamber, and the total pressure is regulated. Due to its high atomic weight, argon is commonly used as a sputtering gas, and the total pressure is typically in the milliTorr range. To ignite the plasma, a high voltage is applied between the cathode behind the sputter target and the anode, which is connected as an electrical ground. Electrons in the sputtering gas are accelerated away from the cathode and collide

with nearby atoms of the sputtering gas, ionizing these gas atoms. The strong magnets behind the sputter target confine the electrons close to the target surface to increase the plasma density.¹¹¹ The positively charged ions are accelerated towards the negatively charged cathode, resulting in collisions with the target. These high-energy collisions cause atoms from the target surface to be ejected. Some of these target atoms have enough kinetic energy to reach the surface of the substrate and are deposited as a thin film of material on the substrate. For a reactive sputtering process, gases like oxygen and nitrogen can be introduced into the chamber during film growth to produce oxide and nitride films

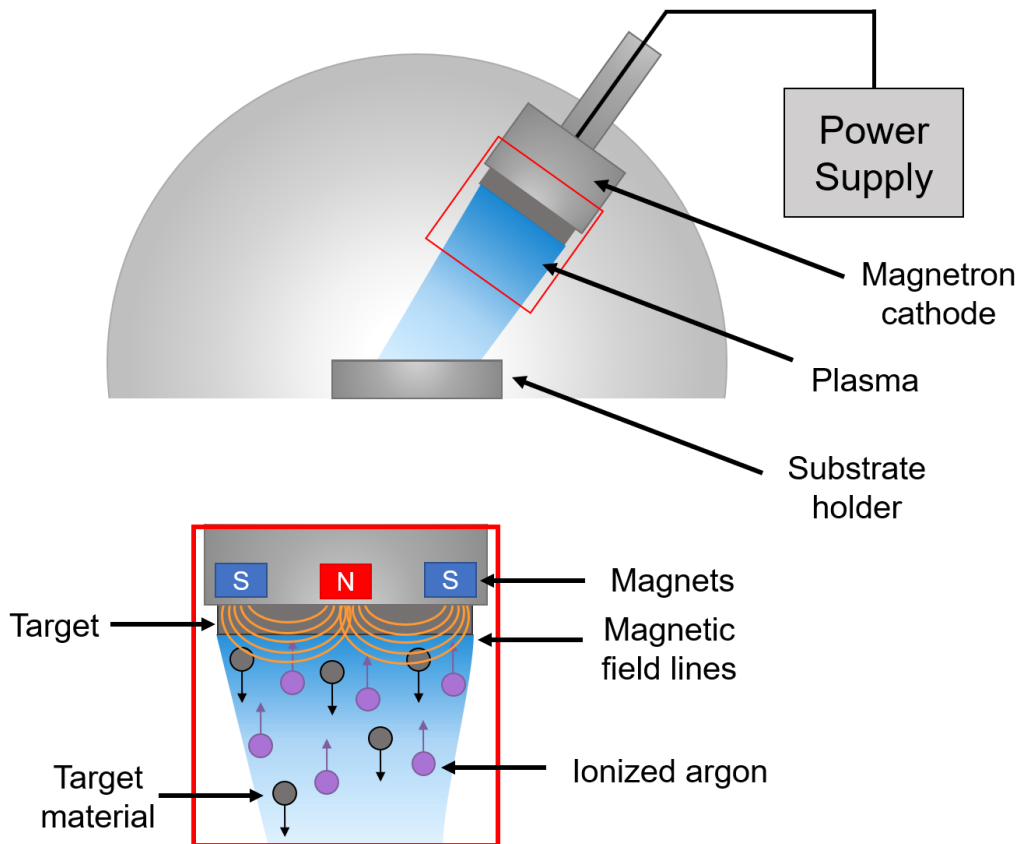


Figure 3.3: Schematic diagram of magnetron sputtering.

3.5.5. Pulsed DC Magnetron Sputtering and High-Power Impulse Magnetron Sputtering

Conventional magnetron sputtering utilizes either direct current (DC) or radio frequency (RF) power, the choice of which typically depends on the target material's resistivity. DC sputtering is commonly used for metallic targets, while ceramic and other high-resistivity targets are used in conjunction with RF sputtering. RF sputtering can be used to deposit insulating

materials (i.e., oxides) from an insulating target or via reactive sputtering. However, RF sputter rates are low in comparison to DC sputtering. Reactive DC sputtering can be challenging because as the deposition proceeds, areas on the target become covered with an insulating layer in a process known as ‘target poisoning.’ This target poisoning leads to charge accumulation until breakdown occurs in the form of an arc. These arcs can produce droplets of material which can cause defects in the film.¹¹² Target poisoning also leads to reduced deposition rates because the chemical bonds in compounds are typically stronger than metal atom bonds.¹¹³

Within the past 20 years, pulsed DC sputtering has become more common due to its ability to overcome the challenges associated with reactive sputter deposition of insulating films.¹¹⁴ During the pulsed DC sputtering process, a negative bias is applied at frequencies ranging from a few to several hundred kHz. Between pulses, a positive reverse bias is applied to remove any built-up charge that accumulates on the surface of the target, thus preventing target poisoning.¹¹² In addition to its benefits for reactive sputtering, pulsed DC sputtering allows for more control of plasma dynamics through the duty cycle and power applied to the target. These parameters enable access to a wider range of plasma densities and ion bombardment energies, which can enable deposition of films with high densities and low roughness.

One variation of pulsed DC sputtering that was developed by Kouznetsov *et al.* in the late 1990s is high-power impulse magnetron sputtering, or HiPIMS (sometimes referred to as HPPMS).¹¹⁵ In HiPIMS, low duty cycle (<10 %), high-power pulses (with power densities of several kW/cm²) are applied to the sputter target to produce dense plasmas with a high degree of sputtered atom ionization.¹¹⁶ HiPIMS pulse widths can range from 20 to 500 μ s with repetition rates of 50 to 5000 Hz. To distinguish HiPIMS from other pulsed magnetron deposition techniques, Anders defines HiPIMS as pulsed magnetron sputtering in which the peak power exceeds the time-averaged power by approximately two orders of magnitude.¹¹⁷ To further compare HiPIMS with other pulsed DC sputter techniques, **Figure 3.4** shows the duty cycle versus peak power density at the target for traditional pulsed DC sputtering, modulated pulsed power (MPP) sputtering, and HiPIMS. MPP refers to a pulsed sputtering technique in which the pulse is modulated such that in the initial stage (a few hundred microseconds), the power level is moderate, followed by a high-power pulse (a few hundred microseconds up to a millisecond). Above the DC power limit, the higher peak power densities must be compensated for by a lower duty cycle to avoid the target damage range.

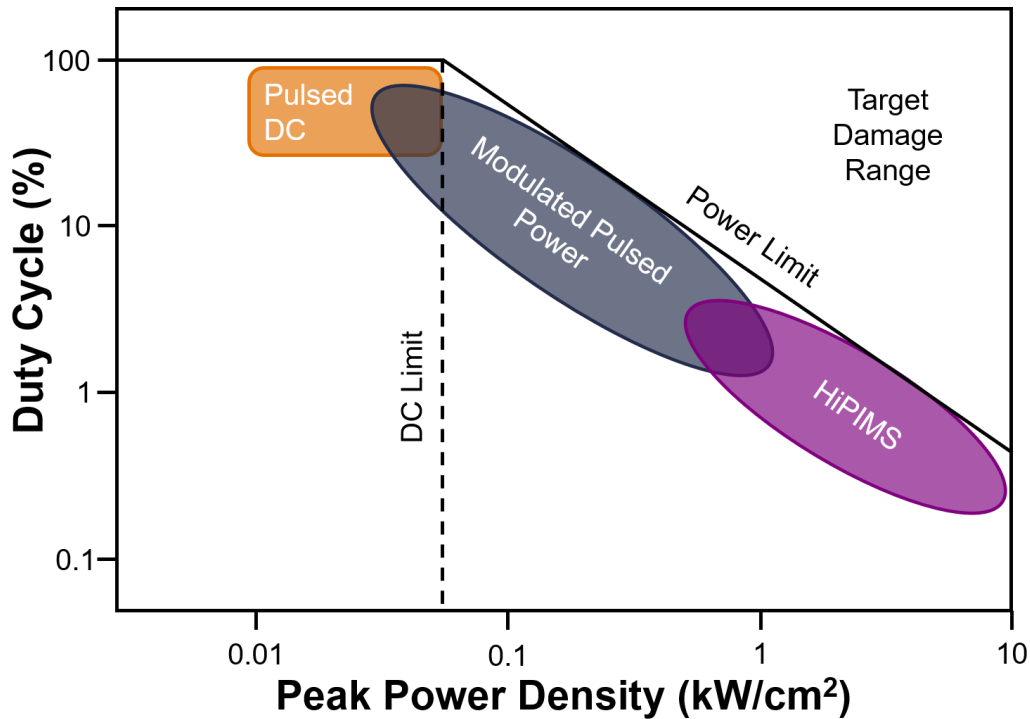


Figure 3.4: Duty cycle vs. peak power density for different sputtering regimes, including pulsed DC, modulated pulsed power (MPP), and high-power impulse magnetron sputtering (HiPIMS). The dashed line indicates the DC sputter limit, or target damage threshold. Adapted from Gudmundsson *et al.*¹¹⁶

HiPIMS offers several potential advantages over conventional sputtering techniques. First, the directionality and energy of the depositing species can be controlled through the use of a substrate bias because of the high degree of ionization of both the sputter gas and target material.^{118,119} Additionally, the energetic bombardment during the film growth facilitates the growth of films with superior properties in comparison to those deposited by conventional magnetron sputtering techniques. For example, HiPIMS has been used to obtain denser films,^{120,121} tailor film microstructure,^{122–126} and improve the mechanical^{123,127,128} and electrical properties of thin films.^{129–131}

3.5.6. Control of Microstructure by HiPIMS

To better understand how HiPIMS can impact microstructure, the structure zone diagram (SZD), sometimes referred to as the structure zone model, can be examined. The SZD is a qualitative graphical representation that illustrates the relationship between the deposition conditions and the resulting microstructure of thin films. The first structure zone model was published by Movchan and Demichishin in 1969 and was based on trends seen in the microstructure of thick evaporated coatings of Ti, Ni, W, ZrO, and Al₂O₂.¹³² The only parameter in this SZD was the homologous temperature (T_h), defined as the film growth temperature normalized by the melting temperature of the deposited film material. Movchan and Demchishin identified three main zones: fine-grained structure, columnar growth, and coalescence. In the zone of fine-grained structure ($T_h < 0.3$), films exhibit small textured grains with a significant amount of pores at grain boundaries. In the columnar growth region ($0.3 < T_h < 0.5$), films have a columnar microstructure, with grains growing perpendicular to the substrate. Finally, in the zone of coalescence ($T_h > 0.5$), the grains are large and well-connected, resulting in a continuous film. In 1974, Thornton expanded the model to magnetron-sputtered metal films; this SZD had axes of argon pressure and substrate temperature.¹³³ Since then, the SZD has evolved and expanded as new deposition technologies have been developed.

In 2010, Anders proposed an extended SZD that includes energetic deposition that is relevant for HiPIMS.¹³⁴ This SZD is shown in **Figure 3.5**. The proposed extended SZD has three axes: generalized homologous temperature (T^*), a normalized kinetic energy flux (E^*), and the net film thickness (t^*). The generalized homologous temperature accounts for the film growth temperature normalized by the melting temperature of the deposited film material. The normalized kinetic energy flux represents the displacement and heating effects caused by the kinetic energy of bombarding particles. Lastly, the net film thickness can be negative due to ion etching. Anders stresses that the number of primary physical parameters affecting growth exceeds the number of available axes in the SZD, so it can only provide an approximate and simplified illustration of the growth condition-structure relationships. This SZD consists of four main zones, shown in Figure 4.5. While distinct boundaries are shown in this SZD, in reality, the boundaries are gradual. Additionally, the axis values are provided for orientation purposes; the actual values depend on the material and many other conditions.

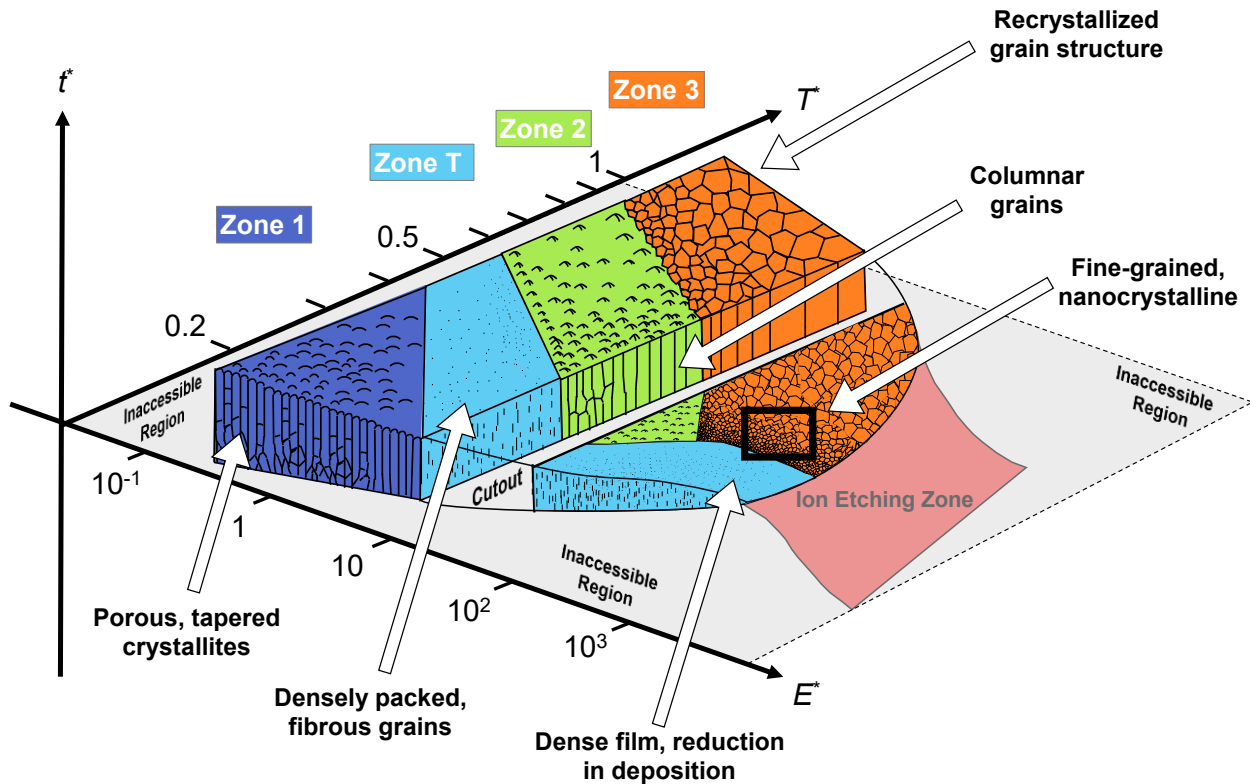


Figure 3.5: Adaptation of the extended structure diagram proposed by Anders.¹³⁴ Axis values are provided for orientation reference and do not represent quantitative values. The black rectangle represents the region targeted for the HiPIMS depositions of HfO₂.

The microstructure of a thin film is primarily determined by bulk and surface diffusion processes that are affected by the deposition temperature and energetic bombardment.¹³⁵ Conventional magnetron sputtering has limitations in accessing different regions of the SZD due to the relatively low ionization and energy of the sputtered particles. However, HiPIMS generates high-density plasma pulses by applying short, high-power pulses to the sputtering target. These pulses lead to a significant increase in the ionization of the sputtered species, resulting in a higher flux of energetic ions bombarding the growing film. This increased ionization and ion energy provide more kinetic energy to the atoms during deposition, facilitating the growth of denser films. Additionally, the ionization can be controlled by varying the pulse parameters, such as pulse duration, frequency, and voltage. By optimizing these parameters, the ion energy and flux can be tailored, enabling precise control over the film's microstructure and properties. This level of control allows for the deposition conditions necessary to access specific regions of the SZD that were

previously difficult to achieve using conventional sputtering techniques. Furthermore, the increased ion energy assists in the formation of smaller grains with reduced columnar growth since the high-energy ions can break up the columnar structure and promote the growth of smaller grains with more random orientations. As a result, HIPIMS allows for deposition conditions that favor the zone of fine-grained, nanocrystalline structure.

3.6. HiPIMS Deposition of Ferroelectric HfO₂-Based Thin Films

As previously mentioned, ALD is the most common technique used to deposit ferroelectric HfO₂-based thin films. These films are typically amorphous as-deposited and must be annealed at an elevated temperature to form the ferroelectric phase. The stochastic nature of nucleation results in films with a broad grain size distribution³⁷ and are typically multi-phase. Because conventional thermal ALD has few adjustable parameters, controlling microstructure using this method is difficult. Additionally, ALD-prepared films possess carbon impurities from residual precursor ligands, which may affect the ferroelectric properties of the films.^{103,104,136}

Therefore, other deposition techniques, such as physical vapor deposition (PVD) methods, which offer greater freedom in engineering deposition conditions, are promising candidates for the preparation of ferroelectric hafnia. To date, several reports on the PVD of HfO₂ have been made. Olsen, *et al.* reported ferroelectricity in Y-doped HfO₂ prepared by co-sputtering from HfO₂ and Y₂O₃ sources via RF sputtering,¹³⁷ Mittmann, *et al.* demonstrated ferroelectricity in undoped HfO₂ films varying in thickness from 8-40 nm deposited by RF sputtering,⁴⁷ and Mimura, *et al.* demonstrated ferroelectricity in epitaxial Y-doped HfO₂ films deposited by RF sputtering at room temperature.¹³⁸ Still, these studies, among others,^{51,139-142} leave room for exploration of this film preparation approach.

HiPIMS has been shown to be effective for reactive oxide synthesis of ZrO₂,¹⁴³ TiO₂,¹⁴⁴ ITO,¹⁴⁴ VO₂,^{145,146}, CdO,¹⁴⁷ and SiO₂.¹⁴⁸ While HiPIMS has been used for deposition of nanocrystalline HfO₂ films for optical coating applications¹⁴⁹ and amorphous HfO₂ for electronic applications,¹⁵⁰ it has not been applied to ferroelectric HfO₂ thin films before this work. The high degree of sputtered atom ionization made possible by HiPIMS is beneficial for ferroelectric HfO₂, where grain size has been tied to phase stability. As described previously, HiPIMS enables access to regions of the structure zone diagram where equiaxed nanocrystalline microstructures result, whereas traditional sputtering techniques are restricted to regions of columnar microstructure and

thus are limited in their ability to control grain size.¹³⁴ As an example, a comparison between CrN films prepared by DC sputtering and HiPIMS reveals a transition from a porous columnar morphology for the DC sputtered film to a uniform, dense, nanocrystalline structure for the HiPIMS film.¹⁵¹ Further, HiPIMS offers a number of controllable process parameters such as pulse power, pulse duration, background pressure, and gas atmosphere that all impact depositing species energy and are not accessible using conventional ALD or PVD processes.

3.6.1. Sputter System and Deposition Details

A custom 460 mm diameter spherical stainless steel vacuum chamber (**Figure 3.6**) with balanced 2" MeiVac MAK magnetron sputter guns was used for all depositions. The load-locked chamber was evacuated using a turbomolecular pump backed by a rotary vane pump. The base pressure of the system ranged from 2×10^{-7} to 7×10^{-7} Torr. The source-to-substrate distance was 80 mm, and the gun-to-substrate angle was 45° . Gas flow was controlled by Alicat Scientific mass flow controllers, and the total process pressure was controlled by a conductance flow valve located in front of the turbomolecular pump. HfO₂ films were reactively sputtered from a 2" diameter hafnium metal target of 99.9% purity, with a mixture of Ar and O₂ gases in the plasma. For HiPIMS depositions, a Starfire Impulse HiPIMS power module was used in conjunction with a DC power supply to deliver square voltage pulses. The HiPIMS current and voltage waveforms were monitored by an oscilloscope connected to the Starfire module.



Figure 3.6: Sputter system used for HiPIMS depositions of HfO_2 -based thin films.

3.6.2. HiPIMS Process Development

To begin developing a process for HiPIMS deposition of HfO_2 , the process space was explored. Three main parameters were identified – pulse width, pulse frequency, and gas atmosphere. **Figure 3.7** shows the effects of (a) pulse width, (b) pulse frequency, and (c) gas atmosphere on the instantaneous plasma voltage and current during a HiPIMS deposition of HfO_2 under constant average power conditions. It is shown that stable plasma can be obtained with a wide range of plasma oxygen concentrations, calculated by dividing the O_2 flow rate by the $\text{O}_2 + \text{Ar}$ flow rate. For a given plasma oxygen concentration, pulse duration, and frequency are directly correlated to target poisoning, with short pulses or low frequencies resulting in poisoning. **Figure 3.7(a)** shows the waveforms for a pulse duration series with a 4.8 % oxygen content in the background pressure at 200 Hz for pulse durations between 20 and 60 μs after 2 minutes of deposition. The non-saturating current for the 20 μs pulse duration is indicative of target poisoning,

in which an oxide forms on the surface of the hafnium target.¹⁵² Longer pulse durations result in saturation of the current, which is typical of self-sputtering of a metallic target during HiPIMS. These results suggested that pulse widths above 20 μs at this oxygen content could be used for the deposition of HfO_2 .

Figure 3.7(b) shows the voltage and current waveforms for a fixed pulse duration of 40 μs with a 4.8 % O_2 gas composition with the pulse frequency varied between 100 and 300 Hz after 2 minutes of deposition. The lowest frequency displays evidence of target poisoning with a non-saturating current during the pulse and voltage oscillation after the removal of the bias. Combined, these data suggest that as the time between pulses increases, oxidation of the target occurs, leading to a poisoned state. **Figure 3.7(c)** shows the voltage and current waveforms for a 40 μs pulse at 200 Hz as the oxygen content was varied between 4.8 and 9.1 % at a fixed total pressure of 5 mTorr. The current waveforms saturate in every case, suggesting that the target remains unpoisoned throughout. Target poisoning should be avoided because it results in instabilities in the plasma, which affect the deposition. These data indicate that relatively high plasma oxygen concentrations can be utilized to prepare oxidized deposits while avoiding target poisoning.

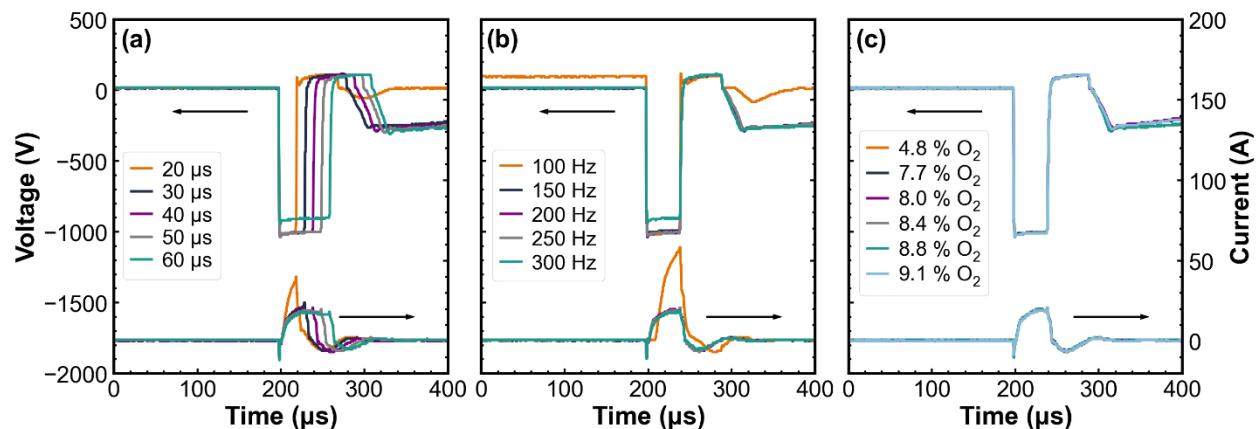


Figure 3.7: Instantaneous plasma current and voltage waveforms during HiPIMS depositions of HfO_2 with varied (a) pulse width, (b) pulse frequency, and (c) oxygen content in the plasma.

Based on these results, thick films (< 100 nm) were prepared with a 40 μs pulse width, 200 Hz frequency, and varied oxygen content. These films were not annealed. The θ -2 θ XRD patterns are shown in **Figure 3.8**. The high intensity peak at approximately 69° in 2θ is the Si (004) reflection. Low oxygen content (i.e., 4.8% and 7.7% by flow ratio) results in XRD peaks

attributable to non-ferroelectric monoclinic phases. Increasing the oxygen content to 8.0, 8.4, and 8.8% results in XRD peaks that are consistent with orthorhombic or tetragonal phases or mixtures thereof. Further increases in oxygen content in the sputter gas result in a broad peak centered at $\sim 34^\circ$ in 2θ , which could be attributed to a proto- or nano-crystalline phase. These results highlighted the importance of oxygen content for controlling the phase composition in these films.

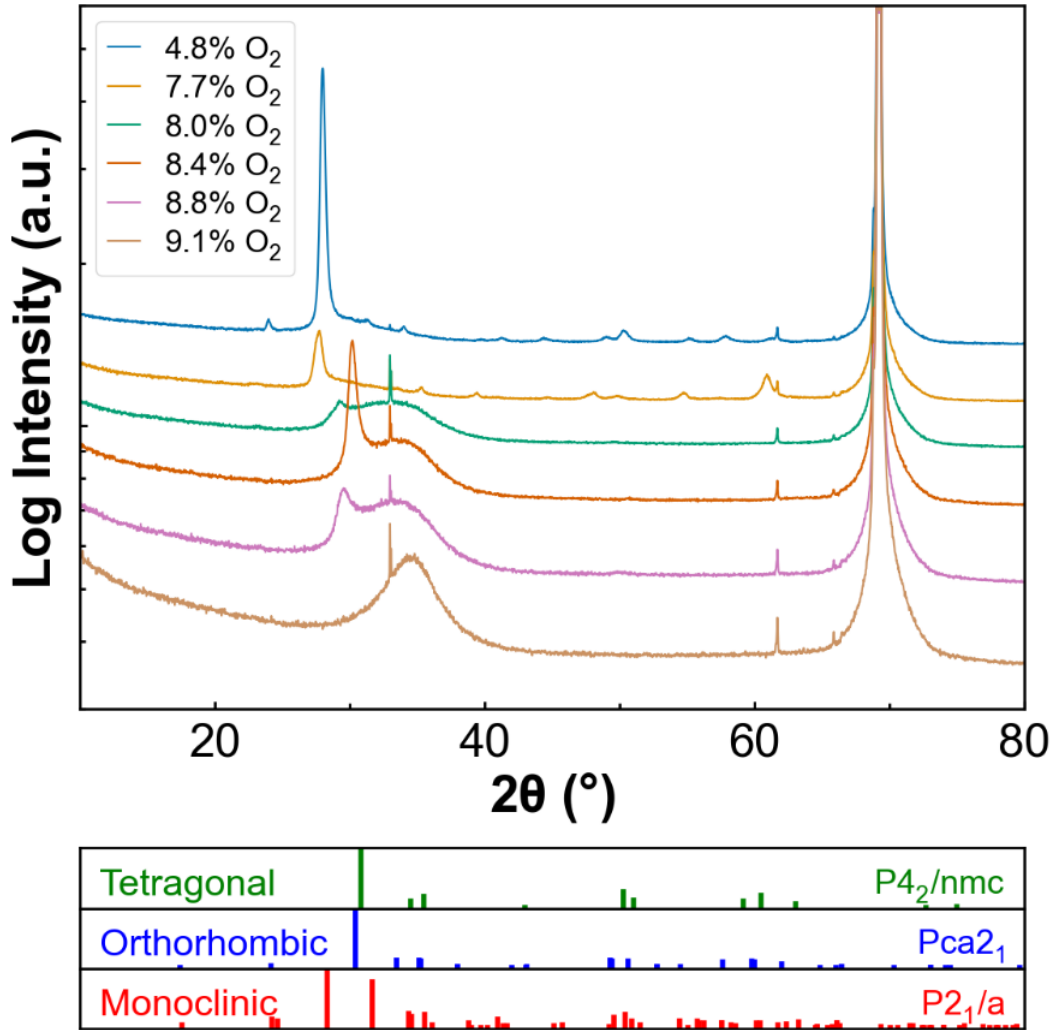


Figure 3.8: θ - 2θ X-ray diffraction patterns for thick HfO₂ films deposited by HiPIMS with a 40 μs pulse width, 200 Hz pulse frequency, and varying oxygen content. The indices for the tetragonal, polar orthorhombic, and monoclinic phases are shown below the data.

Next, thinner films (estimated to be approximately 20 to 40 nm in thickness) were prepared using a 40 μs pulse width, 200 Hz pulse frequency, and intermediate oxygen content. GIXRD patterns are shown in **Figure 3.9**. Again, low oxygen content results in a diffraction

peak in a location most similar to the monoclinic phase. Increased oxygen content results in a peak that can be indexed to either the orthorhombic phase or the tetragonal phase.

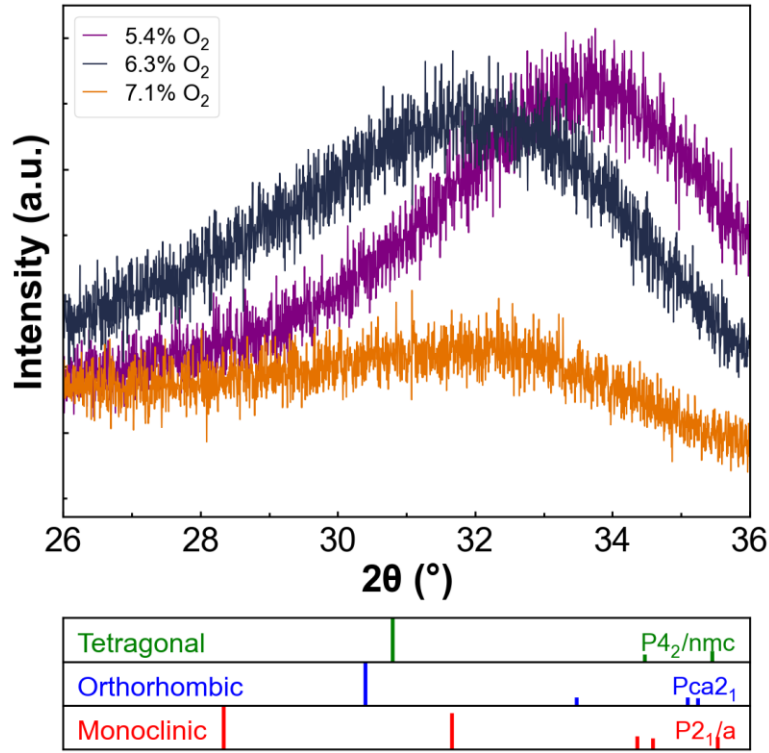


Figure 3.9: Grazing-incidence X-ray diffraction patterns for HfO₂ films (approximately 20-40 nm thick) deposited by HiPIMS with a 40 μs pulse width, 200 Hz pulse frequency, and varying oxygen content. The indices for the tetragonal, polar orthorhombic, and monoclinic phases are shown below the data.

A rapid thermal anneal was performed for a 9 nm thick film prepared with a 40 μs pulse width, 200 Hz pulse frequency, and 6.3% oxygen background content at 600 °C for 30 s in an N₂ atmosphere to observe changes to phase assemblage; the GIXRD pattern for this film before and after annealing is shown in **Figure 3.10**. Before annealing, no peaks are present, suggesting that the film has large amorphous volume fractions as-deposited. After annealing, a peak forms at approximately 30.5°. The crystalline phase that develops has a peak position that is consistent with a ferroelectric orthorhombic or non-ferroelectric tetragonal phase. These results suggest that thinner films require annealing and are not crystalline as-deposited.

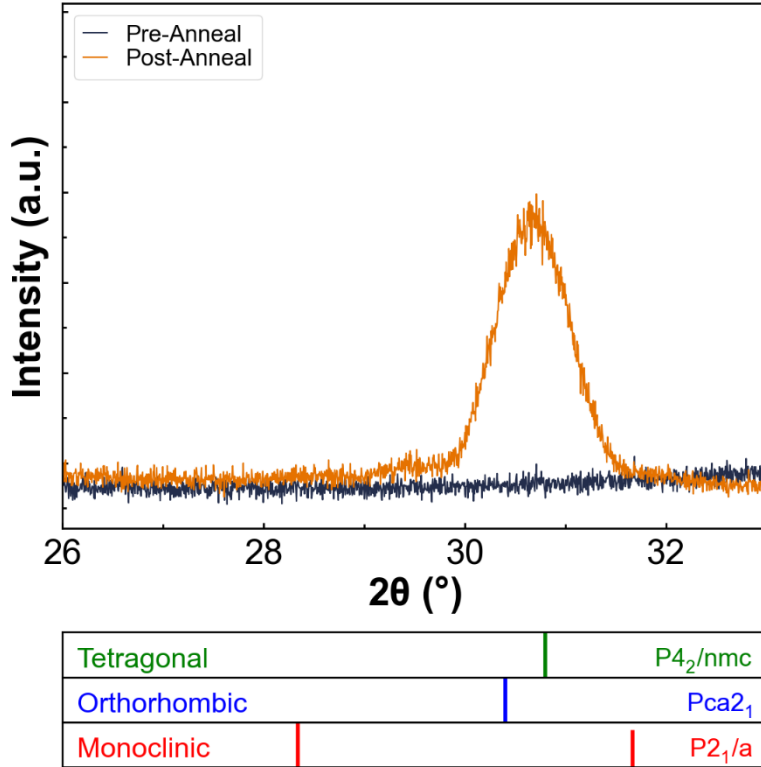


Figure 3.10: Grazing-incidence X-ray diffraction patterns for a 9 nm thick HfO₂ film before and after rapid thermal annealing at 600 °C in N₂ for 30 s. The indices for the tetragonal, polar orthorhombic, and monoclinic phases are shown below the data.

3.6.3. HiPIMS Pulse Width and Plasma Oxygen Content

To further understand the effects of HiPIMS pulse width and oxygen content, a number of films were deposited with pulse widths varying from 50 to 140 μs, plasma oxygen content ranging from 6.7 to 9.6%, and pulse frequency constant at 200 Hz. For each pulse width of 50, 80, 110, and 140 μs, a ‘low,’ ‘medium,’ and ‘high’ plasma oxygen content was chosen, as shown in **Table 3.1**; the instantaneous power calculated from the current and voltage waveforms is shown on the top row. Overall, lower pulse widths required lower plasma oxygen content to avoid target poisoning since target poisoning occurs during the ‘off state’ of the plasma, and shorter pulses have longer off times. A high oxygen content could not be achieved for the 50 μs condition due to target poisoning. Each of these films was rapid thermal annealed at 800 °C in Ar for 30 s to crystallize the films. The resulting GIXRD patterns are shown in **Figure 3.11**. Two

conditions result in higher fractions of the monoclinic phase – lower pulse widths and higher plasma oxygen content.

Table 3.1: HfO₂ films deposited with 50, 80, 110, and 140 μs pulse widths and the corresponding ‘low,’ ‘medium,’ and ‘high’ plasma oxygen content for each one. The top row shows the instantaneous power calculated from voltage and current waveforms.

	21.5 kW	14.1 kW	12.2 kW	11.5 kW
	50 μs	80 μs	110 μs	140 μs
6.7% O ₂	Low			
7.1% O ₂	Medium			
7.4% O ₂		Low	Low	
7.6% O ₂		Medium	Medium	
8.0% O ₂		High	High	Low
8.8% O ₂				Medium
9.6% O ₂				High

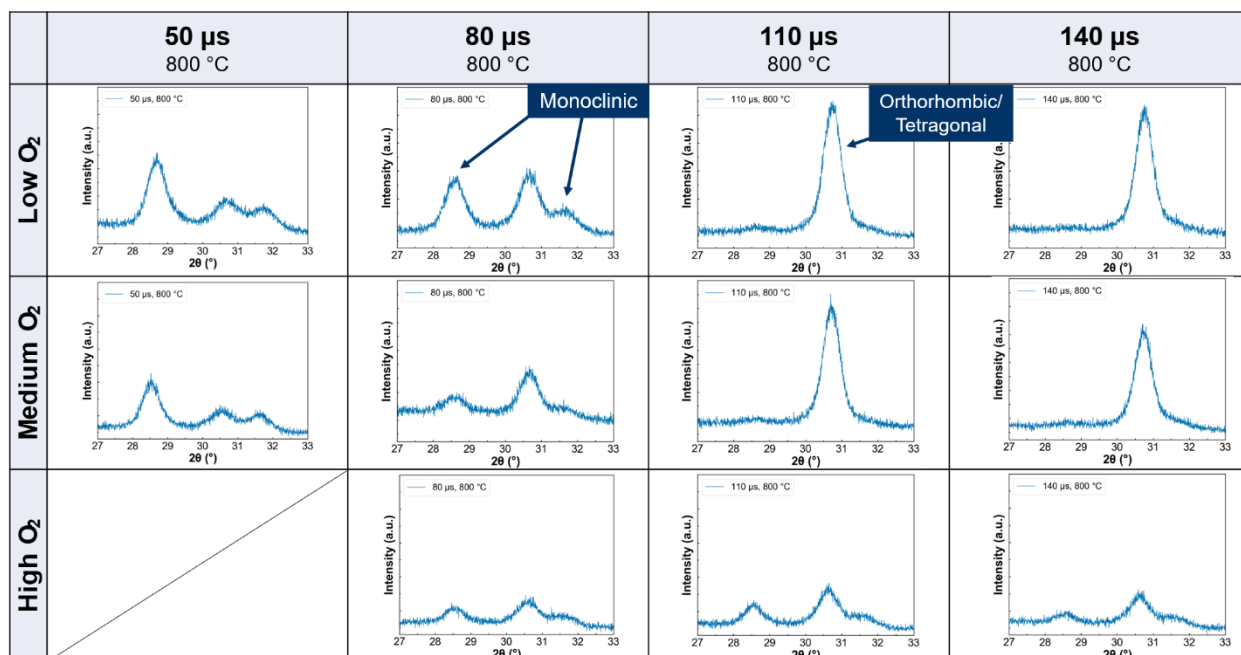


Figure 3.11: Grazing-incidence XRD patterns for 20 nm thick HfO_2 films deposited by HiPIMS with varying pulse widths and plasma oxygen content. Monoclinic phase fractions increase as pulse width decreases and plasma oxygen content increases.

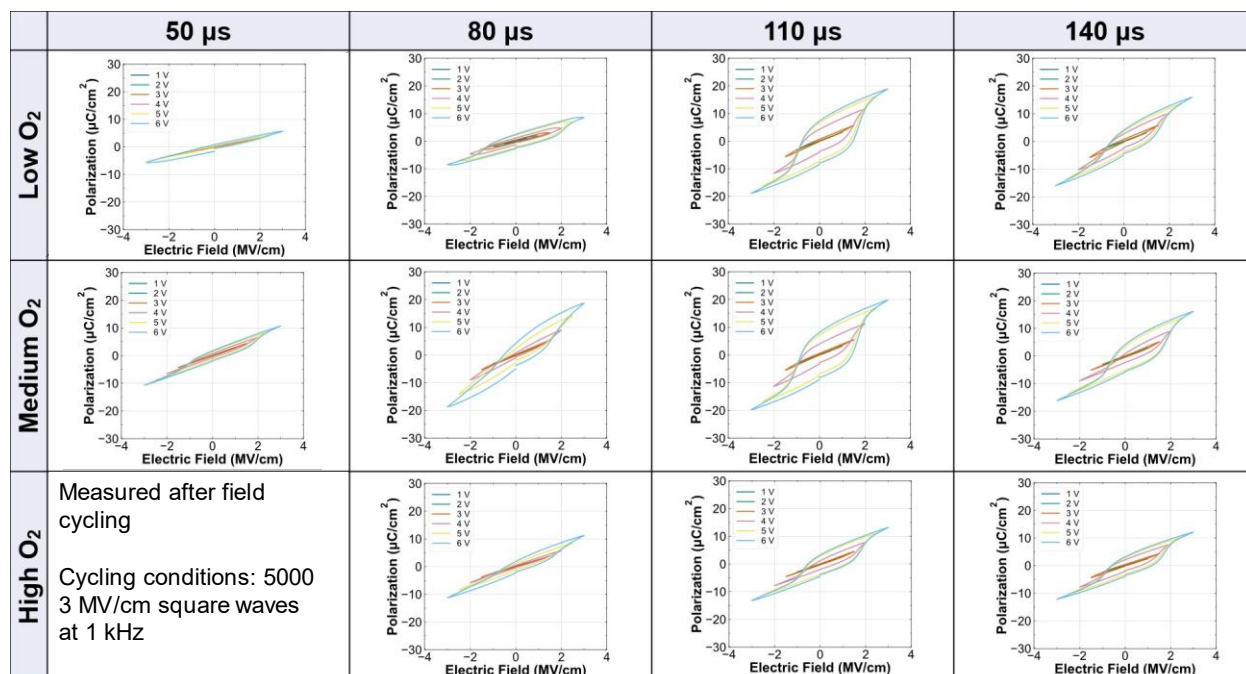


Figure 3.12: Polarization-electric field measurements after field cycling for 20 nm thick HfO_2 films deposited by HiPIMS with varying pulse widths and plasma oxygen content.

The corresponding polarization-electric field ($P(E)$) measurements are shown in **Figure 3.12**. The films were cycled with 5000 3 MV/cm square waves at 1 kHz. At the lower pulse widths, the films primarily show linear dielectric behavior due to the dominating non-ferroelectric monoclinic phase present. At the higher pulse widths, the hysteresis loops open up and exhibit a ferroelectric response typical of the orthorhombic phase. Since HiPIMS parameters in this processing space demonstrated the ability to affect phase composition and electrical properties, these conditions were explored further and the results are shown in Chapters 5 and 7.

3.6.4. Challenges Associated with Reactive HiPIMS Deposition of HfO₂-Based Thin Films

HiPIMS has been introduced as a means to control phase constitution, microstructure, and ferroelectric properties in HfO₂ thin films through various deposition parameters. However, the inability to monitor changing target composition, and thus, changing plasma composition, over time has resulted in difficulties in reproducibility. More specifically, identical deposition conditions have resulted in different film properties.

Figure 3.13 shows GIXRD patterns of 20 nm HfO₂ films deposited under identical conditions at different periods of time. Over the course of time, the films go from containing only orthorhombic and/or tetragonal phases to containing primarily monoclinic phase. The increase in the monoclinic phase present suggests that the films have increasing oxygen content over time, likely due to the incorporation of oxygen into the target. Different strategies to combat this issue were attempted. These include monitoring voltage and current waveforms and pre-sputtering and post-sputtering the target in Ar to remove oxide build-up on the surface. However, none of these strategies proved effective for reproducibility purposes. Due to these issues, ALD was shown to be a more reliable deposition method to fabricate ferroelectric HfO₂-based thin films. Although conventional ALD does not offer process parameters that can be used to control the energy of the depositing species like HiPIMS, other approaches can be used. One such approach is the use of ion bombardment, which is examined in Chapter 9.

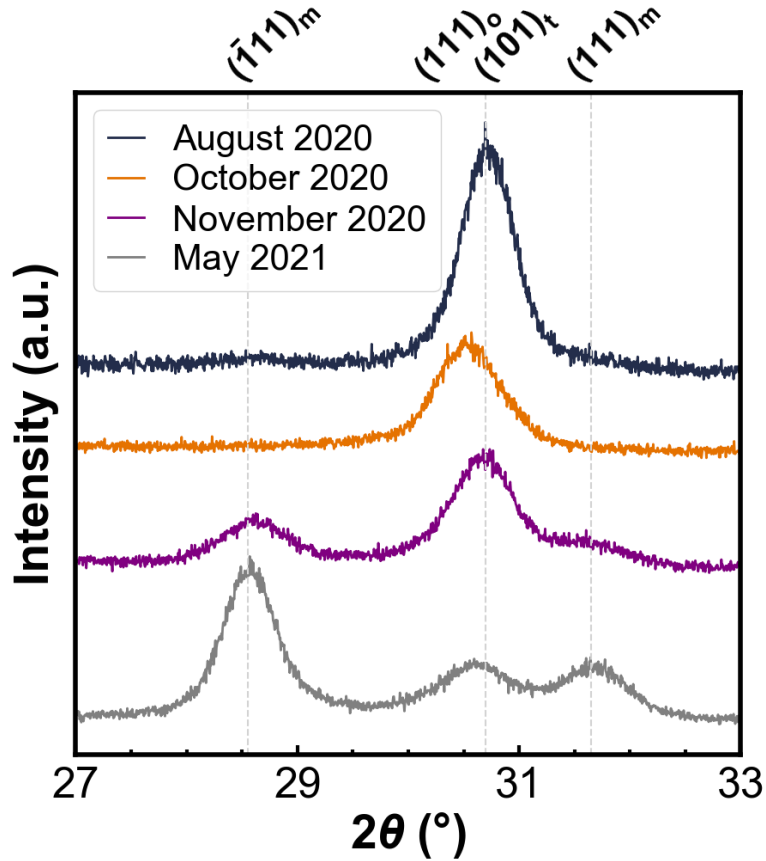


Figure 3.13: GIXRD patterns for 20 nm thick HfO_2 films deposited with identical deposition conditions, deposited between August 2020 and May 2021.

3.7. Metal-Ferroelectric-Metal Capacitor Structures

Metal-ferroelectric-metal (MFM) capacitor structures are often used to measure the electrical properties of ferroelectric HfO_2 -based thin films. These structures are fabricated by depositing a bottom electrode material like tantalum nitride (TaN) or tungsten on a substrate (typically silicon), followed by the ferroelectric layer, and then a top electrode. Then, the stack is rapid thermal annealed, contacts are deposited, and the top electrode is etched to reveal individual capacitors, as shown in **Figure 3.14**.

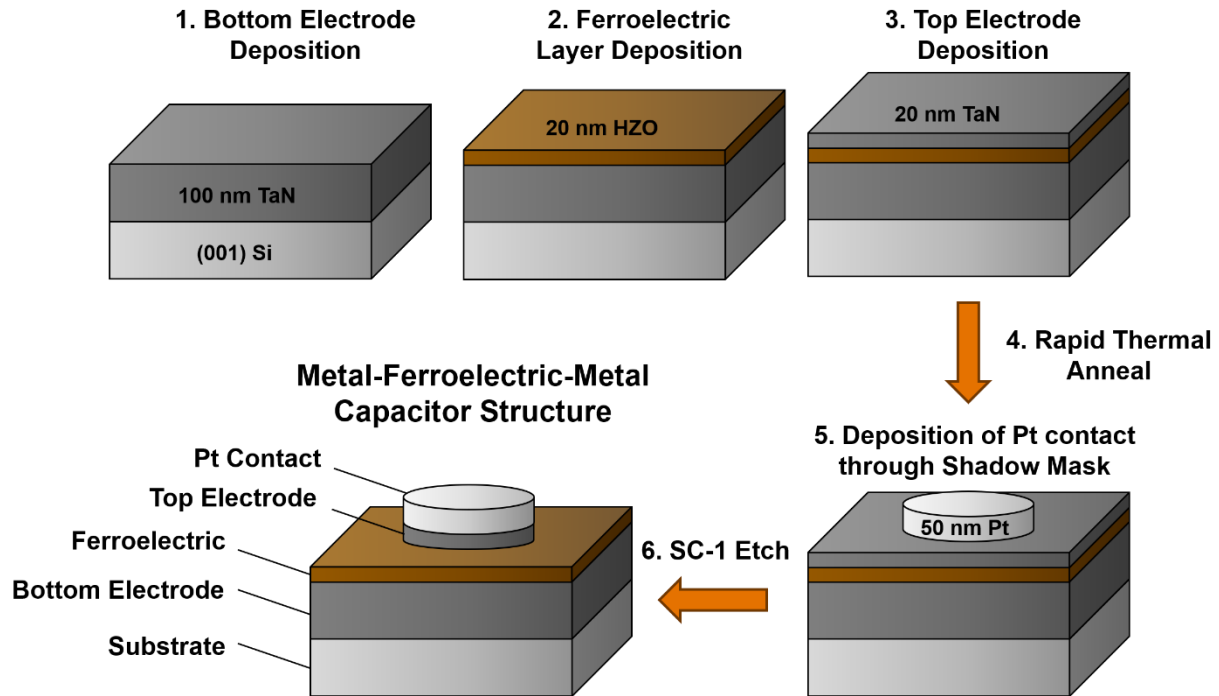


Figure 3.14: Process flow for fabrication of a metal-ALD ferroelectric-metal capacitor structure used for electrical characterization of ferroelectric HfO_2 -based thin films.

Two deposition methods were used for the fabrication of HfO_2 and HZO thin films in this dissertation – ALD and HiPIMS, which were discussed in the previous sections. It should be noted that this process flow differed slightly for capacitor stacks using HiPIMS-deposited HfO_2 films. In this case, a blanket top electrode deposition was not performed. Rather, the top electrode (TiN) and contact material were both deposited through the shadow mask after the RTA process, and no SC-1 etch was performed.

3.7.1. Substrate, Electrode, and Contact Materials

The substrate used for the depositions shown in this work is (001)-oriented *p*-type silicon substrates. Tantalum nitride, titanium nitride, palladium, and platinum sputter deposition processes were developed to use as electrode and contact materials. The sputter system and sputter guns described above were used for all depositions. Direct current (DC) magnetron sputtering with an Advanced Energy MDX 1.5K DC power supply was used for these depositions. Details about the deposition conditions for each electrode/contact material are shown in **Table 3.2**.

Table 3.2: Deposition details and conditions for electrode and contact materials used for MFM capacitors.

Material	Target	Target Power Density	Deposition Pressure	Gas Flow
TaN	TaN, 99.5% pure, sintered 2” (Kurt J. Lesker)	3.31 W/cm ²	5 mTorr	20 sccm Ar
TiN	Ti, 99.9% pure, 2” (Kurt J. Lesker)	7.40 W/cm ²	0.9 mTorr	5 sccm Ar, 1 sccm N ₂
Pd	Pd, 99.9% pure, 2” (Kurt J. Lesker)	3.31 W/cm ²	5 mTorr	20 sccm Ar
Pt	Pt, 99.99% pure, 2” (Kurt J. Lesker)	3.31 W/cm ²	5 mTorr	20 sccm Ar

In addition to TaN sputtered at UVA, TaN was provided by Sandia National Labs. This TaN was prepared on Si by pulsed DC magnetron sputtering (30 kHz, 4 μs reverse time) from a TaN target within a Denton Discovery 550 system. All HiPIMS depositions described in this work utilize this TaN.

Contacts were deposited through a shadow mask using one of the two mask designs shown in **Figure 3.15**.

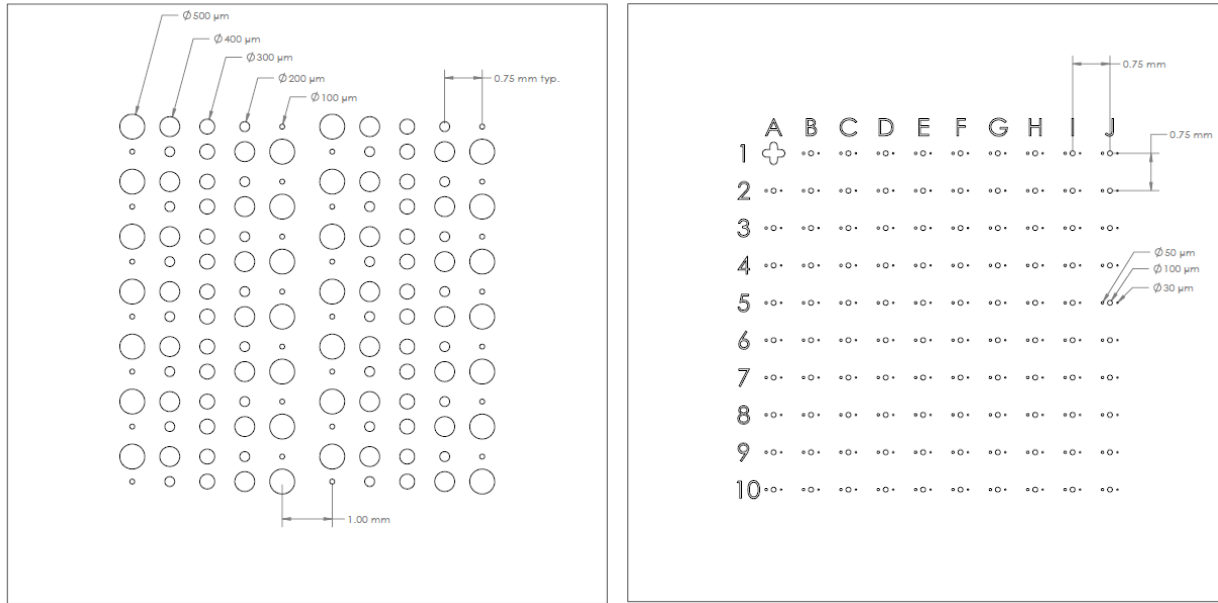


Figure 3.15: Shadow mask designs used to pattern contacts onto HfO₂-based thin films.

3.7.2. Rapid Thermal Anneal

Since films deposited by ALD and HiPIMS were amorphous as-deposited, an annealing step was necessary to crystallize them. An Allwin21 AccuThermo 610 Rapid Thermal Processor was used to perform a rapid thermal anneal, which is commonly used to crystallize HfO₂-based thin films. These 30 s anneals ranged in temperature from 600 to 800 °C with ramp rates from 50 to 67 °C/s and were performed in argon or nitrogen environments at atmospheric pressure. Undoped HfO₂ films deposited by HiPIMS required higher temperature anneals to obtain the ferroelectric phase (750 – 800 °C) in comparison to HZO films deposited by ALD, for which annealing at a temperature of 600 °C was sufficient.

3.7.3. SC-1 Etch

For films with ALD ferroelectric layers, an SC-1 etch was used following the deposition of Pd or Pt top contacts through the shadow mask. These contacts acted as a hard mask so that the blanket top electrode layer could be removed by the etch, resulting in defined capacitors. This etch consists of a 1:1:5 volumetric ratio of NH₄OH (30% in water), H₂O₂ (30% in water), and deionized water. A typical etch procedure is described as follows. 40 mL of deionized water was added to a 400 mL beaker. The deionized water was heated to 45 °C, as measured by a thermometer. 8 mL

of H_2O_2 was added to the beaker, followed by 8 mL of NH_4OH once the temperature reached 55 °C. The samples were added to the beaker, and the temperature was monitored so that it stayed between 55 and 60 °C. The etch rate was approximately 2.3 nm/min. Following the etch, the sample was removed and thoroughly rinsed with deionized water.

3.8. Summary

This chapter details the methods used for the deposition of HfO_2 -based thin films and the processing conditions used to fabricate metal-ferroelectric-metal capacitor structures for electrical characterization. A brief overview of the underlying principles of atomic layer deposition and sputtering is provided. High-power impulse magnetron sputtering is introduced as a new method that can be used to control the energy and ionization of the depositing species, allowing access to previously inaccessible regions of microstructure on the structure zone diagram. The process development for HiPIMS deposition of HfO_2 is discussed, and the processing space relevant for deposition of this material is highlighted.

Chapter 4: Characterization of HfO₂ Thin Films

4.1. Motivation

Understanding ferroelectricity in HfO₂-based thin films relies upon a combination of structural, chemical, and electrical characterization techniques. In this chapter, characterization techniques used throughout this work are described. These techniques include grazing incidence X-ray diffraction (GIXRD), X-ray reflectivity (XRR), $\sin^2\psi$ stress analysis, X-ray photoelectron spectroscopy (XPS), scanning electron microscopy (SEM), atomic force microscopy (AFM), transmission electron microscopy (TEM), Fourier Transform Infrared Spectroscopy (FTIR), and several electrical characterization techniques.

4.2. Grazing-Incidence X-ray Diffraction

X-ray diffraction (XRD) is a characterization technique that can be used to determine the crystal structure of a material. The basic principle behind XRD involves an X-ray source that emits X-rays of a specific wavelength. X-rays are used because their wavelength is typically of the same order of magnitude as the d -spacing between planes of a crystal. Many lab-based diffractometers use a copper source, resulting in Cu K α radiation with a wavelength of 1.5406 Å. The incident X-rays are collimated, and the beam is directed at the sample being analyzed. In crystalline materials, the X-rays interact with the lattice where they constructively and destructively interfere. Bragg's Law defines the angles at which constructive interference occurs as

$$n\lambda = 2d\sin\theta,$$

where n is the order of reflection, λ is the wavelength of the beam, d is the spacing between diffracting planes, and θ is the diffraction angle.¹⁵³ This constructive interference produces a pattern that is collected on a detector and is presented as a series of peaks that correspond to the structure of the material. Since each peak corresponds to a specific interference condition, often, a peak or combination of peaks can be used to identify the phases present in a film. The relative intensities of the peaks provide information about the amounts of each phase present in the material, and the full width at half maximum (FWHM) of the peaks can be used in the Scherrer equation to calculate crystallite size.¹⁵⁴ The Scherrer equation is as follows:

$$\tau = \frac{K\lambda}{\beta \cos \theta},$$

where τ is the mean size of the crystallites, K is a dimensionless shape factor, λ is the X-ray wavelength, β is FWHM, and θ is the Bragg angle. Instrumental broadening effects can be corrected for using a standard; in this work, Standard Reference Material[®] 660c lanthanum hexaboride powder¹⁵⁵ from the National Institute of Standards and Technology was used.

Although X-ray diffraction of crystals is over 100 years old, the instrumentation used for these measurements is constantly evolving, allowing for new geometries that enable a wider range of applications. Due to the small volume of material available in thin films, XRD techniques that maximize signal from the film and minimize background intensity must be used. One such method is grazing-incidence X-ray diffraction (GIXRD), developed by Marra, Eisenberger, and Cho in 1979.¹⁵⁶ GIXRD is a surface-sensitive X-ray diffraction technique that utilizes a small fixed incident angle beam (close to the critical angle, typically $< 1.5^\circ$) to limit penetration depth and optimize intensity from the film. At incidence angles higher than a few degrees, the intensity of X-rays within a material is given by

$$I = I_0 \exp\left(-\frac{\mu z}{\sin \omega}\right),$$

where I is the intensity of the X-rays within the material, I_0 is the intensity at the surface, μ is the linear absorption coefficient, which depends on the composition and density of the material, z is the distance from the surface, and ω is the incident angle. The depth at which I is at $1/e$ of its I_0 value, $z_{1/e}$, is defined as

$$z_{1/e} = \frac{\sin(\omega)}{\mu}.$$

However, at incidence angles less than a few degrees, the above relationships are not valid. The refractive index of solids at X-ray wavelengths is slightly less than 1, so at these low incidence angles, refraction is significant, and total external reflection (TER) occurs at a critical angle. At incident angles at or below the critical angle, TER will occur, and the X-rays will not penetrate into the bulk of the material. Additionally, close to the critical angle, the positions of the XRD peaks shift as a result of the refraction of the incident X-rays.¹⁵⁷ This peak shift is evident in **Figure 4.1**, which shows the GIXRD patterns from a 20 nm thick hafnium zirconium oxide (HZO) film that contains multiple phases. As the incident angle is decreased from 2° to 0.4° , the peaks shift to a higher 2θ angle. However, the intensity of the peaks also increases as the incident angle is decreased from 2° to 0.4° because there is more signal from the film at lower angles. Thus, a

balance between maximizing signal intensity and minimizing peak shift should be considered when selecting an incident angle for GIXRD measurements.

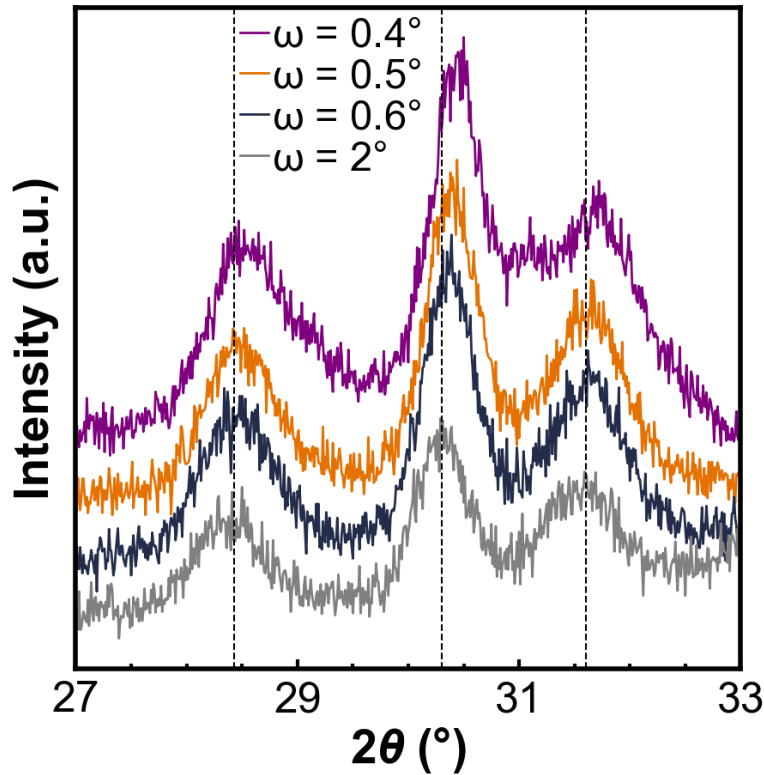


Figure 4.1: GIXRD patterns as a function of incident angle (ω) collected from a 20 nm thick HZO thin film. As the incident angle is increased, a shift in peak position is observed.

For GIXRD measurements shown in this dissertation, an incident angle of 0.7° was used to maximize signal intensity and minimize peak shifts. Two diffractometers were utilized – a Rigaku SmartLab and a Panalytical Empyrean. For most measurements, a 2θ range of $26\text{-}33^\circ$ was selected due to the presence of 100% intensity reflections of the monoclinic $P2_1/c$ phase, tetragonal $P4_2/nmc$ phase, antipolar orthorhombic $Pbca$, and orthorhombic $Pca2_1$ phase in this range. An example GIXRD pattern collected from an HZO film that contains a mixture of the ferroelectric and non-ferroelectric phases is shown in **Figure 4.2**. The peaks at approximately 28.5 and 31.6° are the $(\bar{1}11)$ and (111) monoclinic reflections. The peak at approximately 30.7° presents challenges in indexing due to similar d -spacings of the orthorhombic and tetragonal phases; therefore, it is not possible to distinguish if this peak results from the tetragonal phase, either orthorhombic phases, or a combination of these phases.

By fitting these peaks using LIPRAS fitting software¹⁵⁸ with Pearson VII peak shapes and taking the ratio of the integrated peak intensity of the orthorhombic + tetragonal peak to the integrated intensity sum of all three peaks,

$$\left(\frac{t_{101} + o_{111}}{t_{101} + o_{111} + m_{\bar{1}11} + m_{111}} \right),$$

the relative orthorhombic + tetragonal (o+t) phase fractions can be calculated. The LIPRAS fit is also shown in **Figure 4.2**.

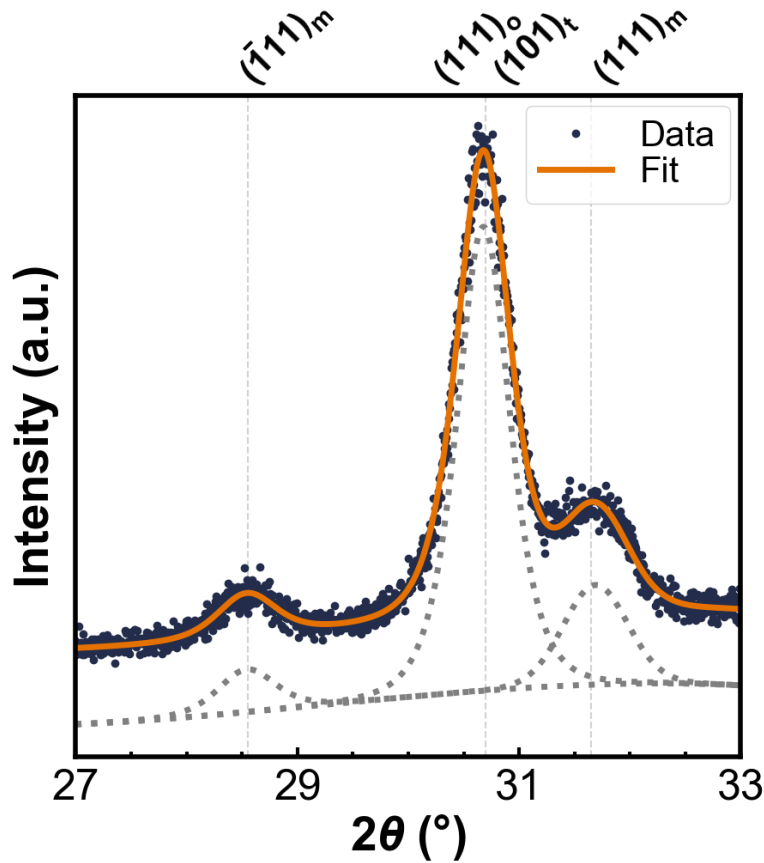


Figure 4.2: GIXRD pattern collected from a 20 nm thick HZO film, with the fit from LIPRAS superimposed. Indices for the possible phases present are shown above the plot.

Another XRD technique that maximizes the intensities from a thin film and minimizes the substrate intensity is in-plane XRD. In-plane XRD utilizes a grazing-incident X-ray beam so that the incident beam can travel a long distance within the thin film, resulting in high diffraction intensity from the film. In-plane XRD measurements diffract from lattice planes that are normal to the surface of the sample rather than parallel to the surface of the sample in the case of

symmetrical out-of-plane XRD measurements, as shown in **Figure 4.3**. In-plane XRD measurements require an instrument with an in-plane horizontal axis. In this dissertation, in-plane XRD measurements were performed in order to calculate crystallite sizes; combined with GIXRD measurements which primarily sample planes perpendicular to the sample surface, these measurements can provide information about lateral and vertical crystallite size.

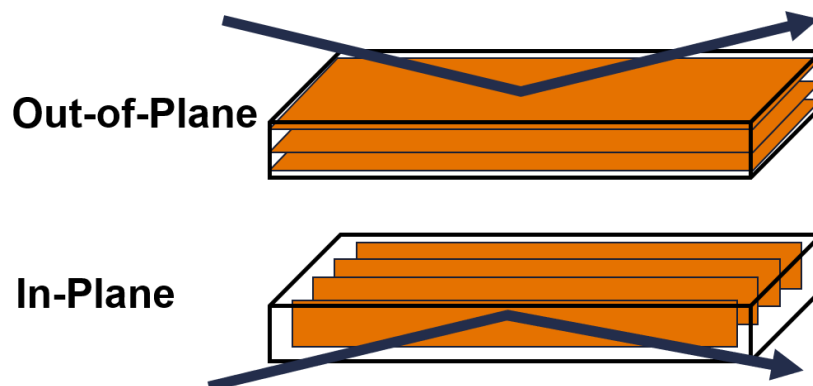


Figure 4.3: Geometries of out-of-plane and in-plane XRD measurements.

4.3. X-ray Reflectivity

X-ray reflectivity (XRR) is a technique that uses X-rays to probe the electron density perpendicular to the surface of a sample to obtain information about thin film thickness, density, and surface roughness of crystalline or amorphous samples. In reflectivity measurements, the X-ray reflection of the sample is measured around the critical angle. The index of refraction of materials for X-rays is slightly less than one. When X-rays enter the surface of a flat sample at a grazing-incidence angle, the X-rays are reflected. At each interface where the electron density changes, X-rays are reflected. By measuring the total reflection intensity, also known as the reflectivity, as a function of the incident angle with respect to the sample surface, a profile is obtained. This profile provides information about structural parameters such as film thickness, density, and surface roughness of each layer of the sample. XRR measurements are analyzed by fitting the measured data to a simulated curve. In this dissertation, XRR measurements are used to obtain density, thickness, and roughness values of HfO_2 layers in addition to the electrode layers in contact with the ferroelectric.

An example measurement of a 20 nm thick HfO_2 film on 85 nm of TaN on Si is shown in **Figure 4.4**. The profile was fit using GSAS-II software¹⁵⁹ to extract the density, thickness, and

roughness of each layer. Important features of the XRR profile are labeled, including the critical angle, which is used to extract density, the period of oscillations, which provides thickness information, the intensity decay rate, which is related to surface roughness, and the decay of the oscillations at high angles which is associated with the surface and interface roughness.

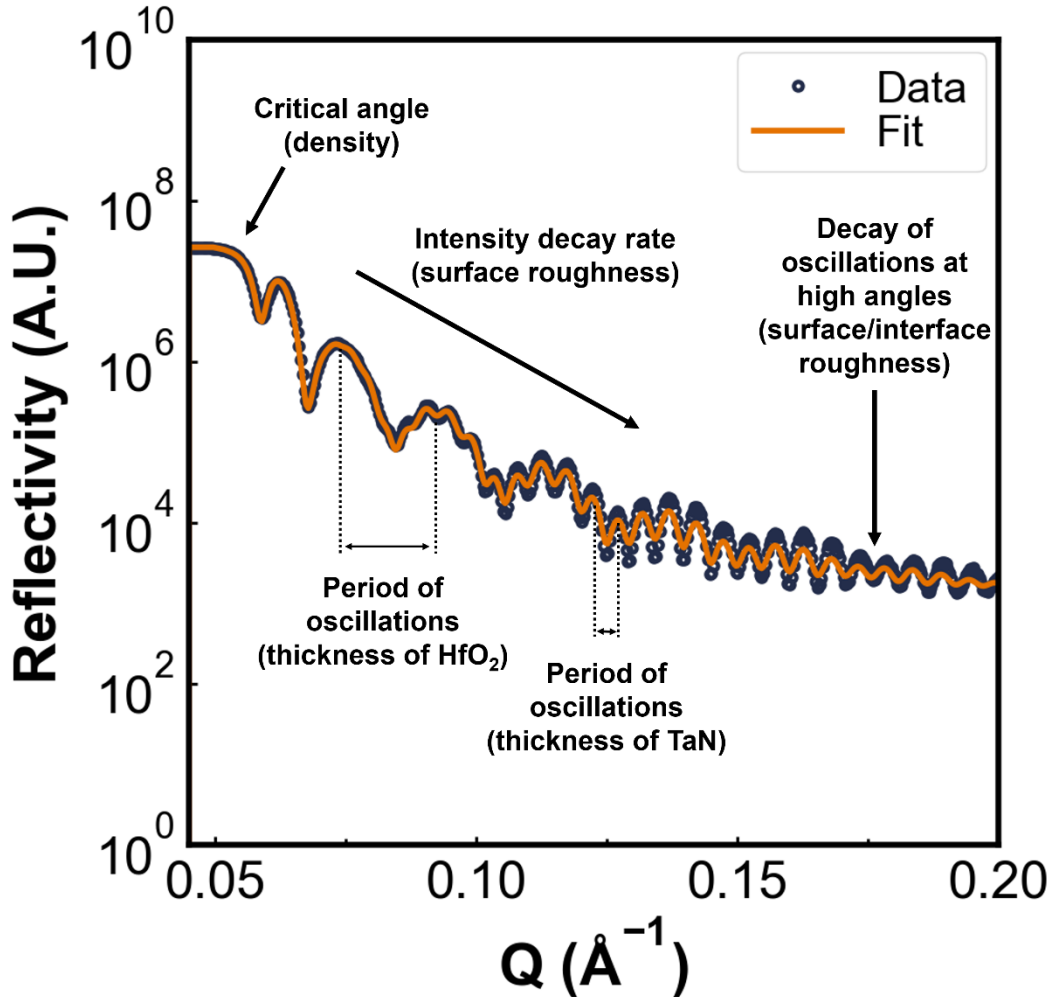


Figure 4.4: X-ray reflectivity profile of a 20 nm thick HfO_2 thin film on 85 nm of TaN on Si with important features labeled.

4.4. Quantification of Biaxial Stress Using the $\text{Sin}^2\Psi$ Technique

As discussed in Chapter 2, biaxial stress plays a role in the stability of the ferroelectric phase^{33,160} in HfO_2 -based thin films, and larger tensile biaxial stress has been shown to correlate with higher remanent polarization values in this material.^{35,161} Therefore, characterization of the

stress in HfO₂ thin films can provide insight into the mechanisms stabilizing the ferroelectric phase.

Earlier, it was shown through Bragg's Law that there is a relationship between interplanar spacing (*d*-spacing) and diffraction angle when X-rays are diffracted by crystal lattices; thus, when the *d*-spacing changes, so does the diffraction angle. When a material is strained, the crystal lattice undergoes elongations and contractions that change the *d*-spacings of the lattice planes. These changes in *d*-spacing result in a shift in the diffraction angle. By precisely measuring this shift, the change in *d*-spacing can be determined, and strain in the material can be deduced. The sin²ψ technique is a method for determining biaxial stress in thin films that uses these principles. More specifically, the change in *d*-spacing for a specific plane is examined relative to the angle between the plane and film normal, known as the ψ angle. The *d*-spacing is plotted linearly against the corresponding sin²ψ angle, and the resulting slope can be used to calculate the lattice strain.

Equations 4.1 and 4.2 can be used to relate *d*-spacing and ψ angle:

$$\varepsilon_{\psi} = \frac{1+\nu}{E} \sigma_{\parallel} \sin^2(\psi) - \frac{2\nu}{E} \sigma_{\parallel} \quad 4.1$$

$$\varepsilon_{\psi} = \frac{d_{\psi} - d_0}{d_0}, \quad 4.2$$

where *d*_ψ is the *d*-spacing at each ψ angle, ν is Poisson's ratio, *E* is the elastic modulus, and σ_∥ is the biaxial stress. Assuming a randomly oriented polycrystalline film, the strain-free *d*-spacing (*d*₀) can be calculated at a ψ angle (ψ*) where Equation 4.3 is satisfied.¹⁶²

$$\sin(\psi^*) = \sqrt{\frac{2\nu}{1+\nu}} \quad 4.3$$

A positive slope in the plot of *d*-spacing versus sin²ψ indicates that the film is under tensile biaxial stress, while a negative slope indicates that the film is under compressive biaxial stress.

This technique was performed at the University of Virginia using a Bruker D8 Venture diffractometer with a Photon III detector. This instrument has an Incoatec IμS Cu Kα microfocus source that is significantly brighter than traditional X-ray tubes in laboratory-based X-ray diffractometers, thus allowing for an improved signal from thin films. Additionally, its area detector is capable of collecting a wide range of γ angles (which can be converted to ψ angles) in a single frame. The measurement setup and geometry is shown in **Figure 4.5**.

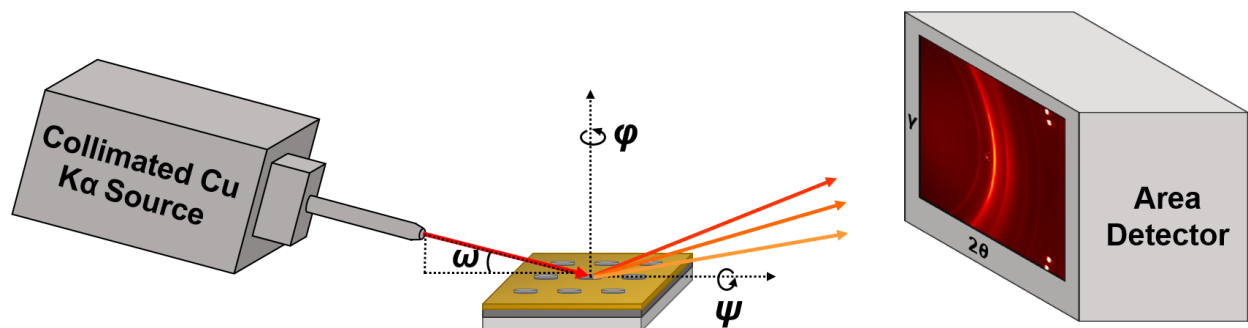


Figure 4.5: Measurement set up and geometry of area detector X-ray diffraction measurements for $\sin^2\psi$ analysis.

4.5. X-ray Photoelectron Spectroscopy

X-ray photoelectron spectroscopy (XPS) is a quantitative surface analysis technique that can provide information about the elemental composition, chemical state, and electronic structure of a material. XPS works on the principle of the photoelectric effect. The process involves irradiating a sample surface with X-rays, typically generated from an X-ray source like monochromatic Al $K\alpha$. When the X-rays interact with the sample, they can be absorbed by the inner shell electrons of the atoms, causing these electrons to be ejected from the material; these ejected electrons are known as photoelectrons. These emitted electrons are then collected by an electron energy analyzer which separates the electrons based on their kinetic energy. Using the energy of the emitted electrons, the binding energy can be calculated using the photoelectric effect equation,

$$E_{\text{binding}} = h\nu - E_{\text{kinetic}},$$

where E_{binding} is the binding energy of the electrons in the specific atomic shells they originated from, $h\nu$ is the energy of the X-ray photons used, E_{kinetic} is the kinetic energy of the electron measured by the instrument. The result is a spectrum that represents the number of photoelectrons detected at a certain binding energy, which provides information about the elemental composition and chemical state of the sample surface. The binding energies of the electrons can be used to identify the elements present, while the shape and intensity of the peaks reveal information about the chemical environment and electronic structure of the atoms.

By comparing the obtained spectrum with reference spectra of known elements and compounds, it is possible to determine the composition of the sample and identify specific

chemical species. XPS can also provide quantitative information about the elemental composition by measuring the intensity of the spectral peaks. In this work, XPS was used to calculate the ratio of oxygen to hafnium. To do so, the Hf 4*f* and O 1*s* spectra shown in **Figure 4.6** were analyzed using KolXPD fitting software.¹⁶³ Voigt functions were used to fit all core levels in combination with a Shirley background,¹⁶⁴ and then peak areas were corrected by cross-sections provided by Scofield *et al.* for each core level.¹⁶⁵ Then, the ratio of the corrected O 1*s* peak area to the corrected Hf 4*f*_{5/2} and Hf 4*f*_{7/2} was calculated. Two peaks are present in the O 1*s* spectra. The higher intensity peak at 531.7 eV corresponds to lattice oxygen and was used for the stoichiometry calculations. The peak at 533.5 eV is a hydroxyl peak that results from adventitious hydroxyls of water adsorbed onto the sample at ambient conditions.¹⁶⁶ This peak is frequently mislabeled in literature as an ‘oxygen vacancy’ peak. However, a missing oxygen atom cannot produce a photoelectron signal since XPS involves measuring the kinetic energy of an electron removed from an atom. Therefore, the absence of an atom could not produce a peak in XPS.

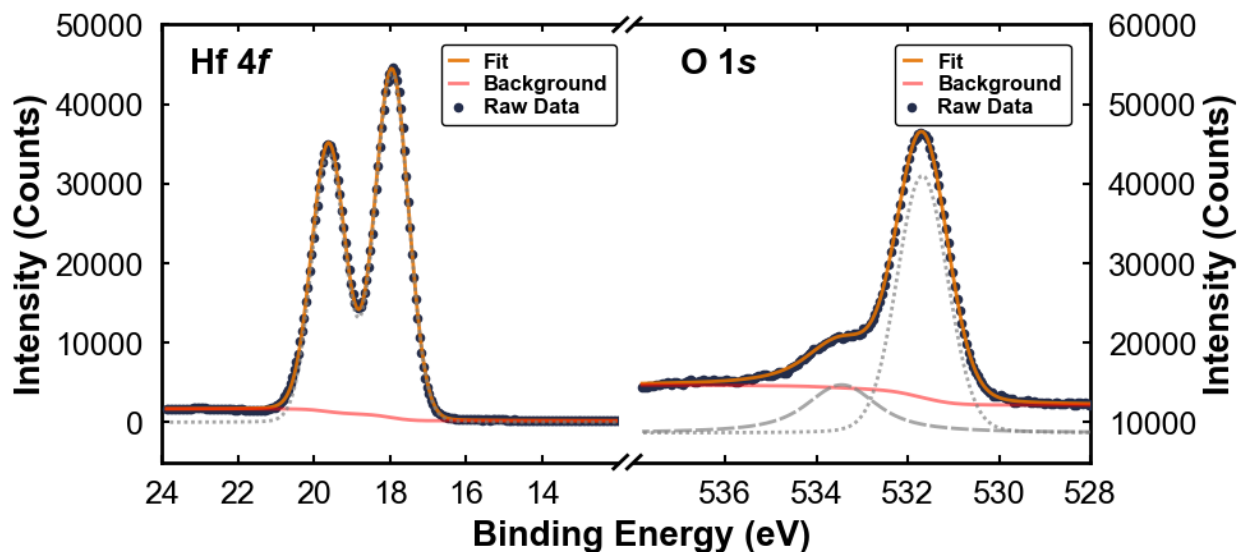


Figure 4.6: Hf 4*f* and O 1*s* XPS spectra acquired from a 20 nm thick HfO₂ film. The spectra are fit using KolXPD software.

To investigate the presence of oxygen vacancies in HfO₂ by XPS, the Hf³⁺ signal may also be evaluated. The Hf 4*f* core levels collected from an amorphous 20 nm thick HfO₂ film deposited by HiPIMS with varying plasma oxygen content are shown in **Figure 4.7**. The intensity is normalized to the Hf 4*f*_{7/2} peak maximum for these spectra. The inset shows the tail on the low binding energy side of the Hf 4*f*_{7/2} peak, which is known to correlate with the presence of a sub-

oxide Hf^{3+} peak. This sub-oxide peak results from oxygen vacancies in which the two electrons remaining at the vacancy site from the removed neutral oxygen atom are distributed among two neighboring Hf^{4+} atoms to produce the Hf^{3+} species.^{92,167–169} The corresponding Hf^{3+} $4f_{5/2}$ peak is positioned in the valley between the Hf^{4+} doublet and leads, therefore, to a concomitant change in the depth of this valley.

As shown in **Figure 4.7**, as oxygen content is decreased, an increasing Hf^{3+} signal is present. In this case, the intensity of the Hf^{3+} peak is too low to allow for a quantitative assessment with a fit; however, groups have fit this peak and used the intensity to calculate oxygen vacancy concentrations.^{92,170} It should be noted that these calculations ignore the possibility of neutral oxygen vacancies that would not contribute to the intensity of the Hf^{3+} peak.

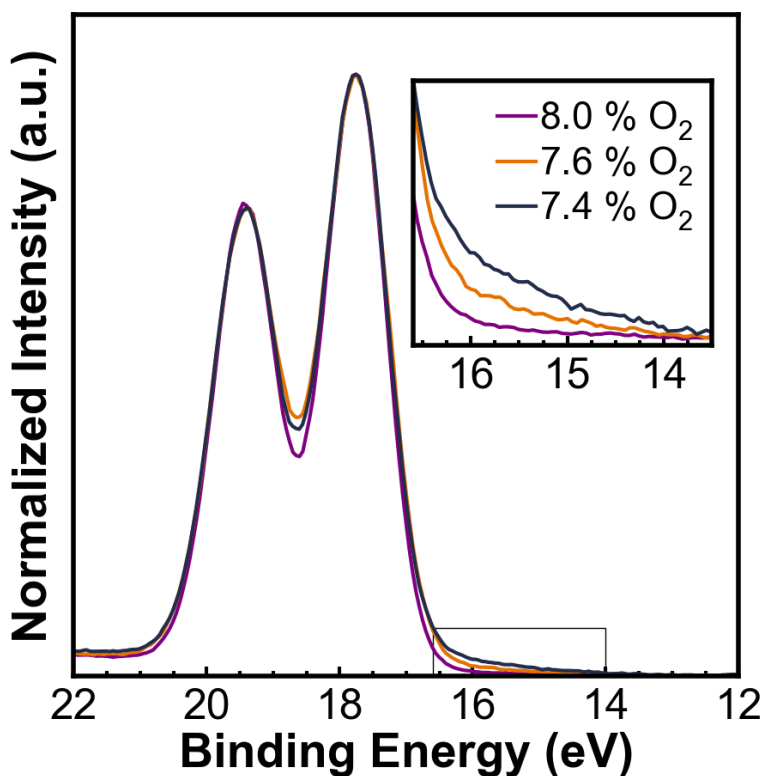


Figure 4.7: Hf $4f$ core levels for HfO_2 films with varying oxygen content, with the intensity normalized to the Hf $4f_{7/2}$ peak maximum. The inset shows the tail of the Hf $4f_{7/2}$ peak where evidence of a Hf^{3+} peak resides.

4.6. Scanning Electron Microscopy

Scanning electron microscopy is a characterization technique that produces images of a sample by collecting emitted electrons resulting from scanning a beam of electrons over the surface of a sample. The electron beam interacts with the sample to produce a variety of signals at various depths within the sample to provide information about surface topography and composition, among other information. The depth of interaction depends on the accelerating voltage and sample material. There are two main modes of imaging in SEM: backscattered electron and secondary electron mode. In addition to these two main modes, which produce signals made up of electrons, other modes measure photons as the signal.

Secondary electrons originate from inelastic energy transfer from the beam to loosely bound electrons of the conduction band or tightly bound valence electrons. The energy transfer allows the electrons to overcome the work function so that they are ejected. Secondary electrons are emitted from the surface, or near the surface (top 5-10 nm), of the sample. Secondary electrons are used to image surface features at high resolution. Backscattered electrons originate from elastic or near elastic coulombic interactions with positively charged nuclei of the sample that scatter electrons from 0 to 180°. Backscattered electron images are highly sensitive to differences in atomic number. The backscattered electron yield is proportional to the sample's atomic number. Because secondary electrons are surface sensitive, they have higher resolution for surface features than backscattered electrons. Backscattered electrons can originate from deeper regions of the sample, so the resolution of surface features is impaired.

In Chapters 5 and 6, plan-view SEM images collected using an FEI Helios UC G4 microscope in secondary electron mode and a through-the-lens detector were used to examine the microstructure of HfO₂ and HZO thin films. These images were analyzed to determine the average lateral grain size using ASTM standard E112,¹⁷¹ and the Heyn lineal intercept procedure. This method involves counting the number of grain boundary intersections with a test line per unit length of the test line in order to calculate the mean lineal intercept length. An example plan-view micrograph of a 20 nm thick HZO film deposited by HiPIMS is shown in **Figure 4.8**.

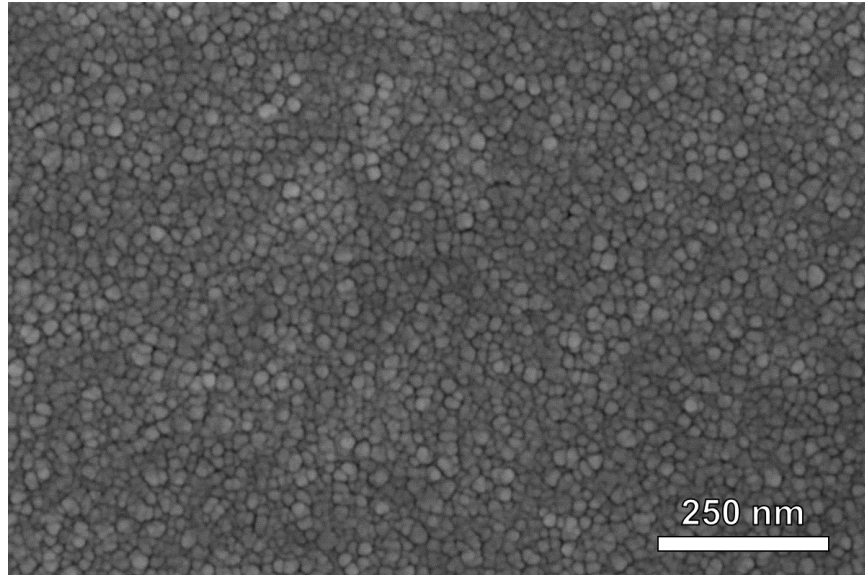


Figure 4.8: Plan-view secondary electron SEM image of a 20 nm thick HZO film deposited by HiPIMS.

Due to the size of the grains in the HfO_2 and HZO thin films shown in this work, there were challenges associated with acquiring SEM images with high enough resolution to discern individual grains and carry out the linear intercept procedure to calculate the average lateral grain size. Some of these challenges included carbon contamination¹⁷² of the films and charging. Methods to mitigate these issues, such as coating the films in a thin layer of palladium, were employed; however, other characterization techniques like atomic force microscopy ultimately provided better images of sample microstructure.

4.7. Atomic Force Microscopy

Atomic force microscopy (AFM) is a high-resolution imaging technique, first introduced by Binnig, Quate, and Gerber in 1986,¹⁷³ used to visualize the surface topography and mechanical properties of materials at the nanoscale. It operates based on the interaction between a sharp probe tip and the sample surface. AFM employs a probe consisting of a sharp tip attached to a flexible cantilever. The tip is typically made of silicon or diamond and has a radius on the order of nanometers. The cantilever acts as a spring, allowing it to deflect in response to surface forces. The sample is mounted on a scanning stage, which allows precise movement in the x , y , and z directions. The AFM probe is positioned above the sample surface, and then the probe tip is

brought into close proximity to the sample surface. Various types of interactions can occur between the tip and the surface, including van der Waals forces, electrostatic forces, and chemical bonding forces. As the probe tip scans the surface, the deflection of the cantilever changes due to the interactions with the sample. The deflection is measured using a laser beam focused on the back of the cantilever, which is reflected onto a position-sensitive detector. This detection system provides real-time feedback on the position of the cantilever and allows for precise control of the tip-to-sample distance.

AFM can operate in different modes depending on the desired information. One commonly used mode is contact mode, where the tip maintains constant contact with the sample surface. In AC, or non-contact mode, the cantilever is vibrated near its resonance frequency, and changes in the amplitude and phase of the oscillation are measured. This mode offers enhanced sensitivity and can provide information about surface properties such as stiffness. The scanning stage moves the sample laterally while the cantilever measures the deflection, resulting in a raster scan of the surface. The measured deflection data is used to generate an image of the surface topography with nanoscale resolution. The resulting image reveals the height variations and surface features of the sample.

In this work, an Oxford Instruments Asylum Research Cypher-S instrument in AC tapping mode was used to acquire topography images of HfO₂ and HZO thin films, with an example shown in **Figure 4.9**. The linear intercept procedure described above was applied to these images to calculate the mean linear intercept length. In general, the AFM images offered improved resolution when evaluating microstructure in comparison to SEM.

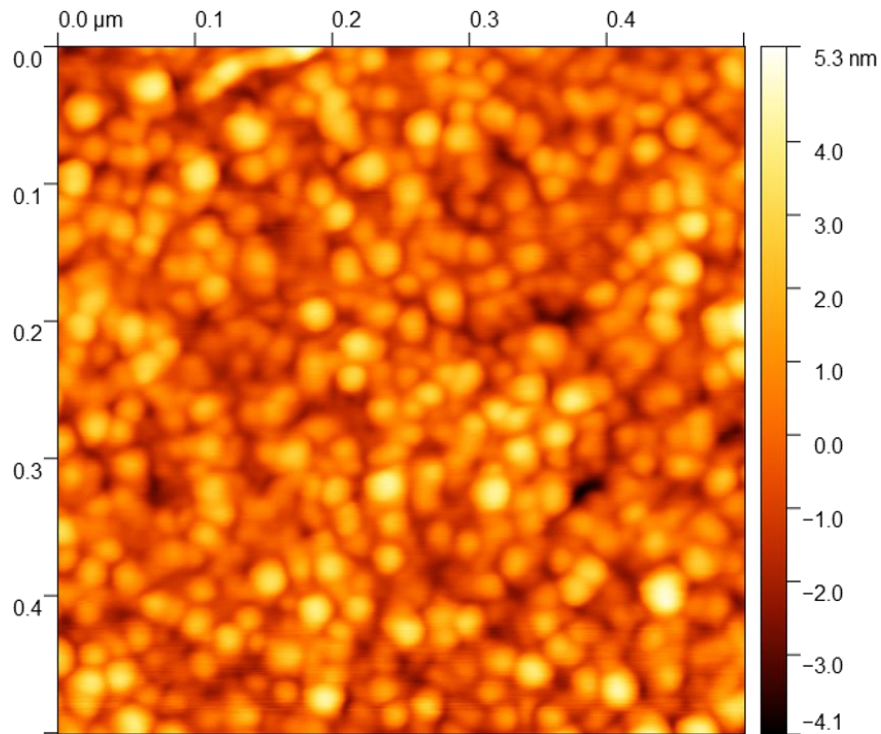


Figure 4.9: AFM topography image of a 20 nm thick HfO₂ thin film deposited by HiPIMS.

In addition to imaging, AFM was used to perform AFM tomography, a method in which contact mode is implemented with high loads in order to selectively mill the surface of the sample with the tip.¹⁷⁴ This technique was used to thin small regions of the electrode on a sample so that nano-FTIR measurements of the underlying ferroelectric layer could be performed in those areas. For AFM tomography, NanoWorld CDT-NCHR diamond-coated tips were used with a scan size of 5 x 5 μm, scan rate of 0.8 Hz, and 0.2 V set point. Several passes were made, intermittently scanning at 90° in AC mode to check the progress of the electrode thinning. **Figure 4.10** shows the AC mode scan of an HZO film with electrodes consisting of 5 nm of Pt on top of 5 nm of TaN that has undergone AFM tomography with 20 passes. The accumulated removed electrode material is evident at the top and bottom of the image.

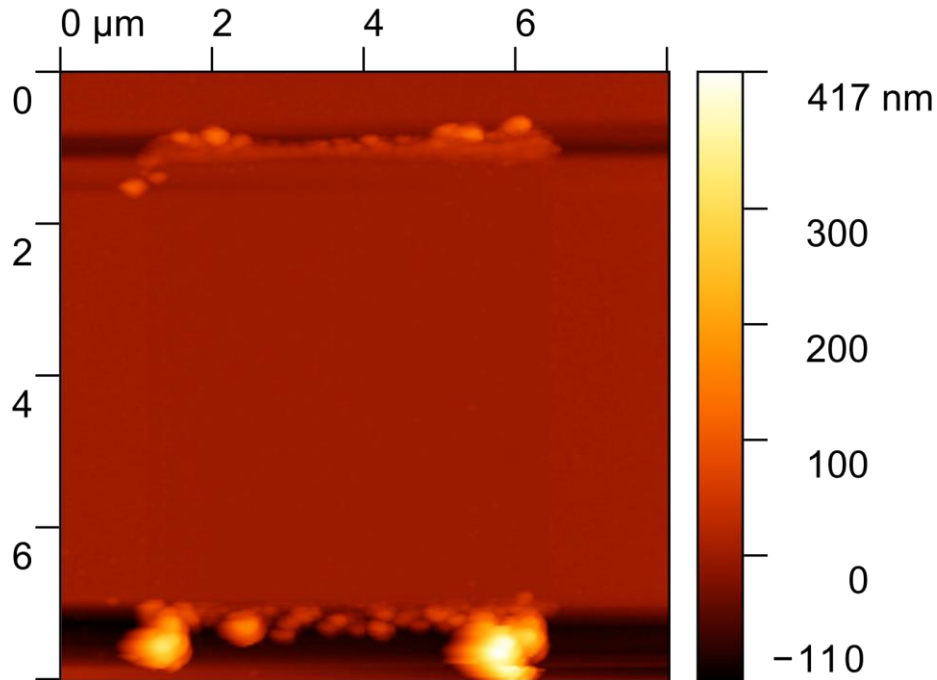


Figure 4.10: AC mode scan of an HZO film with electrodes consisting of 5 nm of Pt on top of 5 nm of TaN that has undergone 20 passes with a diamond-coated tip in contact mode to selectively thin a 5 x 5 μm area on the electrode.

4.8. Transmission Electron Microscopy

Transmission electron microscopy (TEM) is an imaging technique that operates by passing an electron beam through a thin sample, enabling high-resolution imaging and analysis of materials at the atomic scale. A TEM system consists of an electron source that generates a beam of high-energy electrons. This electron beam is condensed and focused using electromagnetic lenses to form a fine probe. The focused electron beam is directed onto the thin sample. As the electron beam passes through the sample, it interacts with the atoms in the material. Several interactions occur, including elastic scattering, inelastic scattering, and diffraction. TEM can operate in different imaging modes to extract various types of information. In bright-field imaging, the transmitted electrons are collected and form an image based on the intensity of the transmitted beam. Dark-field imaging involves selectively collecting scattered electrons at specific angles, providing contrast from specific regions or crystallographic features. Electron diffraction can also be used to analyze the crystal structure of the sample. TEM requires thin specimens with a thickness of approximately 100 nanometers or thinner, depending on the accelerating voltage and

desired information. Samples are prepared by slicing or mechanically thinning the material to a suitable thickness.

In early investigations of ferroelectric HfO₂-based thin films, TEM and scanning TEM (STEM) were used to examine capacitor structures and evaluate the crystallinity of layers.^{64,66,69,175} Following these early studies, TEM and STEM have been used to identify the phases present in HfO₂ layers. Because phase differentiation can be difficult in this material by conventional X-ray approaches, these techniques have aided in the development of understanding the phase composition and phase transformations that may occur in this material. Sang *et al.* used atomic resolution high-angle annular dark-field (HAADF) STEM to provide experimental evidence of an orthorhombic phase in a Gd-doped HfO₂ film.¹⁷⁶ To differentiate between the orthorhombic *Pca2₁*, *Pbca*, and *Pbcm* space groups, Sang utilized position-averaged convergent beam electron diffraction (PACBED), which enables visualization of the oxygen sublattice that is not visible in HAADF STEM images. By combining the HAADF images showing the Hf positions with the PACBED patterns, they were able to conclude that the film contained the orthorhombic *Pca2₁* phase. The presence of this phase in other ferroelectric HfO₂-based thin films has been confirmed using STEM-based techniques in numerous studies.^{56,63,177,178} TEM has also been used to study field cycling effects in HfO₂-based films. STEM on Gd-doped HfO₂ capacitors showed that phase transformations from non-ferroelectric phases to ferroelectric phases occurred during field cycling in addition to the presence of the tetragonal phase at the HfO₂/electrode interface.¹⁷⁹

In this work, TEM performed was performed on a Thermo Fisher Scientific Themis Z-STEM operating at 200 kV equipped with an Ulti-Monochromator at the University of Virginia. Additionally, energy-loss spectra were collected to examine oxygen content in HfO₂ films and will be further discussed in Chapter 5. Additionally, STEM images were acquired at Carnegie Mellon University on a Thermo Fisher Scientific Themis. These images were used for phase identification.

4.9. Fourier Transform Infrared Spectroscopy

Fourier Transform Infrared Spectroscopy (FTIR) is a type of infrared (IR) spectroscopy based on the principle that radiation in IR spectral regions is sensitive to molecular and electronic properties of materials. Thus, FTIR spectra can be thought of as a ‘fingerprint’ for identification in materials. IR spectroscopy relies on resonance and absorption to provide information about the chemical structure and bonding of materials. Resonance occurs when the frequency of the incident

IR radiation matches the natural frequency of the vibration or rotation of the molecules or atoms in the material. Each molecule or atom has specific energy levels associated with these vibrational and rotational motions. When the incident IR radiation matches one of these energy levels, resonance absorption occurs, leading to the excitation of the molecule or atom. Absorption of IR light involves the transfer of energy from the incident photons to the material. When IR light interacts with a material, it can be absorbed by the molecules or atoms present. The absorbed photons can cause electronic transitions, vibrational excitations, or rotational excitations, depending on the energy of the incident IR radiation and the specific properties of the material.

Because the different phases in HfO₂ have different symmetries, bonding, and polarity, FTIR has the potential to differentiate between these phases where diffraction-based techniques fall short. Several computation predictions have suggested that vibrational spectroscopy techniques, including IR and Raman spectroscopy, can be used to identify phases in HfO₂-based thin films.^{34,44,180,181} FTIR measurements have been made on doped-HfO₂ thin films,^{71,182} although differentiation between the orthorhombic and tetragonal phases was not demonstrated. However, differentiation between the monoclinic, antipolar orthorhombic, and polar orthorhombic phases was shown on FTIR measurements of bulk (200 μm) single crystals of HfO₂ stabilized with yttrium.⁴⁴

The wavelength of IR radiation is on the order of micrometers, so it is fundamentally limited in applications where nanoscale information is required. To overcome this limitation, near-field techniques have been developed. One such technique is infrared scattering-scanning near-field microscopy (IR *s*-SNOM). This technique involves scattering the incident light with the tip of an atomic force microscope that is scanning on the sample surface,¹⁸³ enabling imaging at a spatial resolution ranging from 10 to 40 nm.^{184,185} When paired with synchrotron IR radiation which is bright, spatially coherent, and has improved spectral bandwidth over laser sources,¹⁸⁶ imaging over the entire mid-IR with nanometer spatial resolution and high sensitivity is enabled.¹⁸⁷ In this work, synchrotron nano-Fourier infrared spectroscopy (nano-FTIR) was employed in order to measure the vibrational spectra of HfO₂ and HZO thin films. Nano-FTIR measurements were performed at Beamline 2.4 at the Advanced Light Source at Lawrence Berkeley National Laboratory using a tip-based scattering approach on an Attocube Systems Neaspec instrument.

4.10. Electrical Characterization

4.10.1. Polarization-Electric Field Measurement

Polarization-electric field ($P(E)$) measurements, as discussed in Chapter 2, are commonly used to assess switching in ferroelectric materials. $P(E)$ measurements shown in this work were performed on a Radiant Technologies Precision LC II Ferroelectric Property Analyzer.

4.10.2. Positive-Up, Negative-Down Measurement

While $P(E)$ measurements are one of the most common methods used to examine the ferroelectric characteristics of thin films, hysteresis loops can have external contributions to the polarization response, like leakage currents, which can artificially inflate remanent polarization values. Additionally, they are performed at a relatively low frequency (typically 1 kHz) and with a triangle wave that may not accurately represent what the material sees in device applications. Thus, positive-up, negative-down (PUND) pulsed polarization measurements can be performed as a more accurate assessment of the remanent polarization device.¹⁸⁸ This measurement consists of one negative pulse to pre-switch the device (the preset pulse), followed by two positive pulses and two negative pulses, as shown in **Figure 4.11**. The function of each pulse is described below:

1. The preset pulse sets the initial polarization.
2. Pulse 2 switches the polarization.
3. Pulse 3 is a non-switching pulse.
4. Pulse 4 switches the polarization into the opposite state.
5. Pulse 5 is a non-switching pulse.

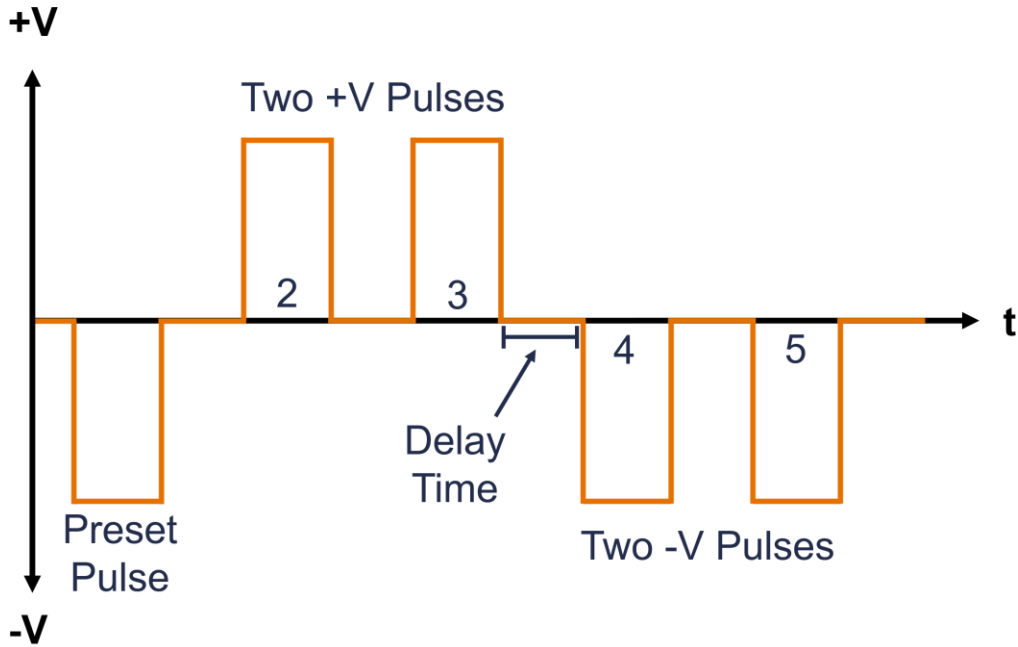


Figure 4.11: Pulse sequence for a positive-up, negative-down measurement.

The remanent polarization is calculated by subtracting the non-switching polarization from the total polarization at zero applied voltage. The pulse width and delay time can influence the measurement and should be chosen carefully. Smaller pulse widths decrease the amount of switched charge in the ferroelectric and may more accurately represent the switching properties in high-frequency applications. The delay time should be at least 1000 ms to account for any polarization relaxation that may occur. A Radiant Technologies Precision LC II Ferroelectric Property Analyzer was used for all PUND measurements shown in this dissertation.

4.10.3. Capacitance-Voltage Measurement

Capacitance-voltage (C-V) measurements are another way to examine the ferroelectric behavior of ferroelectric thin films. These measurements are performed by applying a sweeping DC voltage with a small AC signal (in the range of 50 mV) superimposed. The frequency generally ranges from 1 kHz to 100 kHz. Using Equation 4.4, the relative permittivity, ϵ_r , of the material can be calculated from the capacitance:

$$\epsilon_r = \frac{\epsilon_0 A}{Cd}, \quad 4.4$$

where ϵ_0 is the permittivity of free space, A is the electrode area, C is the capacitance, and d is the film thickness. The relative permittivity can provide insight into the phases present in the film since each phase has been shown to have a specific range of relative permittivity values.¹⁷⁹

Ferroelectric materials will produce a distinctive butterfly loop, as shown in the C-V measurement made on a 20 nm thick HZO film in **Figure 4.12**. The two peaks in the loop are associated with the switching of domains and occur near the coercive field of the material. These maxima occur near the coercive fields because only a small AC voltage is required to switch ferroelectric domains when the sweeping DC voltage approaches the coercive field.¹⁸⁹ A Keysight E4980A Precision LCR Meter was used for C-V measurements in this work with a 50 mV, 10 kHz oscillator.

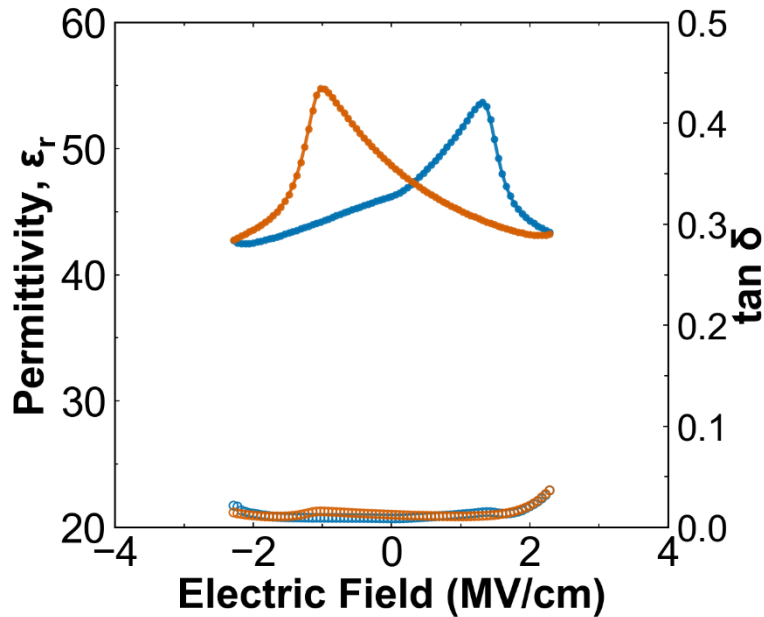


Figure 4.12: Relative permittivity (left axis) and loss tangent (right axis) versus electric field for a 20 nm thick HZO film.

4.11. Summary

The techniques described above are used throughout this work to understand the structural, chemical, and electrical properties of HfO₂-based thin films. These techniques include grazing incidence X-ray diffraction (GIXRD), X-ray reflectivity (XRR), $\sin^2\psi$ stress analysis, X-ray photoelectron spectroscopy (XPS), scanning electron microscopy (SEM), atomic force

microscopy (AFM), transmission electron microscopy (TEM), Fourier Transform Infrared Spectroscopy (FTIR), and electrical characterization techniques.

Chapter 5: Impact of Oxygen Content on Phase Constitution and Ferroelectric Behavior of Hafnium Oxide Thin Films Deposited by Reactive High-Power Impulse Magnetron Sputtering

The contents of this chapter are published in *Acta Materialia* (239, 118220, 2022, DOI: <https://doi.org/10.1016/j.actamat.2022.118220>) with the following authors. Supplemental information and figures have been included as necessary.

Samantha T. Jaszewski^a, Eric R. Hoglund^a, Anna Costine^a, Marc H. Weber^b, Shelby S. Fields^a, Maria Gabriela Sales^a, Jaykumar Vaidya^c, Leah Bellcase^d, Katie Loughlin^d, Alejandro Salanova^a, Diane A. Dickie,^{a,e} Steven L. Wolfley^f, M. David Henry^f, Jon-Paul Maria^g, Jacob L. Jones^d, Nikhil Shukla^c, Stephen J. McDonnell^a, Petra Reinke^a, Patrick E. Hopkins^{a,h,i}, James M. Howe^a, and Jon F. Ihlefeld^{a, c}

^a *Department of Materials Science and Engineering, University of Virginia, Charlottesville, Virginia 22904, USA*

^b *Institute of Materials Research, Washington State University, Pullman, WA 99164, USA*

^c *Charles L. Brown Department of Electrical and Computer Engineering, University of Virginia, Charlottesville, Virginia 22904, USA*

^d *Department of Materials Science and Engineering, North Carolina State University, Raleigh, North Carolina 27695, USA*

^e *Department of Chemistry, University of Virginia, Charlottesville, Virginia 22904, USA*

^f *Sandia National Laboratories, Albuquerque, New Mexico 87185, USA*

^g *Department of Materials Science and Engineering, Pennsylvania State University, University Park, Pennsylvania 16802, USA*

^h *Department of Mechanical and Aerospace Engineering, Charlottesville, Virginia 22904, USA*

ⁱ *Department of Physics, Charlottesville, Virginia 22904, USA*

5.1. Motivation

Oxygen vacancies have been shown to significantly affect the performance of ferroelectric HfO₂-based thin films and devices due to their impact on phase stabilization, electrical properties, wake-up, and fatigue. In parallel, reports have also suggested that microstructure may be the main factor that affects the phases present in HfO₂-based thin films. The purpose of this work was to investigate the relative impacts of oxygen content and microstructure on the phases present and ferroelectric properties of undoped HfO₂ thin films. By utilizing HiPIMS, which affords greater

control of oxygen content and lack of impurities in comparison to ALD, the effects oxygen content and microstructure can be evaluated without the influence of dopants or mechanical stress that are present in ALD films. Additionally, several characterization techniques are used to quantify and characterize the oxygen vacancies in the films to better understand their impacts on this material.

5.2. Abstract

Ferroelectric HfO_2 holds promise for many applications, including non-volatile on-chip memory and ferroelectric field-effect transistors. One challenge preventing the integration of ferroelectric HfO_2 into devices is the difficulty to unambiguously prepare phase-pure material without the benefits of epitaxy. Here, a new method for preparing ferroelectric HfO_2 is presented using High-Power Impulse Magnetron Sputtering (HiPIMS). HiPIMS offers a unique combination of processing parameters such as incident ion energy and gas atmosphere that are inaccessible through conventional HfO_2 synthesis by atomic layer deposition (ALD). In this work, the impact of plasma oxygen content on the crystallization, phase constitution, microstructure, and ferroelectric properties of undoped HfO_2 films deposited by HiPIMS is investigated. HfO_2 thin films were reactively sputtered with plasma oxygen content varied from 7.1 to 8.0 %. The impact of grain size on performance and phases present was assessed, and the results show that the microstructure does not strongly vary between ferroelectric and non-ferroelectric samples. It will be shown that the oxygen content in the plasma directly relates to the oxygen content in the films, as assessed by electron energy-loss spectroscopy, X-ray photoelectron spectroscopy, and positron annihilation spectroscopy. This oxygen content strongly influences phase formation and ferroelectric performance. High concentrations of neutral oxygen vacancies are identified in crystalline ferroelectric samples and allow for low leakage currents. These results show that oxygen content can be used to dictate phase nucleation and provide a path toward phase-pure polycrystalline ferroelectric HfO_2 .

5.3. Introduction

Since the first report of ferroelectricity in hafnium oxide (HfO_2) doped with SiO_2 in 2011,¹ significant research efforts have been directed toward understanding the switchable spontaneous polarization in this material. HfO_2 is chemically compatible with silicon,² is currently used as a high- κ dielectric in complementary metal oxide semiconductor (CMOS) devices,³ and in the

ferroelectric phase is not susceptible to the thickness scaling effects that impose application limitations on traditional ferroelectrics.^{4,5} Thus, this material presents opportunities for technological developments in devices, such as renewed scaling of ferroelectric random access memory (FeRAM), ferroelectric field effect transistors (FeFETS), and new devices such as ferroelectric tunnel junctions (FTJs) that previously required epitaxial growth.

The wide-scale adoption of ferroelectric HfO₂ into devices is constrained, in part, by an inability to prepare phase-pure films. In equilibrium at room temperature and atmospheric pressure, HfO₂ exists in the nonpolar monoclinic $P2_1/c$ phase. Multiple metastable phases exist, including an orthorhombic $Pca2_1$ phase and a tetragonal $P4_2/nmc$ phase, which can be stabilized by various factors. Ferroelectricity in HfO₂ has been attributed to the non-centrosymmetric $Pca2_1$ orthorhombic phase. The factors that have been shown to impact phase constitution include dopant type and concentration,⁶⁻¹⁰ biaxial stress,¹¹ oxygen vacancies,¹² and film thickness or grain size.^{13,14}

The majority of research on ferroelectric HfO₂ thus far has utilized atomic layer deposition (ALD) for film preparation. These films are typically amorphous as deposited and must be annealed at an elevated temperature to form the ferroelectric phase. The stochastic nature of nucleation results in films with a broad grain size distribution¹⁵ and are typically multi-phase. Because conventional thermal ALD has few adjustable parameters, controlling microstructure using this method is difficult. Additionally, most ALD films possess carbon impurities from residual precursor ligands, which may affect the ferroelectric properties¹⁶⁻¹⁸. Therefore, physical vapor deposition (PVD) methods, which offer greater freedom in engineering deposition conditions, are promising candidates for the preparation of ferroelectric HfO₂. To date, several reports on the PVD of HfO₂ have been made. Olsen *et al.* reported ferroelectricity in Y-doped HfO₂ prepared by co-sputtering from HfO₂ and Y₂O₃ sources via radio frequency (RF) sputtering,¹⁹ Mittmann *et al.* demonstrated ferroelectricity in undoped HfO₂ films varying in thickness from 8-40 nm deposited by RF sputtering from a ceramic target,²⁰ Mimura *et al.* observed ferroelectricity in epitaxial and polycrystalline Y-doped HfO₂ films deposited by rf sputtering at room temperature from a ceramic target,²¹ and Lee *et al.* prepared ferroelectric Hf_{0.5}Zr_{0.5}O₂ thin films via reactive rf sputtering from a metal target.²² Still, these studies, among others,²³⁻²⁷ leave room for exploration of this film preparation approach.

A previously unexplored PVD method for ferroelectric hafnia is High-Power Impulse Magnetron Sputtering (HiPIMS). HiPIMS is a technique in which low duty cycle pulses (< 5% duty cycle) are applied to the sputter target to produce dense plasmas with a high degree of sputtered atom ionization.²⁸ HiPIMS offers a number of controllable process parameters such as pulse power, pulse duration, background pressure, and gas atmosphere that all impact depositing species energy and fluence and are not accessible using conventional ALD or PVD processes. These process parameters may allow for additional control of the factors that influence the nucleation behavior, microstructure, and ferroelectric properties in HfO₂.

One factor that appears to be particularly important for stabilizing the ferroelectric phase in HfO₂ is grain size owing to large surface energy contributions to the overall free energy in nanoscale materials. Computational work by Materlik *et al.* predicted that the orthorhombic phase in pure HfO₂ can be stabilized by grain sizes ranging from 3-5 nm, with the tetragonal (t-) and monoclinic (m-) phases stabilized by smaller and larger grain sizes, respectively.¹³ This computational prediction is supported by experiments: in ALD-prepared films, degradation of the ferroelectric properties of doped HfO₂ has been observed with film thicknesses over 20 nm due to increasing grain size with film thickness, resulting in stabilization of the monoclinic phase.^{29,30} Similarly, degradation of ferroelectric properties with film thickness was avoided in chemical solution deposited (CSD) doped HfO₂ films where layer-by-layer thermal treatment during the deposition process allowed for control of the grain size as the microstructure was equiaxed rather than columnar.^{31,32} It should be noted that the film thickness dependence of ferroelectric properties was not observed in Y-doped HfO₂ films deposited by pulsed laser deposition with thicknesses ranging from 10 to 930 nm,³³ however, the crystallite sizes in those films also appeared to be on the order of nanoscale.

While grain size control appears to be a critical factor for obtaining phase-pure films, another factor shown to play a significant role in the stability of the orthorhombic phase is the concentration and distribution of oxygen vacancies.^{20,34,35} First-principles calculations of HfO₂ films have shown that incorporation of oxygen vacancies into the lattice reduces the total energy of the orthorhombic and tetragonal phases in comparison to the monoclinic phase.^{36,37} In addition to stabilization of the orthorhombic phase, oxygen vacancies have also been shown to play a role in the “wake-up” effect, in which the remanent polarization increases during electric field cycling due to the redistribution of oxygen vacancies with the applied fields.³⁶

In the present work, the relative impacts of grain size and oxygen content on the phase composition and electrical properties of pure HfO₂ thin films deposited by HiPIMS are studied. HiPIMS enables the use of a high purity hafnium metal target, which results in low levels of impurities compared to ALD-prepared films, for example. This allows for the characterization of properties without the ambiguity associated with dopants and contamination. Phases present are characterized by X-ray diffraction (XRD) and supported by electrical properties, including relative permittivity and polarization. Microstructure is examined using scanning electron microscopy (SEM) and transmission electron microscopy (TEM). Oxygen stoichiometry and oxygen vacancies are characterized using electron energy-loss spectroscopy (EELS), X-ray photoelectron spectroscopy (XPS), and positron annihilation spectroscopy (PAS). Through these characterizations, the impact of oxygen content and microstructure is decoupled, and it is shown that oxygen vacancies play a critical role in phase nucleation and phase stability in hafnium oxide.

5.4. Experimental Procedures

5.4.1. Deposition Parameters

HfO₂ films were deposited on 100 nm thick TaN bottom electrodes on (001)-oriented *p*-type silicon substrates. The TaN was prepared by pulsed dc magnetron sputtering (30 kHz, 4 μs reverse time) from a TaN target within a Denton Discovery 550 system and had a (111)-orientation, as described in prior work.³⁸ Hafnium oxide films were prepared from a 50 mm diameter hafnium metal target of 99.9 % purity (excluding zirconium impurities) affixed to a balanced magnetron sputter gun (Meivac, MAK) within a custom 460 mm diameter spherical stainless steel vacuum chamber. The source to substrate distance was 80 mm and the gun to substrate angle was 45°. The load-locked chamber was evacuated using a turbomolecular pump backed by a rotary vane pump to reach a base pressure of 10⁻⁷ Torr. For HiPIMS depositions, a Starfire Impulse HiPIMS power module was used in conjunction with a dc power supply to deliver square voltage pulses with a duration of 110 μs, a frequency of 200 Hz, and a magnitude of -700 V. These parameters represent a duty cycle of 2.0 % and per-pulse peak plasma power density of 600 W/cm². Following each negative high-power pulse, a +100 V positive pulse of length 200 μs was applied to the target. Argon was used as the sputter gas, and O₂ gas was used as the reactive gas. Argon and O₂ gas flows were controlled by electronic mass flow controllers, and the total process pressure was controlled by a conductance flow valve located in front of the turbomolecular pump. A gas flow

of 15.00 sccm of argon with 1.15, 1.19, 1.23, and 1.30 sccm of O₂ was used to produce oxygen concentrations in the background gas of 7.1, 7.4, 7.6, and 8.0 %, respectively. A constant background pressure of 5 mTorr was measured by a heated capacitance manometer with active PID feedback to the conductance flow valve. Nominally 20 nm thick HfO₂ films were deposited. Films were continuously rotated during growth to minimize thickness gradients, and the substrate platen was grounded. The substrate was not intentionally heated during deposition.

Following deposition, one set of the films was annealed in a pure argon atmosphere (99.999% purity) for 30 seconds at 800 °C in a rapid thermal processor (Allwin 21, Heatwave 610) with a ramp rate of 66.7 °C/s, while the other set was left in the as-deposited state. Finally, top electrodes consisting of 20 nm of titanium nitride and 50 nm of palladium were dc-magnetron sputtered through a shadow mask to create a capacitor structure for electrical measurements. TiN was reactively sputtered from a titanium target with a gas atmosphere of 5 sccm of argon and 1 sccm of nitrogen, pressure of 0.9 mTorr, and dc power density of 7.40 W/cm². Palladium was deposited with an argon background pressure of 5 mTorr and dc power density of 3.31 W/cm². Circular electrode diameters were 100 μm and areas were confirmed by optical microscopy.

5.4.2. Characterization

A Rigaku Smartlab X-ray diffractometer using Cu K α radiation in a parallel beam configuration with a fixed incident angle of 0.7° was used for grazing-incidence X-ray diffraction (GIXRD) measurements to assess crystallinity and phase constitution of films in the as-deposited and annealed states. A 2θ range of 26-33° was selected due to the presence of 100% intensity reflections of the monoclinic $P2_1/c$ phase, tetragonal $P4_2/nmc$ phase, and orthorhombic $Pca2_1$ phase in this range. Crystallite sizes calculated using Scherrer's equation³⁹ were corrected for instrumental broadening effects using Standard Reference Material[®] 660c lanthanum hexaboride powder from the National Institute of Standards and Technology. Area detector XRD measurements were completed using a Bruker APEXII Duo Single Crystal X-Ray diffractometer with a collimated Cu K α radiation source, a fixed omega angle of 15°, and an APEXII CCD area detector. Magnesium oxide powder was adhered to the film surface as a height reference standard. Phase evolution during crystallization was measured using a PANalytical Empyrean X-ray diffractometer with Cu K α radiation in a Bragg-Brentano geometry with a linear detector and an Anton Paar HTK1200 high temperature chamber in a nitrogen environment. The samples were

heated at a rate of 2 °C/min from 25 °C to 1000 °C and diffraction patterns were collected every 6 °C, similar to the parameters used in prior studies of crystallization of hafnia-based films.^{40,41}

Electrical characterization was performed on capacitor structures for the annealed films. Polarization versus electric field ($P(E)$), pulsed positive up, negative down (PUND) polarization switching, and relative permittivity measurements were performed. A Radiant Technologies Precision LC II Ferroelectric Property Analyzer was used to perform $P(E)$ measurements with a period of 10 ms (100 Hz equivalent frequency) and PUND measurements with a 1 ms pulse width, 1000 ms delay, and 2.5 MV/cm applied field. The initial relative permittivities, which contains both the intrinsic permittivity of the lattice and the extrinsic reversible domain wall contributions of the samples, were extracted from dielectric nonlinearity measurements conducted using a Keysight E4980A LCR meter with a frequency of 10 kHz and oscillator levels ranging from 0.002 to 0.500 V, root mean square. Leakage current measurements were performed on a Keithley 4200A-SCS Parameter Analyzer.

Plan-view SEM images were collected using an FEI Helios UC G4 microscope in secondary electron mode with an accelerating voltage of 2.00 kV, beam current of 0.1 nA, dwell time of 15 μ s, working distance of 2.3 mm, and a through-the-lens detector. TEM cross-sections were prepared using the FEI Helios dual-beam focused ion beam. Preparation started with a 30 kV gallium ion beam and high current that was incrementally lowered to a final 5 kV low current setting. TEM experiments used a Thermo Fisher Scientific Themis Z-STEM operating at 200 kV equipped with an Ulti-Monochromator. All energy-loss spectroscopy used a Gatan Imaging Filter equipped with an UltraScan CCD camera. Energy-loss spectra were acquired in micro-probe mode with a semi-convergence angle of 0.77 mrad and an acceptance angle of 5.47 mrad such that elastic contributions were minimized. The energy resolution measured at the zero-loss full-width at half-maximum (FWHM) was 0.16 eV, providing an energy resolution comparable to the lifetime broadening of most core loss events. Individual spectra were acquired across a spectrum image of the film to reduce the dwell time in any position and minimize the possibility of beam damage. The spectrum images were then averaged to provide high signal-to-noise spectra representative of the films. The oxygen K-edge spectra were background subtracted using a power law. Then, the spectra underwent Fourier-ratio deconvolution using the low loss signal that was acquired simultaneously to the core loss spectra. This removes thickness effects and provides single-scattered electron probabilities. Conical darkfield images were acquired in TEM mode with a

10 μm objective aperture selecting first-order reflections. The conical darkfield was recorded on a Thermo Fisher Ceta camera while the electron beam dynamically rotated around the optic-axis. Frames highlighting various grains of each film were then combined to aid in discriminating the nanometer size grains that were diffracting with similar net intensity.

XPS was performed with a Scienta Omicron Multiprobe MXPS system with an XM1200 monochromator. Monochromatic Al K α ($h\nu = 1486.6$ eV) radiation was used to obtain core level spectra, which were collected at the center of the samples. The samples were introduced into ultrahigh vacuum and measured without sputtering or annealing to avoid any process which could modulate the defect population in the near-surface region. All samples had acquired a contamination layer consisting of adventitious carbon and oxygen during transport through air. For an inelastic mean free path of 3.0 nm at the kinetic energy of the Hf 4*f* core electrons, the information depth in these experiments was approximately 9.0 nm. The adventitious carbon layer was approximately 0.8 nm in thickness, which was calculated using the Lambert-Beer law attenuation of the Hf signal, but did not account for the inherent heterogeneity and roughness of this layer. However, its small thickness and the large cross-section of the Hf 4*f* core level enabled analysis of the Hf and O signals without any additional surface cleaning. Survey spectra measured with a pass energy of 100 eV were used to confirm the presence of Hf, O, and C; no other elements were detected. A pass energy of 50 eV and energy steps of 0.05 eV were used for all core level spectra. The resolution is 0.41 eV for this pass energy as defined by the width of the Ag 3*d*_{5/2} core level measured from a standard. The spectra were aligned to the Fermi Level of a clean gold sample set to 84.0 eV. A small charging induced shift of the core levels of less than 2 eV was corrected by alignment of the spectra at the energy of the Hf 4*f*_{7/2} core level with the lowest binding energy in the series: 17.8 eV for the as-deposited samples, which agrees with published values.⁴²⁻⁴⁴ The FWHM of Hf and O peaks was constant throughout the sample series and therefore excluded differential charging. All XPS data were analyzed using KolXPD software.⁴⁵ A Voigt function was suitable for fitting all core levels and was combined with a Shirley background.⁴⁶ Peak areas were corrected by cross-sections provided by Scofield *et al.* for each core level.⁴⁷ Compositions of as-deposited and annealed films were calculated by taking a ratio of the corrected O 1*s* peak area to the corrected Hf 4*f*_{5/2} and Hf 4*f*_{7/2} peak areas.

PAS was performed using the Washington State University monoenergetic variable energy positron beam. Doppler broadening spectra of the 511 keV annihilation line were measured for the

samples as a function of incident positron energy, E , with an energy resolution of 1.32 keV FWHM. The positron beam was generated by a ^{22}Na positron-emitting isotope, and the positron energy was varied from 25 eV to 70 keV, which was sufficient to scan the mean implantation depth through the HfO_2 and TaN into the silicon substrate. Line shape (S) and wing (W) parameters were extracted and fit using VEPFIT.⁴⁸ S was defined as the fraction of events ± 0.74 keV around the centroid of the 511 keV photoelectric peak. A window of 3.26 keV on either side of the centroid channel with an inside edge at 2.61 keV contributed to W. S and W values were normalized with the total background-subtracted counts in the photoelectric peak. Further analysis details have been reported elsewhere.⁴⁹

5.5. Results and Discussion

5.5.1. Phase Characterization

GIXRD measurements were performed before and after rapid thermal annealing the films to assess the crystallinity and identify the phases present. These measurements confirmed that the as-deposited films were amorphous to the extent discernable by XRD, as shown in **Figure 5.1**.

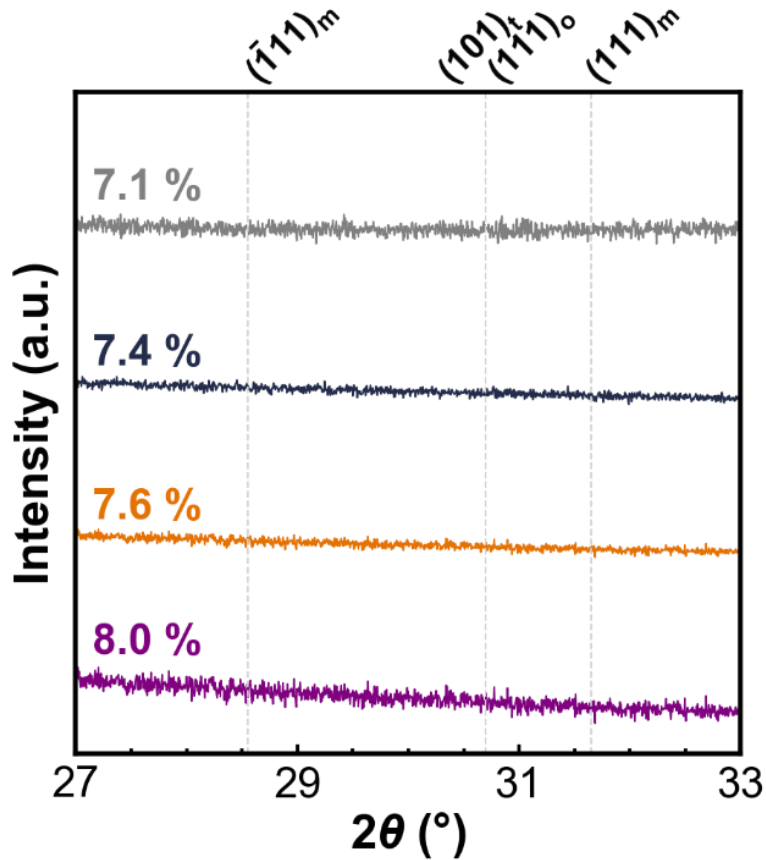


Figure 5.1: GIXRD patterns for as-deposited films.

Figure 5.2 shows the GIXRD measurements performed on annealed films with oxygen concentration in the plasma varied from 7.1 % to 8.0 %. The positions of tetragonal (t), orthorhombic (o), and monoclinic (m) reflections in this region are shown above the diffractogram. The films with 7.1, 7.4, and 7.6 % oxygen in the plasma had an intense peak around 30.5° in 2θ . This peak presents challenges in indexing due to similar d -spacings of the orthorhombic and tetragonal phases; therefore, it could be the result of the orthorhombic (111) reflection, the tetragonal (101) reflection, or a superposition of the two reflections. These phases may be differentiated by electrical property characterization where the orthorhombic phase will display polarization hysteresis while the tetragonal phase will have an antiferroelectric-like response. Low intensity monoclinic phase peaks are discernable in the 7.4 and 7.6 % oxygen samples but not the 7.1 % sample. The film deposited with the highest concentration of oxygen in the plasma, 8.0 %, contained peaks indexed as the monoclinic phase in addition to the orthorhombic and/or tetragonal phases.

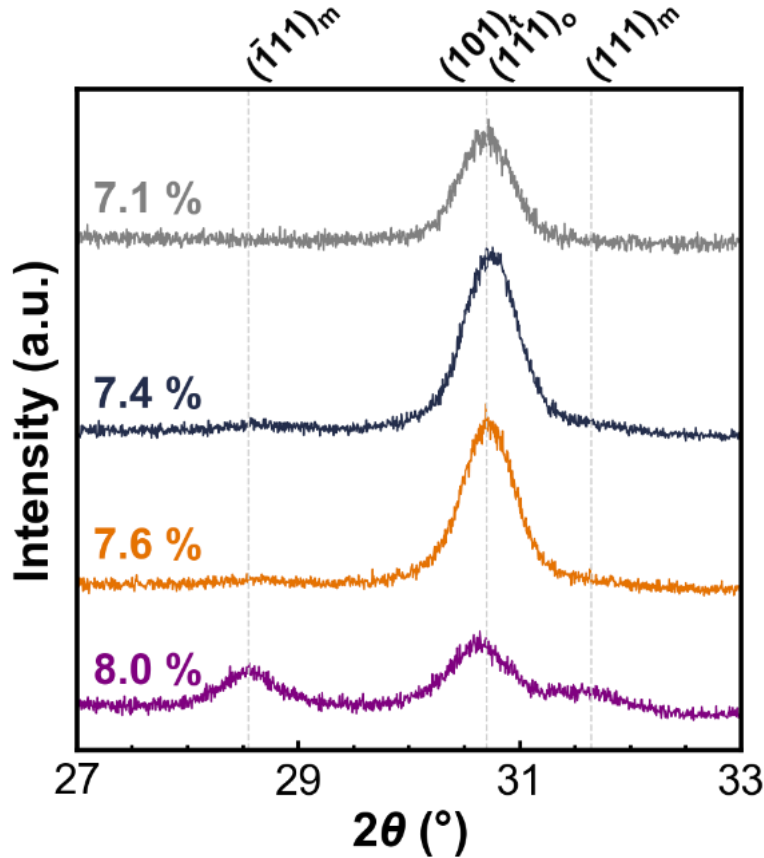


Figure 5.2: GIXRD patterns of crystallized HfO₂ samples with varying oxygen content in the plasma. Indexing for each peak is provided above the panel.

The relative orthorhombic + tetragonal (o+t) phase fractions were calculated by fitting the GIXRD patterns using LIPRAS fitting software⁵⁰ and taking the ratio of the integrated peak intensity of the orthorhombic + tetragonal peak to the integrated intensity sum of all three peaks, $\left(\frac{t_{101}+o_{111}}{t_{101}+o_{111}+m_{111}+m_{111}}\right)$. The relative o+t phase fractions are shown in **Figure 5.3**. Also shown are crystallite sizes that were calculated using Scherrer's equation.³⁹ The films deposited with 7.1, 7.4, and 7.6 % oxygen concentration in the plasma contain primarily orthorhombic + tetragonal phase with relative o+t phase fractions greater than 0.9 and crystallite sizes of approximately 18 nm. The film deposited with 8.0 % oxygen had a relative o+t phase fraction of 0.57 and a crystallite size of 14.9 ± 0.7 nm. It should be noted that the crystallite size was calculated using the orthorhombic + tetragonal peak, so the crystallite size calculation for the 8.0 % sample may be affected by its relatively lower signal-to-noise ratio in comparison with the films that contained

primarily orthorhombic phase, as well as the smaller volume fraction of orthorhombic + tetragonal phases that may result in smaller crystallites. Additionally, the crystallite size is measured in a direction that is approximately 15 degrees off surface normal due to the geometry of the grazing incidence measurement. Effectively, this results in the measured crystallite size to primarily comprise the out-of-plane dimension, but with a minor in-plane contribution.

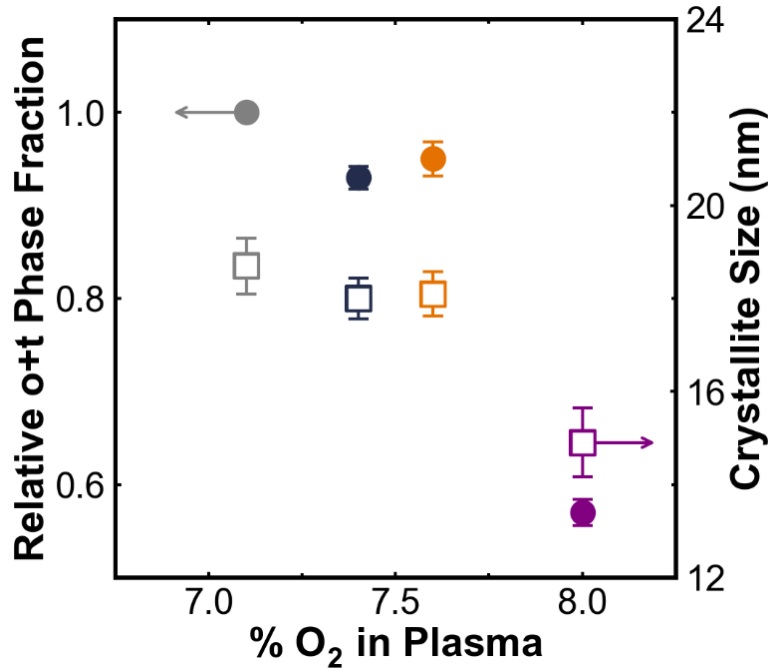


Figure 5.3: Relative o+t phase fractions (closed circles) and crystallite sizes (open squares) calculated from GIXRD patterns.

Area detector XRD measurements were performed to assess the crystallographic texture of the films, and the patterns are shown in **Figure 5.4**. Non-uniform intensity in the $111_o/101_t$ Debye-Scherrer rings indicated the presence of preferred crystallographic texture in the 7.4 and 7.6 % samples. For example, if this peak is primarily due to the orthorhombic phase, then these films crystallized with a preference for a 111 out-of-plane texture. This texture was also observed in the 8.0 % sample along with slight texture of the monoclinic phase, with the higher angle 111_m reflection having an increased out-of-plane component. The origin of this texture is unclear, as it was not previously observed on atomic layer deposited hafnium zirconium oxide (HZO) films prepared on identically processed TaN electrodes⁵¹, but may indicate that the HiPIMS deposition impacts nucleation from the amorphous deposit.

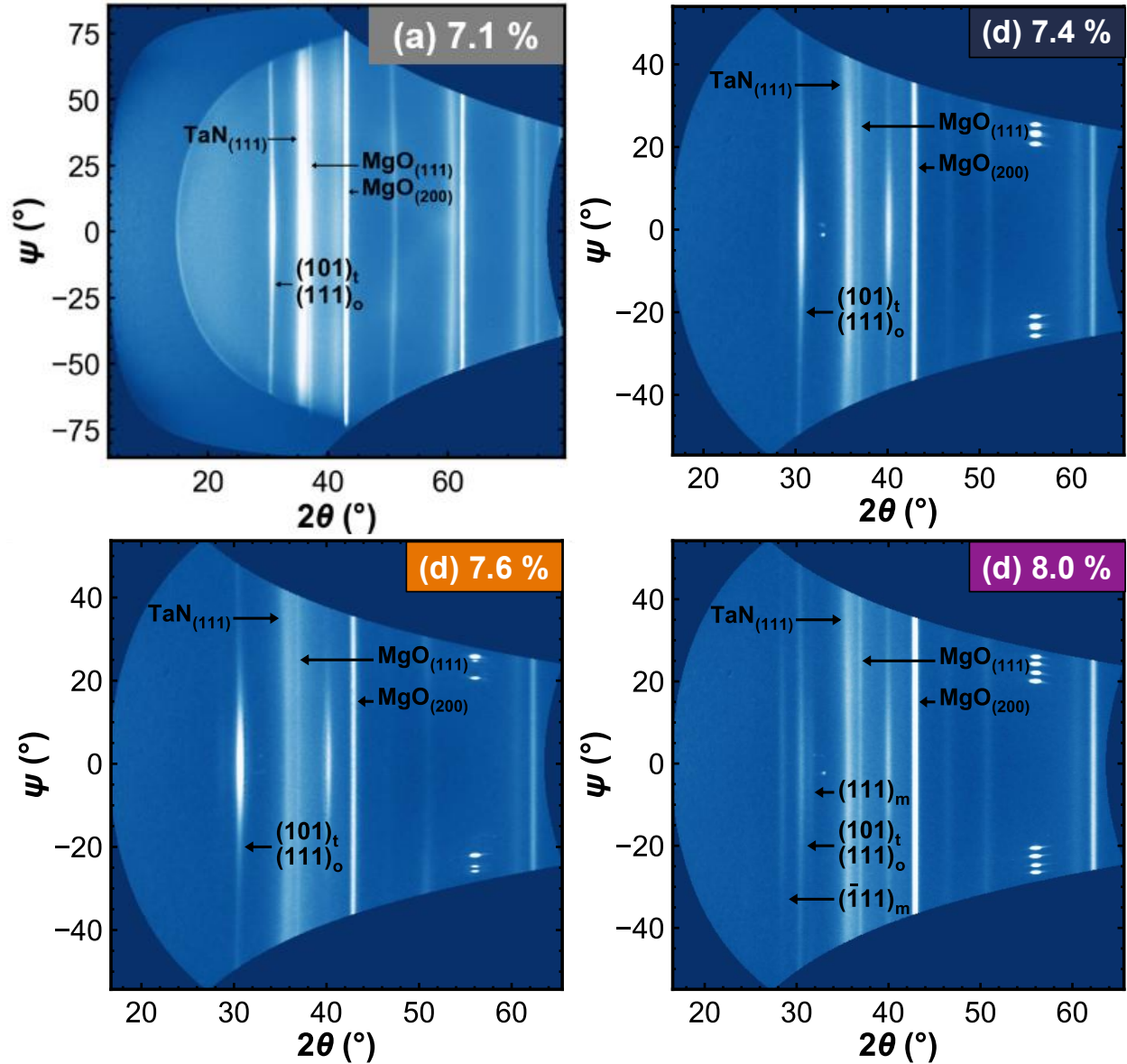


Figure 5.4: Area detector XRD measurements for crystallized (a) 7.1, (b) 7.4, (c) 7.6, and (d) 8.0 % films.

Differences in the nucleation behavior leading to the varied phases in the films prepared with different oxygen contents were sought using in-situ, high-temperature X-ray diffraction (HTXRD) measurements. These experiments were performed on films prepared with the three highest oxygen contents, with the results provided in **Figure 5.5**. Significant differences in crystallization temperatures or phases between these films were not observed, with all films containing significant fractions of the monoclinic phase, which formed at 460 °C. These results

differed from the observations for rapid thermal annealed films, where the lower oxygen content films had virtually no monoclinic phase. However, the heating rate used for these HTXRD experiments was significantly slower than the films which underwent a rapid thermal anneal (2 °C/minute compared to 67 °C/second), and studies have shown that heating rate significantly affects phase formation in HfO₂-based thin films.^{52,53} Additionally, at sufficiently high temperatures and long times, the high kinetic barrier of the transition from the tetragonal or orthorhombic phases to the monoclinic phase can be overcome and the monoclinic phase can be formed during the annealing process.^{54,55} Thus, the kinetic mechanisms for monoclinic phase formation may be responsible for the differences observed here. Further, the presence of oxygen impurities in the nitrogen gas, desorption from the furnace insulation, and desorption from the alumina sample stage and sample holder during these measurements may have eliminated the differences in the original oxygen content within the films and altered the nucleation behavior.

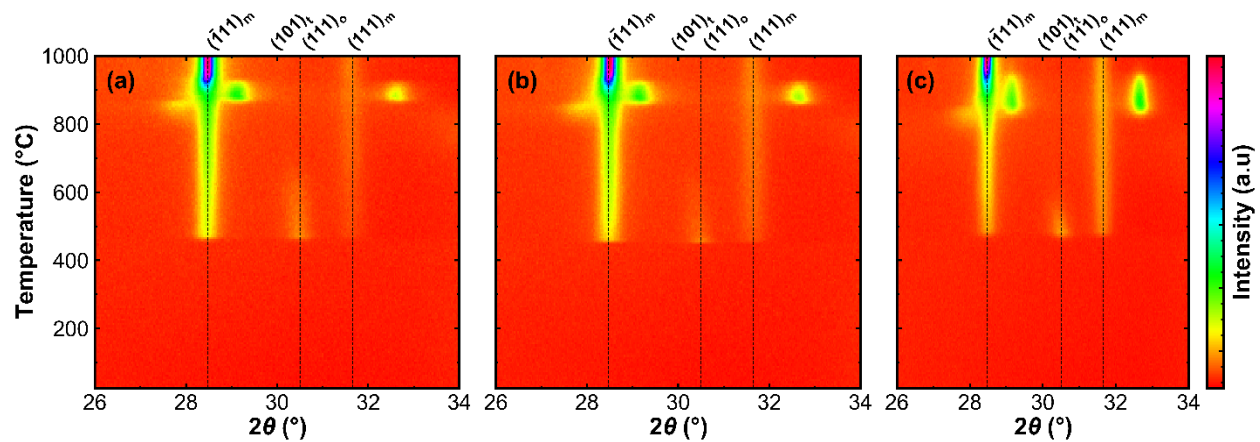


Figure 5.5: High temperature XRD measurements of films deposited with equivalence of (a) 7.4, (b) 7.6, and (c) 8.0 % oxygen.

5.5.2. Electrical Characterization

Figure 5.6 shows the polarization response of films deposited with (a) 7.4 %, (b) 7.6 %, and (c) 8.0 % oxygen in the plasma following field cycling with 5000 3 MV/cm square waves. The remanent polarizations obtained using PUND measurements and relative permittivity values, assessed as the initial permittivity from a Rayleigh formalism, are shown in **Fig. 5.6(d)**. The previously discussed film with 7.1 % oxygen in the plasma was electrically shorted in the pristine condition (before field cycling), so the characterization of electrical properties focused on the films

deposited with higher oxygen content in the plasma. Before field cycling, the polarization hysteresis loops were pinched (**Figure 5.7**), as is commonly observed for hafnia-based ferroelectrics, and may be attributed, in part, to domain pinning or presence of the tetragonal phase. Relative permittivities of the three samples were 34, 35, and 26 for the 7.4, 7.6, and 8.0 % samples, respectively. After field cycling, the loops opened up, and the polarization response for all of the films was well-saturated, indicative of low leakage current contributions and large orthorhombic phase contents. The films deposited with 7.4 % and 7.6 % oxygen in the plasma had remanent polarization values of 8.0 and 8.7 $\mu\text{C}/\text{cm}^2$, respectively and similar coercive fields of +1.3/-0.7 MV/cm. The 8.0% sample had a lower remanent polarization of 3.5 $\mu\text{C}/\text{cm}^2$, lower saturation polarization, and coercive fields of +0.6/-0.3 MV/cm. Relative permittivities of the films after field cycling were 34, 34, and 26 for the 7.4, 7.6, and 8.0 % samples, respectively. The low permittivity of the film deposited with 8.0 % oxygen in the plasma can be explained, in part, by the presence of the monoclinic phase in this film since the monoclinic phase is known to have the lowest relative permittivity of the three phases.⁵⁶ The minimal changes in permittivities of the 7.4 and 7.6 % samples after cycling suggest that domain pinning was largely responsible for the pinched hysteresis response before cycling and that wake-up-driven phase transformations had limited contribution to the observed increase in remanent polarization. This indicates that the diffraction data above is showing largely the orthorhombic phase rather than a combination of tetragonal and orthorhombic phases.

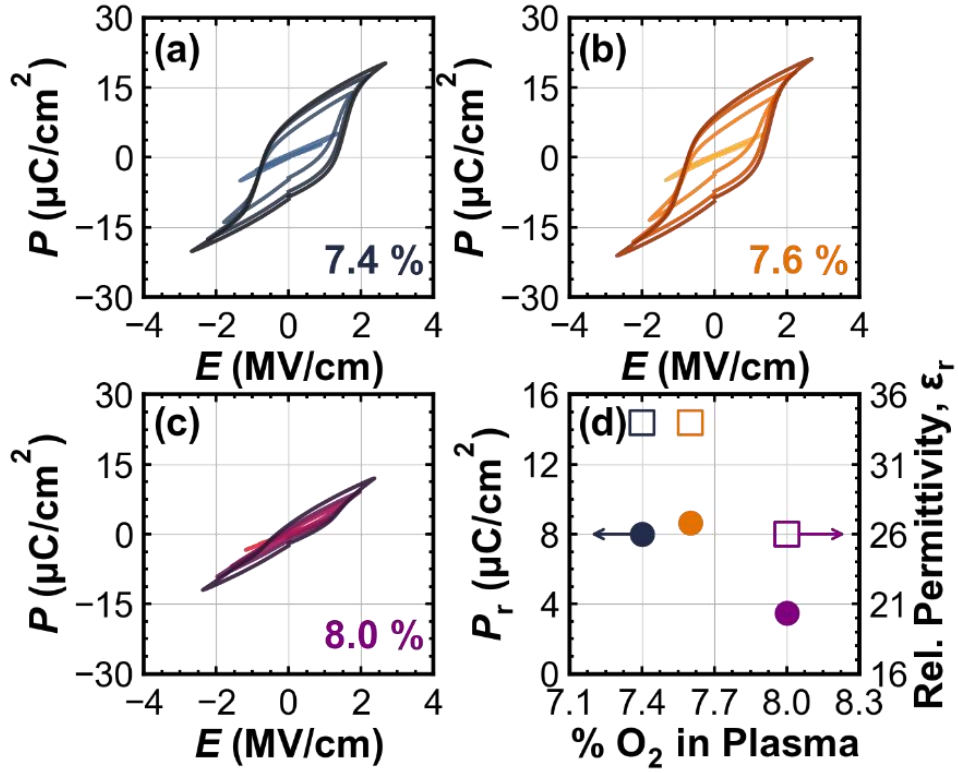


Figure 5.6: Nested polarization hysteresis measurements after field cycling for the samples deposited with oxygen plasma concentrations of (a) 7.4 %, (b) 7.6 %, and (c) 8.0 %. (d) Remanent polarization from PUND (closed circles) and relative permittivity (open squares) versus % O_2 in the plasma.

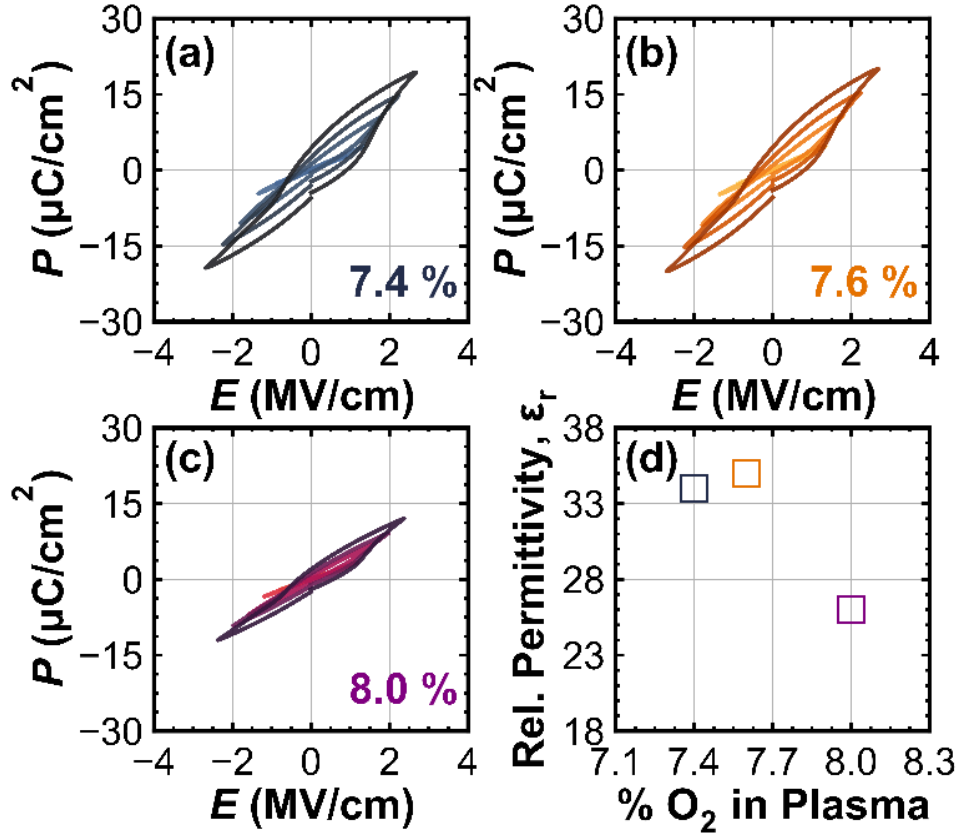


Figure 5.7: Nested polarization hysteresis measurements for the samples deposited with (a) 7.4 % O_2 , (b) 7.6 % O_2 , and (c) 8.0 % O_2 before field cycling. (d) Relative permittivity versus % O_2 in the plasma.

5.5.3. Microstructural Characterization

Since grain size was anticipated to play a significant role in phase stability in HfO_2 thin films, the microstructure was examined using plan-view SEM with images shown in **Figure 5.8**. From visual inspection of these micrographs, the grains appear to be similar in size and morphology. To further quantify the grain sizes, the lineal intercept procedure was used, and the mean intercept length is reported in **Figure 5.9**, with error bars representing 95% confidence intervals.⁵⁷ Quantification of the mean intercept length reveals sizes between 19.1 ± 1.3 to 20.6 ± 1.1 nm and virtually no difference in the lateral grain sizes between samples.

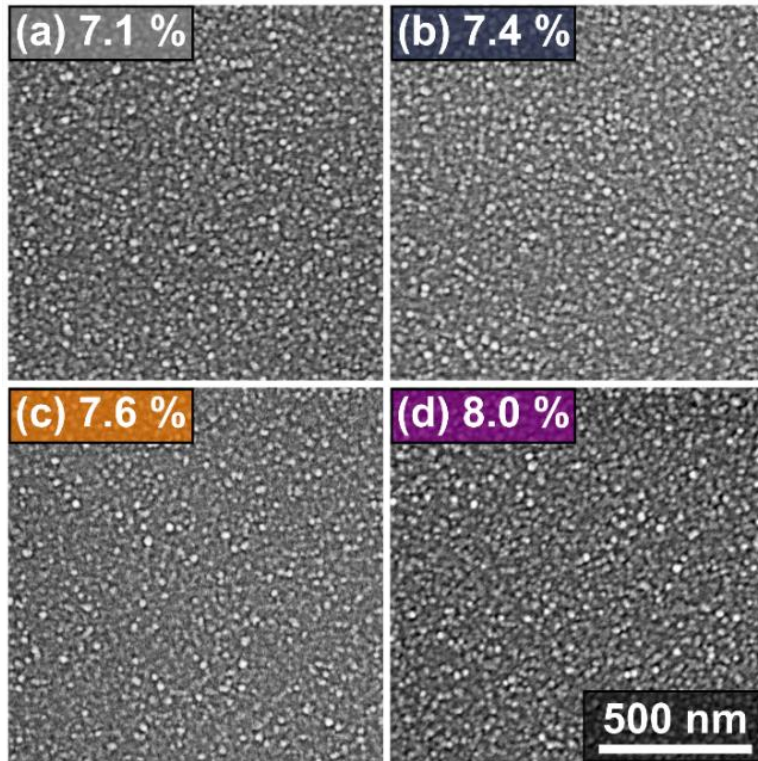


Figure 5.8: Plan-view SEM images of films with varying oxygen content during deposition.

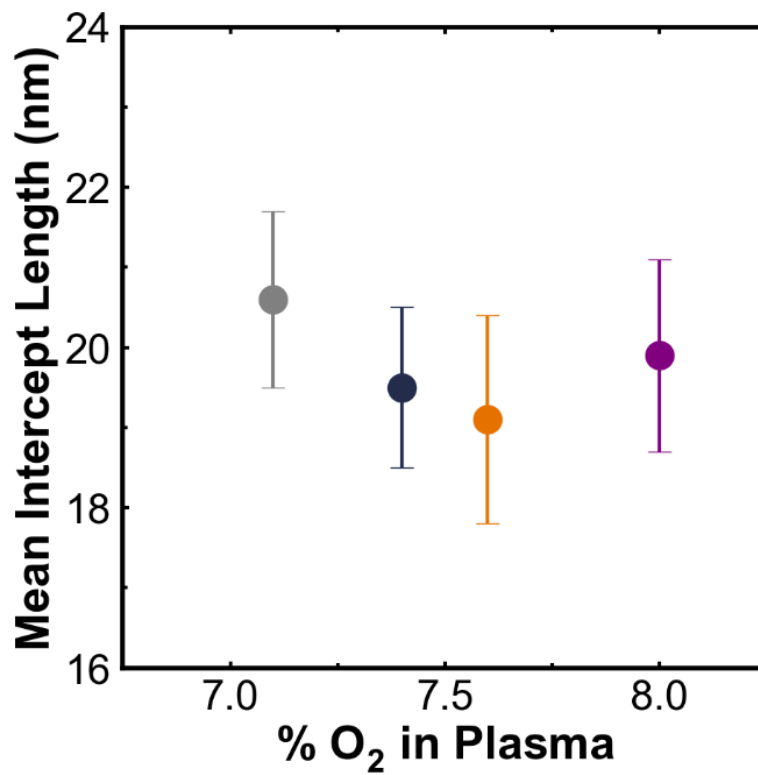


Figure 5.9: Average lateral grain size calculated using the line-intercept method on the plan-view SEM micrographs with error bars representing 95 % confidence intervals.

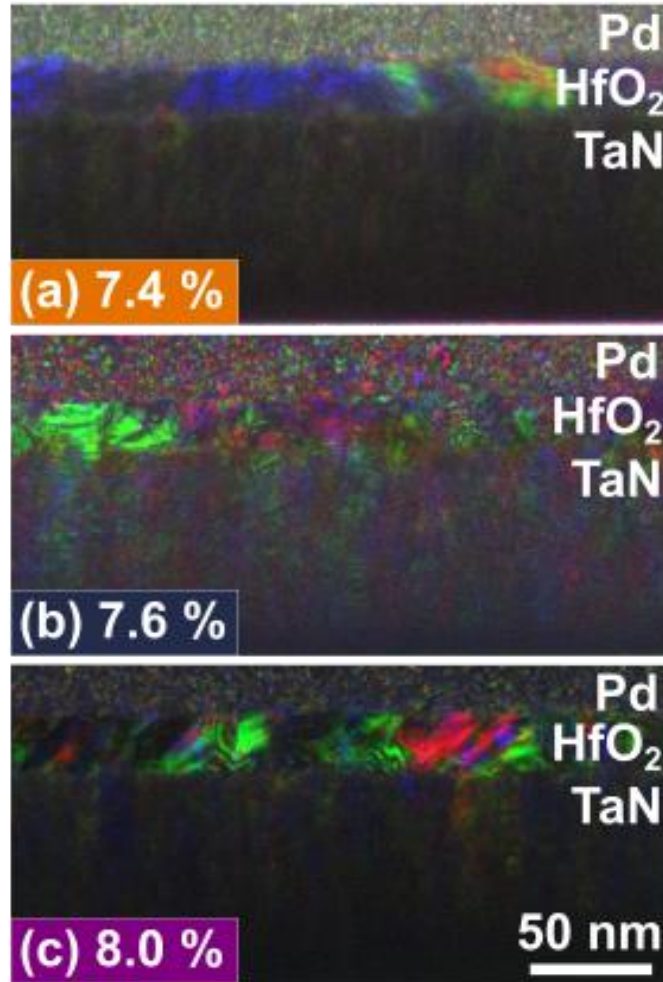


Figure 5.10: Dark-field TEM images of annealed samples deposited with (a) 7.4, (b) 7.6, and (c) 8.0 % oxygen in the plasma. The red, blue, and green colors correspond to data collected for different electron beam rotations about the optic axis.

Composite conical dark-field TEM micrographs of the films are provided in **Figure 5.10**. Conical dark-field was performed instead of conventional bright-field imaging because all grains in the bright-field images had similar diffraction contrast. The conical dark-field images were acquired with the same electron beam tilt-angle and different rotations about the optic axis. Each composite conical dark-field image comprises three individual conical dark-field images and allows the microstructure to be assessed over larger areas. The three different colors of the images represent grains that satisfy diffraction conditions for the three different rotations. The micrographs reveal that the films are one grain thick. Furthermore, it was observed that the films contain approximately 100 nm wide clusters of similarly-oriented grains with average lateral grain sizes

of 20 nm, suggesting that these clusters are approximately five grains across. The average in-plane grain diameters calculated from measurements of 10 grains in each sample are shown in **Table 5.1** and are, in general, consistent with the plan-view measurements. Because of the presence of ferroelastic twin boundaries in the monoclinic grains, the calculated average grain diameter is effectively half of its actual size. Taking domains into account, the dark-field results agree with the conclusions drawn from the SEM grain size measurements and the crystallite size measurements from XRD data, which show that the grain size does not significantly vary with oxygen content.

Table 5.1: Average grain size and 95% confidence interval from SEM images and average in-plane grain diameter and standard deviation from dark-field TEM images.

% O₂ in Plasma	Average Grain Size from SEM (nm)	95% Confidence Interval (nm)	Average Grain Diameter from TEM (nm)	Standard Deviation (nm)
7.4	19.5	1.0	28.66	12.64
7.6	19.1	1.3	22.15	12.31
8.0	19.9	1.2	14.14	3.55

Combined, the SEM and TEM microstructure analysis showed minimal variations in grain sizes for each sputter condition. However, X-ray diffraction and electrical analysis showed significant variations in phases present and ferroelectric behavior. These results suggest that the phase constitution and performance cannot be explained by differences in grain size. The oxygen content in the sputter atmosphere appears to play a much stronger role. Although the oxygen content in the plasma during sputtering is known, it is unknown how this affects the oxygen content in the deposited films and how the oxygen content may change after annealing. Thus, several techniques were used to evaluate the oxygen content in the films to enable the correlation of phase formation and ferroelectric response with oxygen stoichiometry.

5.5.4. Leakage Current Measurements

To start, leakage current measurements were performed as an indirect method to assess oxygen vacancy concentrations. Several groups have used leakage current measurements to estimate oxygen vacancy concentrations via trap-assisted tunneling fits for HfO_2 -based thin films.^{34,51,58} It is known that higher oxygen vacancy concentrations result in higher leakage currents due to oxygen vacancies acting as charge carrier traps and electroneutrality conditions dictating that each oxygen vacancy be compensated by two electrons.⁵⁹⁻⁶¹ However, measurements of leakage current in the crystalline films in this study (**Figure 5.11**) revealed values of 10^{-10} to 10^{-7} A/cm^2 even at fields as high as 2.5 MV/cm . These low leakage currents are consistent with the well-saturating polarization hysteresis measurements, which showed no indications of leakage current artifacts despite the relatively low measurement frequency. No obvious signature of trap-assisted tunneling could be observed in these films, and this precluded the use of the leakage current measurement and fitting approach to estimate oxygen vacancy concentrations.

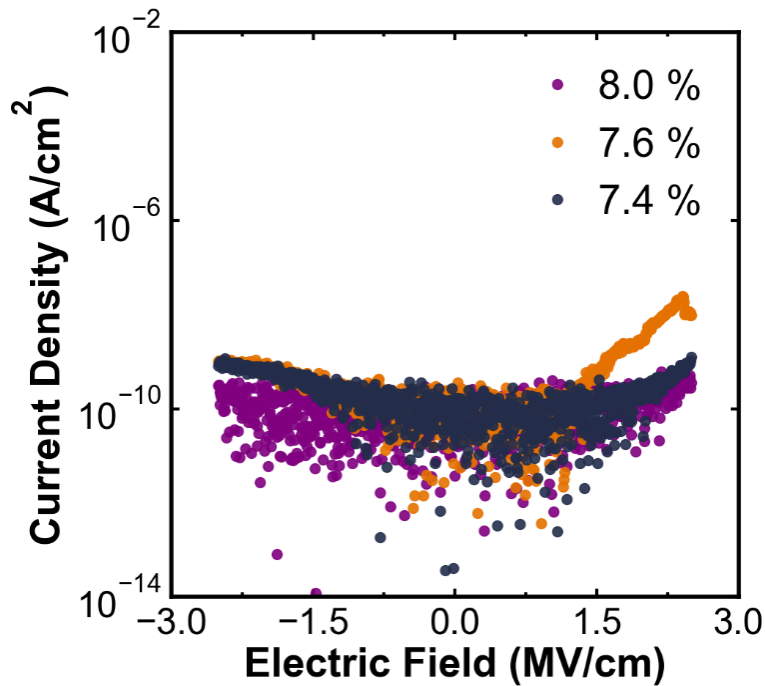


Figure 5.11: Leakage current density measurements for annealed films deposited with 7.4, 7.6, and 8.0 % oxygen in the sputtering atmosphere.

5.5.5. Electron Energy Loss Spectroscopy

EELS was conducted via TEM to further investigate the oxygen stoichiometry and electronic structure of the crystalline films. **Figure 5.12a** shows the single-scattered O-*K* ionization edge, which measures excitations from O 1*s* core levels to unoccupied O 2*p* states.⁶² The energy-loss near-edge fine structures (ELNES) provide information about the local electronic structure around the oxygen ions.⁶³ A higher intensity in this region is indicative of more oxygen in the films, and a trend of higher signals with increasing oxygen in the plasma during deposition is evident. The doublet peak, consisting of the peaks labeled A and B, at the edge onset are due to crystal field splitting of the Hf 5*d* states, which are hybridized with the O 2*p* states.⁶⁴ The reduced intensity of peak A in comparison to peak B has been attributed to the presence of oxygen vacancies in zirconium oxide, and has also been observed in low-oxygen content ALD-prepared HfO₂ films.^{65,66} The reduced intensity of peak A for the 7.4 % oxygen sample is more pronounced in **Figure 5.12b**, where the intensity was normalized to the peak B maximum, indicating that this sample may have a higher concentration of oxygen vacancies than the 7.6 and 8.0 % samples. Additionally, the 8.0 % sample shows increased asymmetry of peak A in comparison to the other samples. This is likely due to the presence of the monoclinic phase, in addition to the orthorhombic/tetragonal phases, in this sample, which will lead to broadening of these peaks due to variations in bond lengths, angles, and ion coordination.^{67,68}

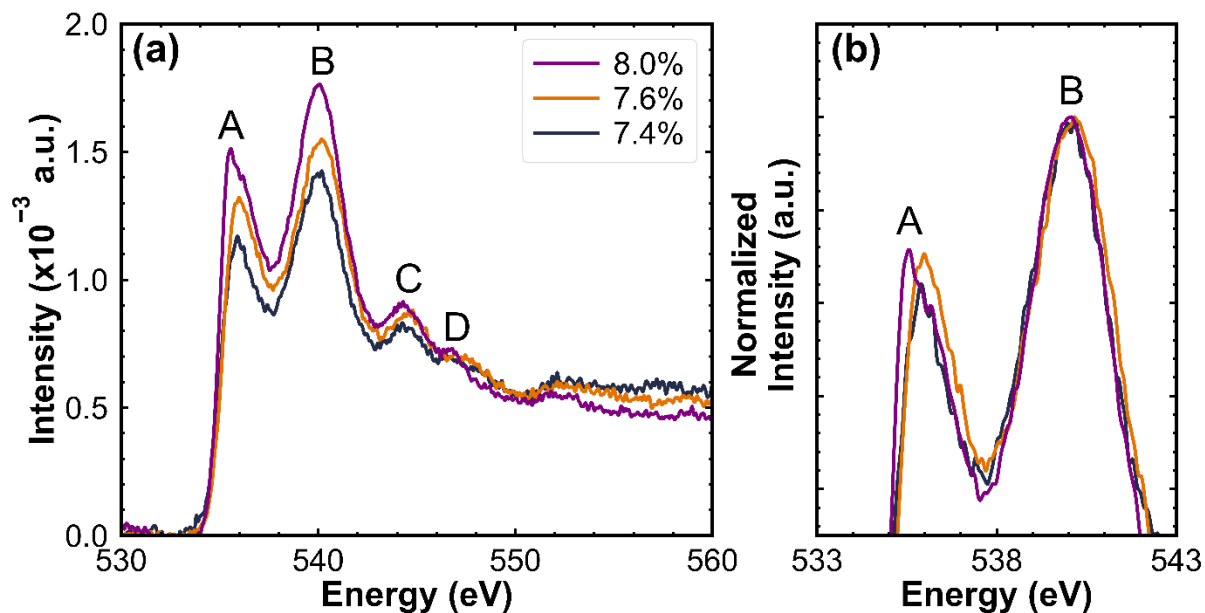


Figure 5.12: (a) Single-scattered core-loss EELS spectra showing the O-K ionization edge of films deposited with 7.4, 7.6, and 8.0 % oxygen. (b) Doublet peaks (A and B) at the edge onset with normalized maximum intensity of peak B.

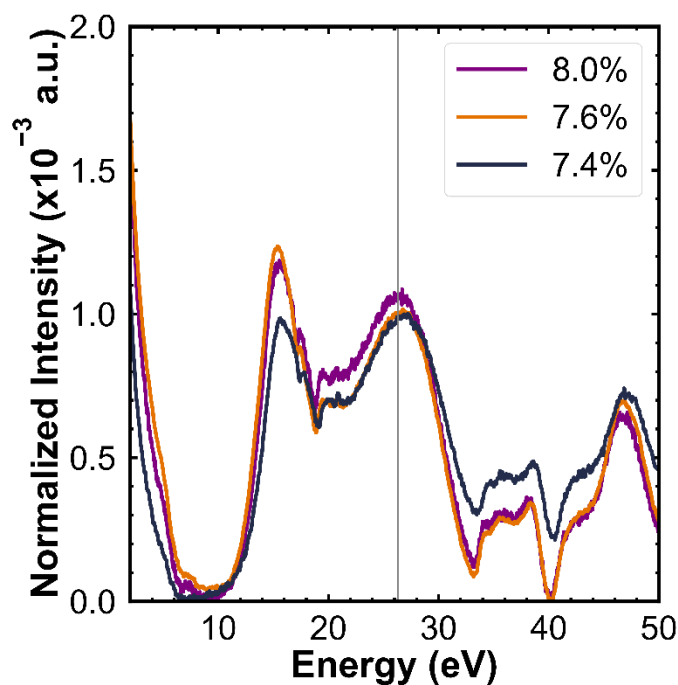


Figure 5.13: Low-loss EELS spectra for hafnium oxide with varying oxygen. The grey line marks the center of the plasmon peak for the 8.0 % sample.

Figure 5.13 shows the low-loss EELS spectra for the samples. The peak marked with the grey line results from a plasmon excitation.⁶⁹ There are a number of factors that can affect the position of this peak, including oxygen vacancy concentration. A shift in the position of this peak indicates a change in carrier concentration, where a shift to higher energy indicates more carriers.⁶⁸ The 7.4 and 7.6 % oxygen samples have shifted to higher energies in comparison to the 8.0 % sample, suggesting that these samples contain more oxygen vacancies in agreement with previous research.⁶⁸ This is supported by the calculated stoichiometry, x in HfO_x , shown in **Table 5.2**, which was assessed using the O- K edge, measured from 530 to 560 eV (**Fig. 5.12**), and Hf- M edges, measured from 1650 to 1840 eV shown in **Figure 5.14**. Using edges separated by large energies can affect background fitting and may result in quantification errors. However, the relative differences in the stoichiometries between samples are able to be used for comparison. From this analysis, it can be observed that the sample deposited with the lowest amount of oxygen in the plasma is the most oxygen-deficient, likely correlating with a higher concentration of oxygen vacancies.

Table 5.2: Compositions of the amorphous films (from XPS) and crystallized films (from XPS and EELS).

% O ₂ in Plasma	x in HfO _x from	x in HfO _x from	x in HfO _x from
	EELS (Crystalline)	XPS (Amorphous)	XPS (Crystalline)
7.4	1.51	1.60	1.30
7.6	1.63	1.79	1.47
8.0	1.68	1.83	1.70

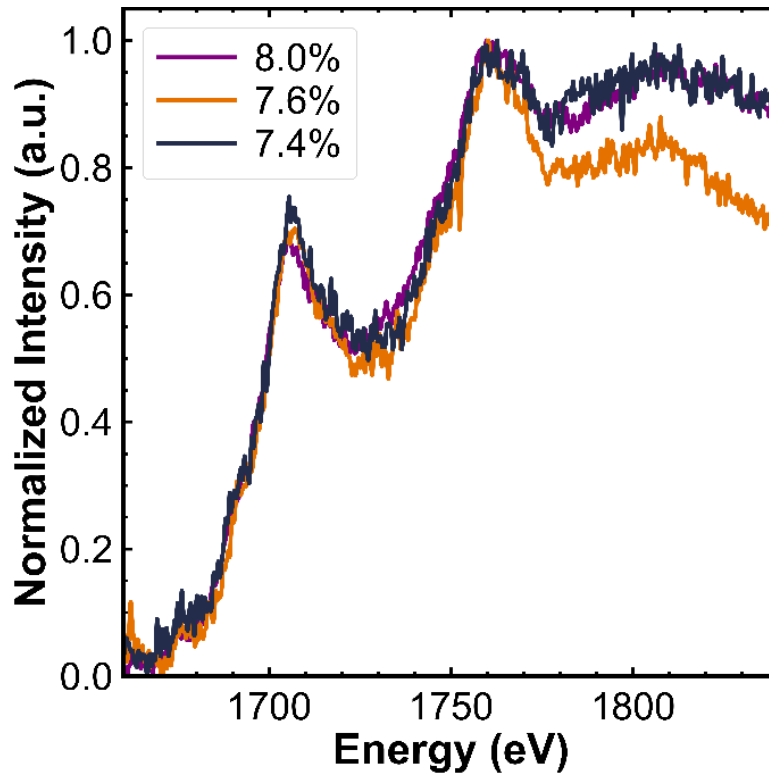


Figure 5.14: EELS spectra showing the Hf-M edge used for stoichiometry calculations of annealed films deposited with 7.4, 7.6, and 8.0 % oxygen in the sputtering atmosphere.

5.5.6. X-Ray Photoelectron Spectroscopy

To further investigate the oxygen content, XPS was used to study films in both the amorphous and crystalline states. The composition in the surface and near-surface region were obtained by fitting the Hf $4f$ and O $1s$ spectra to calculate the ratio of oxygen to hafnium. The value of x in HfO_x obtained from XPS for amorphous and crystalline films is included in **Table 5.2**. Because the O $1s$ core electrons have a lower kinetic energy than the Hf $4f$ core electrons, the adventitious carbon layer will attenuate the O $1s$ signal more than the Hf $4f$ signal, resulting in compositions that are more oxygen deficient. However, these values are similar to those obtained from EELS measurements, and can be used for qualitative comparison. Thus, it is evident that the films are oxygen-deficient, and the oxygen content increases as expected with the oxygen concentration in the plasma during deposition, consistent with the EELS results.

To gain more insight into the electronic structure, **Figure 5.15** shows the Hf $4f$ core levels for (a) amorphous and (b) crystalline films with the intensity normalized to the Hf $4f_{7/2}$ peak maximum. The insets show the tail on the low binding energy side of the Hf $4f_{7/2}$ peak, which is

known to correlate with the presence of a sub-oxide Hf^{3+} peak. This signature has been attributed to the presence of oxygen vacancies in which the two electrons remaining at the vacancy site from the removed neutral oxygen atom are distributed among two neighboring Hf^{4+} atoms.⁷⁰⁻⁷³ Evidence of this sub-oxide Hf^{3+} contribution is visible in the tail of the $\text{Hf } 4f_{7/2}$ peak for the amorphous films deposited with 7.4 and 7.6 % oxygen. Although the intensity of the Hf^{3+} peak is too low to allow for a quantitative assessment with a fit, a comparison of the spectra shows a clear trend: increasing contribution from the Hf^{3+} peak, and thus increasing concentration of charged oxygen vacancies correlates with decreasing oxygen percentage during sputtering. The corresponding $\text{Hf}^{3+} 4f_{5/2}$ peak is positioned in the valley between the Hf^{4+} doublet and leads, therefore, to a concomitant change in the depth of this valley. In the crystalline films, however, there are no observable differences in the tails of the $\text{Hf } 4f_{7/2}$ peaks or in the valleys. These results suggest that there is a larger concentration of positively charged oxygen vacancies in the amorphous films than in the films after rapid thermal annealing and crystallization. This is despite the stoichiometry quantification by EELS and XPS showing large oxygen deficiencies in both the amorphous and crystallized states. It is speculated that after crystallization, the oxygen vacancies are neutral and have electrons trapped to their local sites; that is, the electrons that charge compensate for the missing oxygen are not localized at adjacent hafnium ions where they would be expected to lower the hafnium valence.

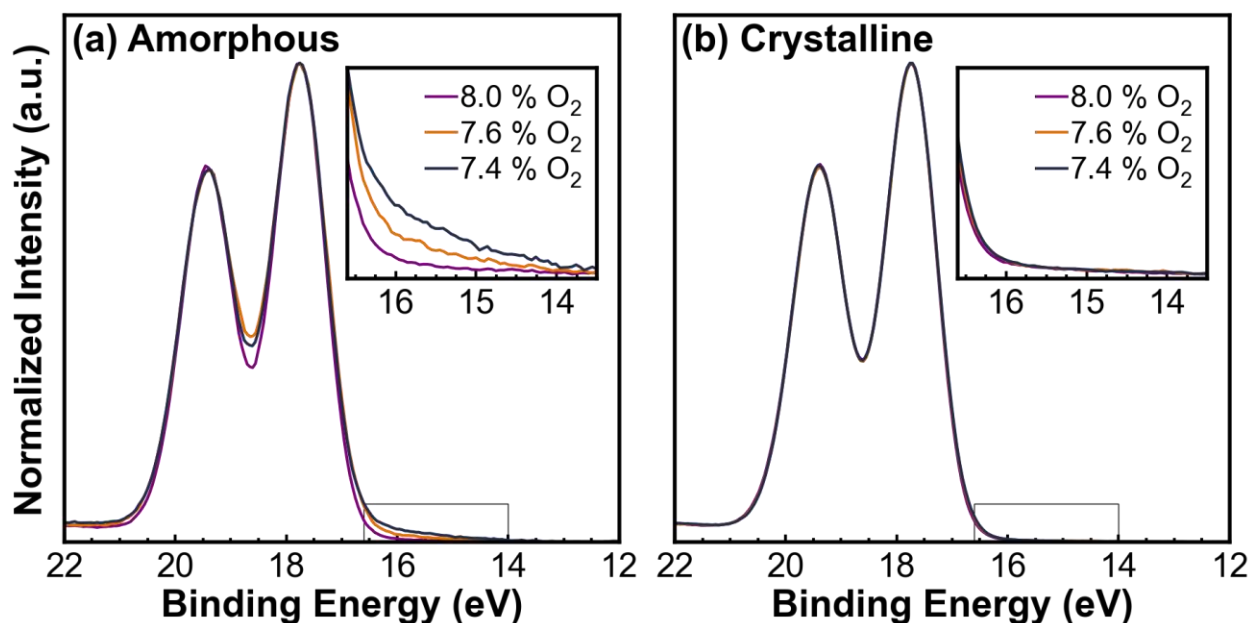


Figure 5.15: Hf $4f$ core levels for (a) amorphous and (b) crystalline films with the intensity normalized to the Hf $4f_{5/7/2}$ peak maximum. The insets show the tail of the Hf $4f_{7/2}$ peak where evidence of a Hf^{3+} peak resides.

5.5.7. Positron Annihilation Spectroscopy

To further investigate the nature of the oxygen vacancies in these films, PAS was used. PAS is a sensitive technique used to characterize defects and vacancies in solids.⁷⁴ When a positron is implanted into a solid, it rapidly thermalizes within a few picoseconds and then diffuses throughout the volume, where it may be trapped at open-volume defects. The probability of trapping depends on the defect charge state, with the probability of trapping at neutral or negatively charged states orders of magnitude above that for positively charged states at room temperature.⁷⁵ Trapped positrons are more likely to annihilate with an electron than delocalized positrons, and the combined momentum results in a Doppler shift of the two annihilation photons. Because the momentum distribution of electrons in a defect differs from that in the bulk, these defects can be detected by measuring the Doppler broadening spectra of annihilation radiation. The change in Doppler broadening spectra is characterized by the S (line shape) and W (wing) parameters, which describe different shapes in the spectra.⁷⁶ A larger S value corresponds to a larger concentration

and/or volume of defects and vacancies, while the W parameter provides information about the chemical and structural environment.

Depth-resolved Doppler Broadening Spectroscopy was used to obtain the S and W parameters of the three HiPIMS-deposited HfO₂ films in both the amorphous and crystallized states. **Figure 5.16a** shows a plot of the S parameter versus W parameter for the oxide layer. Two standards, sintered bulk ceramic HfO₂ and hafnium metal, are shown in this plot in addition to the HiPIMS-deposited HfO₂ films. The amorphous samples fall on a line that runs parallel to that connecting the sintered HfO₂ and hafnium metal. This implies that the positrons are experiencing an environment that is partially HfO₂ and partially metal Hf and is consistent with the presence of oxygen vacancies where the nearest neighbor atoms around the missing oxygen would be hafnium atoms. Positrons, owing to their positive charge, are most sensitive to neutral or negatively charged vacancies or defects in materials. Based on defect chemistry, it may be expected that oxygen vacancies in HfO₂ would be positively charged, so they would not effectively trap positrons. However, neutral oxygen vacancies can exist if the electrons do not delocalize, and these vacancies can be responsible for the change in S parameter observed here.^{61,77-79} It is possible that neutral Hf-O divacancies exist as well; however, the structural disorder required given the high concentrations of oxygen vacancies as measured by EELS and XPS would suggest that these are not the dominant defect. These results, therefore, indicate that neutral oxygen vacancies are the dominant defect and that the concentration increases with decreasing oxygen content during sputtering for the amorphous films.

Figure 5.16b and c show the S parameter versus percentage of oxygen in the plasma for the amorphous samples and crystalline samples, respectively. Overall, the crystalline samples have higher S parameters than the amorphous samples, demonstrating that these films have a higher concentration of defects detectable by PAS after annealing. This may suggest that there is an increase in the population of neutral oxygen vacancies after crystallization. This is consistent with the XPS spectra (**Fig. 5.15**) that showed a reduction in the Hf³⁺ peak that correlates with positively charged oxygen vacancies after annealing, in addition to the quantification of stoichiometry by XPS that demonstrated that the films were more oxygen-deficient after crystallization (**Table 5.2**). Neutral oxygen vacancies would not manifest as an Hf³⁺ peak in XPS, but would be more easily detectable by PAS. Further, these observations are consistent with the low leakage currents

measured in these films as the oxygen vacancy compensating electrons appear to not be ionized in the crystallized films.

Additionally, the S versus W parameter trends of the crystalline samples run perpendicular to the line connecting the sintered HfO₂ and hafnium metal due to differences in their W parameters. This indicates that there are differences in the chemical environment that the positrons are experiencing related to coordination number. These differences in coordination number are supported by the XRD data (**Fig. 5.2**), which showed that the sample prepared with 8.0 % oxygen in the plasma contained significant volume fractions of monoclinic phase in addition to the orthorhombic and/or tetragonal phases and the ELNES EELS spectra, which showed complexity in peak A for the 8.0 % sample due to a difference in the distribution of bonding in this sample (**Fig. 5.12b**). Given the large concentrations of oxygen point defects in these samples, as quantified by both EELS and XPS, it is plausible that defect clusters such as divacancies exist as well, which would impact the local environment experienced by positrons.

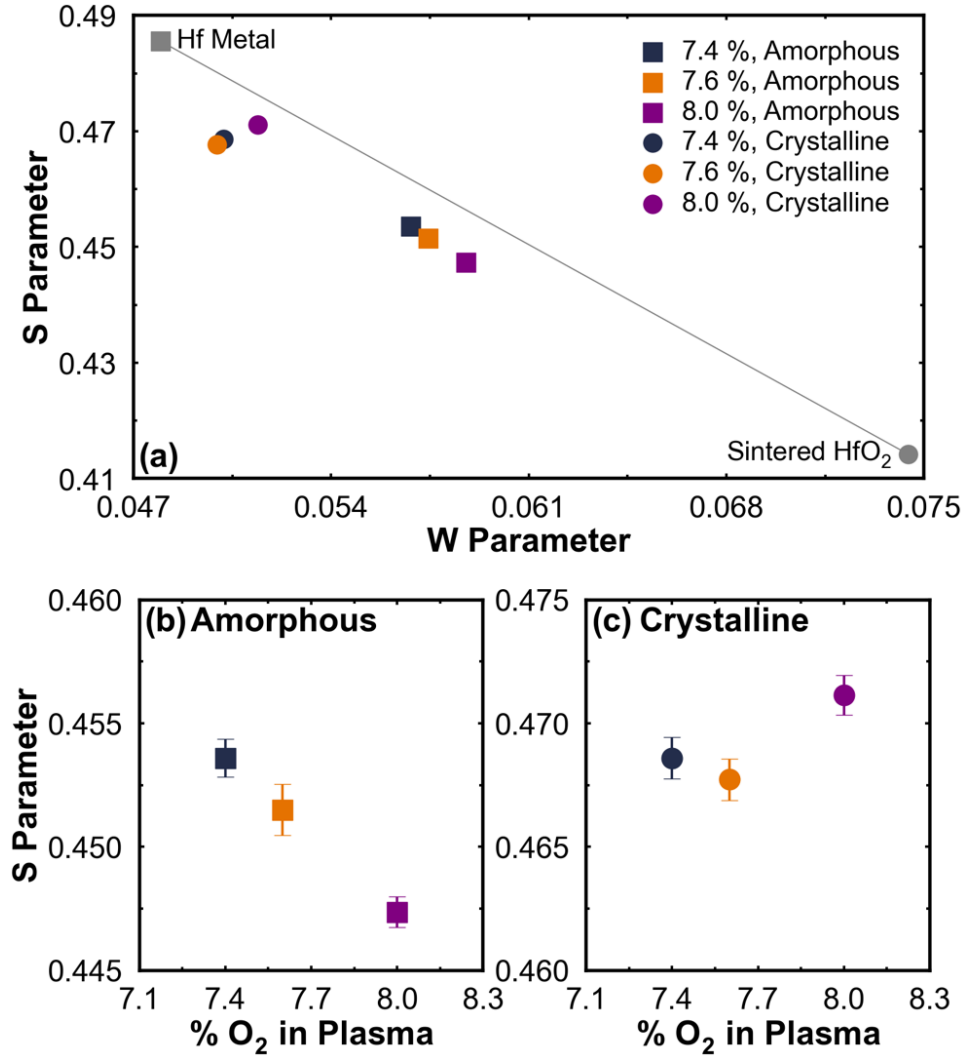


Figure 5.16: (a) Positron annihilation spectroscopy S versus W parameters for amorphous and crystalline samples. Error bars are smaller than marker size. S parameter versus % O_2 in the plasma for (b) amorphous and (c) crystalline samples.

Combined, the EELS, XPS, and PAS analysis show that the oxygen content in the plasma has a direct correlation with the amount of oxygen and oxygen point defects present in the films – both in the amorphous and crystalline states. While measuring oxygen content precisely is challenging, the relative consistency of the stoichiometries measured across the same samples with multiple techniques suggests that the oxygen vacancy concentrations required to stabilize the ferroelectric phase in pure HfO₂ are significant. Furthermore, HfO₂ phase stability is extremely sensitive to the amount of oxygen present, and oxygen variations of less than 1% in the sputter gas atmosphere are sufficient to change nucleation behavior from being primarily the ferroelectric

orthorhombic phase to significantly the non-ferroelectric monoclinic phase. The small change in oxygen content in the sputter atmosphere leads to large variations in oxygen content in the deposited films. The XPS data suggest that x can vary by as much as 0.2 in the amorphous films for a 0.6% change in sputter atmosphere oxygen content. Additionally, the oxygen content boundary separating preparation of the orthorhombic ferroelectric phase and the non-ferroelectric monoclinic phase is relatively small at x of just ~ 0.05 . Fine control of oxygen content is, therefore, vital in the preparation of the ferroelectric phase in pure HfO_2 .

In the amorphous films, a high concentration of oxygen vacancies was measured and observed across all three films. The Hf^{3+} signature in XPS suggests that some fraction of these oxygen vacancies were ionized. In the crystalline state, large concentrations of oxygen vacancies were still observed; however, they appear to be largely neutral due to the lack of Hf^{3+} signature as well as the extremely low leakage currents and the increased S parameter in the PAS experiments. The presence of these oxygen vacancies stabilizing the ferroelectric phase is consistent with many other experimental reports as well as a recent computational result.⁸⁰ Furthermore, the computational predictions revealed that the fraction of ionized vacancies should be many orders of magnitude lower than neutral vacancies in pure HfO_2 . This is consistent with the measurements in this study and confirms that in this very wide band gap ferroelectric, the oxygen vacancies do not necessarily ionize at room temperature and that high point defect densities can be tolerated without leading to performance-degrading leakage currents. By comparison, HZO films with high oxygen vacancy concentrations resulted in high leakage currents, and clear trap-assisted tunneling.⁸¹ It should be noted that HZO has been reported to have a lower band gap than pure HfO_2 for the same phases.⁸² and that this lower band gap may result in lower barriers for ionization of electrons from oxygen vacancies leading to higher leakage currents. It is also not clear what role carbon contamination in ALD-prepared films may play in sub-band gap defect states, but this work suggests that they may contribute to leakage because large leakage currents and trap-assisted tunneling were observed in undoped ALD-prepared HfO_2 films³⁴. This indicates that in the absence of chemical impurities, dopant-free HfO_2 may be more robust against leakage currents and attractive for devices such as FTJs and FeFETs where non-direct tunneling and charge-trapping, respectively, impact device performance.

5.6. Conclusions

HiPIMS is a promising method to prepare ferroelectric HfO₂ films. It allows for high chemical purity and enabled the study of oxygen defect impacts to phase nucleation and ferroelectric performance in pure HfO₂ films. Specifically, in this study, 20 nm HfO₂ films were deposited from a high purity hafnium metal target via reactive HiPIMS with oxygen in the plasma varied from 7.1 to 8.0 %. The film deposited with the highest amount of oxygen contained the monoclinic phase in addition to the orthorhombic and/or tetragonal phases, while films with lower oxygen contained significant fractions of the orthorhombic phase after crystallization. These differences extended to electrical properties, where the 7.4 and 7.6 % films had the highest remanent polarization values of 8.0 and 8.7 $\mu\text{C}/\text{cm}^2$, respectively, and the 8.0 % film had a remanent polarization of 3.5 $\mu\text{C}/\text{cm}^2$. Assessment of the microstructure of these films showed that the films had similar grain sizes; however, the phases present and electrical properties varied, suggesting that these differences cannot be explained by variations in grain sizes. Several methods were used to assess the oxygen content in the films; EELS and XPS showed that the films were significantly oxygen-deficient, that lower oxygen content in the plasma resulted in lower oxygen in the films, and that the films were more oxygen-deficient after annealing. Thus, differences in oxygen content and oxygen vacancy concentration are responsible for the phase constitutions and electrical properties of these films. Additionally, in spite of the large oxygen non-stoichiometries in these films, the leakage currents remained extremely low. XPS measurements revealed the presence of Hf³⁺ in the amorphous phase, which signifies the presence of positively charged oxygen vacancies, suggesting that the electrons compensating the oxygen point defects were delocalized from the vacancies. In the crystalline samples, however, no Hf³⁺ signature could be observed, although the films were more oxygen deficient. These results, combined with the low leakage currents and increased S parameter in PAS experiments, indicate that the electrons are localized to the oxygen point defects and are not ionized. This study demonstrates that the properties of ferroelectric HfO₂ thin films are highly sensitive to oxygen content and that high oxygen vacancy concentrations do not necessarily lead to large leakage currents. Controlling the concentrations of oxygen vacancies in the film preparation process is of utmost importance for enabling the integration of phase-pure hafnium oxide into devices.

5.7. Addendum

This work refers to the possible presence of three phases in these films – the monoclinic, polar orthorhombic, and tetragonal phases, with differentiation between the polar orthorhombic and tetragonal phases being difficult. Since the time of publication, the presence of the antipolar *Pbca* phase in other HfO₂ films deposited by HiPIMS has been identified in nano-Fourier transform infrared spectroscopy measurements. Thus, the presence of the antipolar orthorhombic phase in these films should be considered a possibility.

Additionally, the XPS O1s spectra were not published, and are shown in **Figure 5.17**, below.

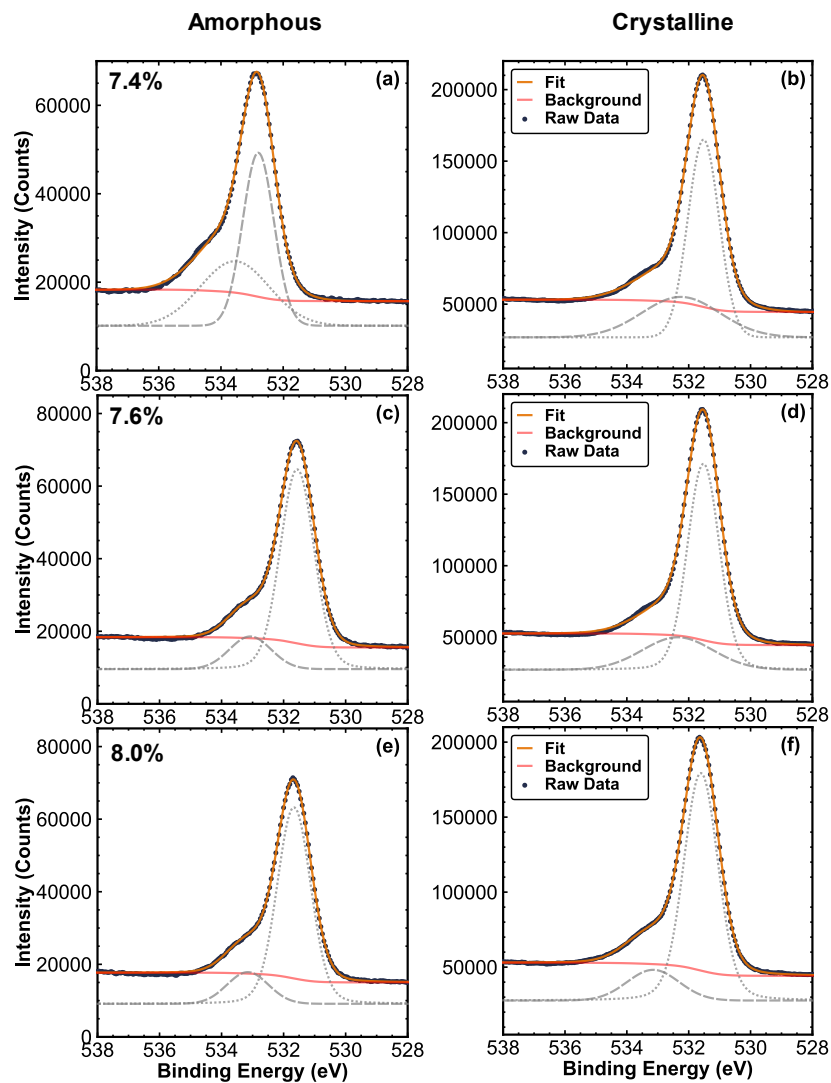


Figure 5.17: XPS O1s spectra for the films deposited with 7.4 (a, b), 7.6 (c, d), and 8.0% (e, f) plasma oxygen in the amorphous (a, c, e) and crystalline (b, d, e) states.

5.8. Acknowledgements

This work was supported by the Semiconductor Research Corporation (SRC) within the Nanomanufacturing, Materials, and Processes (NMP) Program under task 2875.001. S.T.J. acknowledges support from the U.S. National Science Foundation's Graduate Research Fellowship Program under grant DGE-1842490. E.R.H. and P.E.H. appreciate support from the Army Research Office, Grant No. W911NF-16-1-0406. The XPS instrument acquisition (Reinke group) was supported by a DURIP award (Office of Naval Research) Grant N00014-16-1-2842, program manager Dr. David Shifler. This work was performed, in part, at the Analytical Instrumentation Facility (AIF) at North Carolina State University, which is supported by the State of North Carolina and the National Science Foundation (award number ECCS-2025064). The AIF is a member of the North Carolina Research Triangle Nanotechnology Network (RTNN), a site in the National Nanotechnology Coordinated Infrastructure (NNCI). Sandia National Laboratories is a multimission laboratory managed and operated by National Technology and Engineering Solutions of Sandia, LLC, a wholly owned subsidiary of Honeywell International, Inc., for the U.S. Department of Energy's National Nuclear Security Administration under contract DE-NA0003525. This paper describes objective technical results and analysis. Any subjective views or opinions that might be expressed in the paper do not necessarily represent the views of the U.S. Department of Energy or the United States Government.

Chapter 6: Optical Properties as Identifiers of the Phases of Hafnium Oxide Thin Films

The contents of this chapter are in preparation for submission for publication with the following authors.

Samantha T. Jaszewski,^a Sebastian Calderon,^b Bishal Shrestha,^c Shelby S. Fields,^a Fernando Vega^d, Nikolas J. Podraza,^b Elizabeth C. Dickey,^b Thomas E. Beechem,^d and Jon F. Ihlefeld^{a,d}

^a Department of Materials Science and Engineering, University of Virginia,
Charlottesville, Virginia 22904, USA

^b Department of Materials Science and Engineering, Carnegie Mellon University,
Pittsburgh, Pennsylvania 15213, USA

^c Department of Physics and Astronomy, Wright Center for Photovoltaic Innovation &
Commercialization, University of Toledo, Toledo, OH 43606, USA

^d School of Mechanical Engineering and Birck Nanotechnology Center,
Purdue University, West Lafayette, 47907, IN, USA

^e Charles L. Brown Department of Electrical and Computer Engineering, University of
Virginia, Charlottesville, Virginia 22904, USA

6.1. Motivation

Integration of ferroelectric HfO₂-based materials into devices will require high fractions of the ferroelectric phase for optimal performance. Other chapters in this dissertation discuss the factors that have been shown to stabilize the ferroelectric phase in HfO₂-based thin films, including oxygen content, microstructure, dopants, and stress; however, in order to exploit these factors, accurate phase identification is vital. The majority of literature in this field identifies three primary phases that can coexist in HfO₂-based films – the polar orthorhombic *Pca2₁* phase responsible for ferroelectricity and the non-ferroelectric tetragonal *P4₂nmc* and monoclinic *P2₁/c* phases. It has been suggested that a phase transformation from the tetragonal to polar orthorhombic phase is, in part, responsible for wake-up in this material. However, a recent report

utilized scanning transmission electron microscopy to observe a transition from the often-overlooked antipolar orthorhombic *Pbca* to the polar orthorhombic phase with field cycling.¹⁹⁰ These results may point to a misidentification of the antipolar orthorhombic phase as the tetragonal phase in the past. This misidentification is not surprising considering the difficulty in phase identification using traditional thin film characterization techniques like grazing-incidence X-ray diffraction due to the similarities in *d*-spacings of the orthorhombic and tetragonal phases. These challenges highlight the necessity of exploring other characterization techniques in order to precisely differentiate between the phases that coexist in this material. Accordingly, the purpose of this chapter is to exploit optical properties, which have not been effectively used as of yet, in order to identify the phases present in HfO₂ thin films.

6.2. Abstract

Phase identification in HfO₂-based materials is a prerequisite to realizing means for stabilizing the material's ferroelectric phase, which holds great promise as a next-generation memory technology. While grazing-incidence X-ray diffraction (GIXRD) is commonly employed to this end, it has difficulty unambiguously differentiating between the ferroelectric orthorhombic phase and other metastable phases that may exist. Optical properties provide an alternative route. Its use in phase identification remains limited, however, as phase control has overwhelmingly been accomplished via doping, thereby convoluting optical signatures between the dopant and phase changes they induce. Herein, we report the visible, ultraviolet, and infrared optical properties of three undoped HfO₂ films that have been confirmed by transmission electron microscopy to consist primarily of the ferroelectric polar orthorhombic *Pca2*₁, antipolar orthorhombic *Pbca*, and monoclinic *P21/c* phases, respectively. The indirect optical band gaps of these films are found to be 6.01, 6.05, and 5.88 eV, respectively. The close similarity in bandgaps for the predominantly orthorhombic films indicates that these films—while not phase pure—are primarily composed of this crystal class and have only small amounts of the tetragonal or monoclinic phase. The two orthorhombic phases can be differentiated via vibrational spectroscopy as shown via unique signatures from synchrotron nano-Fourier transform infrared spectroscopy (nano-FTIR) measurements. This work illustrates that IR spectroscopy is a means by which phases can be unambiguously assessed in this material system in a non-destructive and nanoscale manner.

6.3. Introduction

In 2011, ferroelectricity was first reported in hafnium oxide (HfO_2) thin films doped with Si.²⁸ Interest in this material has since grown tremendously because of the microelectronic-related benefits that HfO_2 has over traditional ferroelectrics like lead zirconate titanate and barium titanate. These benefits include chemical compatibility with mainstream semiconductors,¹⁵ current use as a high- κ dielectric in CMOS devices,²⁶ and ferroelectricity stable to 1 nm in thickness.²⁹ Although promising as a base material for ferroelectric random access memory (FeRAM), ferroelectric field effect transistors (FeFETS), and ferroelectric tunnel junctions (FTJs), significant hurdles remain before HfO_2 can be widely implemented in these devices. A central challenge is the creation and stability of maintaining HfO_2 in its ferroelectric—but non-equilibrium—polar orthorhombic phase (space group $Pca2_1$) in a material that is highly polymorphic.

Within HfO_2 thin films, for example, the non-equilibrium ferroelectric polar orthorhombic phase is most often reported to coexist with the equilibrium nonpolar monoclinic ($P2_1/c$) and non-equilibrium tetragonal ($P4_2nmc$) phases.^{29,179,191,192} Recent reports, meanwhile, have demonstrated a phase transformation from the antipolar orthorhombic phase ($Pbca$) to the polar orthorhombic $Pca2_1$ phase with electric field cycling,¹⁹⁰ suggesting that this often overlooked antipolar orthorhombic phase may play a significant role in the wake-up HfO_2 -devices. The interplay of these four phases—monoclinic ($P2_1/c$), tetragonal ($P4_2nmc$), antipolar ($Pbca$), and polar ($Pca2_1$) orthorhombic—is necessarily complex and affected by several factors including dopant type and concentration,^{58,64,66,69,182} biaxial stress,^{161,193} oxygen vacancies,^{62,194} and film thickness or grain size.^{34,195} Detangling the interplay of these competing effects is difficult, necessary, and requires accurate phase identification in thin films that are less than 50 nm thick.³⁵

Phase identification in thin-film HfO_2 is not straightforward, however. Grazing-incidence X-ray diffraction (GIXRD) is commonly employed for phase identification due to its comparatively high-throughput, non-destructive nature, and surface sensitivity. For these reasons, it is often used to assess phases present in HfO_2 -based thin films. However, definitive differentiation between the orthorhombic ($Pca2_1$ and $Pbca$) and tetragonal ($P4_2nmc$) phases is not easily achieved due to similarities in the d -spacings of these phases and the low scattering intensity of the unique orthorhombic peaks.¹⁹⁶ Thus, other characterization methods are necessary to identify and quantify the phases in HfO_2 .

Vibrational spectroscopy provides one alternative, as it is typically more sensitive to local structure changes than standard X-ray diffraction techniques that are most applicable to thin films. The differences in symmetry, bonding, and polarity amongst the phases necessarily alter the phonon dispersion sampled by these techniques. Several predictions have, therefore, suggested that infrared (IR) and Raman spectroscopy techniques can identify phases in HfO₂-based films.^{34,44,180,181} Experimentally, recent reports have shown the utility of Raman spectroscopy in differentiating the polar orthorhombic, tetragonal, and monoclinic phases in 30 nm thick HfO₂ films.¹⁹⁷ Raman spectroscopy is, however, inherently signal starved relative to other methods necessitating either sampling of thicker HfO₂ layers or the use of higher laser powers having the potential to induce phase changes. Fourier-transform infrared spectroscopy (FTIR) measurements, meanwhile, have enabled phase identification in doped-HfO₂ thin films,^{71,182} although differentiation between the orthorhombic and tetragonal phases was not proven. FTIR signatures differentiating the monoclinic, antipolar orthorhombic, and polar orthorhombic phases were identified, in contrast, in bulk (200 μm) single crystals of HfO₂ stabilized with yttrium.⁴⁴ These results show promise for phase differentiation in more technologically-relevant HfO₂-based thin films.

Optical bandgaps also present an opportunity for differentiating between phases of HfO₂. Experimentally, variations in the bandgap with doping have been observed across the entire composition range of the Hf_{1-x}Zr_xO₂ system.²¹ From a theoretical perspective, density-functional theory (DFT) has predicted relative differences in the bandgaps for tetragonal, orthorhombic, and monoclinic phases that exceed 0.1 eV for both undoped HfO₂ and various compositions of Hf_{1-x}Zr_xO₂. Differences of this magnitude are sufficient for experimental observation. Thus, there is an opportunity to investigate band gap variation as a means of differentiating between orthorhombic, tetragonal, and monoclinic phases in pure HfO₂.

Taken together, optical properties, therefore, hold promise for identifying phases in thin films of HfO₂ and devices fabricated from it. Capitalizing on this promise requires the identification of markers for each technique that differentiates between the phases. Obtaining these markers has been confounded by the difficulty in preparing samples of varying phases having the same chemical composition. For example, the bandgap changes with the majority phase in Hf_{1-x}Zr_xO₂ but is accompanied by variation in Zr-content as well.²¹ Recognizing that electronic and phonon band structures are dependent upon composition as well as phase, it is difficult to

disentangle the effects. Consequently, reports on the phase dependence of the optical properties of HfO₂ thin films having the same composition are lacking and obfuscate how optical responses can be used to unambiguously for phase identification.

With this motivation, three undoped, nominally 20 nm thick, HfO₂ films were prepared using High Power Impulse Magnetron Sputtering (HiPIMS). Sputtering has several advantages over conventional thermal atomic layer deposition for preparing hafnia films, including a lack of carbon impurities and greater freedom in engineering deposition conditions to tailor phase formation. Following identical depositions, films were annealed for different times and temperatures to alter the phase makeup of the films (see **Table 6.1**). Grazing-incidence X-ray diffraction (GIXRD) and electrical measurements verified that the predominant phase consisted of the polar orthorhombic, antipolar orthorhombic, and monoclinic phase. The predominance of these phases was further supported by scanning transmission electron microscopy (STEM). With these results serving as a basis for interpreting the optical response, the band gaps of the different phases in HfO₂ were quantified using spectroscopic ellipsometry and the vibrational spectra obtained with near-field nano-FTIR measurements. Definitive spectroscopic markers differentiating between the monoclinic, polar orthorhombic, and antipolar orthorhombic phases are reported.

Table 6.1. Annealing conditions and resulting primary phase formed in the HfO₂ films.

Anneal Temperature (°C)	Anneal Time (s)	Primary Phase (space group)
700	30	Antipolar orthorhombic (<i>Pbca</i>)
750	30	Polar orthorhombic (<i>Pca2₁</i>)
800	1200	Monoclinic (<i>P2₁/c</i>)

6.4. Results and Discussion

6.4.1. Grazing-Incidence X-Ray Diffraction

GIXRD patterns of the three annealed films reveal different diffraction signatures indicative of phase variation, as shown in **Figure 6.1**. The film annealed at 800 °C for 1200 seconds consists primarily of the monoclinic phase, as demonstrated by the peaks at approximately

28.5° and 31.75°, which are indexed as the ($\bar{1}11$) and (111) monoclinic peaks. The small peak at 30.5° observed in this film suggests the presence of a small fraction of the polar orthorhombic, antipolar orthorhombic, and/or tetragonal phase as well. This film will be denoted as *monoclinic* hereafter in reference to its majority monoclinic phase. Characterization methods discussed in forthcoming sections will further support this assignment.

Films annealed at 700 and 750 °C for 30 seconds have only one peak around 30.7° that can be indexed as the polar orthorhombic (o-p), antipolar orthorhombic (o-ap), and/or tetragonal (t) phase. A shift of the peak of the sample annealed at 750 °C to lower angles suggests that this film primarily contains the polar orthorhombic phase. The sample annealed at 700 °C primarily consists of the tetragonal or antipolar orthorhombic phase since the (101)_t and (211)_{o-ap} peaks are typically indexed at a slightly higher 2θ angle than the (111)_o peak.¹⁹⁸ Still, as discussed above, differentiation between these phases is difficult using diffraction-based techniques alone. Subsequent characterization discussed in the proceeding will, however, verify these assignments. These films are therefore labeled according to their predominant phase and referred to in the following discussion as the *polar* and *antipolar* films.

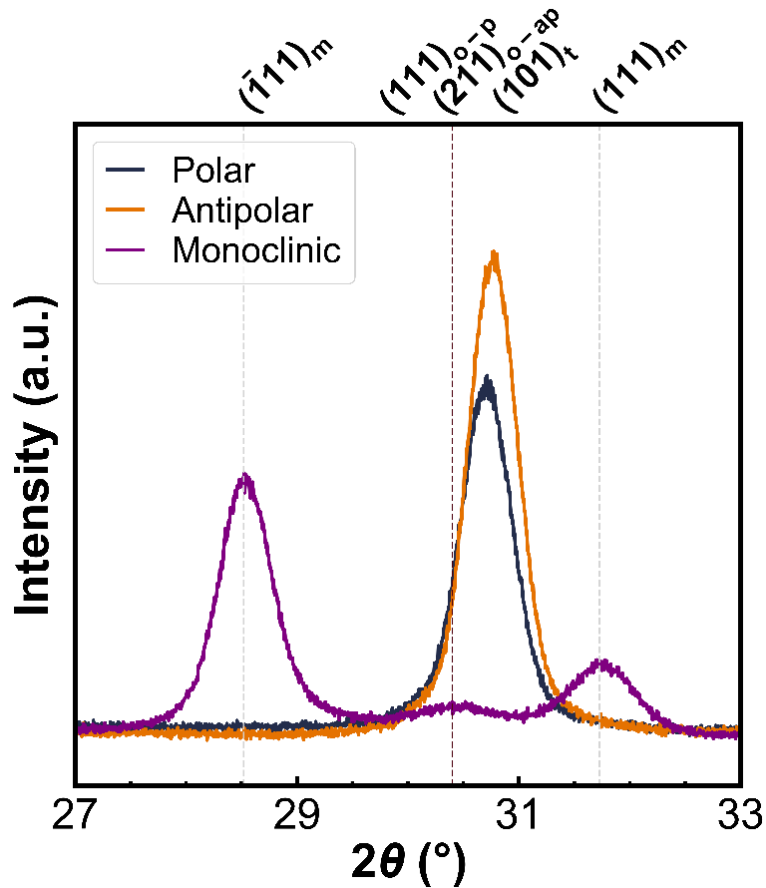


Figure 6.1. GIXRD patterns of the films annealed under different conditions to achieve majority polar orthorhombic (o-p), antipolar orthorhombic (o-ap), and monoclinic phases (m). Indices for peak positions of these phases, in addition to the tetragonal phase (t), are shown at the top of the figure.

6.4.2. Electrical Characterization

Electrical measurements were performed to further characterize the majority phases in the films since each phase possesses a unique polarization and dielectric response. The polar orthorhombic phase is linked to ferroelectric behavior. The antipolar orthorhombic phase exhibits an antiferroelectric response. The tetragonal phase is considered a field-induced ferroelectric, meaning that its centrosymmetry can be broken by applying an electric field.¹⁹⁹ Finally, the monoclinic phase displays linear dielectric behavior.

Figure 6.2 shows the polarization responses for each of the films highlighting their differences in the majority phase. The polar film (*i.e.*, the film having a majority phase consisting

of $Pca2_1$) has a hysteresis loop that is characteristic of ferroelectricity. The loop is well-saturating, indicating that there are low leakage current contributions to polarization. Although the remanent polarization value is lower than typically observed in doped HfO_2 films, it is consistent with observations of ferroelectric response in pure hafnia.^{47,48,104,200} The antipolar film displays, in contrast, a pinched hysteresis response that is consistent with antiferroelectric or field-induced ferroelectric behavior. Lastly, the monoclinic film exhibits linear dielectric behavior.

The corresponding capacitance-voltage (C-V) measurements are provided in **Figure 6.2(d-f)** and further corroborate the phase assignments arrived at from the XRD and polarization responses. The C-V response of the polar film (**d**) exhibits a butterfly shape and two peaks characteristic of a ferroelectric material, while the antipolar film (**e**) has four peaks indicative of an antiferroelectric-like response. The relative permittivity of the polar and antipolar films are similar. The tetragonal phase is reported to have a significantly higher relative permittivity than that seen here.¹⁷⁹ The similarities in relative permittivity support the assignment of the antipolar as being primarily composed of the antipolar orthorhombic ($Pbca$) as opposed to the tetragonal ($P4_2nmc$) phase. Finally, the flat C-V response of the monoclinic film (**f**) is expected for a linear dielectric material, and a relative permittivity near 25 is comparable to that typically reported.¹⁷⁹

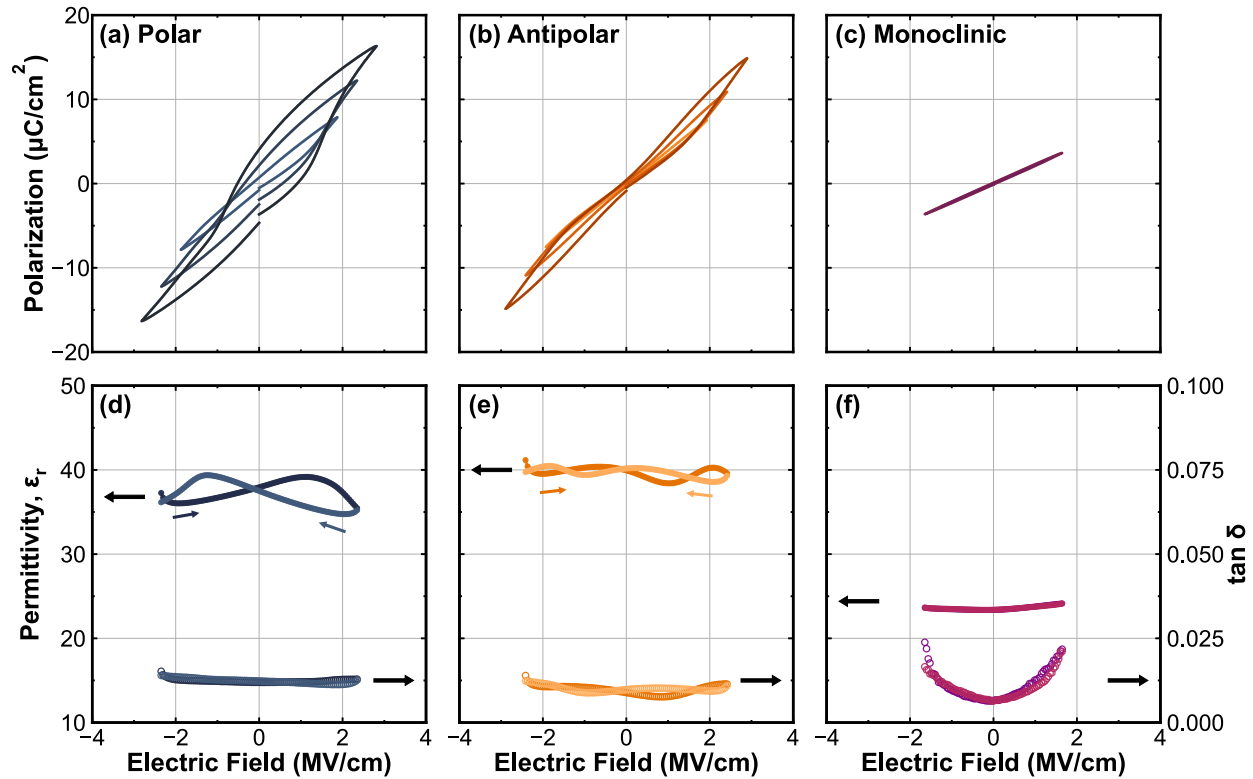


Figure 6.2. Nested polarization hysteresis measurements for pristine films consisting primarily of the (a) polar orthorhombic phase, (b) antipolar orthorhombic phase, and (c) monoclinic phase. Relative permittivity (left axis) and loss tangent (right axis) versus electric field for (d) polar orthorhombic, (e) antipolar orthorhombic, and (f) monoclinic films.

6.4.3. Transmission Electron Microscopy

To confirm the presence of the antipolar ($Pbca$) and polar ($Pca2_1$) orthorhombic phases, STEM images were acquired in differentiated differential phase contrast mode (dDPC). **Figure 6.3a** shows the atomic models for both antipolar and polar orthorhombic phases viewed along a direction that facilitates the differentiation of these phases by the alternating position of the oxygen atomic columns in the $Pbca$ phase (O_2 ions in **Figure 6.3a**). **Figure 6.3b-e** shows annular dark-field (ADF) and dDPC cross-sectional images for the antipolar and polar films with a grain oriented along the zone axis schematized in **Figure 6.3a**. The results confirm the existence of the antiferroelectric orthorhombic $Pbca$ phase in the antipolar film, in which an antipolar arrangement of the projected unit cells is denoted by black and white arrows (**Figure 6.3f**). The polar film, on the other hand, exhibits a coexistence of both orthorhombic polar and antipolar phases, as observed by Cheng *et al.*,¹⁹⁰ with a predominant presence of the polar phase

(Figure 6.3g). The presence of a tetragonal phase is also evident in both samples at the top surface of the films, where the samples are thinner after sample preparation. It should be noted that the presence of the monoclinic phase was also observed in some of the polar TEM samples.

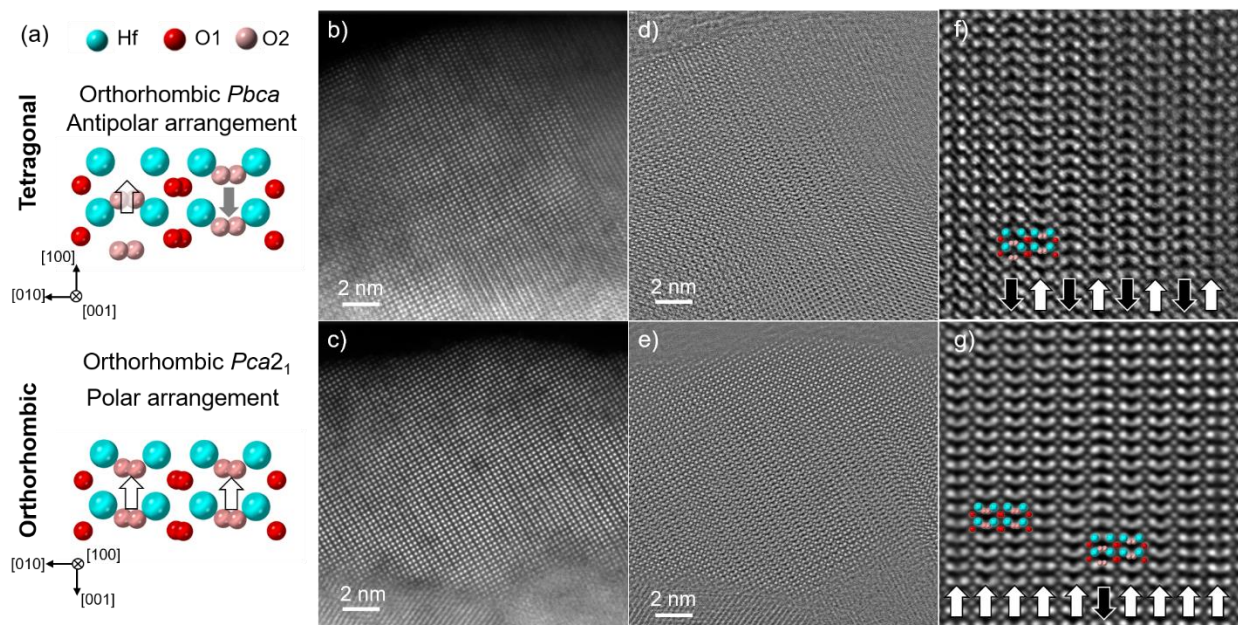


Figure 6.3. Antipolar (*Pbca*) and polar (*Pca21*) orthorhombic atomic models view along [001] and [100] zone axis, respectively (a). ADF (b and c) and dDPC images at low (d and e) and high (f and g) magnifications for both antipolar and polar films, respectively.

6.4.4. Optical Band Gap Measurements

Spectroscopic ellipsometry was utilized to quantify the films' index of refraction, which was then used to deduce the band gap. Briefly, the absorption coefficient (α) was quantified as a function of wavelength (λ) via $\alpha = 4\pi k/\lambda$, where k is the extinction coefficient. The indirect band gap for each film was then obtained via a Tauc plot²⁰¹ (Figure 6.4) by extrapolating the photon energy at which $\alpha^{1/2} = 0$. Further details are provided in the Methods section.

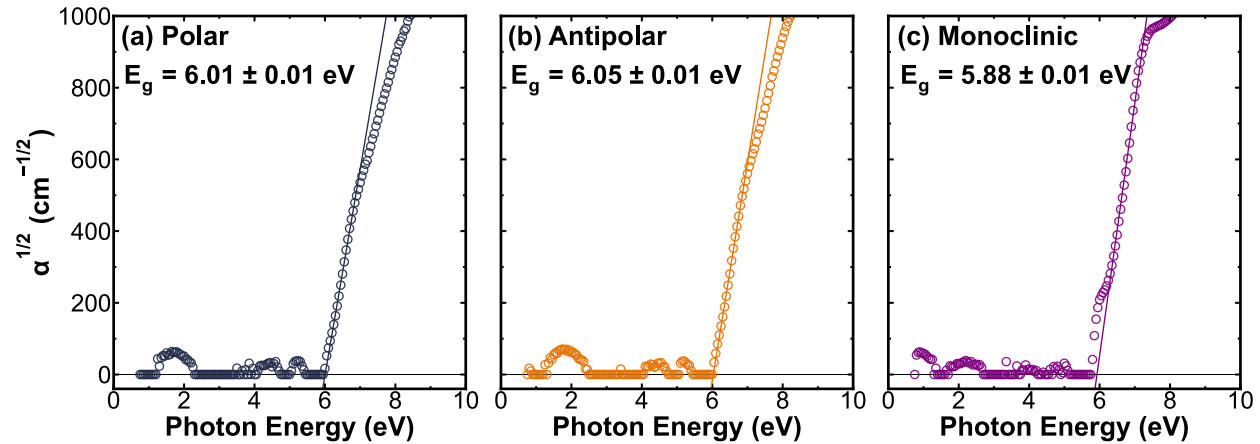


Figure 6.4. Tauc plots of $\alpha^{1/2}$ as a function of photon energy to obtain the indirect optical bandgap energies (E_g) of HfO₂ films consisting primarily of the (a) polar orthorhombic phase, (b) antipolar orthorhombic phase, and (c) monoclinic phase.

In the sub-bandgap region of each of the Tauc plots, a small hump is seen around 2 eV. Recent photoluminescence (PL) spectroscopy measurements of hafnium zirconium oxide films have identified PL modes with energies ranging from 2.3 – 3.0 eV that correspond to defect states resulting from oxygen vacancies.²⁰² Thus, the absorption feature around 2 eV in the Tauc plots may be linked to oxygen vacancy-induced defect states in these films. In addition, the monoclinic film exhibits a low energy shoulder on the absorption edge at approximately 6 eV, which has been shown to be an electronic excitation that is intrinsic to crystalline monoclinic HfO₂, unrelated to oxygen vacancy defects.^{203,204} Taking into account these sub-bandgap features,²⁰⁵ a bandgap of 5.88 ± 0.01 eV was deduced. This value is in agreement with previous reports for the monoclinic phase.^{21–23,206,207} Quantitatively, the band gaps for the polar and antipolar films are quite similar, with values of 6.01 ± 0.01 and 6.05 ± 0.01 eV, respectively.

Measured bandgaps were compared to theoretical predictions arrived at using density functional theory (DFT), as shown in **Table 6.2**. Details on the DFT implementation are provided in the Methods section. The predicted monoclinic bandgap of 5.867 eV agrees well with the experimentally obtained value of 5.88 eV. The predicted bandgap of the tetragonal phase, meanwhile, is more than 0.2 eV larger than any of the measurements. This large difference, combined with a lower permittivity measured compared to that expected for the tetragonal phase, suggests that the presence of the tetragonal phase is comparatively small relative to the orthorhombic phases in the polar and antipolar films. Although the predicted bandgaps of the polar

and antipolar orthorhombic phases differ by 0.265 eV, the experimental values are nearly identical (6.01 and 6.05 eV), having a magnitude that is almost equal to the mean predicted for the two orthorhombic phases (6.05 eV).

Table 6.2. Predicted bandgaps of the monoclinic, polar orthorhombic, antipolar orthorhombic, and tetragonal phases calculated using DFT, and measured bandgaps for the three HfO₂ films primarily consisting of the monoclinic, polar orthorhombic, and antipolar orthorhombic phases.

Phase	Predicted Bandgap (eV)	Measured Bandgap (eV)
Monoclinic	5.867	5.88 ± 0.01
Polar orthorhombic	5.92	6.01 ± 0.01
Antipolar orthorhombic	6.185	6.05 ± 0.01
Tetragonal	6.293	N/A

6.4.5. Fourier-Transform Infrared Spectroscopy

Vibrational spectroscopy provides signatures differentiating between the two orthorhombic phases. Experimentally, infrared spectra were acquired using synchrotron-sourced tip-enhanced Fourier transform infrared spectroscopy (nano-FTIR). Details on the experiment are provided in the Methods section. Normalized phase spectra are shown in **Figure 6.5**, where distinct differences between the films are indicative of their differing dominant phase. The middle and lower panels of **Figure 6.5** provide positions and relative intensities for features obtained from experiment and theory.

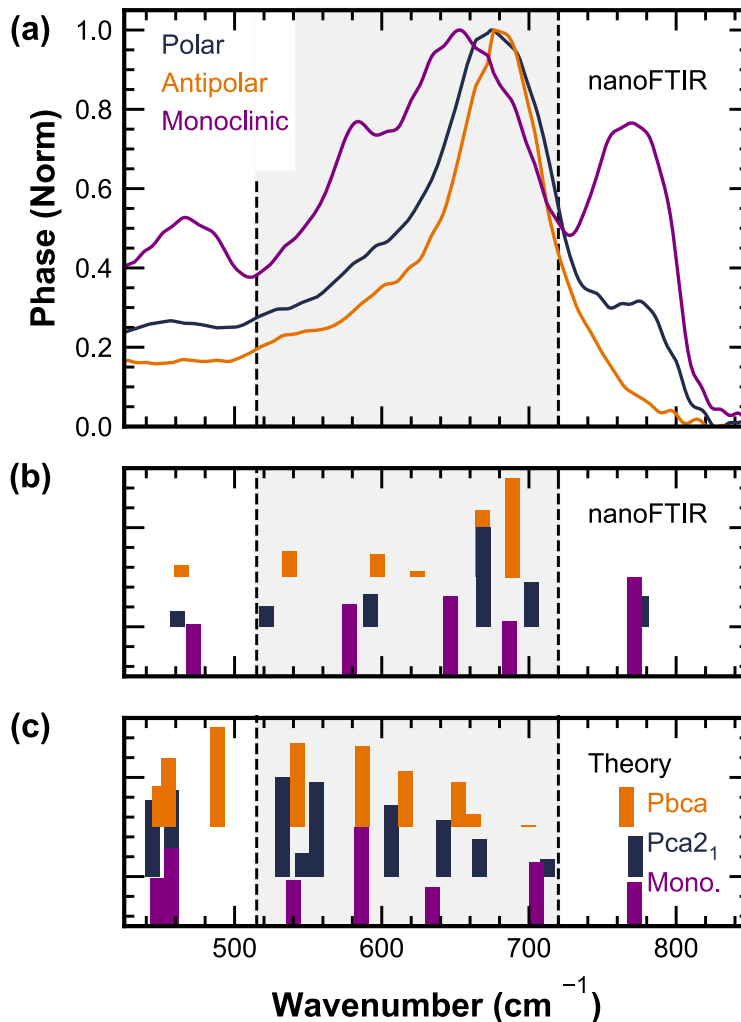


Figure 6.5: (top) Normalized phase spectra of HfO₂ films for the polar, antipolar, and monoclinic films as obtained by nano-FTIR. (middle) Positions of phase maxima in the experimental spectra compared to (bottom) positions predicted from theory.⁴⁴

Differentiation between the monoclinic and orthorhombic phases is accomplished by recognizing the presence of three characteristics in the monoclinic spectrum: (1) broad absorption near 460 cm⁻¹, (2) two distinct maxima of comparable strength at 570, 630 cm⁻¹ accompanied by (3) a strong absorption at 760 cm⁻¹. The polar and antipolar films do not exhibit strong absorption below 500 cm⁻¹ and are marked by an asymmetric absorption feature around 600 cm⁻¹ rather than a spectrum exhibiting two clear maxima. The polar and antipolar films are distinguished by two spectral markers. First, the polar phase has its strongest absorption at lower energies than the antipolar and is significantly broader. Additionally, the polar phase exhibits a weak absorption at

$\sim 770\text{ cm}^{-1}$ whereas no such mode is observed for the antipolar film. Together, these characteristics allow for distinguishing between the primary phase in HfO_2 films. Similar characteristics will likely allow for differentiation in doped- HfO_2 films as well.

These differences are characteristic of the predominant phases themselves and not particular to only the films examined here. To support this assertion, the energies of the major spectral features for each of the films can be compared to the predicted infrared responses calculated for the polar orthorhombic, antipolar orthorhombic, tetragonal, and monoclinic phases by Fan et al.⁴⁴ As it relates to the modes used for phase identification above, the monoclinic responses at 460, 570, 630, and 760 cm^{-1} are each closely correlated with modes predicted by theory. The polar film, meanwhile, is marked by a mode near 770 cm^{-1} , which is the highest observed experimentally. Theoretically, the polar-orthorhombic phase also exhibits the highest energy mode of all the phases. The major feature of the polar mode near 650 cm^{-1} is redshifted relative to the antipolar (660 cm^{-1}). Theoretically, the two closely spaced modes in the polar orthorhombic phase have a weighted average that is also redshifted relative by approximately 10 cm^{-1} relative to the antipolar orthorhombic mode in this region. Increased asymmetric broadening of the polar film, meanwhile, is attributed to the stronger cluster of polar orthorhombic modes near 540 cm^{-1} . Taken together, these results demonstrate FTIR's ability to differentiate between not just the monoclinic and orthorhombic phases but so too the polar and antipolar orthorhombic phases.

6.5. Conclusions

Despite its nascent technological potential, the widespread adoption of ferroelectric HfO_2 -based materials into future technology nodes is predicated upon creating and then stabilizing the metastable ferroelectric phase. The inherent polymorphism of HfO_2 makes this challenging. Numerous factors affect the formation of the ferroelectric phase and its stability, necessitating high-throughput, non-destructive means of identifying phase. Here, through the HiPIMS synthesis of films with nominally equivalent chemical composition, but variable phase fractions, optical signatures of the differing phases are identified using a combination of UV-VIS spectroscopic ellipsometry and synchrotron sourced near-field scanning Fourier transform infrared spectroscopy. The optical signatures not only allow for differentiation between the monoclinic and orthorhombic phases, but also the polar and antipolar orthorhombic phases. Using these signatures in combination with X-ray diffraction, STEM, and electrical characterization, films exhibiting either

polar or antipolar responses are found to be predominately composed of the two orthorhombic phases. The optical band gaps of these films are found to be indirect with values of 6.01 ± 0.01 , 6.05 ± 0.01 , and 5.88 ± 0.01 eV for the polar orthorhombic, antipolar orthorhombic, and monoclinic phases, respectively. While the similarities between the bandgaps of the orthorhombic phases show that it is not a reliable method for differentiation between the polar and antipolar space groups, FTIR measurements demonstrate that each phase has distinct vibrational features that allow for identification. Furthermore, these phases can be identified on the size scale of individual grains using a near-field scanning FTIR instrument, as was used here. This will enable local phase identification without the necessity of advanced TEM-based techniques that require sophisticated sample preparation and analysis. Accurate phase identification is necessary for overcoming the challenges related to phase stability in this material; accordingly, FTIR has been shown to be a valuable and differentiating technique for phase characterization in HfO₂-based thin films.

6.6. Experimental Methods

6.6.1. Sample Preparation

HfO₂ films were deposited on 100 nm thick TaN bottom electrodes on (001) silicon substrates. The TaN was prepared by pulsed dc magnetron sputtering (30 kHz, 4 μ s reverse time) from a TaN target in a Denton Discovery 550 system. HfO₂ films were sputtered via high-power impulse magnetron sputtering (HiPIMS) from a 50 mm diameter hafnium metal target of 99.9 % purity in a custom sputter chamber, as detailed previously.⁶² For HiPIMS depositions, a Starfire Impulse HiPIMS power module was used in conjunction with a dc power supply to deliver square voltage pulses with a duration of 110 μ s, a frequency of 200 Hz, and a magnitude of -700 V. These parameters represent a duty cycle of 2.0 % and per-pulse peak plasma power density of 600 W/cm². Following each negative high-power pulse, a +100 V positive pulse of length 200 μ s was applied to the target. Argon was used as the sputter gas, and O₂ gas was used as the reactive gas. Argon and O₂ gas flows were controlled by electronic mass flow controllers, and the total process pressure was controlled by a conductance flow valve located in front of the turbomolecular pump. A gas flow of 15.00 sccm of argon with 1.23 sccm of O₂ was used to produce oxygen concentrations in the background gas of 7.6 %. A constant background pressure of 5 mTorr was measured by a heated capacitance manometer with active PID feedback to the conductance flow valve. Films

were continuously rotated during growth to minimize thickness gradients, and the substrate platen was grounded. The substrate was not intentionally heated during deposition. Following deposition, the films were annealed in a pure argon atmosphere (99.999% purity) in a rapid thermal processor (Allwin 21, Heatwave 610) at temperature and time durations of 700 °C × 30 s, 750 °C × 30 s, and 800 °C × 1200 s. Lastly, top electrodes consisting of 20 nm of titanium nitride and 50 nm of palladium were dc-magnetron sputtered through a shadow mask to create a capacitor structure for electrical measurements. TiN was reactively sputtered from a titanium target with a gas atmosphere of 5 sccm of argon and 1 sccm of nitrogen, pressure of 0.9 mTorr, and dc power density of 7.40 W/cm². Palladium was deposited with an argon background pressure of 5 mTorr and a DC power density of 3.31 W/cm². Circular electrode diameters were 100 μm, and areas were confirmed by optical microscopy.

6.6.2. Characterization

A Rigaku Smartlab X-ray diffractometer using Cu K α radiation in a parallel beam configuration with a fixed incident angle of 0.7° was used for grazing-incidence X-ray diffraction (GIXRD) measurements to assess crystallinity and phase constitution of films in the as-deposited and annealed states. A 2θ range of 26-33° was selected due to the presence of 100% intensity reflections of the monoclinic $P2_1/c$ phase, tetragonal $P4_2/nmc$ phase, antipolar orthorhombic $Pbca$ phase, and polar orthorhombic $Pca2_1$ phase in this range.

Electrical characterization was performed on capacitor structures for the annealed films. Polarization versus electric field ($P(E)$), pulsed positive up, negative down (PUND) polarization switching, and capacitance-voltage (C-V) measurements were made. A Radiant Technologies Precision LC II Ferroelectric Property Analyzer was used to perform $P(E)$ measurements with a period of 10 ms (100 Hz equivalent frequency). A Keysight E4980A Precision LCR Meter was used for C-V measurements which utilized a 50 mV, 10 kHz oscillator.

STEM images were acquired on samples prepared by the conventional cross-sectional wedge polishing method. Annular dark field (ADF) and differential phase contrast (DPC) images were simultaneously acquired using a ThermoFisher Themis operated at 200kV, with a probe convergence angle of 17.9 mrad and a camera length that resulted in acceptance angles between and 46 – 200 mrad (ADF) and 11- 43 mrad (DPC). All images were acquired as a set of 20

frames using fast-dwell-time (200ns) to avoid significant drift that can cause distortions in the images.

To investigate the band gaps of these films, spectroscopic ellipsometry measurements were taken in addition to standalone thin films of annealed and unannealed tantalum nitride (TaN). These measurements were performed using a near-IR extended rotating analyzer VUV variable-angle spectroscopic ellipsometer (Gen I, VU-302 VUV-VASE, J.A. Woollam Co.)²⁰⁸ with a spectral resolution of 0.05 nm. The samples were mounted in continuous nitrogen purging environment during the measurement to minimize the effect of ambient oxygen and water vapor absorption at higher photon energies. Ellipsometric spectra over a photon energy range of 0.7 to 8.5 eV were collected at a 70° angle of incidence and were fit via iterative least squares regression using a structural and optical model, which minimizes the unweighted error function or mean square error²⁰⁹ to extract the complex dielectric function ($\epsilon = \epsilon_1 + i\epsilon_2$) spectra and structural properties such as layer thickness. Further details of the subsequent analysis are provided in the supplemental materials.

Near-field FTIR measurements were performed at the Advanced Light Source (Beam Line 2.4) using a tip-based scattering approach (Neaspec, Attocube Systems). Absorption was deduced from the amplitude and phase of the scattering measurements via established methods²¹⁰ and normalized such that the baseline of the signal to its maximum in the 600-700 cm^{-1} was common to all films.

6.6.3. Density Functional Theory Calculations

The theoretical simulation was performed using *ab-initio* first-principle density functional theory within a plane wave basis set as implemented in VASP simulation package.^{211,212} The interactions among valence and core-valence electrons were represented by all-electron projector-augmented wave potentials within the pseudopotential approximation.^{213,214} $5p^6 5d^2 6s^2$ and $2s^2 2p^4$ electron configuration for Hf and O was used as valence electron. The exchange-correlation energy of the electron was approximated by the Generalized Gradient Approximation (GGA) within the Perdew-Burke-Ernzerhof (PBE) functional.²¹⁵ The kinetic energy cut-off of the plane-wave basis set used was 500 eV. The structures were relaxed until the forces on every atom were $\leq 10^{-3}$ eV/Å. The Brillouin zone was sampled by a well-converged Monkhorst-Pack (MP) k -mesh.²¹⁶ It is well known that the calculated electronic band gap of a semiconductor

using PBE functional is underestimated, and the hybrid functional approximation provide better prediction of the electronic structure which is close to the experimental value. To have a better description of the electronic structure of HfO₂ polymorphism phase, a Heyd-Scuseria-Ernzerhof (HSE)²¹⁷ exchange–correlation functional was used to calculate the electronic band structure by considering the PBE relaxed structure.

6.7. Acknowledgements

Thin film synthesis and X-ray diffraction characterization was supported by the Semiconductor Research Corporation (SRC) within the Nanomanufacturing, Materials, and Processes (NMP) Program under task 2875.001. S.T.J. acknowledges support from the U.S. National Science Foundation’s Graduate Research Fellowship Program under grant DGE-1842490. Nano-FTIR, electrical characterization, and computation were supported by the Center for 3D Ferroelectric Microelectronics (3DFeM), an Energy Frontier Research Center funded by the U.S. Department of Energy, Office of Science, Basic Energy Sciences under Award No. DE-SC0021118. This research used resources of the Advanced Light Source, which is a DOE Office of Science User Facility under contract no. DE-AC02-05CH11231. The authors acknowledge beamline scientists Hans Bechtel and Stephanie Gilbert Corder for their technical assistance in nano-FTIR measurements.

Chapter 7: Impact of High-Power Impulse Magnetron Sputtering Pulse Width on the Nucleation, Crystallization, Microstructure, and Ferroelectric Properties of Hafnium Oxide Thin Films

The contents of this chapter are in preparation for submission for publication with the following authors.

Samantha T. Jaszewski^a, Shelby S. Fields^a, Ching-Chang Chung^b, Jacob L. Jones^b, Keithen G. Orson^a, Petra Reinke^a, and Jon F. Ihlefeld^{a, c}

^a *Department of Materials Science and Engineering, University of Virginia, Charlottesville, Virginia 22904, USA*

^b *Department of Materials Science and Engineering, North Carolina State University, Raleigh, North Carolina 27695, USA*

^c *Charles L. Brown Department of Electrical and Computer Engineering, University of Virginia, Charlottesville, Virginia 22904, USA*

7.1. Motivation

In Chapter 5, the effect of oxygen content on sputtered undoped HfO₂ films deposited by High-Power Impulse Magnetron Sputtering (HiPIMS) was explored. It was shown that small changes in oxygen content have a significant impact on the phases that form in HfO₂ and the resulting ferroelectric properties. In addition to control of oxygen content, a number of other HiPIMS processing parameters that may be useful for engineering specific film properties are available. In this chapter, the effects of the HiPIMS pulse width on the properties of ferroelectric HfO₂ thin films are explored.

7.2. Abstract

The impact of the high-power impulse magnetron sputtering (HiPIMS) pulse width on the crystallization, microstructure, and ferroelectric properties of undoped HfO₂ films is investigated here. HfO₂ films were sputtered from a Hf target in Ar/O₂ atmosphere, varying the instantaneous power density by changing the HiPIMS pulse width. *In-situ* X-ray diffraction measurements during crystallization demonstrate that the HiPIMS pulse width impacts nucleation and phase formation, with an intermediate pulse width of 110 μs stabilizing the ferroelectric phase over the widest temperature range. Although the pulse width impacts the grain size with the lowest pulse width resulting in the largest grain size, grain size does not strongly correlate with phase content or ferroelectric behavior in these films. These results suggest that more precise control over the energetics of the depositing species may be beneficial for stabilizing the ferroelectric phase in this material.

7.3. Introduction

Since the first report of ferroelectricity in SiO₂-doped hafnium oxide (HfO₂) thin films in 2011,²⁸ interest in this material has grown for a number of microelectronics applications. In particular, ferroelectric HfO₂ is a promising candidate for non-volatile memory devices like ferroelectric random-access memory because it is thermodynamically compatible with silicon¹⁵ and has the potential to overcome some of the limitations of existing non-volatile memory, such as limited scaling and high power consumption. Atomic layer deposition (ALD) is the most widely used technique for the fabrication of HfO₂-based thin films, although chemical solution deposition, pulsed laser deposition (PLD), and sputtering have also been explored.⁹⁷ In comparison to ALD, sputter deposition offers a wide range of processing parameters that can be used to tailor film properties. Still, conventional sputter techniques have limited means to control the energy of the depositing species, so techniques like High-Power Impulse Magnetron Sputtering (HiPIMS) that have a wider processing space should be explored for the deposition of ferroelectric HfO₂-based thin films.

HiPIMS is a physical vapor deposition (PVD) technique in which low-duty cycle pulses (< 5% duty cycle) are applied to a sputter target to produce dense plasmas with a high degree of sputtered atom ionization.^{113,115} This ionization can be controlled by varying pulse parameters such as pulse width, frequency, and voltage. The high degree of sputtered atom ionization and the

resulting ion bombardment during deposition enables access to regions of the structure zone diagram where equiaxed nanocrystalline microstructures result, whereas traditional sputtering techniques are restricted to lower energy regions of the structure zone model and thus are limited in their ability to control grain size.¹³⁴ As an example, CrN films prepared by dc sputtering have a porous columnar morphology, while HiPIMS results in a uniform, dense, equiaxed nanocrystalline structure.¹⁵¹ Control over microstructure may be beneficial for HfO₂ thin films where grain size has been linked to the stability of the ferroelectric phase, with the ferroelectric phase stabilized by an intermediate grain size in comparison to the tetragonal and monoclinic phases.^{34,36} In addition to the pulse parameters, background pressure, and gas atmosphere can be controlled during HiPIMS; these parameters can be optimized to tailor the ion energy and flux of the depositing species, thus providing additional control over the film's microstructure and properties in comparison to conventional ALD and PVD processes. While it has been shown that HiPIMS can produce nanocrystalline films, HfO₂ films shown in Chapter 5 were amorphous as deposited. Still, these HiPIMS parameters can be used to affect the coordination and bonding environments that make up the local amorphous structure. Ostwald's rule of stages states that the most thermodynamically stable phase may not be the first to nucleate. Instead, the phase that most closely resembles the amorphous structure in terms of coordination and bonding will form first. Applying this principle to the amorphous structure of HfO₂ films may enable control over the phases that form after crystallization.

In this work, the effect of HiPIMS pulse width on the nucleation, crystallization, microstructure, and ferroelectric properties will be explored. By varying the HiPIMS pulse width, different instantaneous power densities and positive ion-to-neutral ratios are obtained. To assess the effects of this parameter on crystallization behavior and phase stability, *in-situ* X-ray diffraction patterns are measured and compared to grazing-incidence X-ray diffraction measurements of films that underwent a rapid thermal anneal. The microstructure is examined by taking plan-view scanning electron microscopy images and atomic force microscopy images; while differences in grain size between films are observed, these differences cannot account for the changes in phase formation and ferroelectric properties that are measured for the different pulse widths.

7.4. Experimental Procedures

7.4.1. Deposition Parameters

HfO₂ films were deposited on 100 nm thick TaN bottom electrodes on (001)-oriented *p*-type silicon substrates. The TaN was prepared by pulsed dc magnetron sputtering (30 kHz, 4 μs reverse time) from a TaN target within a Denton Discovery 550 system. Hafnium oxide films were prepared from a 50 mm diameter hafnium metal target of 99.9 % purity (excluding zirconium impurities) affixed to a balanced magnetron sputter gun (Meivac, MAK) in a custom sputter chamber, as described in previous work.⁶² For HiPIMS depositions, a Starfire Impulse HiPIMS power module was used in conjunction with a DC power supply to deliver square voltage pulses with pulse widths ranging from 50 to 140 μs at a frequency of 200 Hz. Following each negative high-power pulse, a +100 V positive pulse of length 200 μs was applied to the target. HiPIMS voltage and current waveforms were extracted for each deposition condition. Argon was used as the sputter gas, and O₂ was used as the reactive gas. A gas flow of 15.00 sccm of argon and varying O₂ flow rates were used with a constant background pressure of 5 mTorr. Films were continuously rotated during growth to minimize thickness gradients, and the substrate platen was grounded. The substrate was not intentionally heated during deposition.

Following deposition, one set of films was left as-deposited for *in-situ* X-ray diffraction studies, and the other set of films was annealed in a pure argon atmosphere (99.999% purity) for 30 seconds at 800 °C in a rapid thermal processor (Allwin 21, Heatwave AW 610) with a ramp rate of 66.7 °C/s. Finally, top electrodes consisting of 20 nm of titanium nitride and 50 nm of palladium were DC-magnetron sputtered through a shadow mask to create a capacitor structure for electrical measurements. TiN was reactively sputtered from a titanium target with a gas atmosphere of 5 sccm of argon and 1 sccm of nitrogen, pressure of 0.9 mTorr, and DC power density of 7.40 W/cm². Palladium was deposited with an argon background pressure of 5 mTorr and a DC power density of 3.31 W/cm². Circular electrode diameters were 100 μm, and areas were confirmed by optical microscopy.

7.4.2. Characterization

The HiPIMS waveforms were extracted from an oscilloscope connected to the voltage and current monitor outputs of the Starfire Impulse module in order to measure the instantaneous

voltage and currents during the deposition. Positive ion-to-neutral ratios were measured using the quartz crystal microbalance (QCM) on an Impedans Quantum Retarding Field Ion Energy Analyzer with grid potentials varied to first block electrons and negative ions from reaching the substrate and then all ions. By taking the ratio of the deposition rates with and without ions, the positive ion-to-neutral ratio was calculated.

X-ray photoelectron spectroscopy (XPS) measurements were performed with a Scienta Omicron Multiprobe MXPS system with an XM1200 monochromator. Monochromatic Al K α ($h\nu = 1486.6$ eV) radiation was used to acquire the spectra. The samples were measured without sputtering to avoid any process that could alter the defect population in the near-surface region. Survey spectra measured with a pass energy of 100 eV were used to confirm the presence of Hf, O, and C; no other elements were detected. A pass energy of 25 eV and energy steps of 0.05 eV were used for all core level spectra. All XPS data were analyzed using KolXPD software.¹⁶³ A Voigt function was used to fit all core levels and was combined with a Shirley background.¹⁶⁴ Peak areas were corrected by cross-sections provided by Scofield *et al.* for each core level.¹⁶⁵ Compositions of as-deposited and annealed films were calculated by taking a ratio of the corrected O 1s peak area to the corrected Hf 4f_{5/2} and Hf 4f_{7/2} peak areas.

A Rigaku Smartlab X-ray diffractometer with Cu K α radiation in a parallel beam configuration was used for in-plane XRD measurements and out-of-plane grazing-incidence X-ray diffraction (GIXRD) measurements with a fixed incident angle of 0.7°. A 2θ range of 26-33° was selected due to the presence of 100% intensity reflections of the monoclinic $P2_1/c$ phase, tetragonal $P4_2/nmc$ phase, antipolar orthorhombic $Pbca$, and orthorhombic $Pca2_1$ phase in this range. Crystallite sizes calculated using Scherrer's equation¹⁵⁴ were corrected for instrumental broadening effects using Standard Reference Material[®] 660c lanthanum hexaboride powder from the National Institute of Standards and Technology.¹⁵⁵ Phase evolution during crystallization was measured using a PANalytical Empyrean X-ray diffractometer with Cu K α radiation in a Bragg-Brentano geometry with a linear detector and an Anton Paar HTK1200 high-temperature chamber in a nitrogen environment. Similar to prior studies of the crystallization of HfO₂-based thin films,^{101,198} the samples were heated at a rate of 2 °C/min from 25 °C to 1000 °C, and diffraction patterns were collected every 6 °C.

Electrical characterization was performed on capacitor structures for the annealed films. A Radiant Technologies Precision LC II Ferroelectric Property Analyzer was used to perform $P(E)$ measurements with a period of 10 ms (100 Hz equivalent frequency).

Plan-view scanning electron microscopy images were collected using an FEI Helios UC G4 microscope in secondary electron mode with an accelerating voltage of 2.00 kV, a beam current of 0.1 nA, a dwell time of 15 μ s, a working distance of 2.3 mm, and a through-the-lens detector. Topographic atomic force microscopy (AFM) images were acquired via an Oxford Instruments Asylum Research Cypher-S instrument in AC tapping mode equipped with NanoSensor PPP-NCHR-10 probes with a resonance frequency of 190 kHz.

7.5. Results and Discussion

7.5.1. HiPIMS Conditions

Four 20 nm HfO₂ films were deposited via HiPIMS with pulse widths of 50, 80, 110, and 140 μ s with corresponding instantaneous power densities of 1023 to 568 W/cm², shown in **Table 7.1**. The instantaneous powers were calculated using the HiPIMS voltage and current waveforms, which are shown in **Figure 7.1**. For all pulse width conditions, these waveforms were monitored to avoid the target poisoning regime in which the current sharply increases without saturating. Target poisoning should be avoided as it affects the sputter yield and secondary electron emission yield.^{218,219} As the pulse width was decreased, the pulse voltage and current increased since the time-averaged power was kept constant at 200 W. Thus, the 50 μ s pulse width had the highest instantaneous power of 1023 W/cm². Previous work has shown that the properties of HfO₂ thin films are highly sensitive to oxygen content, and small changes in plasma oxygen content during HiPIMS deposition can produce large differences in film oxygen content.⁶² Thus, it was important to ensure that the oxygen content in the films was controlled so that the effects of HiPIMS pulse width could be evaluated in isolation. For each pulse width, a different oxygen flow rate was chosen so that the films would have similar oxygen content, as reported in **Table 7.1**. Lower plasma oxygen content was chosen for lower pulse widths to avoid target poisoning since target poisoning occurs during the ‘off state’ of the plasma, and shorter pulses have longer off times.^{220,221} XPS measurements were performed to assess the oxygen content in the films after crystallization, and the oxygen content in the films is shown in **Table 7.1**. The Hf 4*f* and O 1*s* core levels that were fit to obtain these compositions are shown in **Figure 7.2**. No Hf³⁺ signature is present in these

spectra. This indicates that there is not a significant fraction of charged vacancies in these films, although the films are oxygen deficient according to the calculations of film oxygen content.

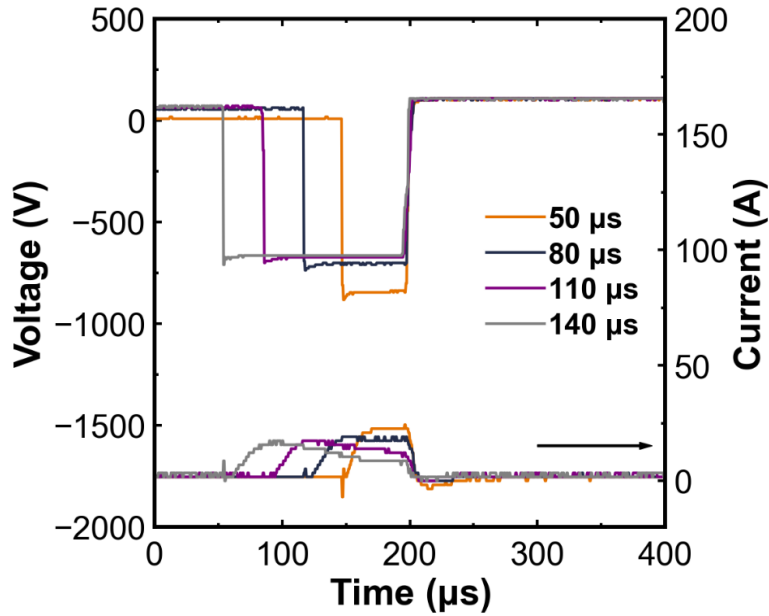


Figure 7.1: HiPIMS voltage and current waveforms collected during the deposition of the films with 50, 80, 110, and 140 μs pulse widths.

Table 7.1: Pulse width, pulse frequency, and plasma oxygen content used for the deposition of the HfO_2 films, and the resulting instantaneous power and film oxygen content measured by XPS.

Pulse Width (μs)	Pulse Frequency (Hz)	Instantaneous Power Density (W/cm^2)	Plasma Oxygen Content (%)	Film Oxygen Content (x in HfO_x)
50	200	1023	7.1	1.48
80	200	696	7.6	1.61
110	200	602	7.6	1.52
140	200	568	8.8	1.44

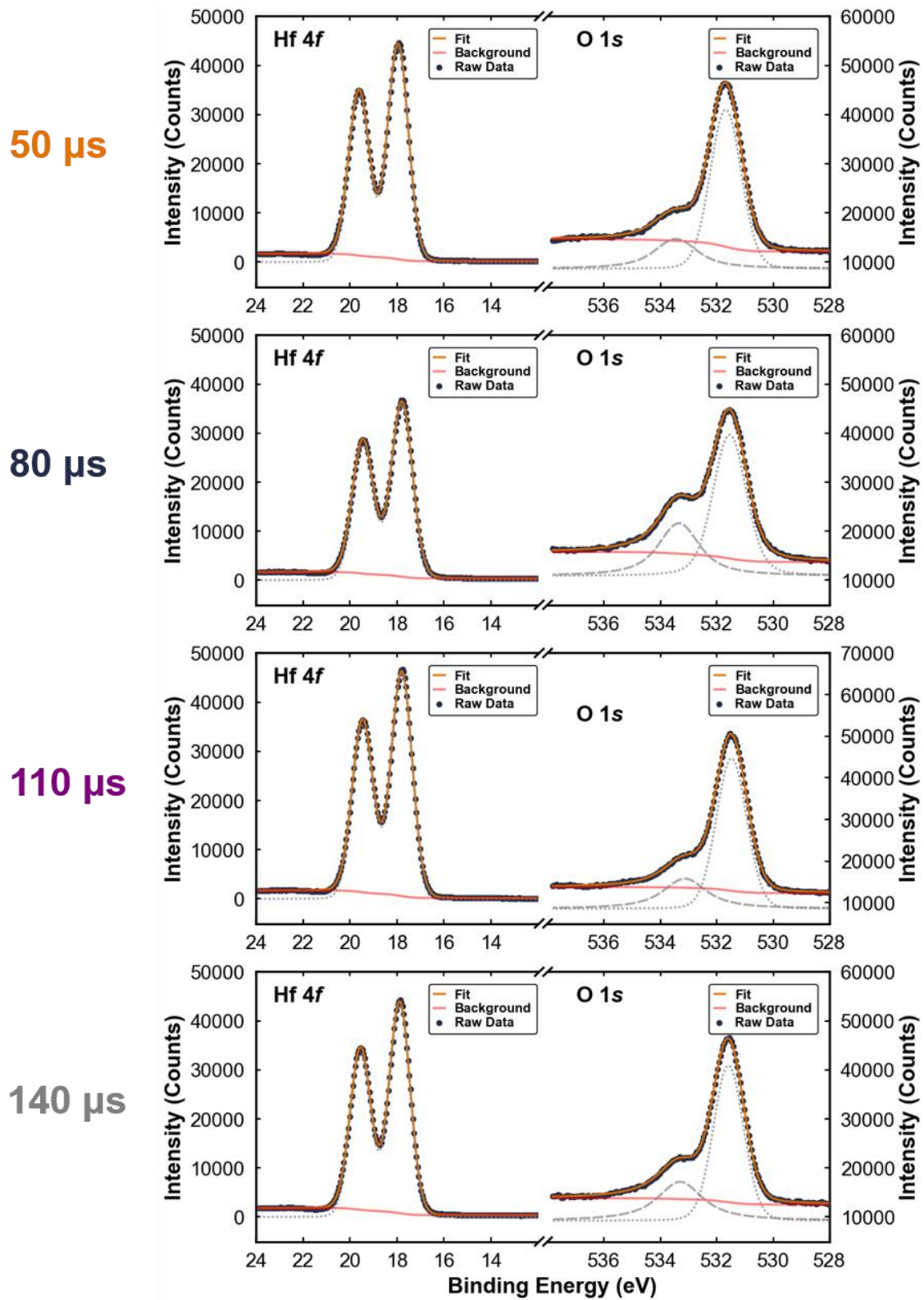


Figure 7.2: Hf 4f and O 1s XPS spectra for the HfO₂ films deposited with 50, 80, 110, and 140 μs pulse widths. The spectra are fit using KolXPD software.

The positive ion-to-neutral ratio measured during the deposition for each HiPIMS pulse width is shown in **Figure 7.3**. Previous studies have shown that shorter HiPIMS pulse widths result in higher ionization fractions.^{222,223} Similarly, here, it is demonstrated that the shortest pulse width of 50 μs results in the highest positive ion-to-neutral ratio of 0.73. A nearly linear decrease in the ion-to-neutral ratio is observed as the pulse width increases, and the 140 μs sample has the lowest ratio of 0.39. The measurements confirm that a shorter pulse width, which corresponds to a higher instantaneous power, results in a larger fraction of positive ions in the plasma. Since each negative pulse is followed by a 100 V positive pulse, a lower pulse width with a larger fraction of positive ions would result in an increase in the number of ions bombarding the growing film.

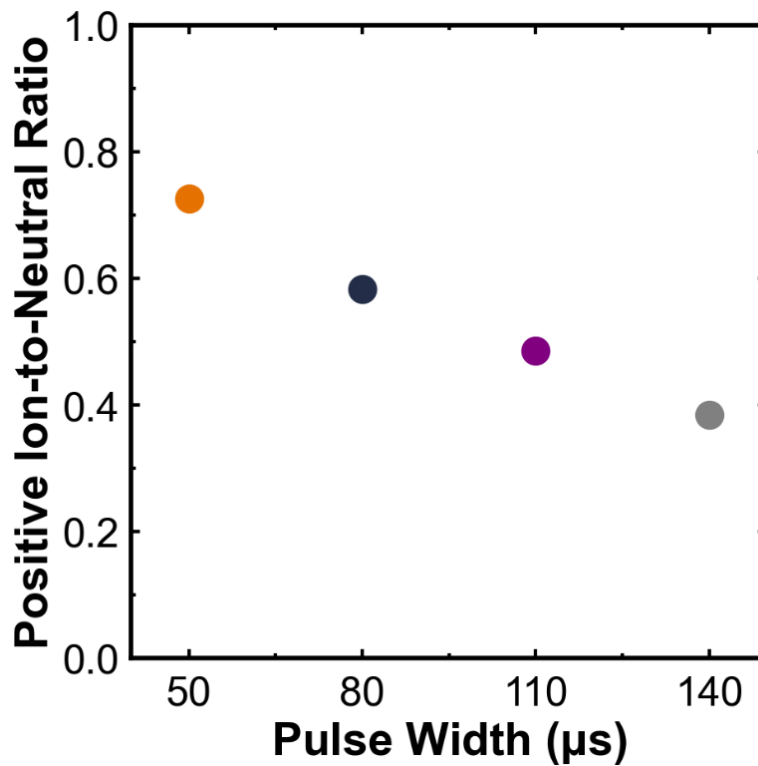


Figure 7.3: Positive ion-to-neutral ratio calculated from the deposition rates of positive ions + neutrals to neutrals alone.

7.5.2. X-ray Diffraction Characterization

To assess the impact of HiPIMS pulse width on the structural evolution of HfO_2 thin films, *in-situ* high-temperature XRD measurements were performed. **Figure 7.4** shows the *in-situ* high-temperature X-ray diffraction patterns for the films that are amorphous as-deposited. All of the films begin to crystallize at around 500 $^{\circ}\text{C}$. For the 50 μs and 80 μs samples, the formation of the

polar orthorhombic (111), antipolar orthorhombic (211), and/or tetragonal (101) peak occurs at approximately 500 °C along with the formation of the monoclinic ($\bar{1}11$) peak. This differs from the 110 μs sample in which the monoclinic phase does not begin to crystallize until much higher temperatures. Once again, for the 140 μs sample, crystallization of the monoclinic phase occurs at a similar temperature to that of the orthorhombic and/or tetragonal phase. In addition, the orthorhombic and/or tetragonal phases are stable from 500 to 900 °C for the films deposited with 110 and 140 μs pulse widths, while these phases are only stable from 500 to 800 °C for films deposited with 50 and 80 μs pulse widths. Although the film oxygen content varies (within error) between the films, the presence of oxygen impurities in the nitrogen gas, desorption from the furnace insulation, and desorption from the alumina sample stage and sample holder during these measurements likely eliminated the differences in the original oxygen content within the films. Therefore, the differences observed here cannot be attributed to differences in oxygen content. These results demonstrate that phase formation is being impacted by the HiPIMS pulse width. However, it should be noted that the rate of heating used for these experiments (2 °C/min) is significantly slower than a typical rapid thermal anneal process.

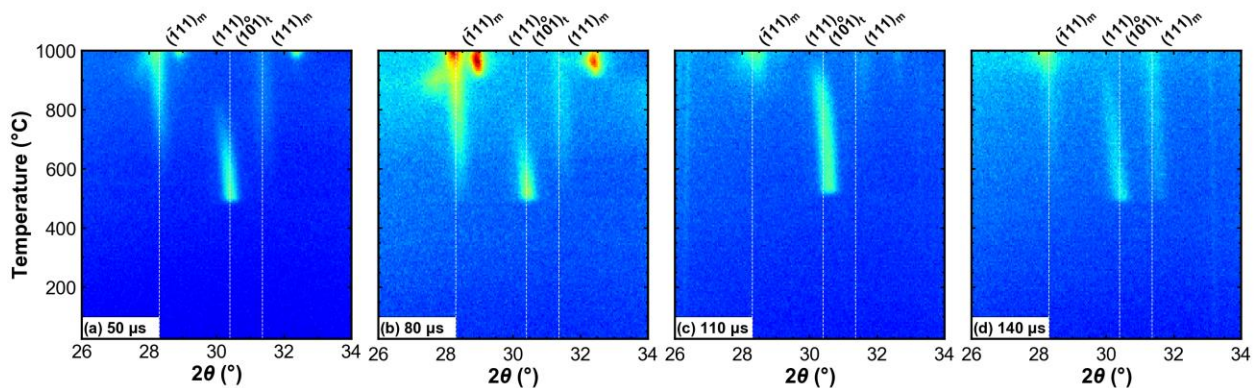


Figure 7.4: *In-situ* high-temperature XRD measurements of films deposited with (a) 50, (b) 80, (c) 110, and (d) 140 μs pulse widths.

The crystallization behavior observed in the *in-situ* XRD experiment was compared to films that underwent a more typical rapid thermal anneal (RTA). **Figure 7.5** shows the GIXRD patterns for identical films that have undergone rapid thermal annealing at 800 °C with a heating rate of 67 °C/second. The relative orthorhombic + tetragonal (o+t) phase fractions were calculated by fitting the GIXRD patterns using LIPRAS fitting software¹⁵⁸ and taking the ratio of the integrated peak intensity of the orthorhombic + tetragonal peak to the integrated intensity sum of

all three peaks. The 50 μs film has the smallest fraction of the orthorhombic/tetragonal phase (0.33 ± 0.07) and predominantly consists of the monoclinic phase. The 80 μs film contains more orthorhombic/tetragonal phase (0.51 ± 0.04) but still has a significant fraction of monoclinic phase. The 110 μs sample has the highest fraction of the orthorhombic/tetragonal phase (0.94 ± 0.03), and together with the 140 μs sample, these films primarily consist of the orthorhombic and/or tetragonal phase.

It has been reported that the heating rate used during annealing can significantly affect the phases that form in HfO_2 thin films, with greater fractions of the monoclinic phase forming at 10 $^\circ\text{C/s}$ than at 66 $^\circ\text{C/s}$;²²⁴ however, in this case, these results are consistent with the *in-situ* diffraction measurements shown above. The lower pulse widths result in large fractions of the monoclinic phase, while the 110 μs pulse width has the highest o+t fraction. The similar results obtained through drastically different heating rates provide additional evidence that the HiPIMS pulse width is impacting nucleation is an important variable to consider when optimizing deposition conditions to obtain phase-pure films.

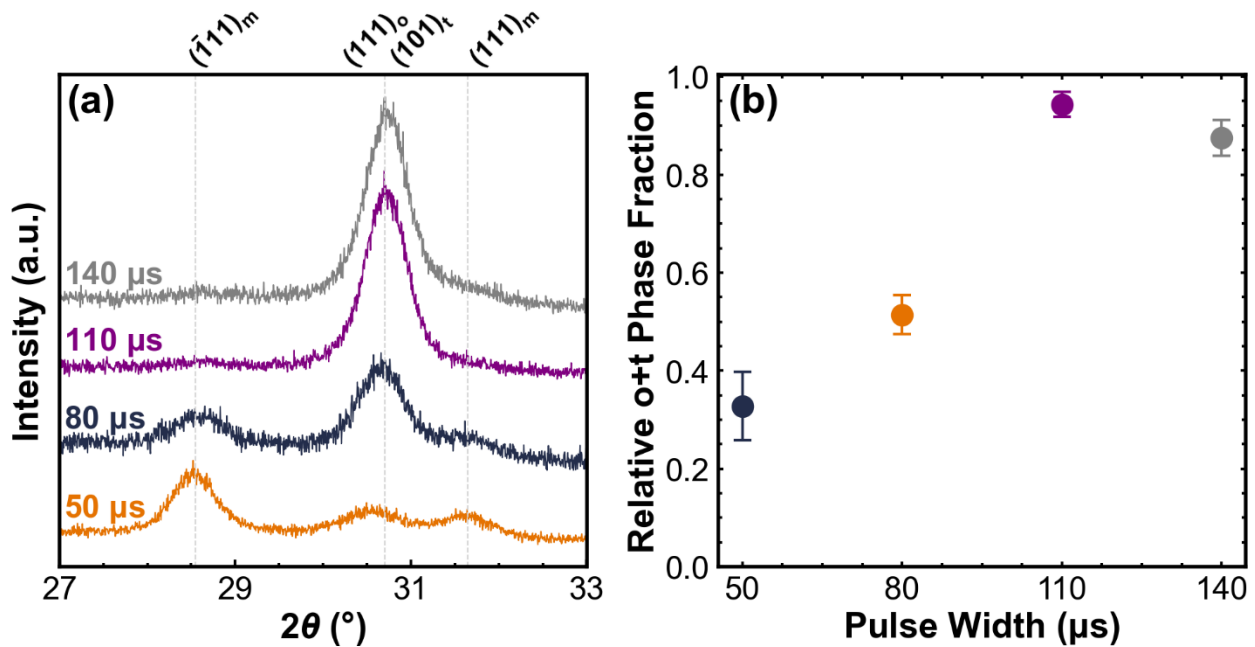


Figure 7.5: (a) GIXRD patterns for films deposited with 50, 80, 110, and 140 μs pulse widths, rapid thermal annealed at 800 $^\circ\text{C}$, and the (b) relative o+t phase fractions calculated from the GIXRD measurements.

7.5.3. Electrical Characterization

In order to assess how the pulse width and phase content affect ferroelectric properties, the polarization-electric field responses of the films after field cycling with 5000 2.5 MV/cm square waves were measured and are shown in **Figure 7.6**. At the lower pulse widths of 50 and 80 μs , the hysteresis loops open very little and have remanent polarization (P_r) values of 1.9 and 3.6 $\mu\text{C}/\text{cm}^2$, respectively. The low P_r values can be explained by the dominating linear dielectric response due to the significant presence of the monoclinic phase in these films. At the higher pulse widths, however, the hysteresis loops open up more and demonstrate a ferroelectric response typical of the ferroelectric orthorhombic phase. The 110 μs film has the largest hysteretic response, with a P_r of 9.4 $\mu\text{C}/\text{cm}^2$, which correlates with the large fraction of the orthorhombic phase observed in the GIXRD measurements. The 140 μs film has the second largest P_r of 4.4 $\mu\text{C}/\text{cm}^2$. Combined with the XRD results, these measurements suggest that 110 μs is the optimal pulse width condition to achieve ferroelectric behavior in these films.

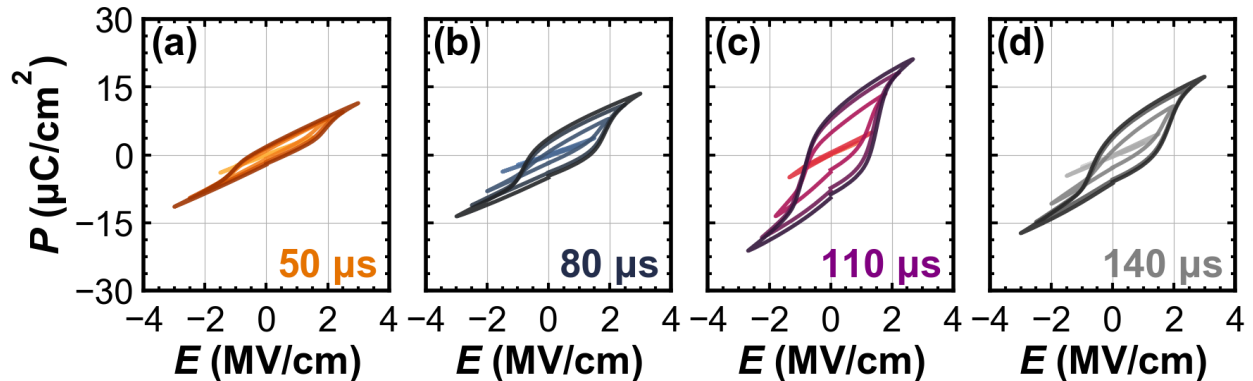


Figure 7.6: Nested polarization hysteresis measurements after field cycling for the samples deposited with (a) 50 μs , (b) 80 μs , (c) 110 μs , and (d) 140 μs pulse widths.

7.5.4. Crystallite Size and Microstructure

To determine if the difference in polarization hysteresis behavior is linked to microstructure, the crystallite size and grain sizes of the films were evaluated through analysis of XRD data, SEM images, and AFM images. In-plane XRD measurements were performed so that the crystallite sizes could be further assessed, and the patterns are shown in **Figure 7.7**. The crystallite sizes calculated using Scherrer's equation from out-of-plane and in-plane XRD

measurements are shown in **Figure 7.8**. Both out-of-plane and in-plane measurements show that the pulse width has an effect on the crystallite size. The 50 μs sample had the lowest in-plane and out-of-plane crystallite sizes. It should be noted that the orthorhombic/tetragonal peak was used for these calculations, and this sample had the lowest fraction of the o+t phase and a lower signal-to-noise than the other films, which should result in smaller crystallite sizes. The other three pulse widths, 80 μs , 110 μs , and 140 μs , have more similar crystallite sizes from approximately 13 – 15 nm, as determined from in-plane and out-of-plane XRD measurements.

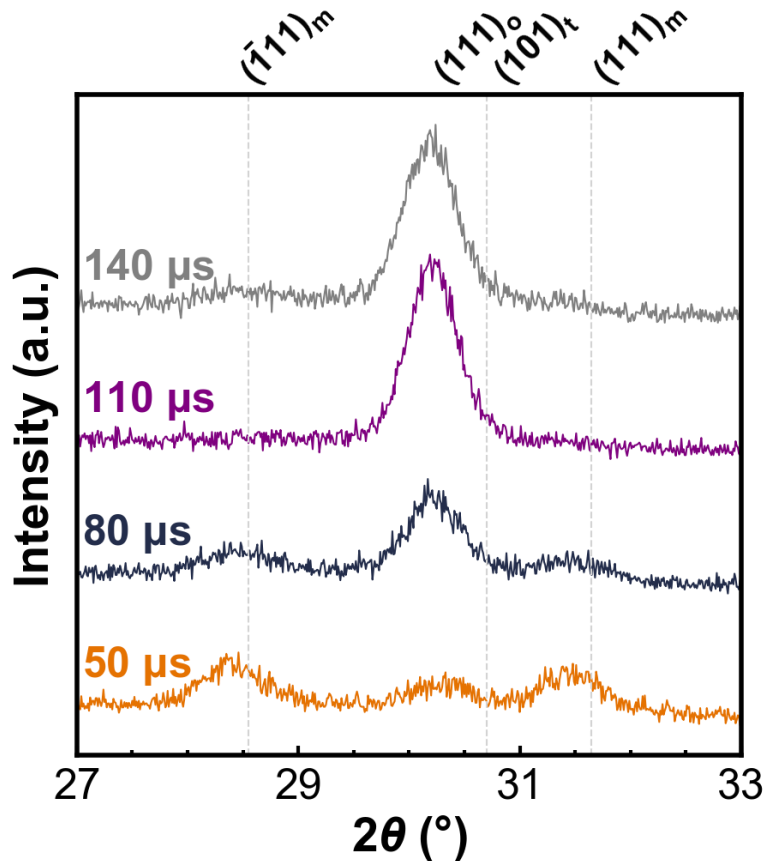


Figure 7.7: In-plane XRD patterns for films deposited with 50, 80, 110, and 140 μs pulse widths.

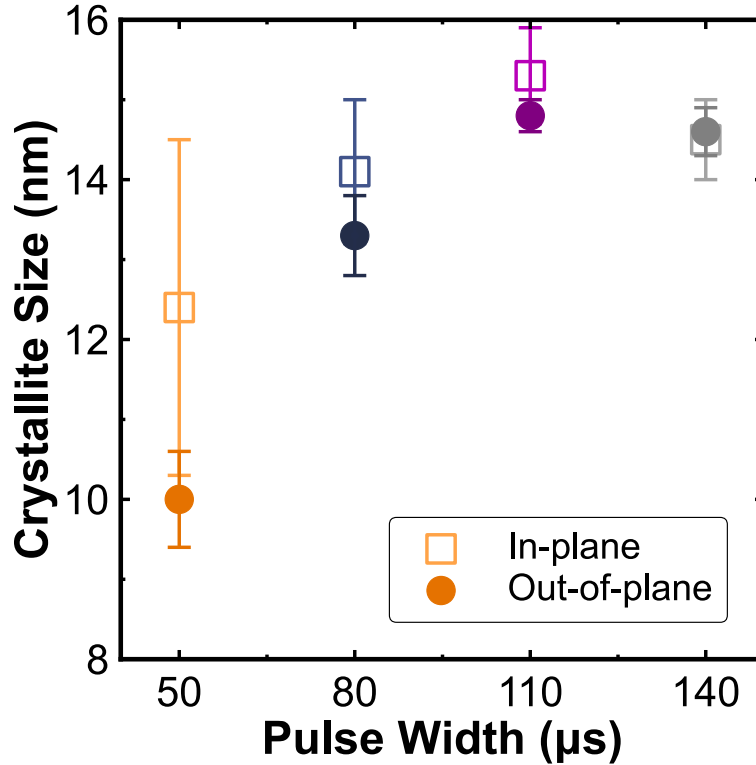


Figure 7.8: Crystallite size calculated from in-plane and out-of-plane XRD measurements.

The microstructure of the films was examined using plan-view SEM with images shown in **Figure 7.9**. Due to the small grain sizes and quick carbon contamination of the samples under the electron beam, the resolution of the images is limited. Thus, AC mode AFM images were collected and are shown in **Figure 7.10**. To quantify the lateral grain sizes, the lineal intercept procedure was used,¹⁷¹ and the mean intercept length is reported in **Figure 7.11**, with error bars representing 95% confidence intervals. The 50 μs sample has the largest grain sizes of 21.3 ± 0.8 nm. The 80, 110, and 140 μs samples have grain sizes of 17.9 ± 0.9 nm, 17.3 ± 1.0 nm, and 17.4 ± 1.4 nm, respectively. Although a small change in microstructure for the 50 μs sample was observed, overall, no clear trend could be established between pulse width, grain size, phase, and electrical properties. More specifically, equivalent grain sizes were observed for the 80, 110, and 140 μs samples even though these samples had differences in phase composition and electrical properties.

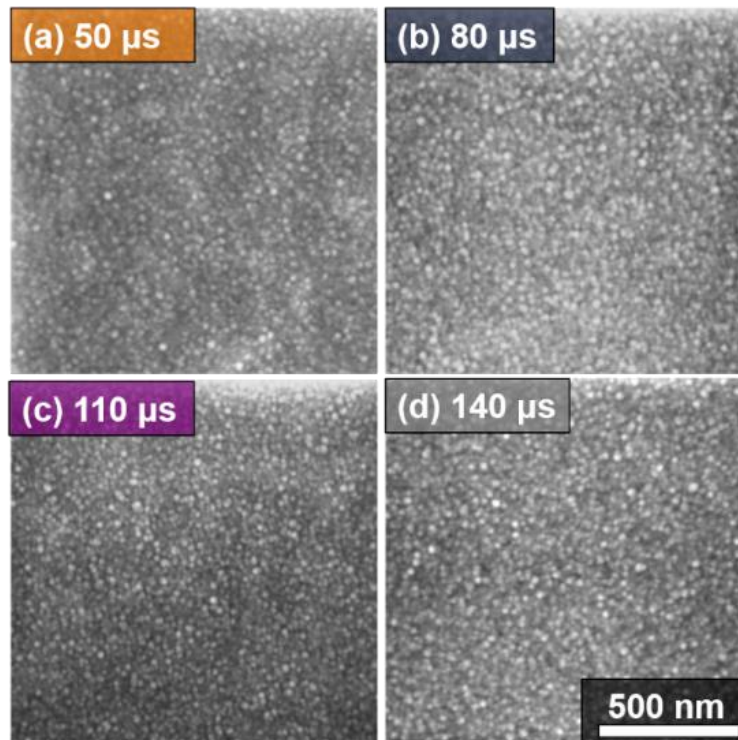


Figure 7.9: Plan-view SEM images of films deposited with (a) 50, (b) 80, (c) 110, and (d) 140 μs pulse widths.

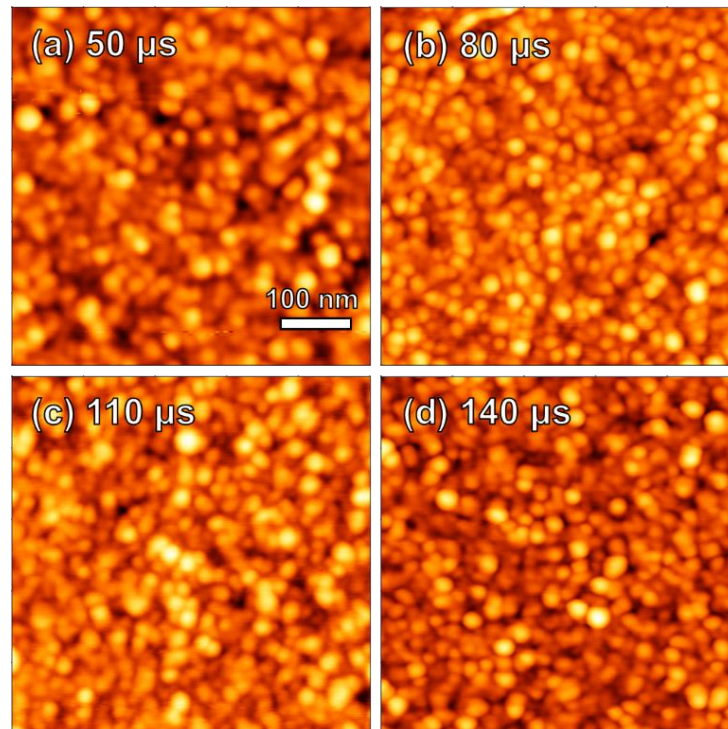


Figure 7.10: AFM topography images of films deposited with (a) 50, (b) 80, (c) 110, and (d) 140 μs pulse widths.

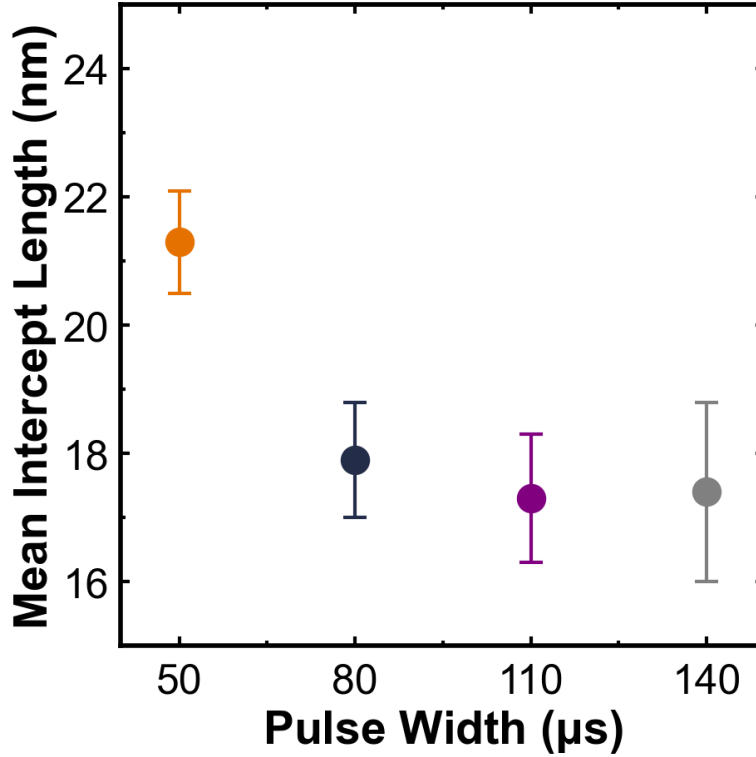


Figure 7.11: Average lateral grain size calculated using the line-intercept method on the AFM images with error bars representing 95% confidence intervals.

7.5.5. Discussion

To summarize, it has been shown that varying the HiPIMS pulse width affects the phases that are formed after annealing. This effect does not appear to be tied to microstructure since grain size was shown to be relatively invariant. Therefore, a different aspect of the HiPIMS pulse width must be responsible. As previously mentioned, the positive ion-to-neutral ratio was inversely correlated to pulse width. During these depositions, a positive pulse was applied after the negative pulse. This positive pulse will have the largest effect on plasmas with higher fractions of positive ions, resulting in greater ion bombardment of positive ions for lower pulse widths. It is hypothesized that these differences in ion bombardment affect the short-range order of the amorphous films through parameters like coordination and bonding environment, thereby affecting the nucleation behavior. Then, upon annealing, different phases are formed. Similar effects were observed in vanadium oxide films deposited with different PLD conditions.²²⁵ Using grazing-incidence total X-ray scattering and pair distribution functions, the authors observed different local structures in the amorphous films of vanadium oxide deposited with different laser

repetition rates. It was found that the starting amorphous structure influenced the phases that crystallized. For metastable polymorphs like the polar orthorhombic phase in HfO₂, it is not only difficult to understand how the phase forms but also what approach(es) to use to stabilize it. These results suggest that controlling the short-range order in the amorphous structure may enable control of the phases that form.

7.6. Conclusions

The effect of HiPIMS pulse width on the nucleation, phase formation, microstructure, and ferroelectric properties of HfO₂ films deposited by HiPIMS has been demonstrated. *In-situ* HTXRD measurements showed that the pulse width affects the nucleation temperatures of the phases in addition to phase stability. The heating rate did not have a significant impact on the crystallization of these films, although the heating rate has been shown to influence crystallization in ALD films. Differences in phase constitution were shown as pulse width was varied, with the lowest pulse width, 50 μ s, resulting in the largest fraction of the monoclinic phase present in these films. Although this sample had the largest average grain size of 21.3 ± 0.8 nm, grain size was not shown to correlate with electrical properties. This is evident because the films with 80, 110, and 140 μ s had similar grain sizes, but the 110 μ s sample had a higher fraction of the o+t phases and a larger remanent polarization. These results demonstrate that while HiPIMS pulse width does not significantly alter microstructure, it has the ability to significantly affect the phases that form and the stability of these phases. Future work will be focused on understanding how the HiPIMS pulse width may be affecting the local structure in the amorphous state. Control of phase formation via local structure in the amorphous state can be used to fabricate phase-pure HfO₂-based films with optimal ferroelectric properties.

Chapter 8: Phase Transformations Driving Biaxial Stress Reduction During Wake-Up of Hafnium Zirconium Oxide Thin Films

The contents of this chapter are in preparation for submission for publication with the following authors.

Samantha T. Jaszewski^a, Shelby S. Fields^a, Sebastian Calderon^b, Benjamin L. Aronson^a, Thomas E. Beechem^c, Kyle P. Kelley^d, Elizabeth C. Dickey^b, and Jon F. Ihlefeld^{a,e}

^a *Department of Materials Science and Engineering, University of Virginia, Charlottesville, Virginia 22904, USA*

^b *Department of Materials Science and Engineering, Carnegie Mellon University, Pittsburgh, Pennsylvania 15213, USA*

^c *School of Mechanical Engineering and Birck Nanotechnology Center, Purdue University, West Lafayette, 47907, IN, USA*

^d *Center for Nanophase Materials Sciences, Oak Ridge National Laboratory, Oak Ridge, 37831, TN, USA*

^e *Charles L. Brown Department of Electrical and Computer Engineering, University of Virginia, Charlottesville, Virginia 22904, USA*

8.1. Motivation

The impact of the stress state on ferroelectric HfO₂-based thin films has received considerable attention due to numerous reports correlating biaxial stress and polarization response. The polarization response in this material is also significantly affected by electric field cycling in the process known as ‘wake-up.’ As of yet, the interplay of these two phenomena has not been studied. The purpose of this chapter is to quantify the evolution of stress during wake-up of HZO thin films and investigate the underlying mechanisms responsible for the change in stress that accompanies wake-up. Two main mechanisms are hypothesized to be responsible for the observed reduction in stress – a phase transformation and ferroelastic switching. The present results provide the first evidence of a phase transformation leading to a change in the stress state.

8.2. Abstract

Biaxial stress has been identified to play an important role in the polar orthorhombic phase stability in hafnium oxide-based ferroelectric thin films. However, thus far, the stress state during various stages of wake-up has not been quantified. In this work, the stress evolution with field cycling in hafnium zirconium oxide capacitors is evaluated. The remanent polarization of a 20 nm thick hafnium zirconium oxide thin film increases from $13.8 \mu\text{C}/\text{cm}^2$ in the pristine state to $17.6 \mu\text{C}/\text{cm}^2$ following 10^6 field cycles at $2.5 \text{ MV}/\text{cm}$. This increase in remanent polarization with field cycling is accompanied by a decrease in relative permittivity by approximately 1.5, which could indicate that a phase transformation has occurred. The presence of a phase transformation is confirmed by nano-Fourier transform infrared spectroscopy (FTIR) measurements that show an increase in polar orthorhombic phase content following wake-up. Using an X-ray diffractometer with a collimated source and a two-dimensional detector, diffraction patterns from individual devices field cycled between pristine and 10^6 cycles are collected, and stress is quantified using the $\sin^2(\psi)$ technique. The biaxial stress was measured in several stages of wake-up and was observed to decrease from 4.3 ± 0.2 to 3.2 ± 0.3 GPa. This work provides new insight into the mechanisms controlling and/or accompanying polarization wake-up in the hafnium zirconium oxide.

8.3. Introduction

Since the first report of the ferroelectric properties of silicon-doped hafnium oxide a decade ago,^{226,227} significant research has been devoted to the development of HfO_2 -based thin films for on-chip memory,^{228,229} sensors,^{230,231} and low-power computing^{232,233} applications. Among the primary candidate alloys for such applications is $\text{Hf}_{1-x}\text{Zr}_x\text{O}_2$ (HZO), which displays several advantages over pure HfO_2 and other HfO_2 -based alloys, including a lower thermal budget,²³⁴ a compositionally-dependent polarization response,^{235,236} and chemical compatibility with silicon.^{237,238} Moreover, the ferroelectricity in this alloy has been characterized down to 1 nm in thickness,²³⁹ and it is commonly prepared through means already present in fabrication facilities,^{240,241} making it an ideal system for implementation into the next generation of silicon technology.

Despite these advantages, the metastability of the ferroelectric phase in this material^{73,74} is one hurdle preventing the immediate implementation of HZO into on-chip applications.³⁵ HfO_2

and ZrO_2 comprise the linear dielectric $P2_1/c$ monoclinic phase at room temperature and pressure,^{242–244} the field-induced ferroelectric $P4_2nmc$ tetragonal phase at high temperatures and in small crystallite sizes,^{245–248} and the antiferroelectric $Pbca$ orthorhombic phase at high pressure.^{249,250} Ferroelectricity in HfO_2 has been attributed to the metastable $Pca2_1$ orthorhombic phase.⁶⁴ Its stability is aided by small crystallite sizes,⁷⁴ incorporation of large quantities of oxygen vacancies,^{48,62,251} and biaxial stress,⁷² all of which destabilize the equilibrium monoclinic phase.

Biaxial stress, in particular, has been identified to play an important role in orthorhombic phase stability in HfO_2 and HfO_2 -based alloy systems. Modeling investigations^{73–75} have demonstrated that compressive biaxial and hydrostatic stresses increase the stability of the small-molar volume orthorhombic and tetragonal phases over the large-molar volume monoclinic structure. Such computational findings are supported by high-pressure processing studies, which have reported larger polarizations and orthorhombic phase fractions in HZO films annealed under 50 atm of N_2 .^{252,253} Additional experimental investigations of stress effects on the ferroelectric properties of HfO_2 and its alloys have revealed tensile biaxial residual stresses in these films following their thermal processing at ambient pressures in contact with common binary nitrides.^{35,57,72,76–80} Such tensile stresses have been correlated with enhanced polarization owing to both larger fractions of the orthorhombic phase and alteration of the ferroelectric domain structure to yield a preferred orientation with the short, polar b -axis aligned normal to the film surface.^{72,254}

Application of HfO_2 -based ferroelectrics into next-generation silicon-based technology is further hindered by polarization instabilities that accompany successive ferroelectric switching through electric field cycling.⁸² These increases and decreases in polarization, termed wake-up and fatigue, respectively,^{83,84} are reportedly driven by the redistribution and generation of oxygen vacancies and charged defects that occur during cycling.^{84–86} Previously, wake-up has been shown to precipitate from a combination of charge redistribution-driven transformations between the tetragonal and orthorhombic phases^{82,87} and reductions in the concentration of pinned ferroelectric domains,^{88,89} both of which contribute to the observed increase in switchable polarization. More recently, Cheng *et al.* have reported that wake-up coincided with a phase transformation from the antipolar orthorhombic $Pbca$ phase to the polar orthorhombic $Pca2_1$ phase that is responsible for ferroelectricity. Alternatively, fatigue has been shown to have contributions from both transformations to the monoclinic phase and increases in the amount of ferroelectric domain pinning, which result in reductions in the amount of switchable polarization.^{83,89,93,94} Polarization

instabilities during field cycling are deleterious for memory and computing applications that require stable polarizations regardless of the number of ferroelectric switches.^{255,256} Thus, substantial research efforts have focused on understanding the role of oxygen vacancies on wake-up and fatigue and the effects of these wake-up and fatigue processes on the phase assemblages present within field-cycled HfO₂-based ferroelectric thin films, which have known mechanical stress dependencies.

In this work, 20 nm thick Hf_{0.5}Zr_{0.5}O₂ films were prepared between TaN electrodes. Electrical characterization demonstrated that the remanent polarization of the film increased from 13.8 to 17.6 $\mu\text{C}/\text{cm}^2$, as is typical of wake-up, following field cycling with 10⁶ 2.0 MV/cm square waves. Synchrotron nano-Fourier transform infrared spectroscopy (FTIR) measurements show an increase in the polar orthorhombic phase content accompanying wake-up. The stress of individual HZO capacitors was measured as a function of field cycling, and it was observed that the stress of the HZO film decreases as capacitors are cycled, showing that phase transformations are accompanied by a decrease in biaxial stress.

8.4. Results and Discussion

8.4.1. Electrical Characterization

Polarization-electric field ($P(E)$) measurements were performed on a device after cycling with 0, 10², 10³, 10⁴, 10⁵, and 10⁶ cycles, as shown in **Figure 8.1(a)**. An increase in the remanent polarization with field cycling is observed, as is typical of wake-up in this material. The polarization response is well-saturated, indicative of low leakage current contributions. The remanent polarization extracted from accompanying pulsed positive-up-negative-down (PUND) measurements is shown in **Figure 8.1(b)**, and shows an increase from 13.8 $\mu\text{C}/\text{cm}^2$ to 17.6 $\mu\text{C}/\text{cm}^2$.

In addition to the increase in remanent polarization with field cycling, there is a decrease in the zero bias relative permittivity, demonstrated by the dielectric nonlinearity measurements shown in **Figure 8.2(a)**. The initial relative permittivities extracted from dielectric nonlinearity measurements, ϵ_{init} , are shown in **Figure 8.2(b)**. This decrease in relative permittivity may indicate that a phase transformation has occurred. The polar orthorhombic phase is known to have a lower relative permittivity than the tetragonal phase; however, the relative permittivity of the antipolar orthorhombic phase is not yet known. The irreversible Rayleigh coefficient, α' , is also shown in **Figure 8.2(b)**. The decrease in α' may indicate that domain depinning is occurring as wake-up

proceeds since smaller α' values are characteristic of smaller irreversible contributions to domain wall movement. However, a decrease in α' can also result from a change in the density or mobility of domain walls.

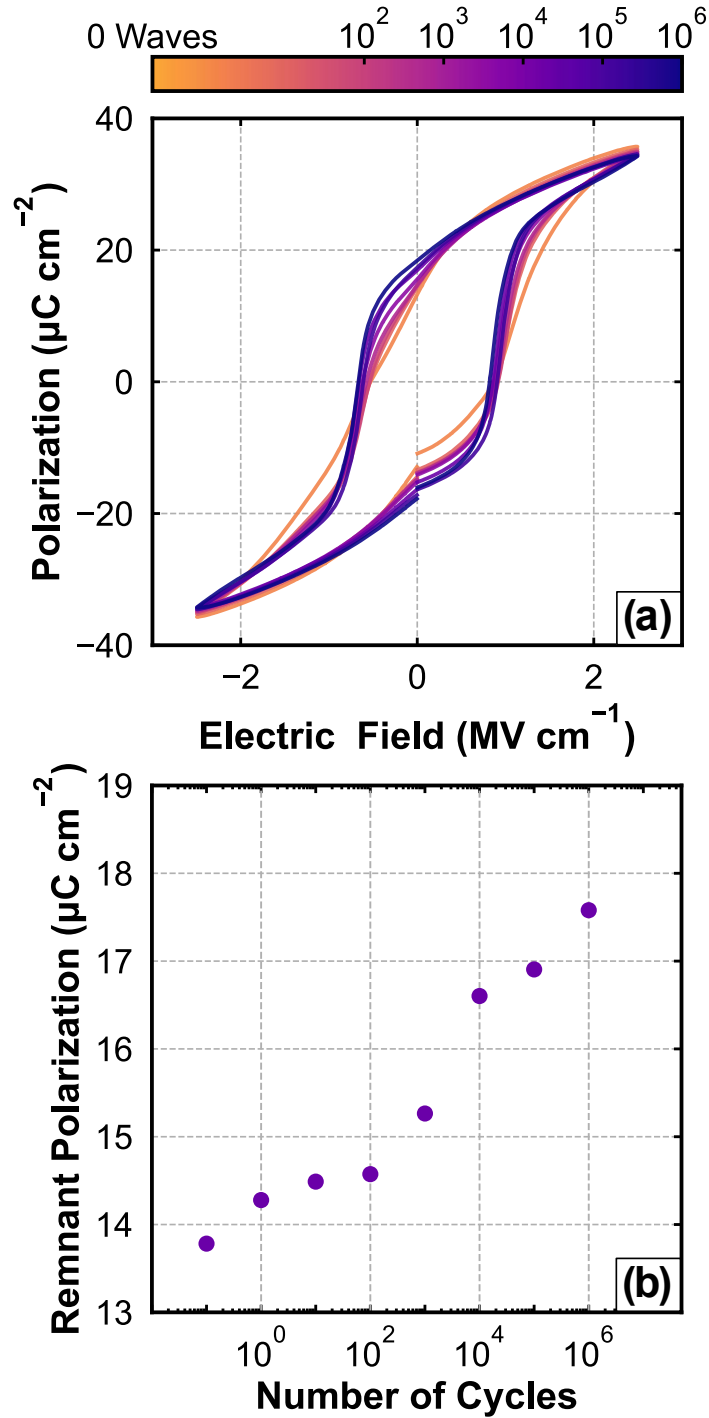


Figure 8.1: (a) $P(E)$ response and (b) remanent polarization from PUND as a function of field cycling.

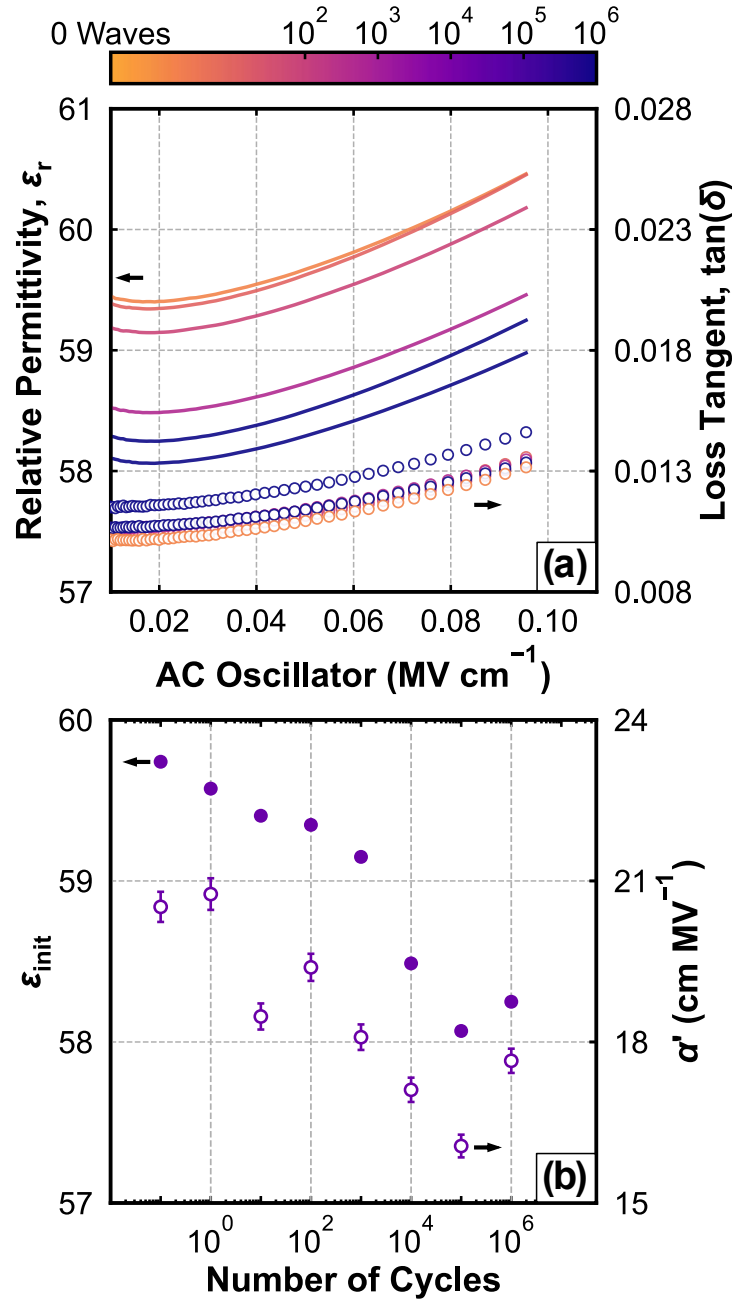


Figure 8.2. (a) Relative permittivity and loss tangent measured at 2.5 MV/cm as a function of field cycling. (b) Intrinsic relative permittivity, ϵ_{init} , and irreversible Rayleigh coefficient, α' , as a function of field cycling.

8.4.2. Nano-Fourier Transform Infrared Spectroscopy

FTIR has the ability to unambiguously differentiate between the phases that coexist in HfO₂-based thin films, as was shown in Chapter 6. To investigate changes in phase composition, the vibrational spectra of individual capacitors cycled with 0, 10³, 10⁴, 10⁵, and 10⁶ square waves were acquired with near-field scattering measurements using synchrotron nano infrared spectroscopy (SINS) at Beamline 2.4 at the Advanced Light Source. After field cycling to specific durations of 10³, 10⁴, 10⁵, and 10⁶ cycles, as well as keeping one capacitor in a pristine state, the top electrode was thinned over a 5 μm × 5 μm area via tomographic atomic force microscopy to enable optical access via SINS. The normalized absorption spectra are shown in **Figure 8.3**. Features at 650 cm⁻¹ and 750 cm⁻¹ have been shown to correlate with the presence of the polar orthorhombic phase. The region around 750 cm⁻¹ shows the clearest increase in intensity as the films are cycled, which would indicate that more polar orthorhombic phase is present. The capacitors cycled with 10⁵ and 10⁶ waves have a significant increase in the intensity of the feature at 750 cm⁻¹ in comparison to the capacitor in the pristine state, and those cycled with 10³ and 10⁴ waves. It should be noted that the sharp peak at 850 cm⁻¹ is due to tantalum oxide on the film surface following electrode thinning.

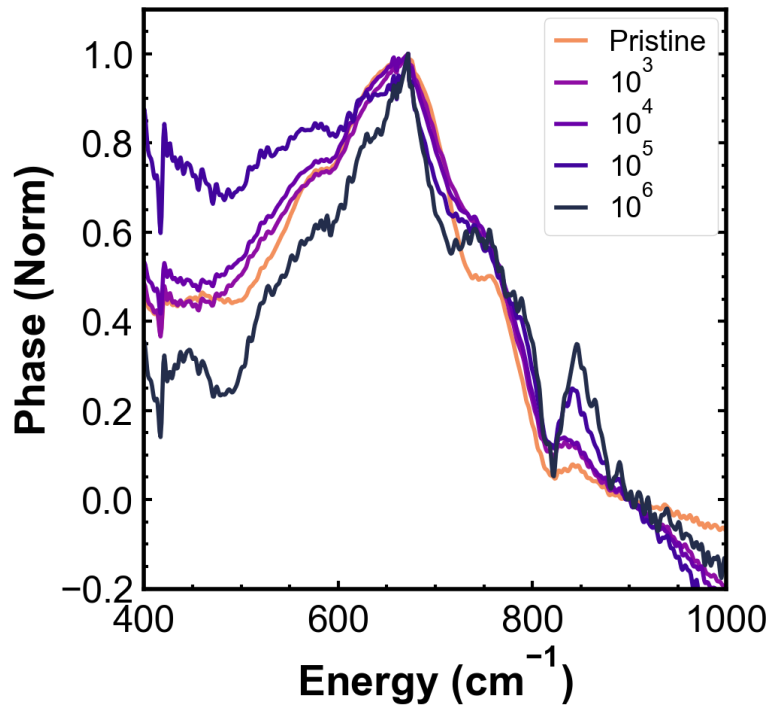


Figure 8.3. Normalized nano-FTIR phase of individual capacitors cycled from the pristine state to 10⁶ square waves.

To further validate the link between an increase in polar orthorhombic phase and the IR feature around 750 cm^{-1} during wake-up, HZO films were woken up using piezoresponse force microscopy (PFM) performed in a glovebox filled with inert gas. HZO films were subjected to +10 V, -10 V, and no bias over $20 \times 20\ \mu\text{m}$ regions to form a checkerboard pattern (**Figure 8.4(b)**). A $5 \times 5\ \mu\text{m}$ image was collected in the center of this checkerboard following poling by PFM, capturing the inner corner of each biased or unbiased region. This image is shown in **Figure 8.4(a)**. The amplitude signal is proportional to the effective piezoelectric coefficient along the normal of the sample surface in this image. Nano-FTIR measurements were made in each region and are shown in **Figure 8.5**. No signal from the top electrode is present in these spectra because the top electrode was completely etched before these measurements. It can be clearly seen that the peak around 750 cm^{-1} has a greater intensity for the positive and negatively biased regions in comparison to the region that was not biased. The differences in these spectra demonstrate that there is an increase in the polar orthorhombic phase after field cycling.

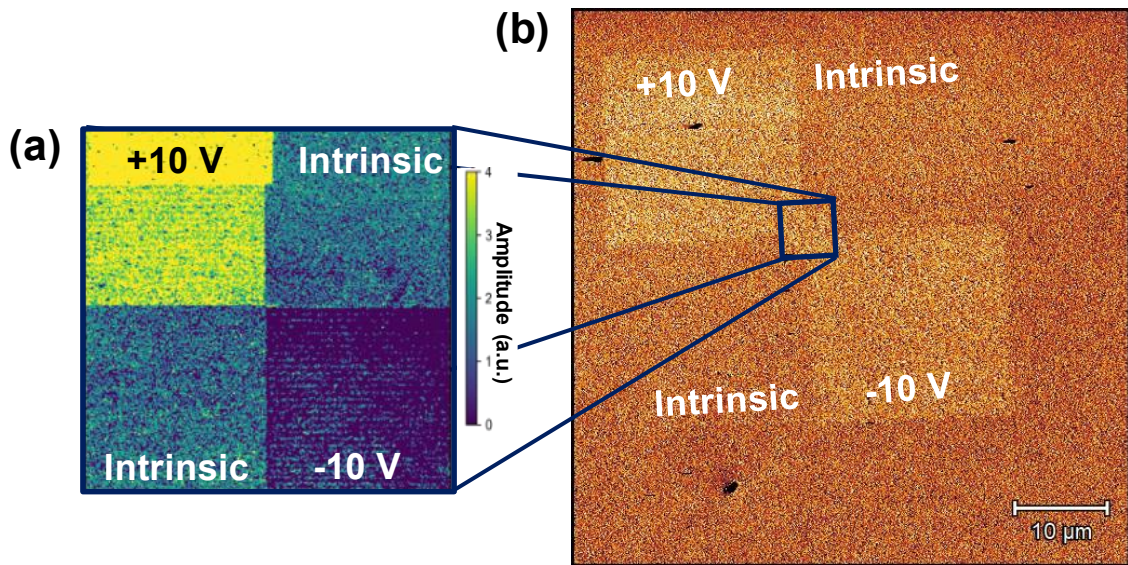


Figure 8.4: (a) PFM image taken after poling the sample with +10 V (top left) and -10 (bottom right), and leaving two intrinsic regions unbiased (bottom left and top right). (b) nano-FITR reflectance that shows reflection differences in the regions that were biased.

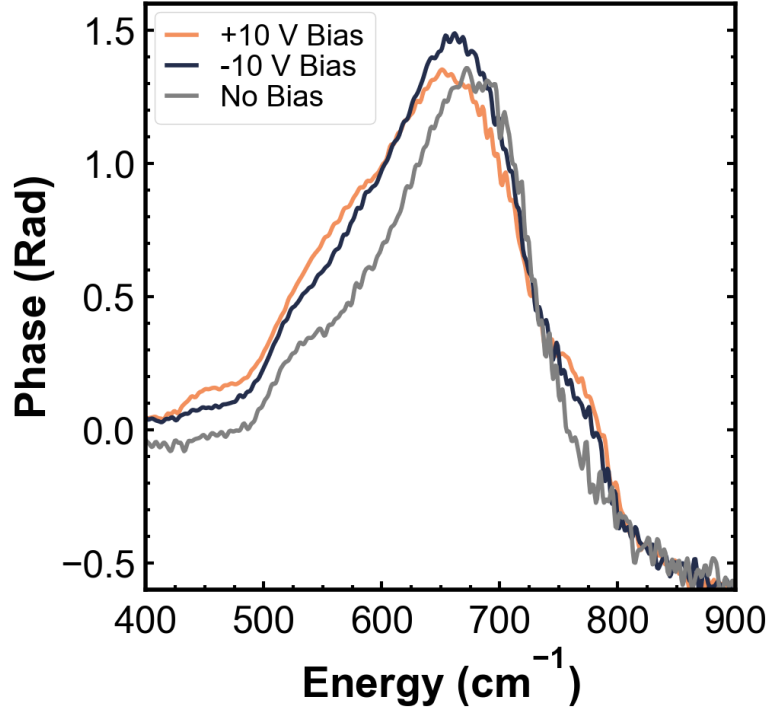


Figure 8.5: Nano-FTIR phase spectra of HZO films that underwent bias via PFM in an inert atmosphere. An increase in the feature at 750 cm^{-1} indicates that more polar orthorhombic phase is forming.

8.4.3. Measurement of Stress

The biaxial stress state of HZO capacitors cycled to varying degrees was quantified using a $\sin^2(\psi)$ analysis of area detector XRD measurements. The changes in d -spacing of the orthorhombic/tetragonal (t+o) diffraction peak as a function of ψ angle were used to quantify the stress state of the HZO capacitors. The changes in d -spacing of the t+o diffraction peak as a function of ψ angle were used to quantify the HZO stress states through fitting to Equation 8.1 and Equation 2:¹⁶²

$$\varepsilon_{\psi} = \frac{1+\nu}{E} \sigma_{\parallel} \sin^2(\psi) - \frac{2\nu}{E} \sigma_{\parallel}, \quad (8.1)$$

$$\varepsilon_{\psi} = \frac{d_{\psi} - d_0}{d_0}, \quad (8.2)$$

where d_{ψ} is the d -spacing at each ψ angle, ν is Poisson's ratio, E is the elastic modulus, and σ_{\parallel} is the biaxial stress. Through an assumption of a randomly oriented polycrystalline film, the strain-free d -spacing (d_0) was calculated at a ψ angle (ψ^*) at which Equation 8.3 was fulfilled:¹⁶²

$$\sin(\psi^*) = \sqrt{\frac{2\nu}{1+\nu}}, \quad (8.3)$$

A value of $0.29^{257-259}$ was assumed for ν and a modulus value of $209 \pm 6 \text{ GPa}^{260}$ was used. Shown in **Figure 8.6(a-h)** are the changes in d -spacings and normalized integrated areas of the t+o diffraction peaks as a function of ψ angle for the HZO capacitors field cycled with 0 to 10^6 waves. The positive linear slope present in data from each sample is an indication that the HZO films are all under tensile biaxial stress following processing.

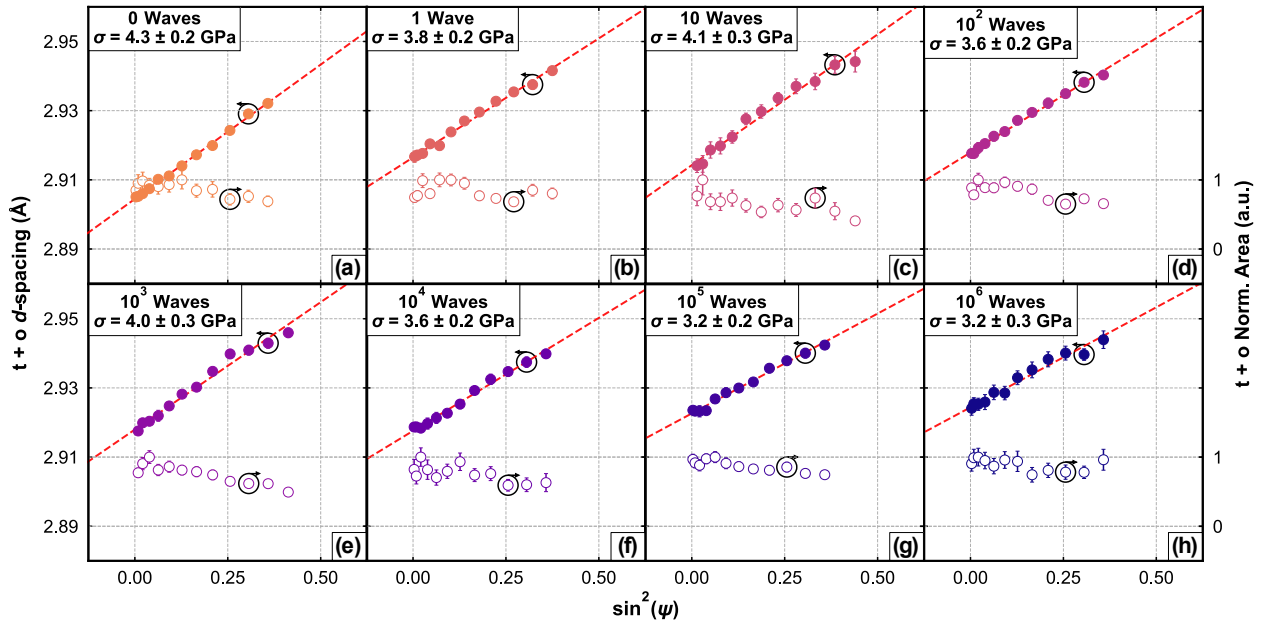


Figure 8.6: t+o d -spacing (filled in points, left axis) and normalized t+o intensity (open points, right axis) dependence on ψ angle and associated linear fit (red lines) used to calculate the post-processing biaxial stress states for the capacitors cycled with (a) 0, (b) 1, (c) 10, (d) 10^2 , (e) 10^3 , (f) 10^4 , (g) 10^5 , and (h) 10^6 square waves.

The resulting biaxial stress as a function of field cycling is shown in **Figure 8.7**. The biaxial stress decreases from 4.3 ± 0.2 in the pristine state to 3.2 ± 0.3 GPa following field cycling with 10^6 square waves, representing a decrease of 26%.

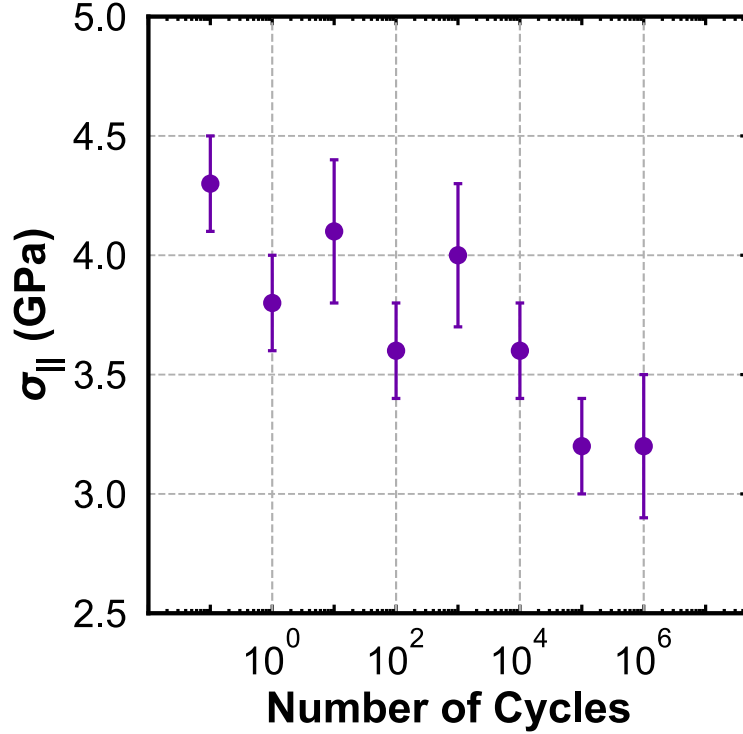


Figure 8.7. Biaxial stress of individual HZO capacitors cycled between pristine to 10^6 cycles.

8.4.4. Mechanisms Responsible for Stress Reduction After Wake-Up

Two possible mechanisms, or a combination thereof, may be responsible for this decrease in biaxial stress. One possible mechanism is a phase transformation from the tetragonal or antipolar orthorhombic phase to the polar orthorhombic phase, which would be accompanied by a volume change and would result in a reduction in the biaxial stress. The unit cell volumes of the tetragonal, antipolar orthorhombic, and polar orthorhombic phases are 33.8, 33.1, and 33.9 Å³, respectively. In order to assess the magnitude of stress reduction that could result from a phase transformation, Equation 8.4,

$$\Delta\sigma = -\left(\frac{1}{3}\right)\left(\frac{\Delta V}{V}\right)\left(\frac{E}{1-\nu}\right), \quad (8.4)$$

is used. ΔV represents the difference in the unit cell volume between the tetragonal or antipolar orthorhombic phase and the polar orthorhombic phase, E is the elastic modulus, and ν is Poisson's ratio. Values of 209 ± 6 GPa²⁶⁰ and $0.29^{257-259}$ were used for E and ν , respectively. A complete transformation from the tetragonal to polar orthorhombic phase is accompanied by a reduction of 0.29 GPa of biaxial stress, as shown below.

$$\Delta\sigma = -\left(\frac{1}{3}\right)\left(\frac{0.1}{33.9}\right)\left(\frac{209}{1-0.29}\right) = 0.29 \text{ GPa}$$

A transformation from the antipolar orthorhombic phase to the polar orthorhombic phase would have a larger reduction in biaxial stress of 2.3 GPa, as shown.

$$\Delta\sigma = -\left(\frac{1}{3}\right)\left(\frac{0.8}{33.9}\right)\left(\frac{209}{1-0.29}\right) = 2.3 \text{ GPa}$$

These calculations represent a theoretical case in which a complete phase transformation is occurring; however, the films contain a significant fraction of the polar orthorhombic phase before field cycling as evidenced by the large remanent polarization in the pristine state. Therefore, a phase transformation can only account for some fraction of the above calculated values. It is evident the stress reduction from a transformation of the tetragonal to polar orthorhombic phase is both significantly smaller than a transformation of the antipolar to polar orthorhombic phase and significantly smaller than the 1.1 GPa of stress reduction observed after field cycling this film with 10^6 waves. Thus, the magnitude of the stress reduction associated with the transformation from the antipolar to polar orthorhombic phase is more consistent with the observed experimental values. Evidence of a phase transformation occurring is seen in the decrease in the relative permittivity with field cycling and is reinforced by FTIR measurements which show an increase in the polar orthorhombic phase content after wake-up.

Ferroelastic domain switching, in which the polar axis that is initially aligned in-plane switches to lie out-of-plane, can also contribute to the reduction in biaxial stress during wake-up. In the polar orthorhombic $Pca2_1$ phase, the polar axis is the intermediate length b -axis (5.09 Å); if ferroelastic switching is occurring, this short, polar axis, which is initially in-plane, would switch out-of-plane. Simultaneously, the long, non-polar c -axis (5.27 Å) would lay in-plane, relieving biaxial tensile stress in the HZO layer. The decrease in α' , which is indicative of domain wall depinning, may support the contribution of this mechanism to the decrease in biaxial stress with wake-up, as domain wall depinning may indicate that ferroelastic domain switching is taking place. The absolute maximum decrease in stress that could be accommodated by ferroelastic switching throughout the entirety of this material is shown below.

$$\Delta\sigma = \varepsilon E = \frac{0.18 \text{ \AA}}{5.27 \text{ \AA}} (209 \text{ GPa}) = 7.4 \text{ GPa}$$

However, only a fraction of this ferroelastic switching can exist because the films comprise randomly oriented polycrystalline grains, and only a fraction will be in the {001} orientation. The

experimental increase in remanent polarization of $3.8 \mu\text{C}/\text{cm}^2$ is 7.5% of the maximum theoretical remanent polarization of $51 \mu\text{C}/\text{cm}^2$ in this material, which correlates with a reduction of stress of 0.56 GPa from ferroelastic switching. Therefore, ferroelastic switching alone cannot explain the 1.1 GPa of stress reduction observed here. Instead, a phase transformation from the antipolar to polar orthorhombic phase or a combination of a phase transformation and ferroelastic switching are responsible.

These results provide insight into the interplay between the wake-up effect and mechanical stress and may help explain recent observations of improved polarization response in HfO_2 -based thin films subjected to an *ex situ* compressive strain. When Kriv *et al.*²⁶¹ applied an in-plane compressive strain to Si-doped HfO_2 films, an increase in the remanent polarization during wake-up was observed. Together with the results presented here, these data suggest that the application of compressive stress aids in lowering the barrier required for the phase transformation from the antipolar orthorhombic phase to the polar orthorhombic phase, which relieves biaxial tensile stress. While some groups claim that ferroelastic switching alone is responsible for wake-up,⁹¹ the results shown here demonstrate that this cannot be the case – if ferroelastic switching is occurring, it is in addition to a phase transformation.

8.5. Conclusions

The biaxial stress state in individual HZO capacitors as wake-up proceeds has been quantified. The biaxial stress decreases from 4.3 ± 0.2 in the pristine state to 3.2 ± 0.3 GPa following field cycling with 10^6 square waves. The decrease in stress coincides with a decrease in relative permittivity, suggesting that a phase transformation has occurred. The FTIR measurements confirm that there is an increase in the polar orthorhombic phase after wake-up. Based on the magnitude of the stress reduction, a transformation from the antipolar to polar orthorhombic phase is more likely than a transformation from the tetragonal to polar orthorhombic phase, which is additionally consistent with the FTIR data. The possibility of ferroelastic domain switching contributing to biaxial stress reduction is currently being investigated, but calculations considering the magnitude of polarization increase with wake-up and the required degree of ferroelastic switching suggest that it cannot account for the full stress reduction. Therefore, this work shows that phase transformations do occur during wake-up and result, in-part, to a reduction in the biaxial

stress in the device. Together, these results are necessary for understanding and controlling the wake-up effect in devices utilizing ferroelectric HZO thin films.

8.6. Experimental Methods

8.6.1. Sample Preparation

TaN/HZO/TaN metal-ferroelectric-metal devices were prepared on (001)-oriented silicon substrates. The 100 nm-thick planar TaN bottom electrodes were deposited via DC sputtering from a sintered TaN target with a power density of 3.3 W/cm^2 under an argon background pressure of 5 mTorr in a 45° off-axis geometry. 20 nm-thick HZO was next deposited using plasma-enhanced ALD within an Oxford FlexAL II system at a temperature of 260°C with tetrakis(ethylmethyamido)hafnium (TEMA Hf) and tetrakis(ethylmethyamido)zirconium (TEMA Zr) as HfO_2 and ZrO_2 precursors, respectively, and an oxygen plasma as the oxidant. Supercycles comprising 6 cycles of HfO_2 and 4 cycles of ZrO_2 were utilized for deposition, resulting in a nominal film composition of $\text{Hf}_{0.5}\text{Zr}_{0.5}\text{O}_2$. Next, a planar 20 nm-thick TaN top electrode was deposited using the same conditions as the bottom electrode. The sample was then rapid thermal annealed at 600°C using an Allwin21 AccuThermo 610 Rapid Thermal Processor for 30 seconds in a N_2 atmosphere. After annealing, 50 nm-thick circular platinum contacts of varying diameters were DC sputtered through a shadow mask. Then, the sample underwent an SC-1 etch (5:1:1 H_2O :30% H_2O_2 in H_2O :30% NH_4OH in H_2O) for 45 minutes at 60°C to remove the blanket top TaN layer, leaving discrete TaN/HZO/TaN/Pd devices. The sample prepared for FTIR measurements received 5 nm top TaN and Pt electrodes, and was subjected to an SC-1 bath for 10 minutes under the same conditions described above.

8.6.2. AFM Tomography

$5 \times 5 \mu\text{m}$ regions on the cycled electrodes of the sample prepared for FTIR were thinned by tomographic AFM as described by Song *et al.*¹⁷⁴ An Asylum Research Cypher AFM with a conductive diamond-coated tip (Nanosensors CDT-NCHR, 80 N/m stiffness) in contact mode with a setpoint of 0.1 or 0.2 V was used with a scan rate of 0.8 Hz to remove electrode material.

8.6.3. Electrical Characterization

Electrical measurements were performed on 100 μm diameter contacts. Polarization-electric field ($P(E)$) and positive up negative down (PUND) measurements were made using a Radiant Technologies Precision LC II Tester. $P(E)$ measurements were made with maximum applied field of 2.5 MV/cm and a period of 1 ms. PUND measurements were performed with maximum applied field of 2.5 MV/cm, a 1 ms pulse width, and a 1000 ms pulse delay. The relative permittivity, which contains both the intrinsic permittivity of the lattice and the extrinsic reversible domain wall contributions of the samples, were extracted from dielectric nonlinearity measurements conducted using a Keysight E4980A LCR meter with a frequency of 10 kHz and oscillator levels ranging from 0.002 to 0.100 V, root mean square. Films were field cycled between pristine and 10^6 cycles using 10 kHz, 2.0 MV/cm square waves.

8.6.4. FTIR

Near-field FTIR measurements were performed at the Advanced Light Source (Beamline 2.4) using a tip-based scattering approach (Neaspec). 48 averages were collected with a 2 cm^{-1} resolution at each point. A reference background was collected using e-beam evaporated gold with 96 averages and a 2 cm^{-1} resolution.

8.6.5. Stress Measurement

To evaluate stress in the HZO films, area detector X-ray diffraction patterns were collected using a Bruker D8 Venture diffractometer equipped with an Incoatec $\text{I}\mu\text{S}$ 3.0 Cu $\text{K}\alpha$ radiation source, an ω incident angle fixed at 18° , and a Photon III detector at a distance of 70 mm. MgO powder on the film surface was used for height alignment. The pyFAI integration package²⁶² was employed for area detector pattern unwarping, and LIPRAS²⁶³ peak fitting software was utilized to fit Pearson VII shapes to area detector line intensity profiles.

8.7. Acknowledgements

Thin film synthesis, electrical characterization, X-ray diffraction, and Nano-FTIR were supported by the Center for 3D Ferroelectric Microelectronics (3DFeM), an Energy Frontier Research Center funded by the U.S. Department of Energy, Office of Science, Basic Energy

Sciences under Award No. DE-SC0021118. S.T.J. acknowledges support from the U.S. National Science Foundation's Graduate Research Fellowship Program under grant DGE-1842490. This research used resources of the Advanced Light Source, which is a DOE Office of Science User Facility under contract no. DE-AC02-05CH11231. The authors acknowledge beamline scientists Hans Bechtel and Stephanie Gilbert Corder for their technical assistance in nano-FTIR measurements. This work utilized a Bruker D8 Venture instrument, which was acquired under Award CHE-2018870 from the U.S. National Science Foundation's Major Research Instrumentation program.

Chapter 9: Effects of Heavy Ion Irradiation on HfO₂-Based Films

9.1. Motivation

In the previous chapters, some of the factors shown to affect the stability of the ferroelectric phase in HfO₂-based thin films have been addressed. These include oxygen content, grain size, and biaxial stress. In Chapter 7, it was shown that the HiPIMS pulse width, which is tied to the ionization of the sputtered species, affects the phases that are formed after rapid thermal annealing HfO₂ thin films. This observation pointed to a change in the structure of the amorphous phase driving an alteration in the nucleation behavior and a new means of controlling crystalline phase formation. However, there are difficulties associated with reactive sputtering of HfO₂ from a metal target that result in process instabilities and, ultimately, issues with reproducibility. ALD is a reliable technique for the deposition of this material. While control of the energy and ionization of the depositing species in ALD is challenging, other methods that alter the amorphous structure and enable control of nucleation should be explored in order to produce phase-pure ferroelectric HfO₂ thin films. In this chapter, the effects of heavy ion irradiation with 2.8 MeV Au²⁺ ions on amorphous HfO₂ and HZO thin films will be evaluated.

9.2. Introduction

Atomic layer deposition (ALD) is the most commonly used deposition method for the preparation of ferroelectric hafnium oxide (HfO₂)-based thin films. It provides atomic-scale control of thickness due to the layer-by-layer growth process and is used for the synthesis of amorphous HfO₂ high- κ gate dielectrics in semiconductor fabrication facilities. However, HfO₂-based thin films grown by ALD are typically amorphous as-deposited and must be annealed to form the crystalline phase. This annealing process results in films with a wide range of grain sizes since nucleation and growth are stochastic processes. Because grain size is, in part, tied to phase stability in this material,³⁴ ALD-deposited films are often multiphase. For optimal device performance, single-phase films consisting only of the ferroelectric phase are desired. Thus, a method to control nucleation of the phases present in HfO₂-based thin films deposited by ALD could assist in the stabilization of a single phase. Ion irradiation is one such method.

Ion irradiation has been studied for applications in microelectronics processing for over 40 years, and, for example, the effects of irradiation in amorphous silicon have been widely explored. Spinella *et al.* demonstrated that irradiation conditions can have a significant impact on the crystallization kinetics in amorphous silicon.²⁶⁴ Increasing the dose rates of Kr⁺ and Ar⁺ ions resulted in a decrease in the nucleation rate. While the lighter Ar⁺ ions led to higher nucleation rates than the heavier Kr⁺ ions, the Kr⁺ ions led to higher crystalline growth rates. The authors, along with others,^{265,266} asserted that ion-induced defects result in an increase in the free energy of the amorphous phase, thereby lowering the nucleation barrier. These results suggest that ion irradiation can be harnessed to impact nucleation and growth in thin films of other materials.

A limited number of studies have examined the effects of irradiation of amorphous HfO₂ and ZrO₂ thin films. Irradiation of amorphous zirconium oxide (ZrO₂) thin films with 2×10¹⁴ ions/cm² doses of 1 MeV Kr⁺ and 5×10¹⁵ ions/cm² doses of 350 keV O⁻ ions has been shown to crystallize the films into the tetragonal phase.^{267,268} HfO₂ films irradiated with 100 MeV Ag ions resulted in the crystallization into the monoclinic phase,²⁶⁹ while 6.3 MeV ⁵⁶Fe ions up to a fluence of 2×10¹⁴ ions/cm² resulted in the cubic or tetragonal phase, according to X-ray diffraction.²⁷⁰ From these studies, it is evident that ion irradiation can induce crystallization of thin films. As only a limited number of irradiation conditions have been studied in HfO₂ and ZrO₂ thin films; other ion conditions should be explored as a new means to nucleate the desired phase in HfO₂-based thin films.

In this work, the effects of the irradiation of amorphous 20 nm thick HfO₂ and hafnium zirconium oxide (HZO) films by 2.8 MeV Au²⁺ ions with fluences ranging from 1×10¹³ ions/cm² to 1×10¹⁵ ions/cm² are studied. This energy was chosen so that the Au ions penetrate the dielectric layer and stop in the bottom electrode or Si substrate. In addition to measuring the electrical properties of the HZO film after irradiation, differences in phase compositions are examined by X-ray diffraction (XRD) and Fourier transform infrared (FTIR) spectroscopy measurements. While early XRD measurements suggested that the films were amorphous after ion irradiation, it was later determined that they crystallized under all irradiation conditions. Thus, irradiated films before and after annealing will be compared.

9.3. Experimental Methods

9.3.1. Sample Preparation

20 nm thick HfO₂ and HZO films were deposited on 100 nm thick TaN bottom electrodes. The planar TaN bottom electrodes were deposited via DC sputtering from a sintered TaN target with a power density of 3.3 W/cm² under an argon background pressure of 5 mTorr in a 45° off-axis geometry. 20 nm-thick HfO₂ and HZO films were next deposited using plasma-enhanced ALD within an Oxford FlexAL II system at a temperature of 260 °C with tetrakis(ethylmethyamido)hafnium (TEMA Hf) and tetrakis(ethylmethyamido)zirconium (TEMA Zr) as HfO₂ and ZrO₂ precursors, respectively, and an oxygen plasma as the oxidant. For HZO films, supercycles comprising 5 cycles of HfO₂ and 5 cycles of ZrO₂ were utilized for deposition, resulting in a nominal film composition of Hf_{0.4}Zr_{0.6}O₂. After irradiation, some samples were rapid thermal annealed at 600 °C using an Allwin21 AccuThermo 610 Rapid Thermal Processor for 30 seconds in a N₂ atmosphere. After annealing, 20 nm of TaN and 50 nm of Pd were DC sputtered through a shadow mask to define individual capacitors for electrical measurements.

9.3.2. Irradiation Conditions

The samples underwent 2.8 MeV Au²⁺ ion irradiation with doses ranging from 1×10¹³ to 1×10¹⁵ ions/cm² and a flux of 9×10¹¹ ions/cm²/s at the Ion Beam Laboratory (IBL) in the Center for Integrated Nano Technologies (CINT) at Sandia National Laboratories. Stopping and Range of Ions in Matter (SRIM) simulations²⁷¹ were performed to evaluate the ion ranges and collision events for these irradiation conditions in HZO and HfO₂, shown in **Figure 9.1**. For both HZO and HfO₂, the end of range is primarily within the Si layer.

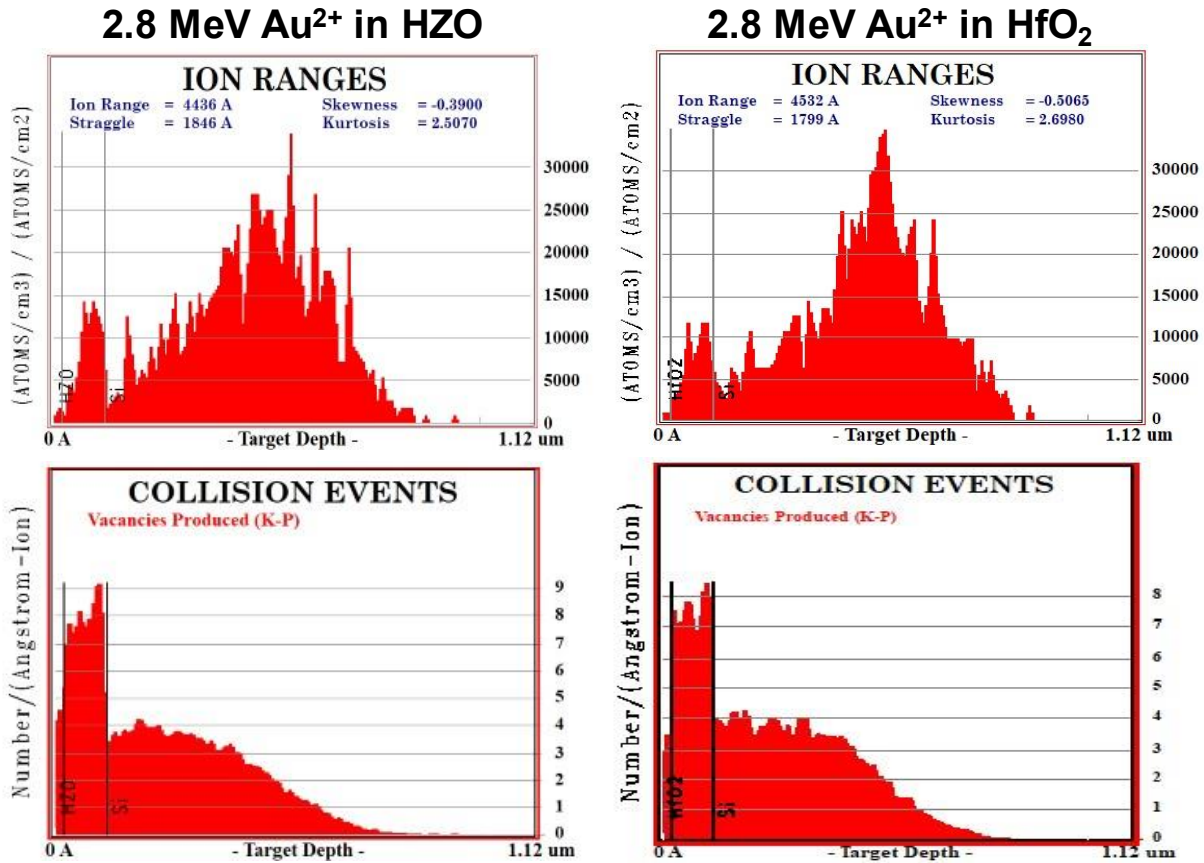


Figure 9.1: Simulation of ion ranges and collision events for 2.8 MeV Au²⁺ in HZO and HfO₂.

9.3.3. Electrical Characterization

Electrical measurements were performed on 100 μm diameter contacts. Polarization-electric field ($P(E)$) measurements were made using a Radiant Technologies Precision LC II Tester with a maximum applied field of 2.5 MV/cm and a period of 1 ms. Electric field cycling was performed with 5000 2.5 MV/cm square waves at a frequency of 1000 Hz. A Keysight E4980A Precision LCR Meter was used for C-V measurements which utilized a 50 mV, 10 kHz oscillator.

9.3.4. FTIR

Near-field FTIR measurements were performed at the Advanced Light Source (Beam Line 2.4) using a tip-based scattering approach (Neaspec). 48 averages were collected with a 2 cm⁻¹ resolution in each point. A reference background was collected using e-beam evaporated gold with 96 averages and a 2 cm⁻¹ resolution.

9.3.5. X-ray Diffraction Measurements

Area detector X-ray diffraction patterns were collected using a Bruker D8 Venture diffractometer equipped with an Incoatec I μ S 3.0 Cu K α radiation source, an ω incident angle fixed at 18°, and a Photon III detector at a distance of 70 mm. MgO powder on the film surface was used for height alignment. The pyFAI integration package²⁶² was employed for area detector pattern unwarping.

9.4. Results and Discussion

9.4.1. X-ray Diffraction

The 20 nm thick HfO₂ and HZO films deposited by ALD underwent 2.8 MeV Au²⁺ ion irradiation. XRD is a widely used tool to examine the phases present in HfO₂-based thin films. Although grazing-incidence XRD (GIXRD), which is optimized for thin films, is typically used, the size of the irradiation area prevented the use of GIXRD in this case. Instead, an instrument with a small spot size was used to target the small irradiation area. Initial XRD measurements suggested that the films were amorphous; however, later measurements on a new instrument with improved intensity revealed that the films had crystallized in the irradiation process. Because it was initially believed that the films had not crystallized, following irradiation, some of the films were rapid thermal annealed at 600 °C in N₂ for 30 seconds. Identical samples that did not receive an ion dose were annealed under these conditions. XRD patterns for the (a) HZO and (b) HfO₂ samples that were annealed are shown in **Figure 9.2**. The HZO film that was not irradiated contains peaks that are indexed as the monoclinic and orthorhombic/tetragonal phases. However, the irradiated films contain a much smaller fraction of the monoclinic phase in comparison, with the film that underwent the highest ion dose having the lowest monoclinic phase fraction. The non-irradiated HfO₂ film consists entirely of the monoclinic phase. After irradiation with 1 \times 10¹⁴ ions/cm², a small orthorhombic/tetragonal peak begins to form. Finally, after irradiation with 1 \times 10¹⁵ ions/cm², an intense orthorhombic/tetragonal peak is present. The significant differences in phase composition with increasing ion dose for both HZO and HfO₂ films demonstrate that ion irradiation has the ability to modify the phases that form in these materials.

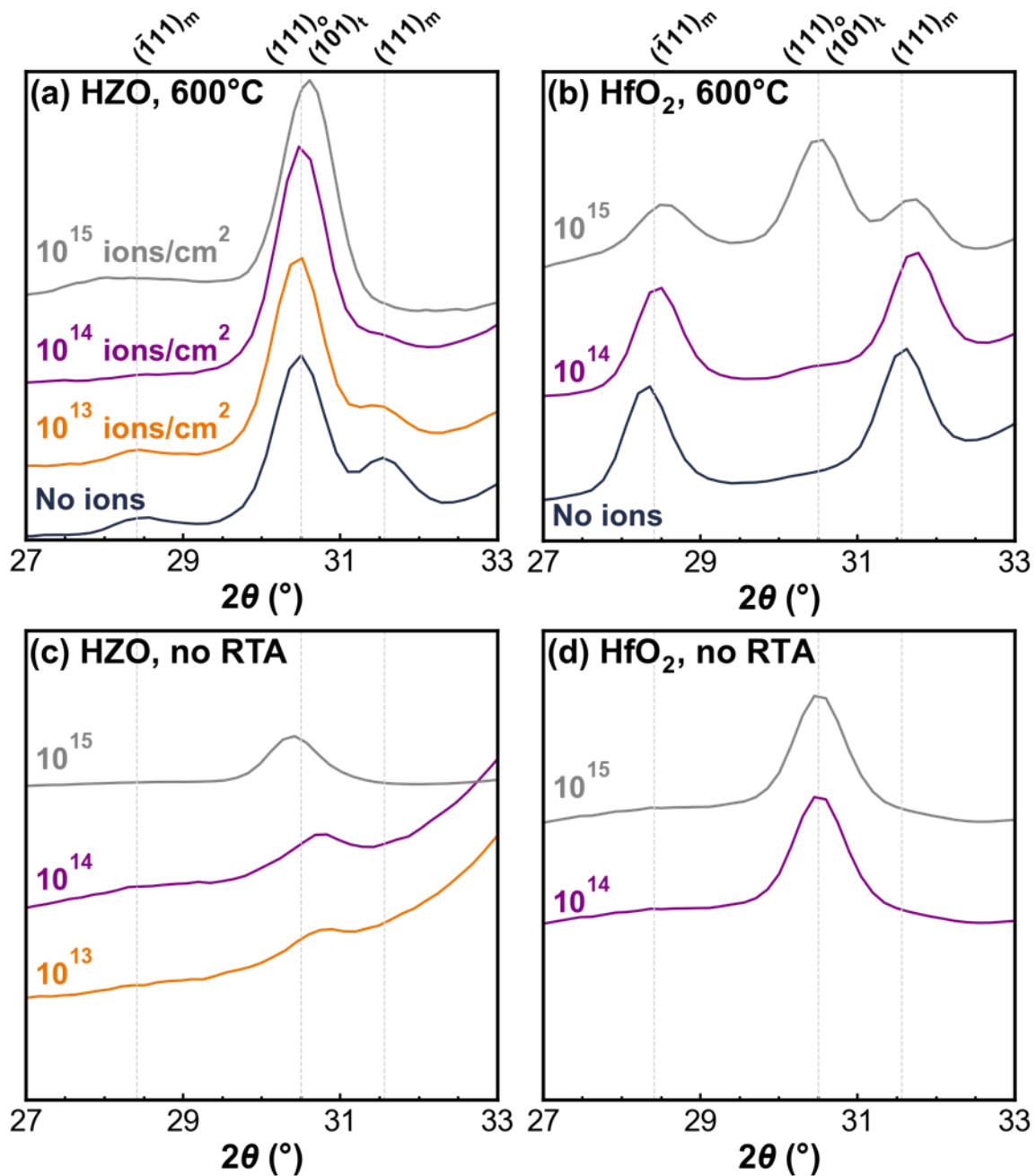


Figure 9.2: XRD patterns of 20 nm thick (a) HZO and (b) HfO₂ films that underwent varying doses of 2.8 MeV Au²⁺ irradiation, followed by a rapid thermal anneal at 600 °C.

XRD patterns for (c) HZO and (d) HfO₂ films that underwent irradiation but were not annealed are also shown in Figure 9.2. For all irradiation conditions, the unannealed HZO has a single peak. A significant shift in the peak position to a lower 2θ angle is observed after irradiation with 1×10^{15} ions/cm², in comparison to those that were irradiated with 1×10^{13} ions/cm² and

1×10^{14} ions/cm². Although it is difficult to differentiate between the tetragonal, polar orthorhombic, and antipolar orthorhombic phases using XRD measurements alone, this peak shift could signify that there is a difference in the phases present between these films. A significant difference in the phase compositions is observed between the HfO₂ films that were irradiated and not annealed, and those that were annealed. The annealed films have monoclinic peaks present for all irradiation conditions. In contrary, the un-annealed films irradiated with 1×10^{14} ions/cm² and 1×10^{15} ions have no monoclinic peaks, indicating that they contain either of the orthorhombic phases, the tetragonal phase, or a mixture thereof. Comparing the HfO₂ films before and after annealing, it is evident that the RTA process is inducing a phase transformation from the orthorhombic/tetragonal phase to the monoclinic phase. It is important to note that peak intensities cannot be compared here because MgO powder on the sample surface was used for height alignment. Differences in the amount of powder can attenuate the film signal, leading to different intensities.

While it is not possible to differentiate between the tetragonal, polar orthorhombic, and tetragonal phases, it is evident that these ion irradiation conditions have impacted the nucleation behavior and the phases that crystallize in this material.

9.4.2. Electrical Measurements

Electrical measurements were performed on HZO films to further characterize the majority phases in the films since each phase possesses a unique polarization and dielectric response. Yield issues prevented electrical measurements of the HfO₂ films. Ferroelectric behavior has been linked to the polar orthorhombic phase. The antipolar orthorhombic phase exhibits an antiferroelectric response. The tetragonal phase is considered a field-induced ferroelectric, meaning that its centrosymmetry can be broken by applying an electric field.¹⁹⁹ Finally, the monoclinic phase displays linear dielectric behavior.

Figure 9.3 shows the polarization responses for annealed HZO films that received no ion dose and 1×10^{15} ions/cm². The response for the film that received no ion dose is pinched in the pristine state (Fig. 9.3(a)), and opens to have a hysteresis loop that is characteristic of ferroelectricity after field cycling with 5000 2.5 MV/cm square waves to wake-up it up (Fig. 9.3(b)). The remanent polarization is low but within the range that is expected for a film annealed without a top electrode that has a significant fraction of the monoclinic phase.¹⁹³ The irradiated

film is also pinched in the pristine state Fig. 9.3(c). While the hysteresis loop does open up after wake-up, it still remains quite pinched in comparison to the film that was not irradiated. This pinched hysteresis response is consistent with antiferroelectric or field-induced ferroelectric behavior. Additionally, more leakage current contributions are evident after field cycling this film in comparison to the film that was not irradiated.

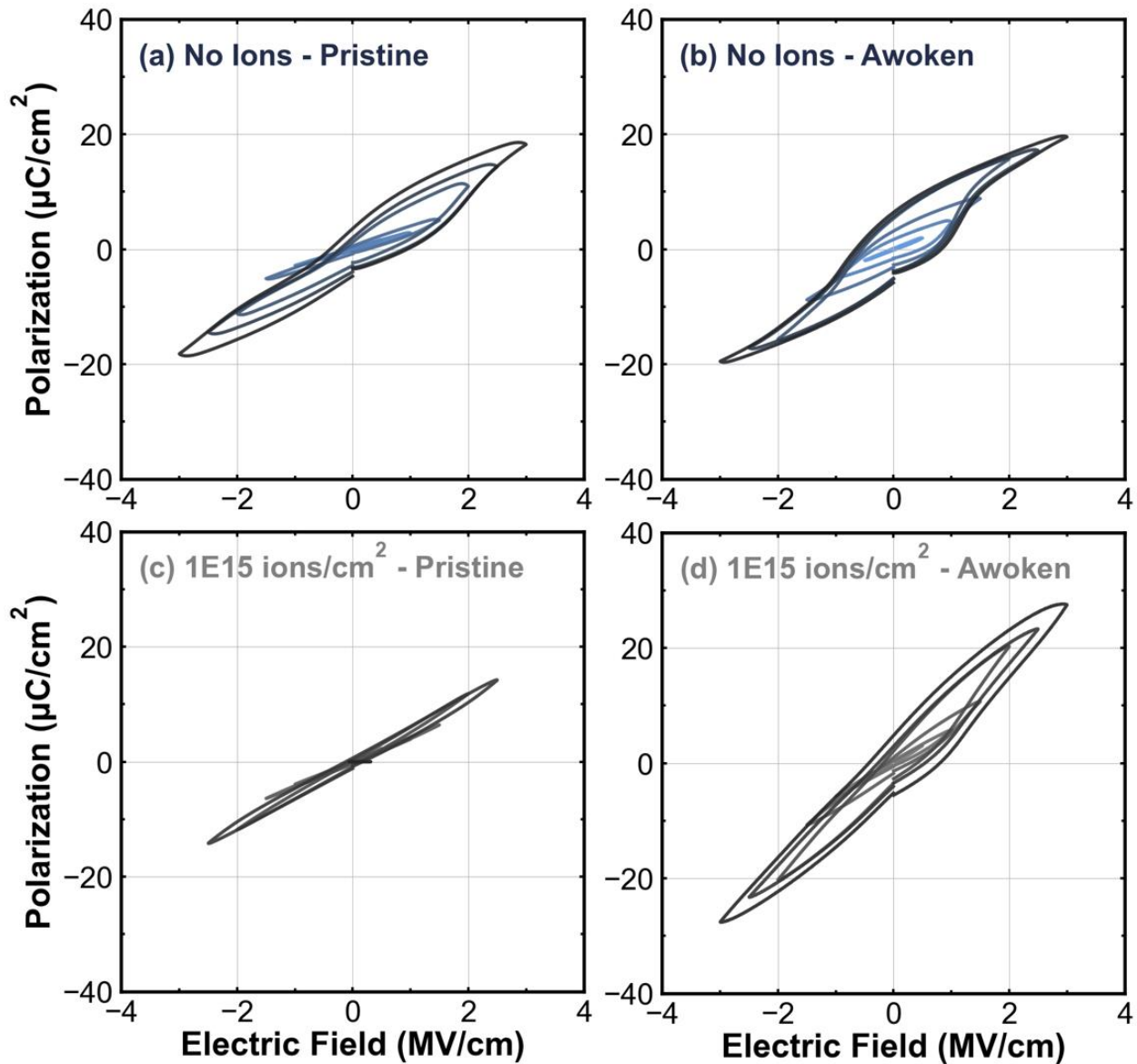


Figure 9.3: Nested polarization hysteresis measurements for HZO films that were not irradiated (a) before field cycling and (b) after field cycling with 5000 2.5 MV/cm square waves, and those irradiated with 10^{15} ions/cm² (a) before field cycling and (b) after field cycling. Both films were rapid thermal annealed.

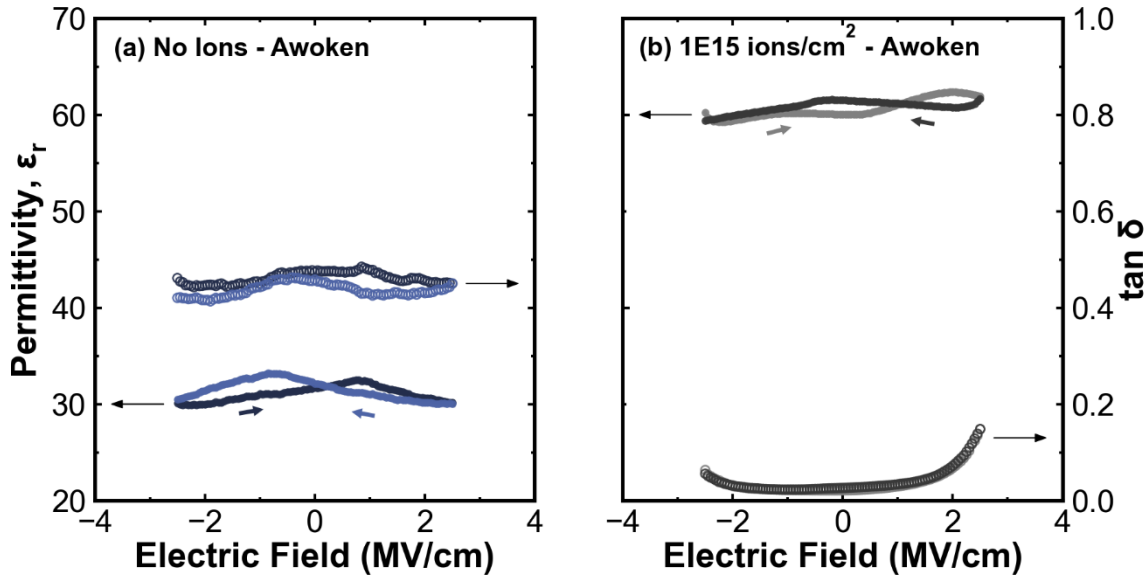


Figure 9.4: Relative permittivity (left axis) and loss tangent (right axis) versus electric field after field cycling with 5000 2.5 MV/cm square waves for HZO films that received (a) no ion dose, and (b) 10^{15} ions/cm² (both RTA at 600 °C).

Next, capacitance-voltage (C-V) measurements were made on the field-cycled HZO films that received (a) no ion dose and (b) 10^{15} ions/cm², as shown in **Figure 9.4**. There is a significant difference in the C-V response and relative permittivity measured for each sample. The C-V response of the film with no ion dose exhibits a butterfly shape and two peaks characteristic of a ferroelectric material, while the irradiated film has a different shape with an extra peak. Additionally, the film that received no ion dose has a relative permittivity of approximately 30, while the irradiated film has a permittivity of around 60. The monoclinic phase is reported to have the lowest relative permittivity, ranging from 16 – 20, while the polar orthorhombic phase has a permittivity in the 27 – 35 range. The tetragonal phase has the highest relative permittivity, with values reported as high as 70.¹⁷⁹ The relative permittivity of the antipolar orthorhombic phase is currently unknown, although it is hypothesized that it is similar to the polar orthorhombic phase due to similarities in bonding. From the XRD measurements shown in Figure 9.2, it was shown that the non-irradiated film contained the monoclinic phase in addition to the orthorhombic/tetragonal phases, while the film that received a 10^{15} ions/cm² dose had no monoclinic phase present. The high permittivity combined with the pinched hysteresis curve suggests that this film could contain some fraction of the tetragonal phase.

9.4.3. FTIR

To further examine the phases in these films, synchrotron tip-enhanced Fourier transform infrared spectroscopy (nano-FTIR) measurements were made on the HZO films with and without irradiation, and before and after annealing. Limitations in access to nano-FTIR prevented the measurement of HfO₂ films. It should be noted that the spectral features of these HZO films may have shifted in comparison to those shown in Chapter 6 because of the presence of Zr in these films. **Figure 9.5** shows the phase-signal spectra for (a) various irradiation conditions, stacked, and (b) the annealed films, layered, to show the differences in their IR features. In **Fig. 9.5(a)**, the film that received no ion dose and no RTA has one broad feature. After receiving 1×10^{15} ions/cm², features at 550 cm⁻¹ and 700 cm⁻¹ are present, indicating that the films have crystallized. The lack of a feature on the high wavenumber side of the 700 cm⁻¹ peak, which was shown to be present for HfO₂ films containing a significant fraction of the polar orthorhombic phase in Chapter 6, suggests that this film contains a significant fraction of the antipolar phase.

In **Fig. 9.5(b)**, a narrowing of the feature around 700 cm⁻¹ as the ion dose is increased is indicative of a transition from the monoclinic phase to either of the orthorhombic phases. Based on the high permittivity of the film that was irradiated with a 1×10^{15} ions/cm² dose, it was hypothesized that this film contained a significant fraction of the tetragonal phase. However, according to Fan *et al.*, the tetragonal phase should have no IR signature between 450 and 850 cm⁻¹. Therefore, the intensity of the IR signal of this film in this region suggests that the tetragonal phase is not the dominating phase. Rather, the polar or antipolar orthorhombic phases are dominating.

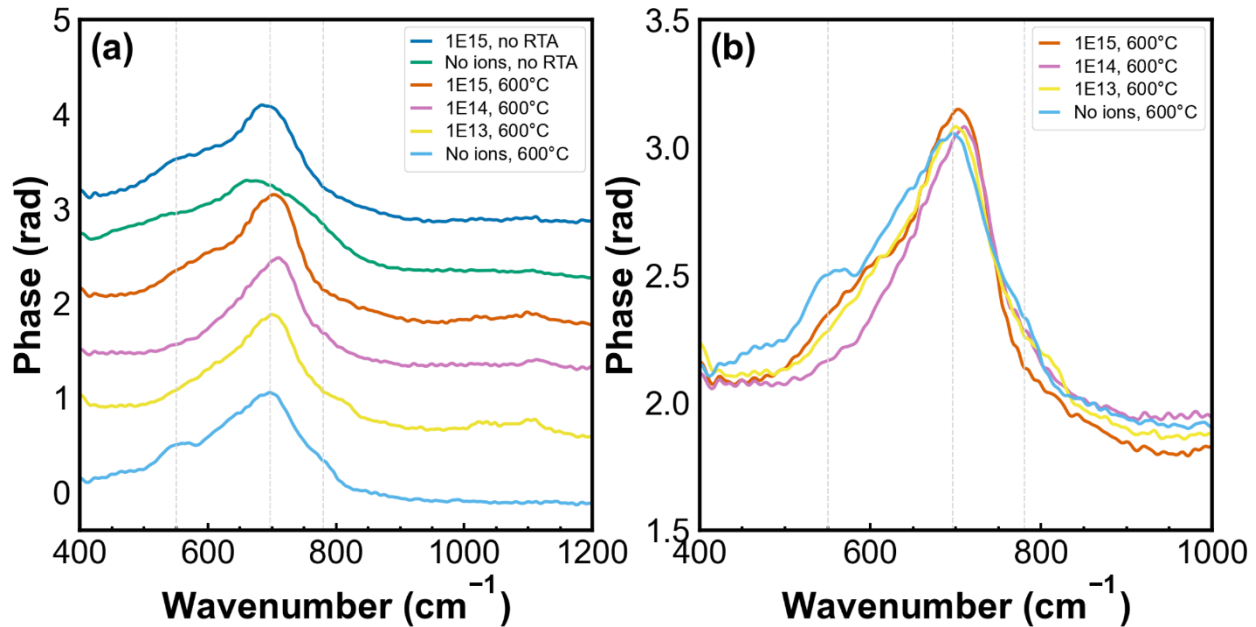


Figure 9.5: IR phase-signal spectra for (a) various irradiation conditions, stacked, and (b) the annealed films, layered, to show the differences in their IR features.

9.5. Discussion

Both XRD and FTIR measurements indicate that 2.8 MeV Au^{2+} ion irradiation has the ability to impact nucleation and the phases that crystallize in HZO and HfO_2 thin films. When materials are irradiated, two mechanisms can be used to describe how energy is imparted to the material – electronic energy loss and nuclear energy loss. Electronic energy loss involves inelastic collisions between the ions and bound electrons in the material that result in thermal spikes. Nuclear energy loss refers to elastic collisions that result in damage cascades that cause disruptions in bonding and atom displacements in addition to thermal spikes. The mechanism that dominates depends on the energy and mass of the ions, as well as the density and mass of the material being irradiated. Higher energy, lighter ions are typically dominated by electronic energy loss, while lower energy, heavier ions are dominated by nuclear energy loss. In this case, the irradiation conditions explored here should result in a mixture of electronic and nuclear stopping, meaning that thermal spikes will occur in addition to damage cascades. These damage tracks appear to affect the local structure, while thermal spikes lead to crystallization of the films; strategies to better understand the effects of irradiation will be discussed in Chapter 10, Future Work.

Previous irradiation of crystalline HfO₂ films with 1.635 GeV Au ions has also demonstrated an increasing number of oxygen vacancies with increasing ion fluence,²⁷² and phase transformations from the monoclinic to tetragonal phase have been observed.²⁷³ This phase transformation was attributed to the creation of oxygen defects during irradiation. In Chapter 5, the impact of oxygen vacancies on phase formation in HfO₂ films deposited by HiPIMS was discussed. Thus, the differences in phase composition here could be a result of oxygen deficiency induced by irradiation damage. Future work should include measurements of oxygen content by XPS to examine the potential oxygen deficiency of these films.

9.6. Conclusions

It was shown that 2.8 MeV Au²⁺ ion doses as low 1×10^{13} ions/cm² and 1×10^{14} ions/cm² can induce crystallization in HZO and HfO₂ thin films, respectively. This method of crystallization is promising for the integration of ferroelectric HfO₂-based materials into circuits where low temperatures are required. According to XRD and FTIR measurements, the irradiated films have lower monoclinic phase fractions than their non-irradiated counterparts, demonstrating that irradiation has the potential to be used to produce phase-pure ferroelectric HfO₂-based films. In Chapter 10, Future Work, additional experiments to better understand the effects of irradiation in this material are proposed. Likewise, a wider range of ion irradiation conditions should be explored so that crystallization of the desired phase can be achieved.

Chapter 10: Future Work

10.1. Nano-FTIR measurements of $\text{Hf}_{1-x}\text{Zr}_x\text{O}_2$ Thin Films

In addition to the nano-FTIR measurements discussed in Chapters 6, 8, and 9, measurements were performed on a series of films deposited by atomic layer deposition (ALD) that span the composition range from pure HfO_2 to ZrO_2 . Different compositions were obtained by varying the ALD Hf:Zr cycle ratios. The phase spectra are shown in Figure 10.1. The grey dashed lines show the locations of some of the spectral features so that their evolution with composition can be evaluated. Clear differences are observed as the composition of these films changes. The primary features in the pure HfO_2 film are located at 460, 630, and 773 cm^{-1} . In pure ZrO_2 , the primary feature is located at 718 cm^{-1} . As the composition varies between these two end-members, a gradual evolution in spectral features is observed. These spectral differences are related to both compositional differences as well as differences in the phases present in the films.

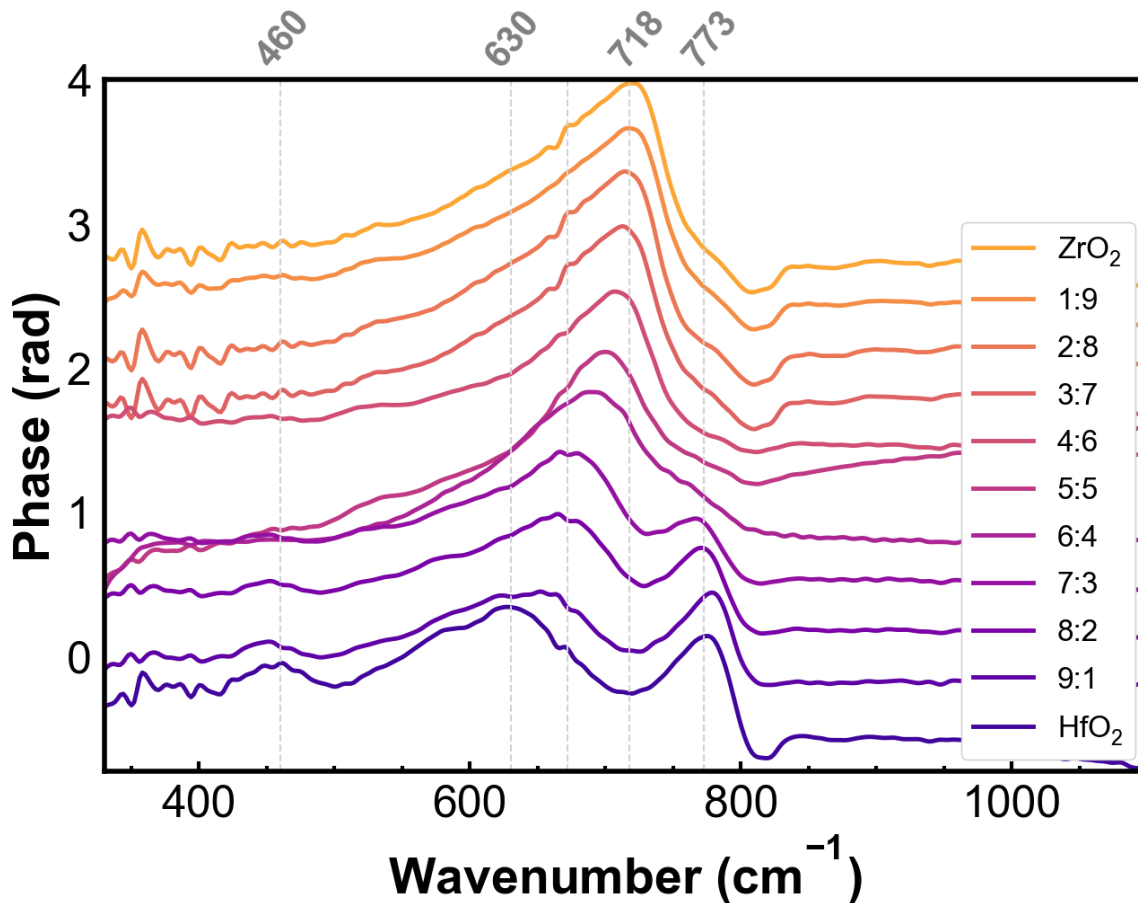


Figure 10.1: Nano-FTIR phase measurements of films with compositions spanning from pure HfO₂ to ZrO₂. The spectra have been offset for clarity. The ratios in the legend represent ALD Hf:Zr cycle ratios.

To evaluate the phases present in these films, grazing-incidence X-ray diffraction (GIXRD) measurements were performed (**Figure 10.2**). As expected, the amount of monoclinic phase decreases as the composition varies from being Hf-rich to Zr-rich. The Zr-rich films only have a single peak that can be indexed as either the polar orthorhombic, antipolar orthorhombic, or tetragonal phase. The phase information provided by GIXRD measurements may help to disentangle the effects of composition and phase on features in vibrational spectra. Further analysis of these data will provide useful information about how to interpret vibrational spectra in doped HfO₂ films. For example, while it is commonly assumed that ZrO₂ forms as a tetragonal phase in films of this thickness, the FTIR spectrum has a peak that is more consistent with an orthorhombic phase, possibly the antipolar phase. The low intensities of the distinct orthorhombic peaks in XRD

preclude the ability to assess structural phase by lab-scale GIXRD and will likely require TEM or synchrotron-based XRD characterization.

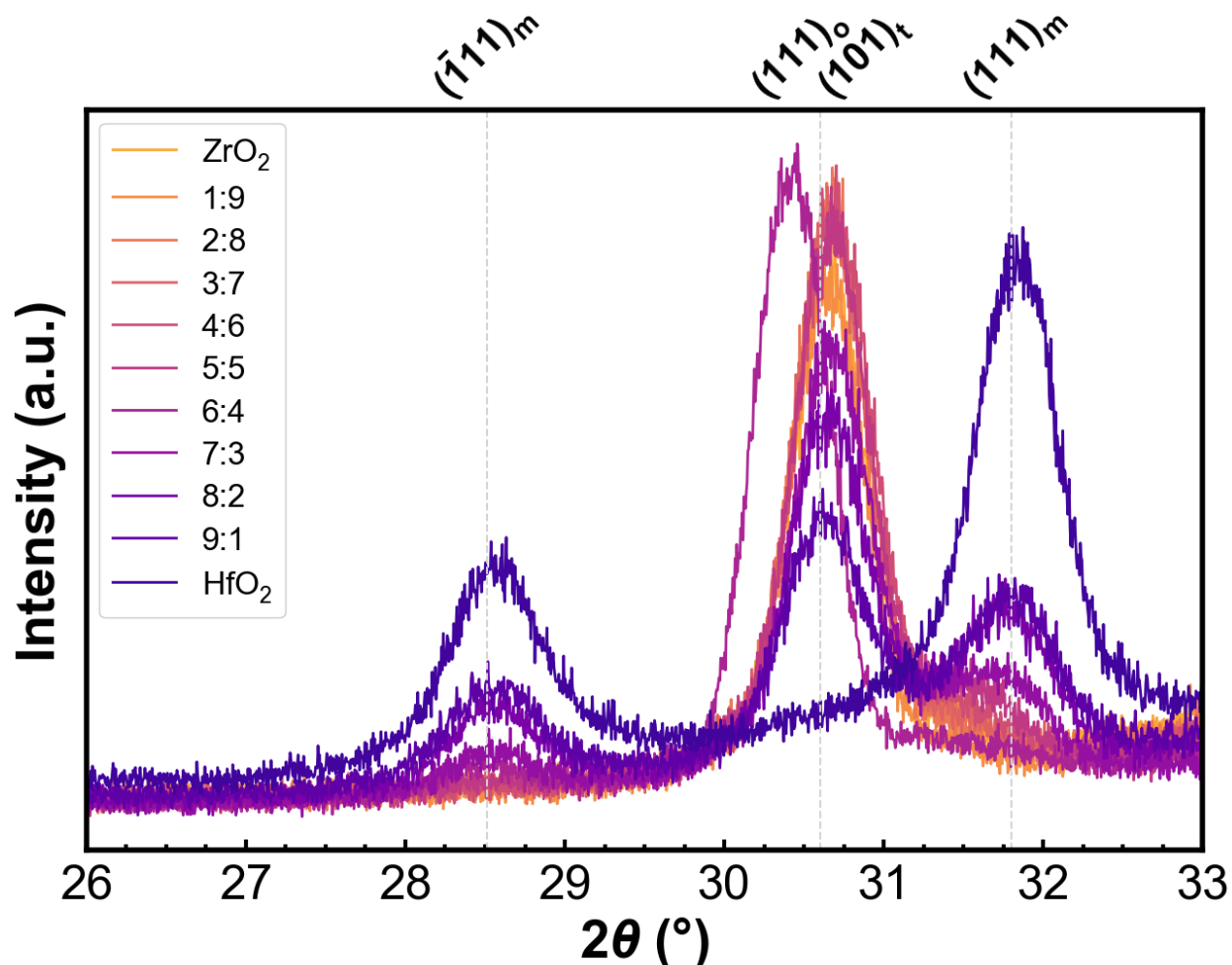


Figure 10.2: Grazing-incidence X-ray diffraction measurements of films with compositions spanning from pure HfO₂ to ZrO₂. The ratios in the legend represent ALD Hf:Zr cycle ratios.

10.2. Ion Irradiation Effects in HfO₂-Based Thin Films

In Chapter 9, 2.8 MeV Au²⁺ ions were used to irradiate HfO₂ and HZO thin films with fluences ranging from 1×10^{13} to 1×10^{15} ions/cm². These irradiation conditions resulted in a mixture of electronic and nuclear stopping, although electronic stopping dominated. X-ray diffraction and nano-FTIR measurements demonstrated that irradiation affected nucleation and the phases that formed, but also crystallized the films. The crystallization likely resulted from thermal spikes induced by electronic stopping.

In future experiments, other ions can be chosen to span the range of electronic to nuclear stopping based on Stopping and Range of Ions in Matter (SRIM) simulations.²⁷¹ *In-situ* TEM can also be performed to identify possible crystal nucleation mechanisms and understand the roles of interfaces and electronic versus nuclear stopping on nucleation and growth. Irradiation conditions that are dominated by nuclear stopping may not result in crystalline films; however, these conditions will still cause damage via atom displacements and disruption of bonding. In this case, characterization of the amorphous state should be performed. Some possible characterization methods include X-ray reflectivity measurements to evaluate how irradiation changes the density of the films. Additionally, X-ray absorption fine structure (XAFS) performed at a synchrotron facility could provide information about local environment such as coordination number and bond length. By correlating the amorphous structure with the phases that form after crystallization, information about how the local structure in the amorphous state affects the nucleation behavior and crystalline state can be obtained. This information can be harnessed to produce phase-pure ferroelectric HfO₂-based thin films.

Conclusions

Ferroelectric HfO₂-based thin films have the potential to significantly impact a wide range of microelectronic applications due to their silicon compatibility and improved scaling in comparison to conventional ferroelectric materials. However, the stability of the ferroelectric phase is an issue that is not yet fully understood, and must be controlled before the material can be integrated in devices. The purpose of this dissertation work was to better understand the factors that affect the stability of the ferroelectric phase in this material. The following is a summary of the work shown here.

Chapter 1 outlined the motivation and outcomes of this dissertation work. Chapter 2 served as an introduction to ferroelectricity, with a focus on ferroelectric HfO₂. Atomic layer deposition (ALD) and high-power impulse magnetron (HiPIMS) were introduced in Chapter 3, and the development of the HiPIMS process for deposition of ferroelectric HfO₂ thin films was detailed. In Chapter 4, various structural, chemical, and electrical characterization techniques that were used throughout this work were described.

Since oxygen vacancies significantly affect the performance of ferroelectric HfO₂-based thin films, the impact of plasma oxygen content during HiPIMS deposition of HfO₂ films was investigated in Chapter 5. It was shown that the oxygen content in the plasma directly related to the oxygen content in the films, and this oxygen content has a strong influence on phase formation and ferroelectric performance. The oxygen vacancy concentration played a larger role in phase stability than grain size at this approximately 20 nm size scale. Neutral oxygen vacancies, which are often overlooked in the literature, were also identified in crystalline HfO₂ films. These results demonstrated that oxygen content could be used to dictate phase nucleation in HfO₂ films.

Next, infrared (IR) spectroscopy was demonstrated as a means by which HfO₂ phases could be unambiguously assessed in Chapter 6. While grazing-incidence X-ray diffraction (GIXRD) is commonly used to distinguish between phases, it has difficulty in differentiating between the ferroelectric orthorhombic phase and other metastable phases. Using three HfO₂ films consisting primarily of the monoclinic, polar orthorhombic, and antipolar orthorhombic phases, respectively, the unique signatures of each phase were identified using synchrotron nano-Fourier transform infrared spectroscopy (nano-FTIR) measurements, and vibrational spectroscopy was demonstrated as a means to characterize phases present in this material.

Ion bombardment was assessed in two ways – during film growth via the HiPIMS pulse width (Chapter 7) and irradiation of HfO₂ and hafnium zirconium oxide (HZO) films with 2.8 MeV Au²⁺ (Chapter 9). The HiPIMS pulse width, which affected the ionization fraction of the depositing species, was shown to alter nucleation behavior and the phases that formed during crystallization. Similarly, heavy ion irradiation was demonstrated to affect nucleation and the phases that formed in films grown by atomic layer deposition (ALD), although this method also resulted in the crystallization of the films.

The ‘wake-up’ effect, in which the remanent polarization increases with electric field cycling, was addressed in Chapter 8 in the context of biaxial stress measurements. The evolution of film stress during wake-up was quantified for the first time, and the magnitudes of biaxial stress reduction provided insight into the mechanisms responsible for wake-up. Further, using nano-FTIR measurements, it was proven that phase transformations contribute to this effect.

Overall, this dissertation describes how processing and field cycling can impact the properties of ferroelectric HfO₂-based thin films. This knowledge can be used to develop engineering strategies to combat phase instabilities in this material so that HfO₂-based thin films can be incorporated into the next generation of microelectronics.

References

- (1) Kell, R. C. Modern Applications of Ferroelectricity. *Br. J. Appl. Phys.* **1963**, *14* (5), 249. <https://doi.org/10.1088/0508-3443/14/5/307>.
- (2) Valasek, J. Piezo-Electric and Allied Phenomena in Rochelle Salt. *Phys. Rev.* **1921**, *17* (4), 475–481. <https://doi.org/10.1103/PhysRev.17.475>.
- (3) Busch, G.; Scherrer, P. A New Seignette-Electric Substance. *Ferroelectrics* **1987**, *71* (1), 15–16. <https://doi.org/10.1080/00150198708224825>.
- (4) Von Hippel, A.; Breckenridge, R. G.; Chesley, F. G.; Tisza, L. High Dielectric Constant Ceramics. *Industrial & Engineering Chemistry* **1946**, *38* (11), 1097–1109.
- (5) Wul, B.; Goldman, J. M. Ferroelectric Switching in BaTiO₃ Ceramics. *CR Acad Sci URSS* **1946**, *51*, 21.
- (6) Miyake, S.; Ueda, R. On Polymorphic Change of BaTiO₃. *Journal of the Physical Society of Japan* **1946**, *1* (1), 32–33.
- (7) Dranetz, A. E.; Howatt, G. N.; Crownover, J. W. Barium Titanates as Circuit Elements: I, II. *Tele-Tech* **1949**, *8* (4), 29–31.
- (8) Scott, J. F. Applications of Modern Ferroelectrics. *Science* **2007**, *315* (5814), 954–959. <https://doi.org/10.1126/science.1129564>.
- (9) Setter, N.; Damjanovic, D.; Eng, L.; Fox, G.; Gevorgian, S.; Hong, S.; Kingon, A.; Kohlstedt, H.; Park, N. Y.; Stephenson, G. B.; Stolitchnov, I.; TagansteV, A. K.; Taylor, D. V.; Yamada, T.; Streiffer, S. Ferroelectric Thin Films: Review of Materials, Properties, and Applications. *Journal of Applied Physics* **2006**, *100* (5), 051606. <https://doi.org/10.1063/1.2336999>.
- (10) Eshita, T.; Wang, W.; Nomura, K.; Nakamura, K.; Saito, H.; Yamaguchi, H.; Mihara, S.; Hikosaka, Y.; Kataoka, Y.; Kojima, M. Development of Highly Reliable Ferroelectric

- Random Access Memory and Its Internet of Things Applications. *Jpn. J. Appl. Phys.* **2018**, *57* (11S), 11UA01. <https://doi.org/10.7567/JJAP.57.11UA01>.
- (11) *FeRAM(Device)*. FUJITSU SEMICONDUCTOR MEMORY SOLUTION. <https://www.fujitsu.com/jp/group/fsm/en/products/feram/device/> (accessed 2023-05-25).
- (12) Moise, T. S.; Summerfelt, S. R.; McAdams, H.; Aggarwal, S.; Udayakumar, K. R.; Celii, F. G.; Martin, J. S.; Xing, G.; Hall, L.; Taylor, K. J.; Hurd, T.; Rodriguez, J.; Remack, K.; Khan, M. D.; Boku, K.; Stacey, G.; Yao, M.; Albrecht, M. G.; Zielinski, E.; Thakre, M.; Kuchimanchi, S.; Thomas, A.; McKee, B.; Rickes, J.; Wang, A.; Grace, J.; Fong, J.; Lee, D.; Pietrzyk, C.; Lanham, R.; Gilbert, S. R.; Taylor, D.; Amano, J.; Bailey, R.; Chu, F.; Fox, G.; Sun, S.; Davenport, T. Demonstration of a 4 Mb, High Density Ferroelectric Memory Embedded within a 130 Nm, 5 LM Cu/FSG Logic Process. In *Digest. International Electron Devices Meeting*,; 2002; pp 535–538. <https://doi.org/10.1109/IEDM.2002.1175897>.
- (13) Rohm Group. Memory Catalog. **2015**.
- (14) Ishiwara, H. Ferroelectric Random Access Memories. *Journal of Nanoscience and Nanotechnology* **2012**, *12* (10), 7619–7627. <https://doi.org/10.1166/jnn.2012.6651>.
- (15) Hubbard, K. J.; Schlom, D. G. Thermodynamic Stability of Binary Oxides in Contact with Silicon. *Journal of Materials Research* **1996**, *11* (11), 2757–2776. <https://doi.org/10.1557/JMR.1996.0350>.
- (16) Ihlefeld, J. F.; Harris, D. T.; Keech, R.; Jones, J. L.; Maria, J.-P.; Trolier-McKinstry, S. Scaling Effects in Perovskite Ferroelectrics: Fundamental Limits and Process-Structure-Property Relations. *Journal of the American Ceramic Society* **2016**, *99* (8), 2537–2557. <https://doi.org/10.1111/jace.14387>.
- (17) Buscaglia, V.; Randall, C. A. Size and Scaling Effects in Barium Titanate. An Overview. *Journal of the European Ceramic Society* **2020**, *40* (11), 3744–3758. <https://doi.org/10.1016/j.jeurceramsoc.2020.01.021>.

- (18) Wang, J.; Li, H. P.; Stevens, R. Hafnia and Hafnia-Toughened Ceramics. *J Mater Sci* **1992**, *27* (20), 5397–5430. <https://doi.org/10.1007/BF00541601>.
- (19) Zhao, X.; Vanderbilt, D. First-Principles Study of Structural, Vibrational, and Lattice Dielectric Properties of Hafnium Oxide. *Phys. Rev. B* **2002**, *65* (23), 233106. <https://doi.org/10.1103/PhysRevB.65.233106>.
- (20) Robertson, J. High Dielectric Constant Oxides. *The European Physical Journal - Applied Physics* **2004**, *28* (3), 265–291. <https://doi.org/10.1051/epjap:2004206>.
- (21) Ihlefeld, J. F.; Luk, T. S.; Smith, S. W.; Fields, S. S.; Jaszewski, S. T.; Hirt, D. M.; Riffe, W. T.; Bender, S.; Constantin, C.; Ayyasamy, M. V.; Balachandran, P. V.; Lu, P.; David Henry, M.; Davids, P. S. Compositional Dependence of Linear and Nonlinear Optical Response in Crystalline Hafnium Zirconium Oxide Thin Films. *J. Appl. Phys.* **2020**, *128* (3), 034101. <https://doi.org/10.1063/5.0012175>.
- (22) Takeuchi, H.; Ha, D.; King, T.-J. Observation of Bulk HfO₂ Defects by Spectroscopic Ellipsometry. *J. Vac. Sci. A* **2004**, *22* (4), 1337–1341. <https://doi.org/10.1116/1.1705593>.
- (23) Nguyen, N. V.; Davydov, A. V.; Chandler-Horowitz, D.; Frank, M. M. Sub-Bandgap Defect States in Polycrystalline Hafnium Oxide and Their Suppression by Admixture of Silicon. *Appl. Phys. Lett.* **2005**, *87* (19), 192903. <https://doi.org/10.1063/1.2126136>.
- (24) Lucovsky, G.; Seo, H.; Lee, S.; Fleming, L. B.; Ulrich, M. D.; Lüning, J.; Lysaght, P.; Bersuker, G. Intrinsic Electronically Active Defects in Transition Metal Elemental Oxides. *Jpn. J. Appl. Phys.* **2007**, *46* (4S), 1899. <https://doi.org/10.1143/JJAP.46.1899>.
- (25) *The High-k Solution / IEEE Journals & Magazine / IEEE Xplore.* <https://ieeexplore.ieee.org/document/4337663> (accessed 2023-05-25).
- (26) Schlom, D. G.; Guha, S.; Datta, S. Gate Oxides Beyond SiO₂. *MRS Bulletin* **2008**, *33* (11), 1017–1025. <https://doi.org/10.1557/mrs2008.221>.

- (27) Choi, J. H.; Mao, Y.; Chang, J. P. Development of Hafnium Based High-k Materials—A Review. *Materials Science and Engineering: R: Reports* **2011**, *72* (6), 97–136. <https://doi.org/10.1016/j.mser.2010.12.001>.
- (28) Böske, T. S.; Müller, J.; Bräuhaus, D.; Schröder, U.; Böttger, U. Ferroelectricity in Hafnium Oxide Thin Films. *Appl. Phys. Lett.* **2011**, *99* (10), 102903. <https://doi.org/10.1063/1.3634052>.
- (29) Cheema, S. S.; Kwon, D.; Shanker, N.; Reis, R. dos; Hsu, S.-L.; Xiao, J.; Zhang, H.; Wagner, R.; Datar, A.; McCarter, M. R.; Serrao, C. R.; Yadav, A. K.; Karbasian, G.; Hsu, C.-H.; Tan, A. J.; Wang, L.-C.; Thakare, V.; Zhang, X.; Mehta, A.; Karapetrova, E.; Chopdekar, R. V.; Shafer, P.; Arenholz, E.; Hu, C.; Proksch, R.; Ramesh, R.; Ciston, J.; Salahuddin, S. Enhanced Ferroelectricity in Ultrathin Films Grown Directly on Silicon. *Nature* **2020**, *580* (7804), 478–482. <https://doi.org/10.1038/s41586-020-2208-x>.
- (30) Zhou, S.; Zhang, J.; Rappe, A. M. Strain-Induced Antipolar Phase in Hafnia Stabilizes Robust Thin-Film Ferroelectricity. *Science Advances* **2022**, *8* (47), eadd5953. <https://doi.org/10.1126/sciadv.add5953>.
- (31) Shin, D.; Arróyave, R.; Liu, Z.-K. Thermodynamic Modeling of the Hf–Si–O System. *Calphad* **2006**, *30* (4), 375–386. <https://doi.org/10.1016/j.calphad.2006.08.006>.
- (32) Ohtaka, O.; Yamanaka, T.; Kume, S.; Hara, N.; Asano, H.; Izumi, F. Structural Analysis of Orthorhombic ZrO₂ by High Resolution Neutron Powder Diffraction. *Proceedings of the Japan Academy, Series B* **1990**, *66* (10), 193–196. <https://doi.org/10.2183/pjab.66.193>.
- (33) Batra, R.; Huan, T. D.; Jones, J. L.; Rossetti, G.; Ramprasad, R. Factors Favoring Ferroelectricity in Hafnia: A First-Principles Computational Study. *J. Phys. Chem. C* **2017**, *121* (8), 4139–4145. <https://doi.org/10.1021/acs.jpcc.6b11972>.
- (34) Materlik, R.; Künneth, C.; Kersch, A. The Origin of Ferroelectricity in Hf_{1-x}Zr_xO₂: A Computational Investigation and a Surface Energy Model. *J. Appl. Phys.* **2015**, *117* (13), 134109. <https://doi.org/10.1063/1.4916707>.

- (35) Ihlefeld, J. F.; Jaszewski, S. T.; Fields, S. S. A Perspective on Ferroelectricity in Hafnium Oxide: Mechanisms and Considerations Regarding Its Stability and Performance. *Appl. Phys. Lett.* **2022**, *121* (24), 240502. <https://doi.org/10.1063/5.0129546>.
- (36) Künneth, C.; Materlik, R.; Kersch, A. Modeling Ferroelectric Film Properties and Size Effects from Tetragonal Interlayer in $\text{Hf}_{1-x}\text{Zr}_x\text{O}_2$ Grains. *Journal of Applied Physics* **2017**, *121* (20), 205304. <https://doi.org/10.1063/1.4983811>.
- (37) Park, M. H.; Lee, Y. H.; Kim, H. J.; Schenk, T.; Lee, W.; Kim, K. D.; Fengler, F. P. G.; Mikolajick, T.; Schroeder, U.; Hwang, C. S. Surface and Grain Boundary Energy as the Key Enabler of Ferroelectricity in Nanoscale Hafnia-Zirconia: A Comparison of Model and Experiment. *Nanoscale* **2017**, *9* (28), 9973–9986. <https://doi.org/10.1039/C7NR02121F>.
- (38) Yurchuk, E.; Müller, J.; Knebel, S.; Sundqvist, J.; Graham, A. P.; Melde, T.; Schröder, U.; Mikolajick, T. Impact of Layer Thickness on the Ferroelectric Behaviour of Silicon Doped Hafnium Oxide Thin Films. *Thin Solid Films* **2013**, *533*, 88–92. <https://doi.org/10.1016/j.tsf.2012.11.125>.
- (39) Park, M. H.; Kim, H. J.; Kim, Y. J.; Lee, W.; Moon, T.; Kim, K. D.; Hwang, C. S. Study on the Degradation Mechanism of the Ferroelectric Properties of Thin $\text{Hf}_{0.5}\text{Zr}_{0.5}\text{O}_2$ Films on TiN and Ir Electrodes. *Appl. Phys. Lett.* **2014**, *105* (7), 072902. <https://doi.org/10.1063/1.4893376>.
- (40) Starschich, S.; Griesche, D.; Schneller, T.; Waser, R.; Böttger, U. Chemical Solution Deposition of Ferroelectric Yttrium-Doped Hafnium Oxide Films on Platinum Electrodes. *Appl. Phys. Lett.* **2014**, *104* (20), 202903. <https://doi.org/10.1063/1.4879283>.
- (41) Chen, H.; Chen, Y.; Tang, L.; Luo, H.; Zhou, K.; Yuan, X.; Zhang, D. Obvious Ferroelectricity in Undoped HfO_2 Films by Chemical Solution Deposition. *J. Mater. Chem. C* **2020**, *8* (8), 2820–2826. <https://doi.org/10.1039/C9TC06400A>.
- (42) Mimura, T.; Shimizu, T.; Funakubo, H. Ferroelectricity in $\text{YO}_{1.5}\text{-HfO}_2$ Films around 1 Mm in Thickness. *Appl. Phys. Lett.* **2019**, *115* (3), 032901. <https://doi.org/10.1063/1.5097880>.

- (43) Xu, X.; Huang, F.-T.; Qi, Y.; Singh, S.; Rabe, K. M.; Obeysekera, D.; Yang, J.; Chu, M.-W.; Cheong, S.-W. Kinetically Stabilized Ferroelectricity in Bulk Single-Crystalline HfO₂:Y. *Nat. Mater.* **2021**, *20* (6), 826–832. <https://doi.org/10.1038/s41563-020-00897-x>.
- (44) Fan, S.; Singh, S.; Xu, X.; Park, K.; Qi, Y.; Cheong, S. W.; Vanderbilt, D.; Rabe, K. M.; Musfeldt, J. L. Vibrational Fingerprints of Ferroelectric HfO₂. *npj Quantum Mater.* **2022**, *7* (1), 1–8. <https://doi.org/10.1038/s41535-022-00436-8>.
- (45) Hoffmann, M.; Schroeder, U.; Schenk, T.; Shimizu, T.; Funakubo, H.; Sakata, O.; Pohl, D.; Drescher, M.; Adelman, C.; Materlik, R.; Kersch, A.; Mikolajick, T. Stabilizing the Ferroelectric Phase in Doped Hafnium Oxide. *J. Appl. Phys.* **2015**, *118* (7), 072006. <https://doi.org/10.1063/1.4927805>.
- (46) Lee, C.-K.; Cho, E.; Lee, H.-S.; Hwang, C. S.; Han, S. First-Principles Study on Doping and Phase Stability of HfO₂. *Phys. Rev. B* **2008**, *78* (1), 012102. <https://doi.org/10.1103/PhysRevB.78.012102>.
- (47) Mittmann, T.; Materano, M.; Lomenzo, P. D.; Park, M. H.; Stolichnov, I.; Cavalieri, M.; Zhou, C.; Chung, C.-C.; Jones, J. L.; Szyjka, T.; Müller, M.; Kersch, A.; Mikolajick, T.; Schroeder, U. Origin of Ferroelectric Phase in Undoped HfO₂ Films Deposited by Sputtering. *Adv. Mater. Interfaces* **2019**, *6* (11), 1900042. <https://doi.org/10.1002/admi.201900042>.
- (48) Pal, A.; Narasimhan, V. K.; Weeks, S.; Littau, K.; Pramanik, D.; Chiang, T. Enhancing Ferroelectricity in Dopant-Free Hafnium Oxide. *Appl. Phys. Lett.* **2017**, *110* (2), 022903. <https://doi.org/10.1063/1.4973928>.
- (49) Materano, M.; Mittmann, T.; Lomenzo, P. D.; Zhou, C.; Jones, J. L.; Falkowski, M.; Kersch, A.; Mikolajick, T.; Schroeder, U. Influence of Oxygen Content on the Structure and Reliability of Ferroelectric Hf_xZr_{1-x}O₂ Layers. *ACS Appl. Electron. Mater.* **2020**, *2* (11), 3618–3626. <https://doi.org/10.1021/acsaelm.0c00680>.
- (50) Schroeder, U.; Yurchuk, E.; Müller, J.; Martin, D.; Schenk, T.; Polakowski, P.; Adelman, C.; Popovici, M. I.; Kalinin, S. V.; Mikolajick, T. Impact of Different Dopants on the

- Switching Properties of Ferroelectric Hafnium Oxide. *Jpn. J. Appl. Phys.* **2014**, *53* (8S1), 08LE02. <https://doi.org/10.7567/JJAP.53.08LE02>.
- (51) Lee, Y. H.; Kim, H. J.; Moon, T.; Kim, K. D.; Hyun, S. D.; Park, H. W.; Lee, Y. B.; Park, M. H.; Hwang, C. S. Preparation and Characterization of Ferroelectric Hf_{0.5}Zr_{0.5}O₂ Thin Films Grown by Reactive Sputtering. *Nanotechnology* **2017**, *28* (30), 305703. <https://doi.org/10.1088/1361-6528/aa7624>.
- (52) Kashir, A.; Oh, S.; Hwang, H. Defect Engineering to Achieve Wake-up Free HfO₂-Based Ferroelectrics. *Adv. Eng. Mater.* **2021**, *23* (1), 2000791. <https://doi.org/10.1002/adem.202000791>.
- (53) Yoon, S.-J.; Na, S.-Y.; Moon, S.-E.; Yoon, S.-M. Polarization Switching Kinetics of the Ferroelectric Al-Doped HfO₂ Thin Films Prepared by Atomic Layer Deposition with Different Ozone Doses. *J. Vac. Sci. B* **2019**, *37* (5), 050601. <https://doi.org/10.1116/1.5110621>.
- (54) Park, M. H.; Lee, Y. H.; Kim, H. J.; Kim, Y. J.; Moon, T.; Kim, K. D.; Müller, J.; Kersch, A.; Schroeder, U.; Mikolajick, T.; Hwang, C. S. Ferroelectricity and Antiferroelectricity of Doped Thin HfO₂-Based Films. *Adv. Mater.* **2015**, *27* (11), 1811–1831. <https://doi.org/10.1002/adma.201404531>.
- (55) H. Park, M.; Schenk, T.; M. Fancher, C.; D. Grimley, E.; Zhou, C.; Richter, C.; M. LeBeau, J.; L. Jones, J.; Mikolajick, T.; Schroeder, U. A Comprehensive Study on the Structural Evolution of HfO₂ Thin Films Doped with Various Dopants. *J. Mater. Chem. C* **2017**, *5* (19), 4677–4690. <https://doi.org/10.1039/C7TC01200D>.
- (56) Schroeder, U.; Richter, C.; Park, M. H.; Schenk, T.; Pešić, M.; Hoffmann, M.; Fengler, F. P. G.; Pohl, D.; Rellinghaus, B.; Zhou, C.; Chung, C.-C.; Jones, J. L.; Mikolajick, T. Lanthanum-Doped Hafnium Oxide: A Robust Ferroelectric Material. *Inorg. Chem.* **2018**, *57* (5), 2752–2765. <https://doi.org/10.1021/acs.inorgchem.7b03149>.
- (57) Schenk, T.; Fancher, C. M.; Park, M. H.; Richter, C.; Künneth, C.; Kersch, A.; Jones, J. L.; Mikolajick, T.; Schroeder, U. On the Origin of the Large Remanent Polarization in

- La:HfO₂. *Adv. Electron. Mater.* **2019**, 5 (12), 1900303.
<https://doi.org/10.1002/aelm.201900303>.
- (58) Starschich, S.; Boettger, U. An Extensive Study of the Influence of Dopants on the Ferroelectric Properties of HfO₂. *J. Mater. Chem. C* **2017**, 5 (2), 333–338.
<https://doi.org/10.1039/C6TC04807B>.
- (59) Huan, T. D.; Sharma, V.; Rossetti, G. A.; Ramprasad, R. Pathways towards Ferroelectricity in Hafnia. *Phys. Rev. B* **2014**, 90 (6), 064111.
<https://doi.org/10.1103/PhysRevB.90.064111>.
- (60) Clima, S.; Wouters, D. J.; Adelman, C.; Schenk, T.; Schroeder, U.; Jurczak, M.; Pourtois, G. Identification of the Ferroelectric Switching Process and Dopant-Dependent Switching Properties in Orthorhombic HfO₂: A First Principles Insight. *Appl. Phys. Lett.* **2014**, 104 (9), 092906. <https://doi.org/10.1063/1.4867975>.
- (61) Jones, J. L. The Effect of Crystal Symmetry on the Maximum Polarization of Polycrystalline Ferroelectric Materials. *Materials Science and Engineering: B* **2010**, 167 (1), 6–11. <https://doi.org/10.1016/j.mseb.2010.01.019>.
- (62) Jaszewski, S. T.; Hoglund, E. R.; Costine, A.; Weber, M. H.; Fields, S. S.; Sales, M. G.; Vaidya, J.; Bellcase, L.; Loughlin, K.; Salanova, A.; Dickie, D. A.; Wolfley, S. L.; Henry, M. D.; Maria, J.-P.; Jones, J. L.; Shukla, N.; McDonnell, S. J.; Reinke, P.; Hopkins, P. E.; Howe, J. M.; Ihlefeld, J. F. Impact of Oxygen Content on Phase Constitution and Ferroelectric Behavior of Hafnium Oxide Thin Films Deposited by Reactive High-Power Impulse Magnetron Sputtering. *Acta Mater.* **2022**, 239, 118220.
<https://doi.org/10.1016/j.actamat.2022.118220>.
- (63) Richter, C.; Schenk, T.; Park, M. H.; Tschardtke, F. A.; Grimley, E. D.; LeBeau, J. M.; Zhou, C.; Fancher, C. M.; Jones, J. L.; Mikolajick, T.; Schroeder, U. Si Doped Hafnium Oxide—A “Fragile” Ferroelectric System. *Adv. Electron. Mater.* **2017**, 3 (10).
<https://doi.org/10.1002/aelm.201700131>.

- (64) Müller, J.; Schröder, U.; Böске, T. S.; Müller, I.; Böttger, U.; Wilde, L.; Sundqvist, J.; Lemberger, M.; Kücher, P.; Mikolajick, T.; Frey, L. Ferroelectricity in Yttrium-Doped Hafnium Oxide. *J. Appl. Phys.* **2011**, *110* (11), 114113. <https://doi.org/10.1063/1.3667205>.
- (65) Lee, Y.; Alex Hsain, H.; Fields, S. S.; Jaszewski, S. T.; Horgan, M. D.; Edgington, P. G.; Ihlefeld, J. F.; Parsons, G. N.; Jones, J. L. Unexpectedly Large Remanent Polarization of Hf_{0.5}Zr_{0.5}O₂ Metal–Ferroelectric–Metal Capacitor Fabricated without Breaking Vacuum. *Appl. Phys. Lett.* **2021**, *118* (1), 012903. <https://doi.org/10.1063/5.0029532>.
- (66) Müller, J.; Böске, T. S.; Schröder, U.; Mueller, S.; Bräuhaus, D.; Böttger, U.; Frey, L.; Mikolajick, T. Ferroelectricity in Simple Binary ZrO₂ and HfO₂. *Nano Lett.* **2012**, *12* (8), 4318–4323. <https://doi.org/10.1021/nl302049k>.
- (67) Park, M. H.; Kim, H. J.; Kim, Y. J.; Lee, Y. H.; Moon, T.; Kim, K. D.; Hyun, S. D.; Fengler, F.; Schroeder, U.; Hwang, C. S. Effect of Zr Content on the Wake-Up Effect in Hf_{1-x}Zr_xO₂ Films. *ACS Appl Mater Interfaces* **2016**, *8* (24), 15466–15475. <https://doi.org/10.1021/acsami.6b03586>.
- (68) Smith, S. W.; Kitahara, A. R.; Rodriguez, M. A.; Henry, M. D.; Brumbach, M. T.; Ihlefeld, J. F. Pyroelectric Response in Crystalline Hafnium Zirconium Oxide (Hf_{1-x}Zr_xO₂) Thin Films. *Appl. Phys. Lett.* **2017**, *110* (7), 072901. <https://doi.org/10.1063/1.4976519>.
- (69) Mueller, S.; Mueller, J.; Singh, A.; Riedel, S.; Sundqvist, J.; Schroeder, U.; Mikolajick, T. Incipient Ferroelectricity in Al-Doped HfO₂ Thin Films. *Adv. Func. Mater.* **2012**, *22* (11), 2412–2417. <https://doi.org/10.1002/adfm.201103119>.
- (70) Zheng, S.; Zhao, Z.; Liu, Z.; Zeng, B.; Yin, L.; Peng, Q.; Liao, M.; Zhou, Y. Improvement of Remanent Polarization of CeO₂–HfO₂ Solid Solution Thin Films on Si Substrates by Chemical Solution Deposition. *Appl. Phys. Lett.* **2020**, *117* (21), 212904. <https://doi.org/10.1063/5.0028200>.
- (71) Mueller, S.; Adelman, C.; Singh, A.; Elshocht, S. V.; Schroeder, U.; Mikolajick, T. Ferroelectricity in Gd-Doped HfO₂ Thin Films. *ECS J. Solid State Sci. Technol.* **2012**, *1* (6), N123. <https://doi.org/10.1149/2.002301jss>.

- (72) Shiraishi, T.; Katayama, K.; Yokouchi, T.; Shimizu, T.; Oikawa, T.; Sakata, O.; Uchida, H.; Imai, Y.; Kiguchi, T.; Konno, T. J.; Funakubo, H. Impact of Mechanical Stress on Ferroelectricity in (Hf_{0.5}Zr_{0.5})O₂ Thin Films. *Appl. Phys. Lett.* **2016**, *108* (26), 262904. <https://doi.org/10.1063/1.4954942>.
- (73) Batra, R.; Huan, T. D.; Jones, J. L.; Rossetti, G.; Ramprasad, R. Factors Favoring Ferroelectricity in Hafnia: A First-Principles Computational Study. *J. Phys. Chem. C* **2017**, *121* (8), 4139–4145. <https://doi.org/10.1021/acs.jpcc.6b11972>.
- (74) Materlik, R.; Künneth, C.; Kersch, A. The Origin of Ferroelectricity in Hf_{1-x}Zr_xO₂: A Computational Investigation and a Surface Energy Model. *J. Appl. Phys.* **2015**, *117* (13), 134109. <https://doi.org/10.1063/1.4916707>.
- (75) Fan, S.-T.; Chen, Y.-W.; Liu, C. W. Strain Effect on the Stability in Ferroelectric HfO₂ Simulated by First-Principles Calculations. *J. Phys. D: Appl. Phys.* **2020**, *53* (23), 23LT01. <https://doi.org/10.1088/1361-6463/ab7fd4>.
- (76) Kim, S. J.; Narayan, D.; Lee, J.-G.; Mohan, J.; Lee, J. S.; Lee, J.; Kim, H. S.; Byun, Y.-C.; Lucero, A. T.; Young, C. D.; Summerfelt, S. R.; San, T.; Colombo, L.; Kim, J. Large Ferroelectric Polarization of TiN/Hf_{0.5}Zr_{0.5}O₂/TiN Capacitors Due to Stress-Induced Crystallization at Low Thermal Budget. *Appl. Phys. Lett.* **2017**, *111* (24), 242901. <https://doi.org/10.1063/1.4995619>.
- (77) Shiraishi, T.; Katayama, K.; Yokouchi, T.; Shimizu, T.; Oikawa, T.; Sakata, O.; Uchida, H.; Imai, Y.; Kiguchi, T.; Konno, T. J.; Funakubo, H. Effect of the Film Thickness on the Crystal Structure and Ferroelectric Properties of (Hf_{0.5}Zr_{0.5})O₂ Thin Films Deposited on Various Substrates. *Mat. Sci. Semicon. Proc.* **2017**, *70*, 239–245. <https://doi.org/10.1016/j.mssp.2016.12.008>.
- (78) Schenk, T.; Bencan, A.; Drazic, G.; Condurache, O.; Valle, N.; Adib, B. E.; Aruchamy, N.; Granzow, T.; Defay, E.; Glinsek, S. Enhancement of Ferroelectricity and Orientation in Solution-Derived Hafnia Thin Films through Heterogeneous Grain Nucleation. *Appl. Phys. Lett.* **2021**, *118* (16), 162902. <https://doi.org/10.1063/5.0045966>.

- (79) Fields, S. S.; Olson, D. H.; Jaszewski, S. T.; Fancher, C. M.; Smith, S. W.; Dickie, D. A.; Esteves, G.; Henry, M. D.; Davids, P. S.; Hopkins, P. E.; Ihlefeld, J. F. Compositional and Phase Dependence of Elastic Modulus of Crystalline and Amorphous $\text{Hf}_{1-x}\text{Zr}_x\text{O}_2$ Thin Films. *Appl. Phys. Lett.* **2021**, *118* (10), 102901. <https://doi.org/10.1063/5.0044702>.
- (80) Fields, S. S.; Smith, S. W.; Fancher, C. M.; Henry, M. D.; Wolfley, S. L.; Sales, M. G.; Jaszewski, S. T.; Rodriguez, M. A.; Esteves, G.; Davids, P. S.; McDonnell, S. J.; Ihlefeld, J. F. Metal Nitride Electrode Stress and Chemistry Effects on Phase and Polarization Response in Ferroelectric $\text{Hf}_{0.5}\text{Zr}_{0.5}\text{O}_2$ Thin Films. *Adv. Mater. Interfaces* **2021**, *8*, 2100018. <https://doi.org/10.1002/admi.202100018>.
- (81) Hyuk Park, M.; Joon Kim, H.; Jin Kim, Y.; Moon, T.; Seong Hwang, C. The Effects of Crystallographic Orientation and Strain of Thin $\text{Hf}_{0.5}\text{Zr}_{0.5}\text{O}_2$ Film on Its Ferroelectricity. *Appl. Phys. Lett.* **2014**, *104* (7), 072901. <https://doi.org/10.1063/1.4866008>.
- (82) Grimley, E. D.; Schenk, T.; Sang, X.; Pešić, M.; Schroeder, U.; Mikolajick, T.; LeBeau, J. M. Structural Changes Underlying Field-Cycling Phenomena in Ferroelectric HfO_2 Thin Films. *Adv. Electron. Mater.* **2016**, *2* (9), 1600173. <https://doi.org/10.1002/aelm.201600173>.
- (83) Pešić, M.; Fengler, F. P. G.; Larcher, L.; Padovani, A.; Schenk, T.; Grimley, E. D.; Sang, X.; LeBeau, J. M.; Slesazeck, S.; Schroeder, U.; Mikolajick, T. Physical Mechanisms behind the Field-Cycling Behavior of HfO_2 -Based Ferroelectric Capacitors. *Adv. Funct. Mater.* **2016**, *26* (25), 4601–4612. <https://doi.org/10.1002/adfm.201600590>.
- (84) Fields, S. S.; Smith, S. W.; Jaszewski, S. T.; Mimura, T.; Dickie, D. A.; Esteves, G.; David Henry, M.; Wolfley, S. L.; Davids, P. S.; Ihlefeld, J. F. Wake-up and Fatigue Mechanisms in Ferroelectric $\text{Hf}_{0.5}\text{Zr}_{0.5}\text{O}_2$ Films with Symmetric RuO_2 Electrodes. *J. Appl. Phys.* **2021**, *130* (13), 134101. <https://doi.org/10.1063/5.0064145>.
- (85) Islamov, D. R.; Gritsenko, V. A.; Perevalov, T. V.; Pustovarov, V. A.; Orlov, O. M.; Chernikova, A. G.; Markeev, A. M.; Slesazeck, S.; Schroeder, U.; Mikolajick, T.; Krasnikov, G. Y. Identification of the Nature of Traps Involved in the Field Cycling of

- Hf_{0.5}Zr_{0.5}O₂-Based Ferroelectric Thin Films. *Acta Mater.* **2019**, *166*, 47–55.
<https://doi.org/10.1016/j.actamat.2018.12.008>.
- (86) Starschich, S.; Menzel, S.; Böttger, U. Evidence for Oxygen Vacancies Movement during Wake-up in Ferroelectric Hafnium Oxide. *Appl. Phys. Lett.* **2016**, *108* (3), 032903.
<https://doi.org/10.1063/1.4940370>.
- (87) Fields, S. S.; Smith, S. W.; Ryan, P. J.; Jaszewski, S. T.; Brummel, I. A.; Salanova, A.; Esteves, G.; Wolfley, S. L.; Henry, M. D.; Davids, P. S.; Ihlefeld, J. F. Phase-Exchange-Driven Wake-Up and Fatigue in Ferroelectric Hafnium Zirconium Oxide Films. *ACS Appl. Mater. Inter.* **2020**, *12* (23), 26577–26585. <https://doi.org/10.1021/acsami.0c03570>.
- (88) Chouprik, A.; Spiridonov, M.; Zarubin, S.; Kirtaev, R.; Mikheev, V.; Lebedinskii, Y.; Zakharchenko, S.; Negrov, D. Wake-Up in a Hf_{0.5}Zr_{0.5}O₂ Film: A Cycle-by-Cycle Emergence of the Remnant Polarization via the Domain Depinning and the Vanishing of the Anomalous Polarization Switching. *ACS Appl. Electron. Mater.* **2019**, *1* (3), 275–287.
<https://doi.org/10.1021/acsaelm.8b00046>.
- (89) Fengler, F. P. G.; Pešić, M.; Starschich, S.; Schneller, T.; Küneth, C.; Böttger, U.; Mulaosmanovic, H.; Schenk, T.; Park, M. H.; Nigon, R.; Muralt, P.; Mikolajick, T.; Schroeder, U. Domain Pinning: Comparison of Hafnia and PZT Based Ferroelectrics. *Adv. Electron. Mater.* **2017**, *3* (4), 1600505. <https://doi.org/10.1002/aelm.201600505>.
- (90) Shimizu, T.; Mimura, T.; Kiguchi, T.; Shiraishi, T.; Konno, T.; Katsuya, Y.; Sakata, O.; Funakubo, H. Ferroelectricity Mediated by Ferroelastic Domain Switching in HfO₂-Based Epitaxial Thin Films. *Appl. Phys. Lett.* **2018**, *113* (21), 212901.
<https://doi.org/10.1063/1.5055258>.
- (91) Lederer, M.; Olivo, R.; Lehninger, D.; Abdulazhanov, S.; Kämpfe, T.; Kirbach, S.; Mart, C.; Seidel, K.; Eng, L. M. On the Origin of Wake-Up and Antiferroelectric-Like Behavior in Ferroelectric Hafnium Oxide. *physica status solidi (RRL) – Rapid Research Letters* **2021**, *15* (5), 2100086. <https://doi.org/10.1002/pssr.202100086>.

- (92) Hamouda, W.; Pancotti, A.; Lubin, C.; Tortech, L.; Richter, C.; Mikolajick, T.; Schroeder, U.; Barrett, N. Physical Chemistry of the TiN/Hf_{0.5}Zr_{0.5}O₂ Interface. *J. Appl. Phys.* **2020**, *127* (6), 064105. <https://doi.org/10.1063/1.5128502>.
- (93) Hoffmann, M.; Schroeder, U.; Schenk, T.; Shimizu, T.; Funakubo, H.; Sakata, O.; Pohl, D.; Drescher, M.; Adelman, C.; Materlik, R.; Kersch, A.; Mikolajick, T. Stabilizing the Ferroelectric Phase in Doped Hafnium Oxide. *J. Appl. Phys.* **2015**, *118* (7), 072006. <https://doi.org/10.1063/1.4927805>.
- (94) Fengler, F. P. G.; Hoffmann, M.; Slesazeck, S.; Mikolajick, T.; Schroeder, U. On the Relationship between Field Cycling and Imprint in Ferroelectric Hf_{0.5}Zr_{0.5}O₂. *J. Appl. Phys.* **2018**, *123* (20), 204101. <https://doi.org/10.1063/1.5026424>.
- (95) George, S. M. Atomic Layer Deposition: An Overview. *Chem. Rev.* **2010**, *110* (1), 111–131. <https://doi.org/10.1021/cr900056b>.
- (96) Johnson, R. W.; Hultqvist, A.; Bent, S. F. A Brief Review of Atomic Layer Deposition: From Fundamentals to Applications. *Materials Today* **2014**, *17* (5), 236–246. <https://doi.org/10.1016/j.mattod.2014.04.026>.
- (97) Hsain, H. A.; Lee, Y.; Materano, M.; Mittmann, T.; Payne, A.; Mikolajick, T.; Schroeder, U.; Parsons, G. N.; Jones, J. L. Many Routes to Ferroelectric HfO₂: A Review of Current Deposition Methods. *J. Vac. Sci. A* **2022**, *40* (1), 010803. <https://doi.org/10.1116/6.0001317>.
- (98) Mittmann, T.; Fengler, F. P. G.; Richter, C.; Park, M. H.; Mikolajick, T.; Schroeder, U. Optimizing Process Conditions for Improved Hf_{1-x}Zr_xO₂ Ferroelectric Capacitor Performance. *Microelectronic Engineering* **2017**, *178*, 48–51. <https://doi.org/10.1016/j.mee.2017.04.031>.
- (99) Chernikova, A.; Kozodaev, M.; Markeev, A.; Negrov, D.; Spiridonov, M.; Zarubin, S.; Bak, O.; Buragohain, P.; Lu, H.; Suvorova, E.; Gruverman, A.; Zenkevich, A. Ultrathin Hf_{0.5}Zr_{0.5}O₂ Ferroelectric Films on Si. *ACS Appl. Mater. Interfaces* **2016**, *8* (11), 7232–7237. <https://doi.org/10.1021/acsami.5b11653>.

- (100) Lomenzo, P. D.; Takmeel, Q.; Moghaddam, S.; Nishida, T. Annealing Behavior of Ferroelectric Si-Doped HfO₂ Thin Films. *Thin Solid Films* **2016**, *615*, 139–144. <https://doi.org/10.1016/j.tsf.2016.07.009>.
- (101) Park, M. H.; Chung, C.-C.; Schenk, T.; Richter, C.; Opsomer, K.; Detavernier, C.; Adelman, C.; Jones, J. L.; Mikolajick, T.; Schroeder, U. Effect of Annealing Ferroelectric HfO₂ Thin Films: In Situ, High Temperature X-Ray Diffraction. *Adv. Electron. Mater.* **2018**, *4* (7), 1800091. <https://doi.org/10.1002/aelm.201800091>.
- (102) Alcalá, R.; Richter, C.; Materano, M.; Lomenzo, P. D.; Zhou, C.; Jones, J. L.; Mikolajick, T.; Schroeder, U. Influence of Oxygen Source on the Ferroelectric Properties of ALD Grown Hf_xZr_{1-x}O₂ Films. *J. Phys. D: Appl. Phys.* **2020**, *54* (3), 035102. <https://doi.org/10.1088/1361-6463/abbc98>.
- (103) Liu, X.; Ramanathan, S.; Longdergan, A.; Srivastava, A.; Lee, E.; Seidel, T. E.; Barton, J. T.; Pang, D.; Gordon, R. G. ALD of Hafnium Oxide Thin Films from Tetrakis(Ethylmethylamino)Hafnium and Ozone. *J. Electrochem. Soc.* **2005**, *152* (3), G213. <https://doi.org/10.1149/1.1859631>.
- (104) D. Kim, K.; H. Park, M.; J. Kim, H.; J. Kim, Y.; Moon, T.; H. Lee, Y.; D. Hyun, S.; Gwon, T.; S. Hwang, C. Ferroelectricity in Undoped-HfO₂ Thin Films Induced by Deposition Temperature Control during Atomic Layer Deposition. *J. Mater. Chem. C* **2016**, *4* (28), 6864–6872. <https://doi.org/10.1039/C6TC02003H>.
- (105) Choi, M.-J.; Park, H.-H.; Jeong, D. S.; Kim, J. H.; Kim, J.-S.; Kim, S. K. Atomic Layer Deposition of HfO₂ Thin Films Using H₂O₂ as Oxidant. *Appl. Surf. Sci.* **2014**, *301*, 451–455. <https://doi.org/10.1016/j.apsusc.2014.02.098>.
- (106) Oviroh, P. O.; Akbarzadeh, R.; Pan, D.; Coetzee, R. A. M.; Jen, T.-C. New Development of Atomic Layer Deposition: Processes, Methods and Applications. *Sci Technol Adv Mater* **2019**, *20* (1), 465–496. <https://doi.org/10.1080/14686996.2019.1599694>.
- (107) Martínez-Puente, M. A.; Horley, P.; Aguirre-Tostado, F. S.; López-Medina, J.; Borbón-Núñez, H. A.; Tiznado, H.; Susarrey-Arce, A.; Martínez-Guerra, E. ALD and PEALD

- Deposition of HfO₂ and Its Effects on the Nature of Oxygen Vacancies. *Materials Science and Engineering: B* **2022**, 285, 115964. <https://doi.org/10.1016/j.mseb.2022.115964>.
- (108) Langmuir, I. Oscillations in Ionized Gases. *Proc Natl Acad Sci U S A* **1928**, 14 (8), 627–637.
- (109) SreeHarsha, K. S. *Principles of Vapor Deposition of Thin Films*, 1st Edition.; Elsevier, 2006.
- (110) Chapin, J. S. The Planar Magnetron. *Research Development* **1974**, 25 (1), 37–40.
- (111) Swann, S. Magnetron Sputtering. *Physics in Technology* **1988**, 19 (2), 67. <https://doi.org/10.1088/0305-4624/19/2/304>.
- (112) Kelly, P. J.; Arnell, R. D. Magnetron Sputtering: A Review of Recent Developments and Applications. *Vacuum* **2000**, 56 (3), 159–172. [https://doi.org/10.1016/S0042-207X\(99\)00189-X](https://doi.org/10.1016/S0042-207X(99)00189-X).
- (113) Anders, A. Tutorial: Reactive High Power Impulse Magnetron Sputtering (R-HiPIMS). *J. Appl. Phys.* **2017**, 121 (17), 171101. <https://doi.org/10.1063/1.4978350>.
- (114) Schiller, S.; Goedicke, K.; Reschke, J.; Kirchhoff, V.; Schneider, S.; Milde, F. Pulsed Magnetron Sputter Technology. *Surf. Coat. Technol.* **1993**, 61 (1), 331–337. [https://doi.org/10.1016/0257-8972\(93\)90248-M](https://doi.org/10.1016/0257-8972(93)90248-M).
- (115) Kouznetsov, V.; Macák, K.; Schneider, J. M.; Helmersson, U.; Petrov, I. A Novel Pulsed Magnetron Sputter Technique Utilizing Very High Target Power Densities. *Surf. Coat. Technol.* **1999**, 122 (2), 290–293. [https://doi.org/10.1016/S0257-8972\(99\)00292-3](https://doi.org/10.1016/S0257-8972(99)00292-3).
- (116) Gudmundsson, J. T.; Brenning, N.; Lundin, D.; Helmersson, U. High Power Impulse Magnetron Sputtering Discharge. *J. Vac. Sci. A* **2012**, 30 (3), 030801. <https://doi.org/10.1116/1.3691832>.
- (117) Anders, A. Discharge Physics of High Power Impulse Magnetron Sputtering. *Surf. Coat. Technol.* **2011**, 205, S1–S9. <https://doi.org/10.1016/j.surfcoat.2011.03.081>.

- (118) Alami, J.; Persson, P. O. Å.; Music, D.; Gudmundsson, J. T.; Bohlmark, J.; Helmersson, U. Ion-Assisted Physical Vapor Deposition for Enhanced Film Properties on Nonflat Surfaces. *J. Vac. Sci. A* **2005**, *23* (2), 278–280. <https://doi.org/10.1116/1.1861049>.
- (119) Bohlmark, J.; Östbye, M.; Lattemann, M.; Ljungcrantz, H.; Rosell, T.; Helmersson, U. Guiding the Deposition Flux in an Ionized Magnetron Discharge. *Thin Solid Films* **2006**, *515* (4), 1928–1931. <https://doi.org/10.1016/j.tsf.2006.07.183>.
- (120) Samuelsson, M.; Lundin, D.; Jensen, J.; Raadu, M. A.; Gudmundsson, J. T.; Helmersson, U. On the Film Density Using High Power Impulse Magnetron Sputtering. *Surf. Coat. Technol.* **2010**, *205* (2), 591–596. <https://doi.org/10.1016/j.surfcoat.2010.07.041>.
- (121) Schmidt, S.; Hänninen, T.; Goyenola, C.; Wissting, J.; Jensen, J.; Hultman, L.; Goebbels, N.; Tobler, M.; Högberg, H. SiN_x Coatings Deposited by Reactive High Power Impulse Magnetron Sputtering: Process Parameters Influencing the Nitrogen Content. *ACS Appl. Mater. Interfaces* **2016**, *8* (31), 20385–20395. <https://doi.org/10.1021/acsami.6b05830>.
- (122) Helmersson, U.; Lattemann, M.; Bohlmark, J.; Ehasarian, A. P.; Gudmundsson, J. T. Ionized Physical Vapor Deposition (IPVD): A Review of Technology and Applications. *Thin Solid Films* **2006**, *513* (1), 1–24. <https://doi.org/10.1016/j.tsf.2006.03.033>.
- (123) Ehasarian, A. P.; Münz, W.-D.; Hultman, L.; Helmersson, U.; Petrov, I. High Power Pulsed Magnetron Sputtered CrN_x Films. *Surf. Coat. Technol.* **2003**, *163–164*, 267–272. [https://doi.org/10.1016/S0257-8972\(02\)00479-6](https://doi.org/10.1016/S0257-8972(02)00479-6).
- (124) Greczynski, G.; Jensen, J.; Bohlmark, J.; Hultman, L. Microstructure Control of CrN_x Films during High Power Impulse Magnetron Sputtering. *Surf. Coat. Technol.* **2010**, *205* (1), 118–130. <https://doi.org/10.1016/j.surfcoat.2010.06.016>.
- (125) Greczynski, G.; Jensen, J.; Hultman, L. CrN_x Films Prepared by DC Magnetron Sputtering and High-Power Pulsed Magnetron Sputtering: A Comparative Study. *IEEE Transactions on Plasma Science* **2010**, *38* (11), 3046–3056. <https://doi.org/10.1109/TPS.2010.2071885>.
- (126) Hsiao, Y.-C.; Lee, J.-W.; Yang, Y.-C.; Lou, B.-S. Effects of Duty Cycle and Pulse Frequency on the Fabrication of AlCrN Thin Films Deposited by High Power Impulse

- Magnetron Sputtering. *Thin Solid Films* **2013**, *549*, 281–291.
<https://doi.org/10.1016/j.tsf.2013.08.059>.
- (127) Lin, J.; Wang, B.; Ou, Y.; Sproul, W. D.; Dahan, I.; Moore, J. J. Structure and Properties of CrSiN Nanocomposite Coatings Deposited by Hybrid Modulated Pulsed Power and Pulsed Dc Magnetron Sputtering. *Surf. Coat. Technol.* **2013**, *216*, 251–258.
<https://doi.org/10.1016/j.surfcoat.2012.11.053>.
- (128) Lin, J.; Sproul, W. D. Structure and Properties of Cr₂O₃ Coatings Deposited Using DCMS, PDCMS, and DOMS. *Surf. Coat. Technol.* **2015**, *276*, 70–76.
<https://doi.org/10.1016/j.surfcoat.2015.06.044>.
- (129) Wu, C.-H.; Yang, F.-C.; Chen, W.-C.; Chang, C.-L. Influence of Oxygen/Argon Reaction Gas Ratio on Optical and Electrical Characteristics of Amorphous IGZO Thin Films Coated by HiPIMS Process. *Surf. Coat. Technol.* **2016**, *303*, 209–214.
<https://doi.org/10.1016/j.surfcoat.2016.03.089>.
- (130) Sarakinos, K.; Wördenweber, J.; Uslu, F.; Schulz, P.; Alami, J.; Wuttig, M. The Effect of the Microstructure and the Surface Topography on the Electrical Properties of Thin Ag Films Deposited by High Power Pulsed Magnetron Sputtering. *Surf. Coat. Technol.* **2008**, *202* (11), 2323–2327. <https://doi.org/10.1016/j.surfcoat.2007.08.028>.
- (131) Horwat, D.; Mickan, M.; Chamorro, W. New Strategies for the Synthesis of ZnO and Al-Doped ZnO Films by Reactive Magnetron Sputtering at Room Temperature. *physica status solidi c* **2016**, *13* (10–12), 951–957. <https://doi.org/10.1002/pssc.201600136>.
- (132) Movchan, B. A.; Demchishin, . Study of the Structure and Properties of Thick Vacuum Condensates of Nickel, Titanium, Tungsten, Aluminium Oxide and Zirconium Dioxide. *Phys. Met. Metallogr.* **1969**, *28* (4), 83–90.
- (133) Thornton, J. A. Influence of Apparatus Geometry and Deposition Conditions on the Structure and Topography of Thick Sputtered Coatings. *Surf. Coat. Technol.* **1974**, *11* (4), 666–670. <https://doi.org/10.1116/1.1312732>.

- (134) Anders, A. A Structure Zone Diagram Including Plasma-Based Deposition and Ion Etching. *Thin Solid Films* **2010**, *518* (15), 4087–4090.
<https://doi.org/10.1016/j.tsf.2009.10.145>.
- (135) Petrov, I.; Barna, P. B.; Hultman, L.; Greene, J. E. Microstructural Evolution during Film Growth. *J. Vac. Sci. A* **2003**, *21* (5), S117. <https://doi.org/10.1116/1.1601610>.
- (136) Jung, H.-S.; Jeon, S. H.; Kim, H. K.; Yu, I.-H.; Lee, S. Y.; Lee, J.; Chung, Y. J.; Cho, D.-Y.; Lee, N.-I.; Park, T. J.; Choi, J.-H.; Han, S.; Hwang, C. S. The Impact of Carbon Concentration on the Crystalline Phase and Dielectric Constant of Atomic Layer Deposited HfO₂ Films on Ge Substrate. *ECS J. Solid State Sci. Technol.* **2012**, *1* (2), N33.
<https://doi.org/10.1149/2.020202jss>.
- (137) Olsen, T.; Schröder, U.; Müller, S.; Krause, A.; Martin, D.; Singh, A.; Müller, J.; Geidel, M.; Mikolajick, T. Co-Sputtering Yttrium into Hafnium Oxide Thin Films to Produce Ferroelectric Properties. *Appl. Phys. Lett.* **2012**, *101* (8), 082905.
<https://doi.org/10.1063/1.4747209>.
- (138) Mimura, T.; Shimizu, T.; Uchida, H.; Funakubo, H. Room-Temperature Deposition of Ferroelectric HfO₂-Based Films by the Sputtering Method. *Appl. Phys. Lett.* **2020**, *116* (6), 062901. <https://doi.org/10.1063/1.5140612>.
- (139) Luo, Q.; Ma, H.; Su, H.; Xue, K.; Cao, R.; Gao, Z.; Yu, J.; Gong, T.; Xu, X.; Yin, J.; Yuan, P.; Tai, L.; Dong, D.; Long, S.; Liu, Q.; Miao, X.; Lv, H.; Liu, M. Composition-Dependent Ferroelectric Properties in Sputtered Hf_xZr_{1-x}O₂ Thin Films. *IEEE Electron Device Letters* **2019**, *40* (4), 570–573. <https://doi.org/10.1109/LED.2019.2902609>.
- (140) Xu, L.; Shibayama, S.; Izukashi, K.; Nishimura, T.; Yajima, T.; Migita, S.; Toriumi, A. General Relationship for Cation and Anion Doping Effects on Ferroelectric HfO₂ Formation. In *2016 IEEE International Electron Devices Meeting (IEDM)*; 2016; p 25.2.1-25.2.4. <https://doi.org/10.1109/IEDM.2016.7838477>.
- (141) Bouaziz, J.; Rojo Romeo, P.; Baboux, N.; Vilquin, B. Characterization of Ferroelectric Hafnium/Zirconium Oxide Solid Solutions Deposited by Reactive Magnetron Sputtering.

Journal of Vacuum Science & Technology B **2019**, 37 (2), 021203.

<https://doi.org/10.1116/1.5060643>.

- (142) Mittmann, T.; Michailow, M.; D. Lomenzo, P.; Gärtner, J.; Falkowski, M.; Kersch, A.; Mikolajick, T.; Schroeder, U. Stabilizing the Ferroelectric Phase in HfO₂-Based Films Sputtered from Ceramic Targets under Ambient Oxygen. *Nanoscale* **2021**, 13 (2), 912–921. <https://doi.org/10.1039/D0NR07699F>.
- (143) Vlček, J.; Rezek, J.; Houška, J.; Kozák, T.; Kohout, J. Benefits of the Controlled Reactive High-Power Impulse Magnetron Sputtering of Stoichiometric ZrO₂ Films. *Vacuum* **2015**, 114, 131–141. <https://doi.org/10.1016/j.vacuum.2014.12.004>.
- (144) Sittinger, V.; Lenck, O.; Vergöhl, M.; Szyszka, B.; Bräuer, G. Applications of HIPIMS Metal Oxides. *Thin Solid Films* **2013**, 548, 18–26. <https://doi.org/10.1016/j.tsf.2013.08.087>.
- (145) Fortier, J.-P.; Baloukas, B.; Zabeida, O.; Klemberg-Sapieha, J. E.; Martinu, L. Thermo-chromic VO₂ Thin Films Deposited by HiPIMS. *Sol. Energy Mater. Sol.* **2014**, 125, 291–296. <https://doi.org/10.1016/j.solmat.2014.03.007>.
- (146) Lin, T.; Wang, L.; Wang, X.; Zhang, Y.; Yu, Y. Influence of Bias Voltage on Microstructure and Phase Transition Properties of VO₂ Thin Film Synthesized by HiPIMS. *Surf. Coat. Technol.* **2016**, 305, 110–115. <https://doi.org/10.1016/j.surfcoat.2016.08.020>.
- (147) Kelley, K. P.; Sachet, E.; Shelton, C. T.; Maria, J.-P. High Mobility Yttrium Doped Cadmium Oxide Thin Films. *APL Materials* **2017**, 5 (7), 076105. <https://doi.org/10.1063/1.4993799>.
- (148) Hála, M.; Vernhes, R.; Zabeida, O.; Klemberg-Sapieha, J.-E.; Martinu, L. Reactive HiPIMS Deposition of SiO₂/Ta₂O₅ Optical Interference Filters. *Journal of Applied Physics* **2014**, 116 (21), 213302. <https://doi.org/10.1063/1.4903285>.
- (149) Vlček, J.; Belosludtsev, A.; Rezek, J.; Houška, J.; Čapek, J.; Čerstvý, R.; Haviar, S. High-Rate Reactive High-Power Impulse Magnetron Sputtering of Hard and Optically

- Transparent HfO₂ Films. *Surf. Coat. Technol.* **2016**, 290, 58–64.
<https://doi.org/10.1016/j.surfcoat.2015.08.024>.
- (150) Ganesan, R.; Murdoch, B. J.; Partridge, J. G.; Bathgate, S.; Treverrow, B.; Dong, X.; Ross, A. E.; McCulloch, D. G.; McKenzie, D. R.; Bilek, M. M. M. Optimizing HiPIMS Pressure for Deposition of High-k (k = 18.3) Amorphous HfO₂. *Appl. Surf. Sci.* **2016**, 365, 336–341. <https://doi.org/10.1016/j.apsusc.2016.01.017>.
- (151) Alami, J.; Sarakinos, K.; Uslu, F.; Wuttig, M. On the Relationship between the Peak Target Current and the Morphology of Chromium Nitride Thin Films Deposited by Reactive High Power Pulsed Magnetron Sputtering. *J. Phys. D: Appl. Phys.* **2008**, 42 (1), 015304. <https://doi.org/10.1088/0022-3727/42/1/015304>.
- (152) Layes, V.; Corbella, C.; Monjé, S.; Schulz-von der Gathen, V.; von Keudell, A.; de los Arcos, T. Connection between Target Poisoning and Current Waveforms in Reactive High-Power Impulse Magnetron Sputtering of Chromium. *Plasma Sources Sci. Technol.* **2018**, 27 (8), 084004. <https://doi.org/10.1088/1361-6595/aad0e2>.
- (153) Bragg, W. H.; Bragg, W. L. The Reflection of X-Rays by Crystals. *Proceedings of the Royal Society of London. Series A, Containing Papers of a Mathematical and Physical Character* **1913**, 88 (605), 428–438. <https://doi.org/10.1098/rspa.1913.0040>.
- (154) Scherrer, P. Estimation of the Size and Structure of Colloidal Particles by Röntgen Rays. *Nachrichten von der Koniglichen Gesellschaft der Wissenschaften zu Gottingen, Mathematisch-Physikalische Klasse* **1918**, 2, 96–100.
- (155) Black, D. R.; Mendenhall, M. H.; Brown, C. M.; Henins, A.; Filliben, J.; Cline, J. P. Certification of Standard Reference Material 660c for Powder Diffraction. *Powder Diffraction* **2020**, 35 (1), 17–22. <https://doi.org/10.1017/S0885715620000068>.
- (156) Marra, W. C.; Eisenberger, P.; Cho, A. Y. X-ray Total-external-reflection–Bragg Diffraction: A Structural Study of the GaAs–Al Interface. *Journal of Applied Physics* **1979**, 50 (11), 6927–6933. <https://doi.org/10.1063/1.325845>.

- (157) Toney, M. F.; Brennan, S. Observation of the Effect of Refraction on x Rays Diffracted in a Grazing-Incidence Asymmetric Bragg Geometry. *Phys. Rev. B* **1989**, *39* (11), 7963–7966. <https://doi.org/10.1103/PhysRevB.39.7963>.
- (158) Esteves, G.; Ramos, K.; Fancher, C. M.; Jones, J. L. Line-Profile Analysis Software (LIPRAS), 2017.
- (159) Toby, B. H.; Von Dreele, R. B. GSAS-II: The Genesis of a Modern Open-Source All Purpose Crystallography Software Package. *J Appl Cryst* **2013**, *46* (2), 544–549. <https://doi.org/10.1107/S0021889813003531>.
- (160) Fan, S.-T.; Chen, Y.-W.; Liu, C. W. Strain Effect on the Stability in Ferroelectric HfO₂ Simulated by First-Principles Calculations. *J. Phys. D: Appl. Phys.* **2020**, *53* (23), 23LT01. <https://doi.org/10.1088/1361-6463/ab7fd4>.
- (161) Shiraishi, T.; Katayama, K.; Yokouchi, T.; Shimizu, T.; Oikawa, T.; Sakata, O.; Uchida, H.; Imai, Y.; Kiguchi, T.; Konno, T. J.; Funakubo, H. Impact of Mechanical Stress on Ferroelectricity in (Hf_{0.5}Zr_{0.5})O₂ Thin Films. *Appl. Phys. Lett.* **2016**, *108* (26), 262904. <https://doi.org/10.1063/1.4954942>.
- (162) Birkholz, M. *Thin Film Analysis by X-Ray Scattering*; Wiley - VCH: KGaA, Weinheim, 2006.
- (163) Libra, J. *KolXPD: Spectroscopy Data Measurement and Processing* **2011**.
- (164) Shirley, D. A. High-Resolution X-Ray Photoemission Spectrum of the Valence Bands of Gold. *Phys. Rev. B* **1972**, *5* (12), 4709–4714. <https://doi.org/10.1103/PhysRevB.5.4709>.
- (165) Scofield, J. H. Hartree-Slater Subshell Photoionization Cross-Sections at 1254 and 1487 EV. *Journal of Electron Spectroscopy and Related Phenomena* **1976**, *8* (2), 129–137. [https://doi.org/10.1016/0368-2048\(76\)80015-1](https://doi.org/10.1016/0368-2048(76)80015-1).
- (166) Idriss, H. On the Wrong Assignment of the XPS O1s Signal at 531–532 EV Attributed to Oxygen Vacancies in Photo- and Electro-Catalysts for Water Splitting and Other Materials

- Applications. *Surface Science* **2021**, *712*, 121894.
<https://doi.org/10.1016/j.susc.2021.121894>.
- (167) Sharath, S. U.; Bertaud, T.; Kurian, J.; Hildebrandt, E.; Walczyk, C.; Calka, P.; Zaumseil, P.; Sowinska, M.; Walczyk, D.; Gloskovskii, A.; Schroeder, T.; Alff, L. Towards Forming-Free Resistive Switching in Oxygen Engineered HfO_{2-x}. *Appl. Phys. Lett.* **2014**, *104* (6), 063502. <https://doi.org/10.1063/1.4864653>.
- (168) Baumgarten, L.; Szyjka, T.; Mittmann, T.; Materano, M.; Matveyev, Y.; Schlueter, C.; Mikolajick, T.; Schroeder, U.; Müller, M. Impact of Vacancies and Impurities on Ferroelectricity in PVD- and ALD-Grown HfO₂ Films. *Appl. Phys. Lett.* **2021**, *118* (3), 032903. <https://doi.org/10.1063/5.0035686>.
- (169) Suzer, S.; Sayan, S.; Banaszak Holl, M. M.; Garfunkel, E.; Hussain, Z.; Hamdan, N. M. Soft X-Ray Photoemission Studies of Hf Oxidation. *J. Vac. Sci. A* **2003**, *21* (1), 106–109. <https://doi.org/10.1116/1.1525816>.
- (170) Hamouda, W.; Lubin, C.; Ueda, S.; Yamashita, Y.; Renault, O.; Mehmood, F.; Mikolajick, T.; Schroeder, U.; Negrea, R.; Barrett, N. Interface Chemistry of Pristine TiN/La:Hf_{0.5}Zr_{0.5}O₂ Capacitors. *Appl. Phys. Lett.* **2020**, *116* (25), 252903. <https://doi.org/10.1063/5.0012595>.
- (171) ASTM E112-13. *Standard Test Methods for Determining Average Grain Size*; ASTM International: West Conshohocken, PA, 2013.
- (172) Hillier, J. On the Investigation of Specimen Contamination in the Electron Microscope. *Journal of Applied Physics* **2004**, *19* (3), 226–230. <https://doi.org/10.1063/1.1715049>.
- (173) Binnig, G.; Quate, C. F.; Gerber, Ch. Atomic Force Microscope. *Phys. Rev. Lett.* **1986**, *56* (9), 930–933. <https://doi.org/10.1103/PhysRevLett.56.930>.
- (174) Song, J.; Zhou, Y.; Huey, B. D. 3D Structure–Property Correlations of Electronic and Energy Materials by Tomographic Atomic Force Microscopy. *Appl. Phys. Lett.* **2021**, *118* (8), 080501. <https://doi.org/10.1063/5.0040984>.

- (175) Kim, H. J.; Park, M. H.; Kim, Y. J.; Lee, Y. H.; Jeon, W.; Gwon, T.; Moon, T.; Kim, K. D.; Hwang, C. S. Grain Size Engineering for Ferroelectric $\text{Hf}_{0.5}\text{Zr}_{0.5}\text{O}_2$ Films by an Insertion of Al_2O_3 Interlayer. *Appl. Phys. Lett.* **2014**, *105* (19), 192903. <https://doi.org/10.1063/1.4902072>.
- (176) Sang, X.; Grimley, E. D.; Schenk, T.; Schroeder, U.; LeBeau, J. M. On the Structural Origins of Ferroelectricity in HfO_2 Thin Films. *Applied Physics Letters* **2015**, *106* (16), 162905. <https://doi.org/10.1063/1.4919135>.
- (177) Shimizu, T.; Katayama, K.; Kiguchi, T.; Akama, A.; Konno, T. J.; Funakubo, H. Growth of Epitaxial Orthorhombic $\text{YO}_{1.5}$ -Substituted HfO_2 Thin Film. *Appl. Phys. Lett.* **2015**, *107* (3), 032910. <https://doi.org/10.1063/1.4927450>.
- (178) Kiguchi, T.; Nakamura, S.; Akama, A.; Shiraishi, T.; Konno, T. J. Solid State Epitaxy of $(\text{Hf,Zr})\text{O}_2$ Thin Films with Orthorhombic Phase. *Journal of the Ceramic Society of Japan* **2016**, *124* (6), 689–693. <https://doi.org/10.2109/jcersj2.16073>.
- (179) Grimley, E. D.; Schenk, T.; Sang, X.; Pešić, M.; Schroeder, U.; Mikolajick, T.; LeBeau, J. M. Structural Changes Underlying Field-Cycling Phenomena in Ferroelectric HfO_2 Thin Films. *Adv. Electron. Mater.* **2016**, *2* (9), 1600173. <https://doi.org/10.1002/aelm.201600173>.
- (180) Zhou, B.; Shi, H.; Zhang, X. D.; Su, Q.; Jiang, Z. Y. The Simulated Vibrational Spectra of HfO_2 Polymorphs. *J. Phys. D: Appl. Phys.* **2014**, *47* (11), 115502. <https://doi.org/10.1088/0022-3727/47/11/115502>.
- (181) Raeliarijaona, A.; Cohen, R. E. First-Principles Calculations of Raman and Infrared Spectroscopy for Phase Identification and Strain Calibration of Hafnia. *Appl. Phys. Lett.* **2022**, *120* (24), 242903. <https://doi.org/10.1063/5.0092247>.
- (182) Adelman, C.; Tielens, H.; Dewulf, D.; Hardy, A.; Pierreux, D.; Swerts, J.; Rosseel, E.; Shi, X.; Bael, M. K. V.; Kittl, J. A.; Elshocht, S. V. Atomic Layer Deposition of Gd-Doped HfO_2 Thin Films. *J. Electrochem. Soc.* **2010**, *157* (4), G105. <https://doi.org/10.1149/1.3301663>.

- (183) Bechtel, H. A.; Muller, E. A.; Olmon, R. L.; Martin, M. C.; Raschke, M. B. Ultrabroadband Infrared Nanospectroscopic Imaging. *Proceedings of the National Academy of Sciences* **2014**, *111* (20), 7191–7196. <https://doi.org/10.1073/pnas.1400502111>.
- (184) Huber, A. J.; Wittborn, J.; Hillenbrand, R. Infrared Spectroscopic Near-Field Mapping of Single Nanotransistors. *Nanotechnology* **2010**, *21* (23), 235702. <https://doi.org/10.1088/0957-4484/21/23/235702>.
- (185) Richards, D.; Zayats, A.; Keilmann, F.; Hillenbrand, R. Near-Field Microscopy by Elastic Light Scattering from a Tip. *Philosophical Transactions of the Royal Society of London. Series A: Mathematical, Physical and Engineering Sciences* **2004**, *362* (1817), 787–805. <https://doi.org/10.1098/rsta.2003.1347>.
- (186) Duncan, W. D.; Williams, G. P. Infrared Synchrotron Radiation from Electron Storage Rings. *Appl. Opt., AO* **1983**, *22* (18), 2914–2923. <https://doi.org/10.1364/AO.22.002914>.
- (187) Bechtel, H. A.; Johnson, S. C.; Khatib, O.; Muller, E. A.; Raschke, M. B. Synchrotron Infrared Nano-Spectroscopy and -Imaging. *Surface Science Reports* **2020**, *75* (3), 100493. <https://doi.org/10.1016/j.surfrep.2020.100493>.
- (188) Bernacki, S.; Jack, L.; Kisler, Y.; Collins, S.; Bernstein, S. D.; Hallock, R.; Armstrong, B.; Shaw, J.; Evans, J.; Tuttle, B.; Hammett, B.; Rogers, S.; Nasby, B.; Henderson, J.; Benedetto, J.; Moore, R.; Pugh, C. R.; Fennelly, A. Standardized Ferroelectric Capacitor Test Methodology for Nonvolatile Semiconductor Memory Applications. *Integrated Ferroelectrics* **1993**, *3* (2), 97–112. <https://doi.org/10.1080/10584589308216704>.
- (189) Brennan, C. J. Characterization and Modelling of Thin-Film Ferroelectric Capacitors Using C-V Analysis. *Integrated Ferroelectrics* **1992**, *2* (1–4), 73–82. <https://doi.org/10.1080/10584589208215733>.
- (190) Cheng, Y.; Gao, Z.; Ye, K. H.; Park, H. W.; Zheng, Y.; Zheng, Y.; Gao, J.; Park, M. H.; Choi, J.-H.; Xue, K.-H.; Hwang, C. S.; Lyu, H. Reversible Transition between the Polar and Antipolar Phases and Its Implications for Wake-up and Fatigue in HfO₂-Based

- Ferroelectric Thin Film. *Nat Commun* **2022**, *13* (1), 645. <https://doi.org/10.1038/s41467-022-28236-5>.
- (191) Künneth, C.; Materlik, R.; Kersch, A. Modeling Ferroelectric Film Properties and Size Effects from Tetragonal Interlayer in $\text{Hf}_{1-x}\text{Zr}_x\text{O}_2$ Grains. *Journal of Applied Physics* **2017**, *121* (20), 205304.
- (192) Estandía, S.; Dix, N.; Gazquez, J.; Fina, I.; Lyu, J.; Chisholm, M. F.; Fontcuberta, J.; Sánchez, F. Engineering Ferroelectric $\text{Hf}_{0.5}\text{Zr}_{0.5}\text{O}_2$ Thin Films by Epitaxial Stress. *ACS Appl. Electron. Mater.* **2019**, *1* (8), 1449–1457. <https://doi.org/10.1021/acsaelm.9b00256>.
- (193) Fields, S. S.; Cai, T.; Jaszewski, S. T.; Salanova, A.; Mimura, T.; Heinrich, H. H.; Henry, M. D.; Kelley, K. P.; Sheldon, B. W.; Ihlefeld, J. F. Origin of Ferroelectric Phase Stabilization via the Clamping Effect in Ferroelectric Hafnium Zirconium Oxide Thin Films. *Adv. Electron. Mater.* **2022**, *n/a* (n/a), 2200601. <https://doi.org/10.1002/aelm.202200601>.
- (194) Shimizu, T.; Yokouchi, T.; Oikawa, T.; Shiraishi, T.; Kiguchi, T.; Akama, A.; Konno, T. J.; Gruverman, A.; Funakubo, H. Contribution of Oxygen Vacancies to the Ferroelectric Behavior of $\text{Hf}_{0.5}\text{Zr}_{0.5}\text{O}_2$ Thin Films. *Appl. Phys. Lett.* **2015**, *106* (11), 112904. <https://doi.org/10.1063/1.4915336>.
- (195) Tian, X.; Shibayama, S.; Nishimura, T.; Yajima, T.; Migita, S.; Toriumi, A. Evolution of Ferroelectric HfO_2 in Ultrathin Region down to 3 Nm. *Appl. Phys. Lett.* **2018**, *112* (10), 102902. <https://doi.org/10.1063/1.5017094>.
- (196) Tharpe, T.; Zheng, X.-Q.; Feng, P. X.-L.; Tabrizian, R. Resolving Mechanical Properties and Morphology Evolution of Free-Standing Ferroelectric $\text{Hf}_{0.5}\text{Zr}_{0.5}\text{O}_2$. *Advanced Engineering Materials* **2021**, *23* (12), 2101221. <https://doi.org/10.1002/adem.202101221>.
- (197) Materano, M.; Reinig, P.; Kersch, A.; Popov, M.; Deluca, M.; Mikolajick, T.; Boettger, U.; Schroeder, U. Raman Spectroscopy as a Key Method to Distinguish the Ferroelectric Orthorhombic Phase in Thin ZrO_2 -Based Films. *physica status solidi (RRL) – Rapid Research Letters* **2022**, *16* (4), 2100589. <https://doi.org/10.1002/pssr.202100589>.

- (198) Hsain, H. A.; Lee, Y.; Parsons, G.; Jones, J. L. Compositional Dependence of Crystallization Temperatures and Phase Evolution in Hafnia-Zirconia ($\text{Hf}_x\text{Zr}_{1-x}\text{O}_2$) Thin Films. *Appl. Phys. Lett.* **2020**, *116* (19), 192901. <https://doi.org/10.1063/5.0002835>.
- (199) Reyes-Lillo, S. E.; Garrity, K. F.; Rabe, K. M. Antiferroelectricity in Thin-Film ZrO_2 from First Principles. *Phys. Rev. B* **2014**, *90* (14), 140103. <https://doi.org/10.1103/PhysRevB.90.140103>.
- (200) Polakowski, P.; Müller, J. Ferroelectricity in Undoped Hafnium Oxide. *Appl. Phys. Lett.* **2015**, *106* (23), 232905. <https://doi.org/10.1063/1.4922272>.
- (201) Tauc, J.; Grigorovici, R.; Vancu, A. Optical Properties and Electronic Structure of Amorphous Germanium. *physica status solidi (b)* **1966**, *15* (2), 627–637. <https://doi.org/10.1002/pssb.19660150224>.
- (202) Mallick, A.; Lenox, M. K.; Beechem, T. E.; Ihlefeld, J. F.; Shukla, N. Oxygen Vacancy Contributions to the Electrical Stress Response and Endurance of Ferroelectric Hafnium Zirconium Oxide Thin Films. *Appl. Phys. Lett.* **2023**, *122* (13), 132902. <https://doi.org/10.1063/5.0142789>.
- (203) Hoppe, E. E.; Sorbello, R. S.; Aita, C. R. Near-Edge Optical Absorption Behavior of Sputter Deposited Hafnium Dioxide. *Journal of Applied Physics* **2007**, *101* (12), 123534. <https://doi.org/10.1063/1.2750406>.
- (204) Park, J.-W.; Lee, D.-K.; Lim, D.; Lee, H.; Choi, S.-H. Optical Properties of Thermally Annealed Hafnium Oxide and Their Correlation with Structural Change. *Journal of Applied Physics* **2008**, *104* (3), 033521. <https://doi.org/10.1063/1.2961326>.
- (205) Makuła, P.; Pacia, M.; Macyk, W. How To Correctly Determine the Band Gap Energy of Modified Semiconductor Photocatalysts Based on UV–Vis Spectra. *J. Phys. Chem. Lett.* **2018**, *9* (23), 6814–6817. <https://doi.org/10.1021/acs.jpcclett.8b02892>.
- (206) Lucovsky, G.; Zhang, Y.; Luning, J.; Afanase'v, V. V.; Stesmans, A.; Zollner, S.; Triyoso, D.; Rogers, B. R.; Whitten, J. L. Intrinsic Band Edge Traps in Nano-Crystalline HfO_2 Gate

- Dielectrics. *Microelectronic Engineering* **2005**, *80*, 110–113.
<https://doi.org/10.1016/j.mee.2005.04.052>.
- (207) Price, J.; Bersuker, G.; Lysaght, P. S. Identification of Electrically Active Defects in Thin Dielectric Films by Spectroscopic Ellipsometry. *Journal of Applied Physics* **2012**, *111* (4), 043507. <https://doi.org/10.1063/1.3684605>.
- (208) Wagner, T.; Hilfiker, J. n.; Tiwald, T. e.; Bungay, C. l.; Zollner, S. Materials Characterization in the Vacuum Ultraviolet with Variable Angle Spectroscopic Ellipsometry. *physica status solidi (a)* **2001**, *188* (4), 1553–1562.
[https://doi.org/10.1002/1521-396X\(200112\)188:4<1553::AID-PSSA1553>3.0.CO;2-A](https://doi.org/10.1002/1521-396X(200112)188:4<1553::AID-PSSA1553>3.0.CO;2-A).
- (209) Alterovitz, S. A.; Johs, B. Multiple Minima in the Ellipsometric Error Function. *Thin Solid Films* **1998**, *313–314*, 124–127. [https://doi.org/10.1016/S0040-6090\(97\)00784-0](https://doi.org/10.1016/S0040-6090(97)00784-0).
- (210) Govyadinov, A. A.; Amenabar, I.; Huth, F.; Carney, P. S.; Hillenbrand, R. Quantitative Measurement of Local Infrared Absorption and Dielectric Function with Tip-Enhanced Near-Field Microscopy. *J. Phys. Chem. Lett.* **2013**, *4* (9), 1526–1531.
<https://doi.org/10.1021/jz400453r>.
- (211) Kresse, G.; Furthmüller, J. Efficiency of Ab-Initio Total Energy Calculations for Metals and Semiconductors Using a Plane-Wave Basis Set. *Computational Materials Science* **1996**, *6* (1), 15–50. [https://doi.org/10.1016/0927-0256\(96\)00008-0](https://doi.org/10.1016/0927-0256(96)00008-0).
- (212) Kresse, G.; Furthmüller, J. Efficient Iterative Schemes for Ab Initio Total-Energy Calculations Using a Plane-Wave Basis Set. *Phys. Rev. B* **1996**, *54* (16), 11169–11186.
<https://doi.org/10.1103/PhysRevB.54.11169>.
- (213) Blöchl, P. E. Projector Augmented-Wave Method. *Phys. Rev. B* **1994**, *50* (24), 17953–17979. <https://doi.org/10.1103/PhysRevB.50.17953>.
- (214) Kresse, G.; Joubert, D. From Ultrasoft Pseudopotentials to the Projector Augmented-Wave Method. *Phys. Rev. B* **1999**, *59* (3), 1758–1775.
<https://doi.org/10.1103/PhysRevB.59.1758>.

- (215) Perdew, J. P.; Burke, K.; Ernzerhof, M. Generalized Gradient Approximation Made Simple. *Phys. Rev. Lett.* **1996**, *77* (18), 3865–3868.
<https://doi.org/10.1103/PhysRevLett.77.3865>.
- (216) Monkhorst, H. J.; Pack, J. D. Special Points for Brillouin-Zone Integrations. *Phys. Rev. B* **1976**, *13* (12), 5188–5192. <https://doi.org/10.1103/PhysRevB.13.5188>.
- (217) Krukau, A. V.; Vydrov, O. A.; Izmaylov, A. F.; Scuseria, G. E. Influence of the Exchange Screening Parameter on the Performance of Screened Hybrid Functionals. *The Journal of Chemical Physics* **2006**, *125* (22), 224106. <https://doi.org/10.1063/1.2404663>.
- (218) Depla, D.; Li, X. Y.; Mahieu, S.; Gryse, R. D. Determination of the Effective Electron Emission Yields of Compound Materials. *J. Phys. D: Appl. Phys.* **2008**, *41* (20), 202003.
<https://doi.org/10.1088/0022-3727/41/20/202003>.
- (219) Marcak, A.; Corbella, C.; de los Arcos, T.; von Keudell, A. Note: Ion-Induced Secondary Electron Emission from Oxidized Metal Surfaces Measured in a Particle Beam Reactor. *Review of Scientific Instruments* **2015**, *86* (10), 106102.
<https://doi.org/10.1063/1.4932309>.
- (220) Ganesan, R.; Akhavan, B.; Partridge, J. G.; McCulloch, D. G.; McKenzie, D. R.; Bilek, M. M. Evolution of Target Condition in Reactive HiPIMS as a Function of Duty Cycle: An Opportunity for Refractive Index Grading. *Journal of Applied Physics* **2017**, *121* (17), 171909. <https://doi.org/10.1063/1.4977824>.
- (221) Kubart, T.; Aijaz, A. Evolution of Sputtering Target Surface Composition in Reactive High Power Impulse Magnetron Sputtering. *J. Appl. Phys.* **2017**, *121* (17), 171903.
<https://doi.org/10.1063/1.4977814>.
- (222) Ferrec, A.; Kéraudy, J.; Jouan, P.-Y. Mass Spectrometry Analyzes to Highlight Differences between Short and Long HiPIMS Discharges. *Appl. Surf. Sci.* **2016**, *390*, 497–505. <https://doi.org/10.1016/j.apsusc.2016.08.001>.

- (223) Viloan, R. P. B.; Zanaška, M.; Lundin, D.; Helmersson, U. Pulse Length Selection for Optimizing the Accelerated Ion Flux Fraction of a Bipolar HiPIMS Discharge. *Plasma Sources Sci. Technol.* **2020**, *29* (12), 125013. <https://doi.org/10.1088/1361-6595/abc6f6>.
- (224) Narasimhan, V. K.; McBriarty, M. E.; Passarello, D.; Adinolfi, V.; Toney, M. F.; Mehta, A.; Littau, K. A. In Situ Characterization of Ferroelectric HfO₂ During Rapid Thermal Annealing. *physica status solidi (RRL) – Rapid Research Letters* **2021**, *15* (5), 2000598. <https://doi.org/10.1002/pssr.202000598>.
- (225) Stone, K. H.; Schelhas, L. T.; Garten, L. M.; Shyam, B.; Mehta, A.; Ndione, P. F.; Ginley, D. S.; Toney, M. F. Influence of Amorphous Structure on Polymorphism in Vanadia. *APL Materials* **2016**, *4* (7), 076103. <https://doi.org/10.1063/1.4958674>.
- (226) Böske, T. S.; Müller, J.; Bräuhaus, D.; Schröder, U.; Böttger, U. Ferroelectricity in Hafnium Oxide Thin Films. *Appl. Phys. Lett.* **2011**, *99* (10), 102903. <https://doi.org/10.1063/1.3634052>.
- (227) Böske, T. S.; Teichert, St.; Bräuhaus, D.; Müller, J.; Schröder, U.; Böttger, U.; Mikolajick, T. Phase Transitions in Ferroelectric Silicon Doped Hafnium Oxide. *Appl. Phys. Lett.* **2011**, *99* (11), 112904. <https://doi.org/10.1063/1.3636434>.
- (228) Müller, J.; Böske, T. S.; Bräuhaus, D.; Schröder, U.; Böttger, U.; Sundqvist, J.; Kücher, P.; Mikolajick, T.; Frey, L. Ferroelectric Zr_{0.5}Hf_{0.5}O₂ Thin Films for Nonvolatile Memory Applications. *Appl. Phys. Lett.* **2011**, *99* (11), 112901. <https://doi.org/10.1063/1.3636417>.
- (229) Mueller, S.; Summerfelt, S. R.; Muller, J.; Schroeder, U.; Mikolajick, T. Ten-Nanometer Ferroelectric Si:HfO₂ Films for Next-Generation FRAM Capacitors. *IEEE Electr. Device L.* **2012**, *33* (9), 1300–1302. <https://doi.org/10.1109/LED.2012.2204856>.
- (230) Mart, C.; Viegas, A.; Esslinger, S.; Czernohorsky, M.; Weinreich, W.; Mutschall, D.; Kaiser, A.; Neumann, N.; Grossmann, T.; Hiller, K.; Eng, L. M. Pyroelectric CMOS Compatible Sensor Element Based on Hafnium Oxide Thin Films. In *2020 Joint Conference of the IEEE International Frequency Control Symposium and International*

- Symposium on Applications of Ferroelectrics (IFCS-ISAF)*; IEEE: Keystone, CO, USA, 2020; pp 1–3. <https://doi.org/10.1109/IFCS-ISAF41089.2020.9234892>.
- (231) Smith, S. W.; Kitahara, A. R.; Rodriguez, M. A.; Henry, M. D.; Brumbach, M. T.; Ihlefeld, J. F. Pyroelectric Response in Crystalline Hafnium Zirconium Oxide ($\text{Hf}_{1-x}\text{Zr}_x\text{O}_2$) Thin Films. *Appl. Phys. Lett.* **2017**, *110* (7), 072901. <https://doi.org/10.1063/1.4976519>.
- (232) Hoffmann, M.; Pešić, M.; Chatterjee, K.; Khan, A. I.; Salahuddin, S.; Slesazeck, S.; Schroeder, U.; Mikolajick, T. Direct Observation of Negative Capacitance in Polycrystalline Ferroelectric HfO_2 . *Adv. Funct. Mater.* **2016**, *26* (47), 8643–8649. <https://doi.org/10.1002/adfm.201602869>.
- (233) Martin, D.; Yurchuk, E.; Müller, S.; Müller, J.; Paul, J.; Sundquist, J.; Slesazeck, S.; Schlösser, T.; van Bentum, R.; Trentzsch, M.; Schröder, U.; Mikolajick, T. Downscaling Ferroelectric Field Effect Transistors by Using Ferroelectric Si-Doped HfO_2 . *Solid-State Electron.* **2013**, *88*, 65–68. <https://doi.org/10.1016/j.sse.2013.04.013>.
- (234) Hsain, H. A.; Lee, Y.; Parsons, G.; Jones, J. L. Compositional Dependence of Crystallization Temperatures and Phase Evolution in Hafnia-Zirconia ($\text{Hf}_x\text{Zr}_{1-x}$) O_2 Thin Films. *Appl. Phys. Lett.* **2020**, *116* (19), 192901. <https://doi.org/10.1063/5.0002835>.
- (235) Müller, J.; Böske, T. S.; Schröder, U.; Mueller, S.; Bräuhaus, D.; Böttger, U.; Frey, L.; Mikolajick, T. Ferroelectricity in Simple Binary ZrO_2 and HfO_2 . *Nano Lett.* **2012**, *12* (8), 4318–4323. <https://doi.org/10.1021/nl302049k>.
- (236) Park, M. H.; Kim, H. J.; Kim, Y. J.; Lee, Y. H.; Moon, T.; Kim, K. D.; Hyun, S. D.; Fengler, F.; Schroeder, U.; Hwang, C. S. Effect of Zr Content on the Wake-Up Effect in $\text{Hf}_{1-x}\text{Zr}_x\text{O}_2$ Films. *ACS Appl. Mater. Inter.* **2016**, *8* (24), 15466–15475. <https://doi.org/10.1021/acsami.6b03586>.
- (237) Schlom, D. G.; Guha, S.; Datta, S. Gate Oxides Beyond SiO_2 . *MRS Bull.* **2008**, *33* (11), 1017–1025. <https://doi.org/10.1557/mrs2008.221>.

- (238) Hubbard, K. J.; Schlom, D. G. Thermodynamic Stability of Binary Oxides in Contact with Silicon. *Journal of Materials Research* **1996**, *11* (11), 2757–2776.
<https://doi.org/10.1557/JMR.1996.0350>.
- (239) Cheema, S. S.; Kwon, D.; Shanker, N.; dos Reis, R.; Hsu, S.-L.; Xiao, J.; Zhang, H.; Wagner, R.; Datar, A.; McCarter, M. R.; Serrao, C. R.; Yadav, A. K.; Karbasian, G.; Hsu, C.-H.; Tan, A. J.; Wang, L.-C.; Thakare, V.; Zhang, X.; Mehta, A.; Karapetrova, E.; Chopdekar, R. V.; Shafer, P.; Arenholz, E.; Hu, C.; Proksch, R.; Ramesh, R.; Ciston, J.; Salahuddin, S. Enhanced Ferroelectricity in Ultrathin Films Grown Directly on Silicon. *Nature* **2020**, *580* (7804), 478–482. <https://doi.org/10.1038/s41586-020-2208-x>.
- (240) Mistry, K.; Chau, R.; Choi, C.-H.; Ding, G.; Fischer, K.; Ghani, T.; Grover, R.; Han, W.; Hanken, D.; Hattendorf, M.; He, J.; Allen, C.; Hicks, J.; Huessner, R.; Ingerly, D.; Jain, P.; James, R.; Jong, L.; Joshi, S.; Kenyon, C.; Kuhn, K.; Lee, K.; Auth, C.; Liu, H.; Maiz, J.; McIntyre, B.; Moon, P.; Neiryneck, J.; Pae, S.; Parker, C.; Parsons, D.; Prasad, C.; Pipes, L.; Beattie, B.; Prince, M.; Ranade, P.; Reynolds, T.; Sandford, J.; Shifren, L.; Sebastian, J.; Seiple, J.; Simon, D.; Sivakumar, S.; Smith, P.; Bergstrom, D.; Thomas, C.; Troeger, T.; Vandervoorn, P.; Williams, S.; Zawadzki, K.; Bost, M.; Brazier, M.; Buehler, M.; Cappellani, A. A 45nm Logic Technology with High-K+Metal Gate Transistors, Strained Silicon, 9 Cu Interconnect Layers, 193nm Dry Patterning, and 100% Pb-Free Packaging. In *2007 IEEE International Electron Devices Meeting*; IEEE: Washington, DC, 2007; pp 247–250. <https://doi.org/10.1109/IEDM.2007.4418914>.
- (241) Hegde, R. I.; Triyoso, D. H.; Samavedam, S. B.; White, B. E. Hafnium Zirconate Gate Dielectric for Advanced Gate Stack Applications. *J. Appl. Phys.* **2007**, *101* (7), 074113.
<https://doi.org/10.1063/1.2716399>.
- (242) Adam, J.; Rogers, M. D. The Crystal Structure of ZrO₂ and HfO₂. *Acta Cryst.* **1959**, *12* (11), 951–951. <https://doi.org/10.1107/S0365110X59002742>.
- (243) Ruh, R.; Garrett, H. J.; Domagala, R. F.; Tallan, N. M. The System Zirconia-Hafnia. *J. Am. Ceram. Soc.* **1968**, *51* (1), 23–28. <https://doi.org/10.1111/j.1151-2916.1968.tb11822.x>.

- (244) Ruh, R.; Corfield, P. W. R. Crystal Structure of Monoclinic Hafnia and Comparison with Monoclinic Zirconia. *J. Am. Ceram. Soc.* **1970**, *53* (3), 126–129.
<https://doi.org/10.1111/j.1151-2916.1970.tb12052.x>.
- (245) Mitsuhashi, T.; Ichihara, M.; Tatsuke, U. Characterization and Stabilization of Metastable Tetragonal ZrO₂. *J. Am. Ceram. Soc.* **1974**, *57* (2), 97–101.
<https://doi.org/10.1111/j.1151-2916.1974.tb10823.x>.
- (246) Garvie, R. C. The Occurrence of Metastable Tetragonal Zirconia as a Crystallite Size Effect. *J. Phys. Chem.* **1965**, *69* (4), 1238–1243. <https://doi.org/10.1021/j100888a024>.
- (247) El-Shanshoury, I. A.; Rudenko, V. A.; Ibrahim, I. A. Polymorphic Behavior of Thin Evaporated Films of Zirconium and Hafnium Oxides. *J. Am. Ceram. Soc.* **1970**, *53* (5), 264–268. <https://doi.org/10.1111/j.1151-2916.1970.tb12090.x>.
- (248) Teufer, G. The Crystal Structure of Tetragonal ZrO₂. *Acta Cryst.* **1962**, *15* (11), 1187–1187. <https://doi.org/10.1107/S0365110X62003114>.
- (249) Desgreniers, S.; Lagarec, K. High-Density ZrO₂ and HfO₂ Crystalline Structures and Equations of State. *Phys. Rev. B* **1999**, *59* (13), 8467–8472.
<https://doi.org/10.1103/PhysRevB.59.8467>.
- (250) Hann, R. E.; Suitch, P. R.; Pentecost, J. L. Monoclinic Crystal Structures of ZrO₂ and HfO₂ Refined from X-Ray Powder Diffraction Data. *Journal of the American Ceramic Society* **1985**, *68* (10), C-285-C–286. <https://doi.org/10.1111/j.1151-2916.1985.tb11534.x>.
- (251) Mittmann, T.; Materano, M.; Chang, S.-C.; Karpov, I.; Mikolajick, T.; Schroeder, U. Impact of Oxygen Vacancy Content in Ferroelectric HZO Films on the Device Performance. In *2020 IEEE International Electron Devices Meeting (IEDM)*; 2020; p 18.4.1-18.4.4. <https://doi.org/10.1109/IEDM13553.2020.9372097>.
- (252) Kim, T.; Jeon, S. Pulse Switching Study on the HfZrO Ferroelectric Films With High Pressure Annealing. **2018**, *65* (5), 3.

- (253) Das, D.; Jeon, S. High-k $\text{Hf}_x\text{Zr}_{1-x}\text{O}_2$ Ferroelectric Insulator by Utilizing High Pressure Anneal. *IEEE TRANSACTIONS ON ELECTRON DEVICES* **2020**, *67* (6), 6.
- (254) Hyuk Park, M.; Joon Kim, H.; Jin Kim, Y.; Moon, T.; Seong Hwang, C. The Effects of Crystallographic Orientation and Strain of Thin $\text{Hf}_{0.5}\text{Zr}_{0.5}\text{O}_2$ Film on Its Ferroelectricity. *Appl. Phys. Lett.* **2014**, *104* (7), 072901. <https://doi.org/10.1063/1.4866008>.
- (255) Chen, K.-Y.; Tsai, Y.-S.; Wu, Y.-H. Ionizing Radiation Effect on Memory Characteristics for HfO_2 -Based Ferroelectric Field-Effect Transistors. *IEEE Electron Device Lett.* **2019**, *40* (9), 1370–1373. <https://doi.org/10.1109/LED.2019.2931826>.
- (256) Islamov, D. R.; Zalyalov, T. M.; Orlov, O. M.; Gritsenko, V. A.; Krasnikov, G. Ya. Impact of Oxygen Vacancy on the Ferroelectric Properties of Lanthanum-Doped Hafnium Oxide. *Appl. Phys. Lett.* **2020**, *117* (16), 162901. <https://doi.org/10.1063/5.0023554>.
- (257) Dole, S. L.; Hunter, O.; Wooge, C. J. Elastic Properties of Monoclinic Hafnium Oxide at Room Temperature. *J. Am. Ceram. Soc.* **1977**, *60* (11–12), 488–490. <https://doi.org/10.1111/j.1151-2916.1977.tb14088.x>.
- (258) Zhao, X.-S.; Shang, S.-L.; Liu, Z.-K.; Shen, J.-Y. Elastic Properties of Cubic, Tetragonal and Monoclinic ZrO_2 from First-Principles Calculations. *J. Nucl. Mater.* **2011**, *415* (1), 13–17. <https://doi.org/10.1016/j.jnucmat.2011.05.016>.
- (259) SelCuk, A.; Atkinson, A. Elastic Properties of Ceramic Oxides Used in Solid Oxide Fuel Cells (SOFC). *J. Eur. Ceram. Soc.* **1997**, *17*, 1523–1532.
- (260) Fields, S. S.; Olson, D. H.; Jaszewski, S. T.; Fancher, C. M.; Smith, S. W.; Dickie, D. A.; Esteves, G.; Henry, M. D.; Davids, P. S.; Hopkins, P. E.; Ihlefeld, J. F. Erratum: “Compositional and Phase Dependence of Elastic Modulus of Crystalline and Amorphous $\text{Hf}_{1-x}\text{Zr}_x\text{O}_2$ Thin Films” [Appl. Phys. Lett. 118, 102901 (2021)]. *Appl. Phys. Lett.* **2021**, *119* (12), 129901. <https://doi.org/10.1063/5.0068886>.
- (261) Kruv, A.; McMitchell, S. R. C.; Clima, S.; Okudur, O. O.; Ronchi, N.; Van den bosch, G.; Gonzalez, M.; De Wolf, I.; Houdt, J. V. Impact of Mechanical Strain on Wakeup of HfO_2

- Ferroelectric Memory. In *2021 IEEE International Reliability Physics Symposium (IRPS)*; 2021; pp 1–6. <https://doi.org/10.1109/IRPS46558.2021.9405159>.
- (262) Kieffer, J.; Valls, V.; Blanc, N.; Hennig, C. New Tools for Calibrating Diffraction Setups. *J. Synchrotron Radiat.* **2020**, *27* (2), 558–566. <https://doi.org/10.1107/S1600577520000776>.
- (263) Esteves, G.; Ramos, K.; Fancher, C. M.; Jones, J. L. *LIPRAS: Line-Profile Analysis Software*; 10.13140/RG.2.2.29970.25282/3.
- (264) Spinella, C.; Battaglia, A.; Priolo, F.; Campisano, S. U. Ion-Assisted Nucleation in Amorphous Silicon: Ion Mass and Dose Rate Effects. *EPL* **1991**, *16* (3), 313–318. <https://doi.org/10.1209/0295-5075/16/3/016>.
- (265) Marques, L. A.; Caturla, M.-J.; Huang, H.; Díaz De La Rubia, T. Molecular Dynamics Studies of the Ion Beam Induced Crystallization in Silicon. *MRS Online Proceedings Library* **1995**, *396* (1), 201. <https://doi.org/10.1557/PROC-396-201>.
- (266) Im, J. S.; Atwater, H. A. Ion Irradiation Enhanced Crystal Nucleation in Amorphous Si Thin Films. *Appl. Phys. Lett.* **1990**, *57* (17), 1766–1768. <https://doi.org/10.1063/1.104061>.
- (267) Lian, J.; Zhang, J.; Namavar, F.; Zhang, Y.; Lu, F.; Haider, H.; Garvin, K.; Weber, W. J.; Ewing, R. C. Ion Beam-Induced Amorphous-to-Tetragonal Phase Transformation and Grain Growth of Nanocrystalline Zirconia. *Nanotechnology* **2009**, *20* (24), 245303. <https://doi.org/10.1088/0957-4484/20/24/245303>.
- (268) Lu, F.; Zhang, J.; Huang, M.; Namavar, F.; Ewing, R. C.; Lian, J. Phase Transformation of Nanosized ZrO₂ upon Thermal Annealing and Intense Radiation. *J. Phys. Chem. C* **2011**, *115* (15), 7193–7201. <https://doi.org/10.1021/jp109558s>.
- (269) Dhanunjaya, M.; Khan, S. A.; Pathak, A. P.; Avasthi, D. K.; Rao, S. V. S. N. Ion Induced Crystallization and Grain Growth of Hafnium Oxide Nano-Particles in Thin-Films Deposited by Radio Frequency Magnetron Sputtering. *J. Phys. D: Appl. Phys.* **2017**, *50* (50), 505301. <https://doi.org/10.1088/1361-6463/aa9723>.

- (270) Li, Z.; Liu, J.; Zhai, P.; Liu, L.; Xu, L.; Zhang, S.; Hu, P.; Zeng, J. The Higher-k Phase Formation in Amorphous HfO₂ Films by Swift Heavy Ion Irradiation. *Journal of Crystal Growth* **2022**, 585, 126600. <https://doi.org/10.1016/j.jcrysgro.2022.126600>.
- (271) Ziegler, J. F.; Ziegler, M. D.; Biersack, J. P. SRIM - The Stopping and Range of Ions in Matter (2010). *Nuclear Instruments and Methods in Physics Research B* **2010**, 268, 1818–1823. <https://doi.org/10.1016/j.nimb.2010.02.091>.
- (272) Vogel, T.; Zintler, A.; Kaiser, N.; Guillaume, N.; Lefèvre, G.; Lederer, M.; Serra, A. L.; Piros, E.; Kim, T.; Schreyer, P.; Winkler, R.; Nasiou, D.; Olivo, R. R.; Ali, T.; Lehninger, D.; Arzumanov, A.; Charpin-Nicolle, C.; Bourgeois, G.; Grenouillet, L.; Cyrille, M.-C.; Navarro, G.; Seidel, K.; Kämpfe, T.; Petzold, S.; Trautmann, C.; Molina-Luna, L.; Alff, L. Structural and Electrical Response of Emerging Memories Exposed to Heavy Ion Radiation. *ACS Nano* **2022**, 16 (9), 14463–14478. <https://doi.org/10.1021/acsnano.2c04841>.
- (273) Vogel, T.; Kaiser, N.; Petzold, S.; Piros, E.; Guillaume, N.; Lefèvre, G.; Charpin-Nicolle, C.; David, S.; Vallée, C.; Nowak, E.; Trautmann, C.; Alff, L. Defect-Induced Phase Transition in Hafnium Oxide Thin Films: Comparing Heavy Ion Irradiation and Oxygen-Engineering Effects. *IEEE Transactions on Nuclear Science* **2021**, 68 (8), 1542–1547. <https://doi.org/10.1109/TNS.2021.3085962>.